The Development and Analysis of a Retinal Imaging Densitometer

Christopher T. Jones

School of Optometry and Vision Sciences and

School of Physics and Astronomy

Cardiff University

Submitted for the Degree of Doctor of Philosophy

2017

Supervised by:

Tom Margrain, Alison Binns, Ashley Wood

Summary

The research described in this thesis presents the development and evaluation of a prototype multispectral, imaging densitometer. Ultimately, the aim was to develop a method of simultaneously isolating the contributions from the three main photoreceptors, across the retina. Thus, providing the clinician with a viable tool for assessing outer retinal function both efficiently and directly.

The construction and use of the prototype multispectral imaging densitometer was described in detail. Healthy participants were recruited and imaged to evaluate the baseline capability of the device. The results were validated through comparison to published values for optical density, regeneration rates and photopigment distribution as obtained through *in vivo*, *in vitro* and *in situ* techniques. A novel ocular reflection model was developed to characterise and mathematically remove the pre-receptoral stray light from the images.

Whilst the preliminary investigation returned regeneration rates in line with values from the literature, a 'red shift' of approximately 30nm was highlighted in the experimental absorption spectra of the visual pigments, hindering their isolation. Investigation into this phenomenon suggested that the cause was pre-receptoral stray light, with both the crystalline lens and the inner retinal layers contributing to the effect. Attempts to remove the crystalline lens component showed a partial reduction of the 'red shift'. Greater success was achieved through the modelling of the experimental ocular reflection data to simultaneously characterise the contribution from both components.

This research has shown that mapping of visual pigment optical density across the retina is possible with the retinal densitometer described. With further development, the technique is likely to become a useful tool in the diagnosis and monitoring of outer retinal disease.

Acknowledgements

I would like to express my sincere gratitude to my supervisors Tom Margrain (Cardiff University), Ashley Wood (Cardiff University) and Alison Binns (City University) for their support and guidance in helping me undertake this research.

This thesis would not have been possible without the dedication and hard work of the entire team who worked on this project at the United Kingdom Astronomy and Technology Centre. Particular thanks must go to Dave Melotte, David Henry, Stephen Todd and David Atkinson (UK Astronomy Technology Centre) for their continual assistance with the design, construction and technical support of the densitometry device described in this thesis.

I am also grateful to James Fergusson (Cardiff University) for his contributions to the design and construction of the model eye described and used in this thesis.

The research presented in this thesis was supported by Cardiff University through the President's Research Scholarship, by the National Institute for Health Research invention for innovation through grant (II-FS-0110-14064) and Science and Technologies Facilities Council through the proof of concept funds (1213-03).

Table of Contents

List of Figures

List of Tables

List of Abbreviations

AMD	Age-Related Macular Degeneration
ATP	Adenosine triphosphate
$BaSO_4$	Barium Sulphate
BNC	the Bayonet Neill–Concelman connector
BRB	Blood Retinal Barrier
Ca+	Calcium Ion
CCD	Charged Coupled Device
cGMP	Cyclic Guanosine Monophosphate (gated ion channel)
CRBP	Cellular Retinoid Binding Protein
DNA	Deoxyribonucleic Acid
DS	Spherical Dioptre
EMCCD	Electron Multiplying Charged Coupled Device
ERG	Electroretinogram
FoI	Field of Illumination
FWHM	Full Width Half Maximum
GUI	Graphical User Interface
HeNe	Helium-neon laser
Hz	Hertz (frequency)
IDL	Interactive Data Language
ILM	Inner Limiting Membrane
IRBP	Interphotoreceptor Retinoid Binding Protein
K+	Potassium Ion
L- cone	Long wavelength sensitive cone photoreceptors
LED	Light Emitting Diode
LOCS III	Lens Opacity Classification System, 3rd iteration
M- cone	Medium wavelength sensitive cone photoreceptors

MLP	the Mahroo, Lamb and Pugh model describing the kinetics of photoreceptor regeneration
Model I	Ocular reflection model, first described by van Norren and Tiemeijer (1986)
Model II	Ocular reflection model, first described by Delori and Pflibsen (1989)
n	Refractive Index
Na+	Sodium Ion
NADPH	Nicotinamide Adenine Dinucleotide Phosphate
OCT	Optical Coherence Tomography
OD	Optical Density
OLM	Outer Limiting Membrane
ONH	Optic Nerve Head
POS	Photoreceptor Outer Segment
r	rate of regeneration, as defined by the MLP model
RMSE	Root Mean Square Error
RNFL	Retinal Nerve Fibre Layer
RPE	Retinal Pigment Epithelium
S- cone	Short wavelength sensitive cone photoreceptors
SD	Standard Deviation
SEM	Standard Error of the Mean
SLO	Scanning Laser Ophthalmoscope
UKATC	United Kingdom Astronomy Technology Centre
UV	Ultra Violet light
VA	Visual Acuity
ΔOD	The measured, double pass, optical density
τ	Tau. The time taken for a visual pigment to return to $1 - {}^{1}/_{e}$ (~63.3%) of it maximum value.
λ	Wavelength

Chapter 1 - Introduction

1.1. Overview

Since the introduction of the ophthalmoscope, it has been possible to observe the fundus *in vivo* (Helmoltz 1851). Clinical techniques, such as slit lamp bio-microscopy, photographic imaging and optical coherence tomography (OCT) provide stereoscopic, enface and cross-sectional assessment of retinal structures, but these imaging techniques provide no information about underlying retinal physiology.

By quantifying changes in ocular reflectance before and after exposure to a light source, retinal densitometry facilitates the objective measurement of the light absorbing visual pigments *in vivo* (Alpern 1971; Alpern and Pugh 1974). Through this technique, the quantity of these pigments and the kinetics of their regeneration may be investigated, both of which are known to change with pathology (Liem et al. 1996). As such, retinal densitometry provides a non-invasive method of probing outer retinal function (Liem et al. 1996; Berendschot et al. 2003). Despite its clinical potential, retinal densitometry remains a technically challenging and laborious technique. Perhaps it is for these reasons that densitometry has, to date, only been employed in a research setting.

This thesis describes the development and evaluation of a novel imaging retinal densitometer capable of measuring visual pigment kinetics over space and time. The ultimate aim was to aid the development of a device for use in a clinical setting.

Chapter 1 describes the key ocular tissues and their specific absorption characteristics. Chapter 2 presents a systematic review of the literature regarding the fundamental principles, history and published results of retinal densitometry. This literature review shaped the specific aims and objectives of the investigations described in this thesis, which are presented at the end of Chapter 2. Chapter 3 introduces, in detail, the retinal densitometer used throughout these investigations,

and outlines the general methods for obtaining densitometry measurements. Two pilot studies are described in Chapter 4, presenting the preliminary results from the densitometer. These results were modelled to derive the rod and cone absorption spectra, regeneration rates and optical densities. Discrepancies between these results and the published literature were identified. These discrepancies highlighted the limitations of the current imaging and analysis techniques, which needed to be addressed. Chapter 5 addresses whether metarhodopsin III may be impacting the results, adds to the current knowledge of rhodopsin bleaching characteristics by investigating the half bleaching constant for rhodopsin and investigates long wavelength retinal reflectivity. Chapter 6 presents investigations carried out to characterise and overcome the attenuation of short wavelength light seen in the preliminary data. The development of a novel and anatomically accurate model eye is described in Chapter 7, where it is shown to be capable of calibrating absolute ocular reflectance. Chapter 8 discusses the literature surrounding ocular reflection modelling. Chapter 9 describes a novel ocular reflection model capable of isolating reflections from the inner retinal layers. This model was used to generate topographical maps of haemoglobin, melanin and visual pigment optical density whilst also characterising the reflectance profile of the inner retinal layers and sclera. Chapter 10 presents a detailed discussion and summary of the work in this thesis followed by plans for future work.

1.2. Ocular structure

The optics of the eye focus light onto the retina. In the human eye, this focussing is performed by the cornea and crystalline lens (Figure 1.1). The light sensitive retina is responsible for converting photons into electrical signals that can be interpreted by the visual cortex (e.g. visual perception). The retina is reliant on the retinal pigment epithelium (RPE), Bruch's membrane and the vascular systems of the inner retina and choroid for nourishment and disposal of waste products (Baker et al. 1991). The following sections will discuss, in more detail, the anatomy integral to ocular densitometry.

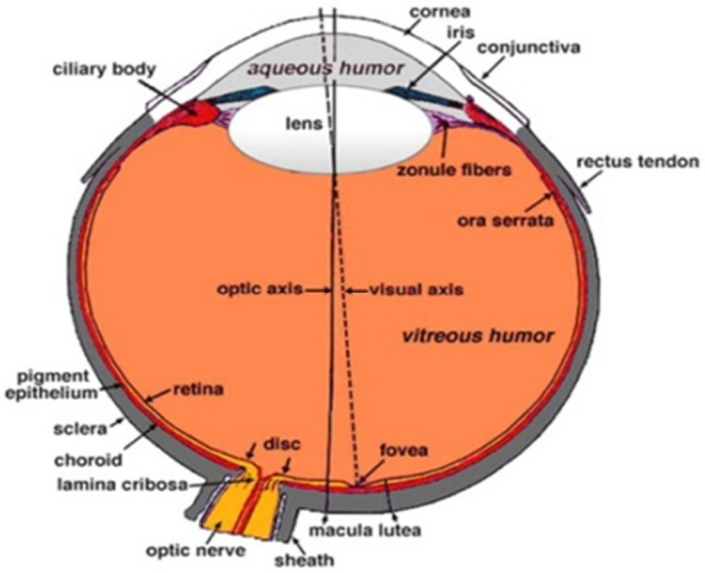

Figure 1.1 Schematic diagram of the human eye highlighting key ocular tissues and features (Kolb 2012).

1.2.1. Cornea

The cornea provides the largest refractive change to light entering the eye. Its shape is similar to a 11mm diameter meniscus lens, with a convex front surface and concave back surface and a centre thickness of ~550µm, comprising a refractive power of ~40DS (Tunnacliffe 1993; Oyster 1999). Structurally, the corneal stroma is composed of tightly packed collagen fibres, which maintain its transparency. The diameter of these collagen fibres, 30-32nm, is less than the wavelength of visible light, which lends itself to the presence of Rayleigh scattering within the cornea (Daxer et al. 1998; Jacques 2013). The absorption properties of the cornea are discussed in Section 1.5.1.

1.2.2. Crystalline lens

Although the majority of refraction is performed by the cornea, the crystalline lens provides additional focusing power and, within limits, can alter its refractive state to ensure a focussed image upon the retina. Known as accommodation, this is achieved by deformation of the crystalline lens caused by the contraction and relaxation of the ciliary muscle. The lens is made up of nuclear and cortical layers. Like in the cornea, the particle size of the lens fibres (7-14nm) is smaller than the wavelength

of light and may therefore contribute to Rayleigh scattering (Wooten and Geri 1987; Jacques 2013). The greater volume of the lens, which is around 4.5mm in thickness, along with a smaller particle size creates more internal scattering than the cornea (Delori and Pflibsen 1989; Jacques 2013). The absorption properties of the crystalline lens are discussed in Section 1.5.1.

1.2.3. Aqueous and vitreous humour

The aqueous and vitreous humour fill the anterior and posterior chambers of the eye. The aqueous is composed almost entirely of water (98-99%) with traces of ions, inflammatory cells and mediators, neurotransmitters and metabolic waste (Goel et al. 2010). The vitreous is composed of a network of collagen fibrils and hyaluronan, creating a gel like structure (Le Goff and Bishop 2008). The absorption properties of the humours are discussed in Section 1.5.1.

1.2.4. Neurosensory retina

The neural retina is a transparent, complex multi-cellular tissue, comprising seven layers, as detailed in Figure 1.2 and visible in Figure 1.4. The exact distribution of the retinal layers depends upon topographical location and functional specialisation. Primarily, it comprises photoreceptor, bipolar, retinal ganglion, horizontal, amacrine and Müller cells. These cells form three layers of cell bodies and two layers of synapses (see Figure 1.2). The basic structure of the retina is supported by Müller cells, which form the inner and outer limiting membranes (ILM and OLM), delineating the neural retina. Photons of light pass through the retinal layers to the photoreceptor outer segments (POS) beyond the OLM, where phototransduction occurs.

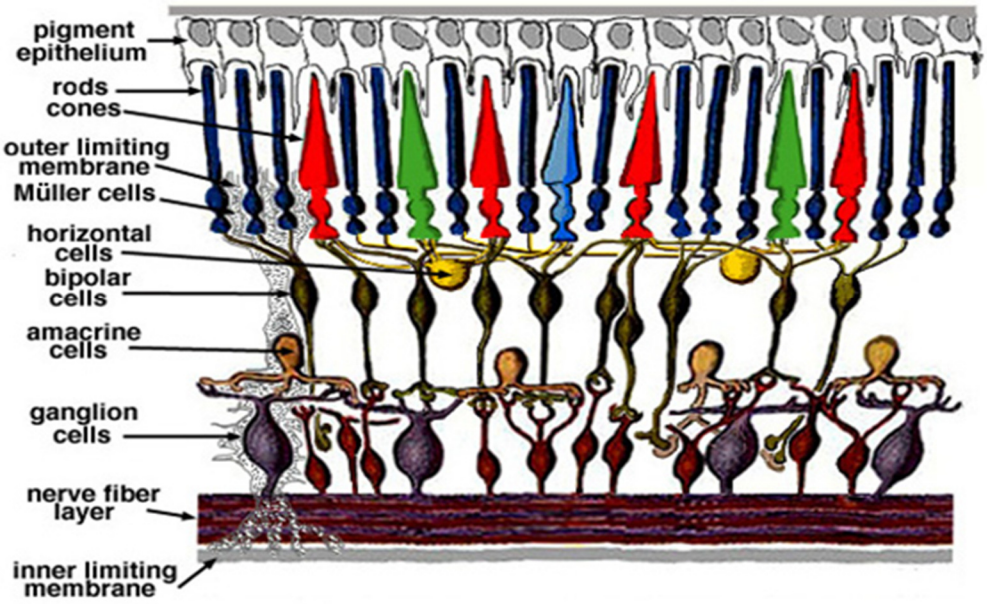

Figure 1.2 Schematic diagram of the retinal layers (Kolb 2011).

Anterior to the OLM are the densely packed layers of photoreceptor cell bodies, synapsing with bipolar and horizontal cells in the outer plexiform layer. Next, the inner nuclear layer contains the nuclei of these cells and the nuclei of Müller and amacrine cells. The bipolar and amacrine cells then synapse with the retinal ganglion cells at the inner plexiform layer, with the ganglion cell layer containing the nuclei for these cells. The innermost layer contains the nerve fibres, which take sensory information out of the eye via the optic nerve to the lateral geniculate nucleus (Baker et al. 1991). The outer retina and RPE are integral in the process of visual pigment regeneration (Section 1.3). The retinal layers will be described in more detail in the following sections.

1.2.4.1. Retinal topography

The primate fundus is unique among mammals, having a highly specialised retinal topography which affects the distribution of the layers. To facilitate high visual acuity (VA), a high degree of specialisation is seen in the macular region. The macula is roughly 3mm in diameter, centred on the visual axis, approximately 4mm temporally and 0.8mm below the optic disc (Polyak 1941). The area is composed of several concentric zones: the central foveola, the fovea, parafovea and perifovea.

The fovea is 1.5mm in diameter (approximately 5° of visual angle) and contains the highest density of cone photoreceptors (Polyak 1941). This concentration peaks at 161,000cones/mm^2 in the foveola, the central 0.35mm or 1.2° of visual angle as shown in Figure 1.3 (Osterberg 1935).

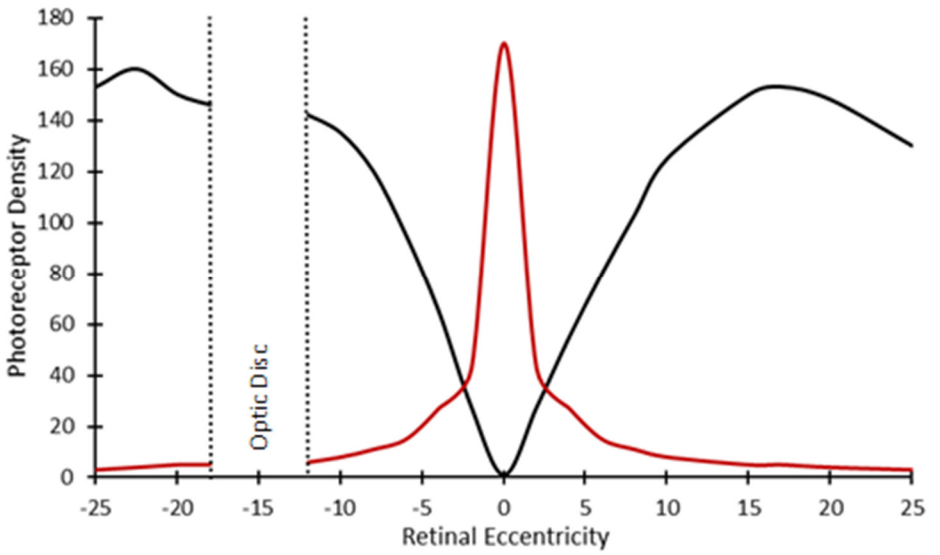

Figure 1.3 Rod (solid black line) and combined L- M- and S- cone (solid red line) densities with retinal eccentricity, adapted from Osterberg (1935).

The foveal region is avascular with second and third order neurones being displaced laterally to reduce pre-receptoral light scatter, creating a foveal pit, see Figure 1.4. Morphology of cone outer segments within the foveal region provides further specialisation; whilst in general the rods (2µm) are thinner than cones (6µm), in the foveal region cones are 1.5µm in diameter (Oyster 1999). Finally, macular pigment is present across the central 2° of visual angle (Snodderly et al. 1984; Kilbride et al. 1989). These anatomical features all combine to facilitate the high visual acuity at this retinal location (Polyak 1941; Curcio et al. 1990).

Beyond the fovea the number of cone photoreceptors drops rapidly, with a density one order of magnitude less only 1° away from the fovea (Curcio et al. 1990). Rod photoreceptors increase in density at a similar rate, becoming the dominant cell type by 5°, with a peak density of 160,000mm^2 by 18° in addition to a central rod free zone, see Figure 1.3 (Osterberg 1935; Curcio et al. 1990). The proportion of photoreceptors to retinal ganglion cell bodies increases in the retinal periphery for

both rod and cone pathways (Oyster 1999). This leads to an increase in spatial summation and a reduction in visual acuity (VA) and increasing sensitivity to dim lights. There are no photoreceptors at the optic nerve head.

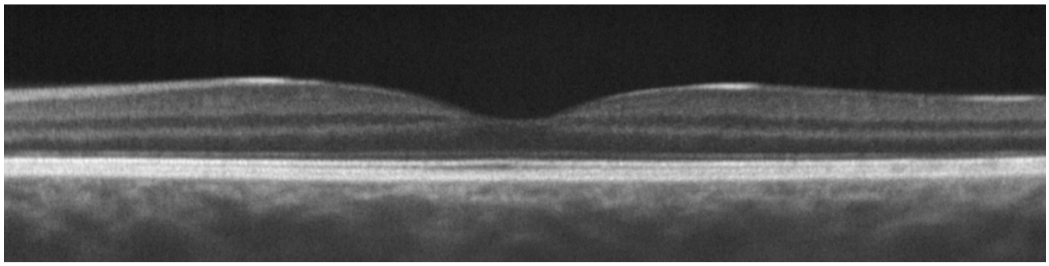

Figure 1.4 A central OCT scan of a healthy macula obtained from a 1040nm research device. The retinal layers, along with some variations in retinal topography can be seen in the image. Of note is the foveal pit (central) with associated reduction in neural retina and increased photoreceptor density.

The retinal nerve fibre layer (RNFL) is the innermost layer of the retina and contains approximately 1,200,000 axons originating from the retinal ganglion cell bodies (Quigley et al. 1982). Each axon leaves the eye via the optic nerve, traversing the retina in an arcuate fashion, but never crossing the horizontal midline. In order not to interfere with vision the axons within the RNFL are unmyelinated, however they do still reflect some light and thus are not present at the fovea (Kolb 2011). As the concentration of photoreceptors increases and the photoreceptor to ganglion cell ratio lowers with foveal proximity there are proportionally more axons in this region, which can often be seen during ophthalmoscopy in the young eye.

1.2.4.2. Photoreceptors

Rod and cone photoreceptors are responsible for phototransduction, the process by which light energy from a photon is converted into an action potential. Both types of photoreceptor comprise distinct inner and outer segments, connected by the cilium. The inner segment contains the cell body, nerve axons, Golgi apparatus and numerous mitochondria. The outer segment contains visual pigment molecules, densely packed in membranous discs, providing a large surface area to increase photon catch (Oyster 1999).

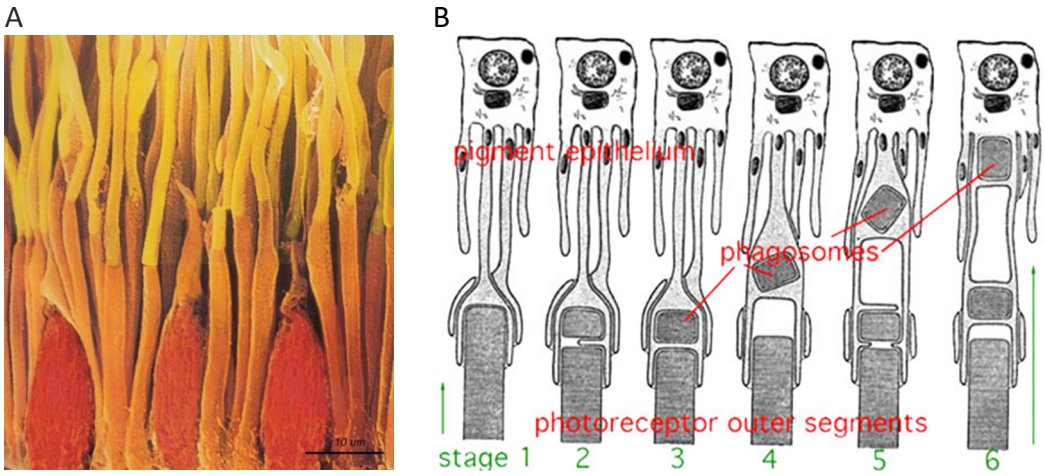

Figure 1.5 A) Shows a scanning election micrograph of rod and cone photoreceptors (Kolb 2013). B) A schematic diagram of rod outer segment disc shedding (Kolb 2013).

The structure of the photoreceptor outer segment (POS) differs between rod and cone photoreceptors, as shown in Figure 1.5. Rods have longer, cylindrical outer segments and stacked disc membranes containing rhodopsin, whilst cones are shorter and conical with their visual opsin contained within a folded disc membrane (Kolb 2013).

The photoreceptor inner segment provides the energy for phototransduction to occur in the outer segment via vast stores of mitochondria. Photoreceptor discs are renewed and shed on a diurnal basis. This disc shedding is thought to be necessitated by damage caused by oxidisation, free radicals and waste products (Kolb 2013). New discs are added to the base of the stack by cilium outpouching whilst older discs are shed from the tip into the extracellular space, then engulfed and phagocytosed by RPE apical membranes, as seen in Figure 1.5 (Kolb 2013). Healthy photoreceptor function is supported by the RPE, which plays a key role in the visual cycle and phagocytosis of spent POS discs and will be discussed next.

1.2.4.3. Retinal pigment epithelium

The RPE is a single layer of cells whose contents include melanin, the enzymes required in the retinoid cycle and organelles for the digestion of shed photoreceptor membranes. The basal side is smooth and adjoins Bruch's membrane, whilst the inner surface is made up of many apical microvilli (Figure 1.6) which, together with a

specialised extra-cellular matrix, facilitates a close interaction with the POS (Strauss, 2005).

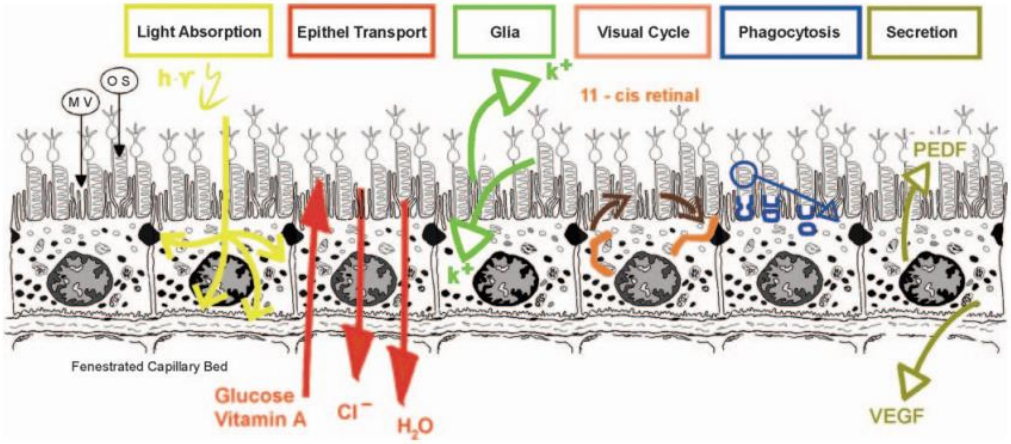

Figure 1.6 A schematic illustration highlighting the location, structure and function of the RPE (Strauss 2005).

The RPE performs many essential functions, highlighted in Figure 1.6, which relate to photoreceptor sensitivity, disc renewal and retinal health. These functions include the following (see Strauss (2005) for a review):

1. absorption of stray light;
2. recycling of retinoid;
3. phagocytosis of shed photoreceptor membranes;
4. secretion of growth factors (vascular endothelial growth factor and pigment epithelium-derived factor) as well as the ability to repair damaged lipids, proteins and DNA;
5. immune modulation and maintenance of the blood retinal barrier (BRB); and
6. control of ion homeostasis and efficient spatial ion buffering during photoreceptor activity (Bok 1993; Strauss 2005).

The array of functions performed by the RPE are essential for visual function to such an extent that the RPE and photoreceptors can be regarded as a single functional

unit (Strauss 2005). Most relevant to this thesis is its role in the recycling of retinoids, which is discussed in detail in Section 1.3.3.

1.2.4.4. Bruch's membrane

Located between the RPE and choroidal blood supply, Bruch's membrane comprises five layers: the basement membranes of the RPE and choriocapillaris, an inner and outer collagenous layer and an elastin layer. Bruch's membrane has two primary functions; the provision of structural support for the RPE and the restriction of choroidal and retinal cellular exchange (Booij et al. 2010). The ability of Bruch's membrane to perform these functions depends upon its structure, with the collagen and elastin layers acting as a molecular sieve. With age, the functionality of this layer decreases because of increasing collagen cross linking, thickening and a reduction in its elastic nature (Booij et al. 2010). These changes are likely to impact on the transport of materials through the structure, leading to the build-up of retinal waste products within and beneath the RPE, and a decrease in the availability of metabolites from the choroidal circulation at the level of the RPE and retina (Pauleikhoff et al. 1990; Booij et al. 2010). Bruch's membrane is the outermost layer of the eye before the choroidal blood supply.

1.2.4.5. Blood supply

The processes involved in phototransduction and the maintenance of the dark current in photoreceptor cells (Section 1.3.1) are metabolically intensive, and necessitate high rates of delivery of oxygen and other metabolites, as well as the removal of waste materials (Sickel 1972; Nowak 2006). These retinal functions are supported by an extensive outer retinal vascular system, a 'wall of blood', known as the choroidal circulation. Present between the retina and sclera, the choroid is the outermost structure of the eye and divided into three vascular layers (Haller's layer, Sattler's layer and choriocapillaris), see Figure 1.7.

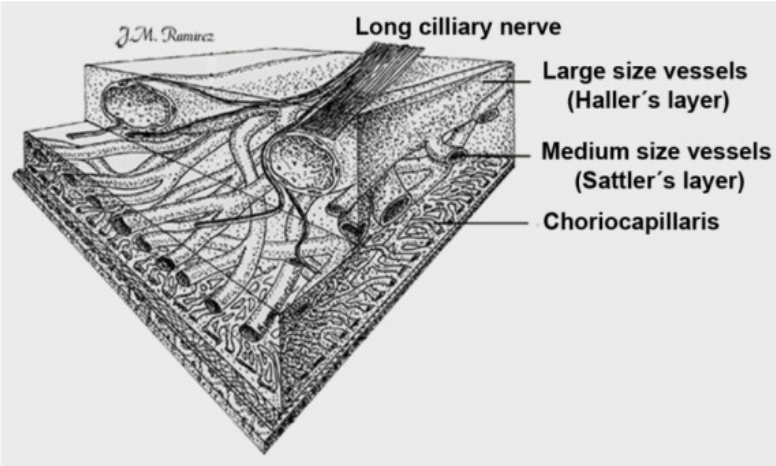

Figure 1.7 A schematic of the choroidal vascular supply (Ramirez et al. 1999).

The choroidal circulation provides the outer retina and central avascular region with its blood supply. Smaller choroidal capillaries comprise a dense network of fenestrated vessels, known as the choriocapillaris, and are fed by the larger vessels of the Sattler and Haller's layers. The main choroidal arteries are supplied by the long and short posterior ciliary arteries. The arteries enter the globe near the optic nerve and divide into three localised vascular layers; outer, medial and inner. Large vortex veins drain the choroidal blood supply, penetrate the sclera and join with the ophthalmic vein (Hayreh 1975). The choroidal system provides 65-85% of the nutrients received by the retina, reflecting the high metabolic rate required for outer retinal processes; in contrast, only 4% of the ocular blood flow is supplied by the retinal vascular system (Alm and Bill 1973).

The central retinal artery enters the retinal space through the optic nerve and subdivides into four main intra retinal branches supplying three capillary networks, all draining through corresponding retinal veins to the central retinal vein (Oyster 1999). A secondary, or cilioretinal, artery provides an alternative blood supply to the macula and is estimated to be present in 30% of eyes (Justice and Lehmann 1976). The inner capillary layer lies within the nerve fibre layer, with the outer layer lying within the ganglion cell layer (Weingeist 1978).

The foveal region is avascular (Figure 1.8). Haemoglobin absorbs light across the visible spectrum, reducing the number of photons reaching the photoreceptors. Hence, an avascular foveal region aids good visual acuity (Berendschot et al. 2003).

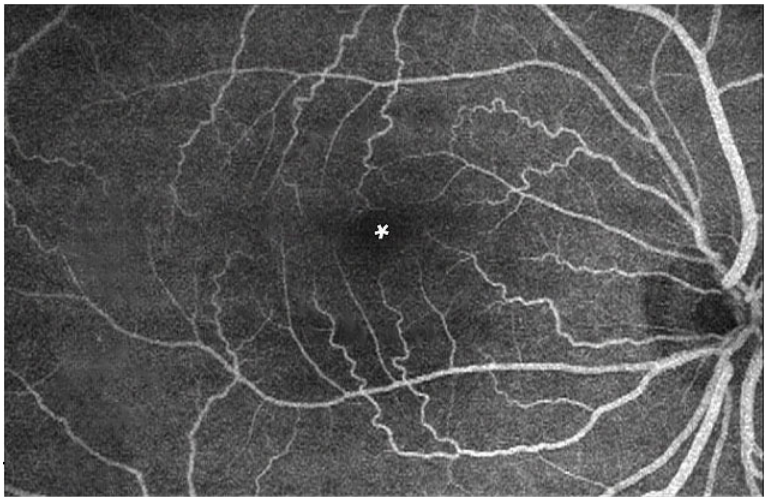

Figure 1.8 Fluorescein angiogram of the central retina. The main retinal blood vessels are obvious, as is the avascular region around the foveola (asterisk) (Kolb 2011).

1.3. Visual pigment kinetics

The absorption of light alters the configuration of the chromophores found within the visual pigment molecules, initiating the phototransduction cascade and converting light energy into the electrical signals required for vision (McBee et al. 2001).

The concentration of visual pigment is reduced by incident light of a high enough intensity to cause a photoisomerisation event (Alpern 1971). Visual pigments are not an infinite resource, the amount of pigment present in the retina is dependent on the balance between the rate at which photons cause photoisomerisation of the visual pigments and the rate at which pigment can be regenerated by the visual cycle (Alpern 1971). A fully regenerated photoreceptor is referred to as 'dark adapted', whilst one with no active visual pigment is referred to as 'bleached'. To aid understanding of visual pigment kinetics, the processes involved will be discussed.

1.3.1. The dark current

In the dark-adapted state, the photoreceptor is in a state of depolarisation due to the dark current. This is maintained by the flow of sodium (Na^+), calcium (Ca^{2+}) and potassium (K^+) ions between the photoreceptors and the intercellular matrix. While the dark current is circulating, the photoreceptor remains depolarised, releasing the neurotransmitter glutamate into the photoreceptor synapse with bipolar and horizontal cells (Copenhagen and Jahr 1989; McBee et al. 2001). The response of bipolar cells is proportional to the amount of glutamate released by the photoreceptors at the synapse. ON-bipolar cells are inhibited (hyperpolarised), whilst OFF-bipolar cells are depolarised by an increased release of glutamate at the synapse.

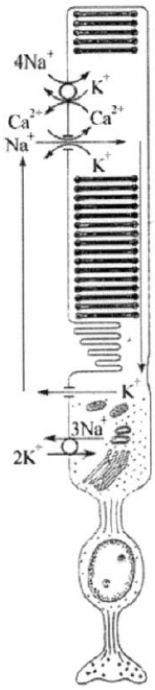

Figure 1.9 A schemtic outlining the ion transfer which generates the dark current (McBee et al. 2001).

The outer segment cell membrane is crossed by cGMP (cyclic guanosine monophosphate) gated ion channels allowing the passage of Na^+, Ca^{2+} and K^+ ions (Figure 1.9**)**. Na^+ ions from the interphotoreceptor matrix (IPM) flow into the photoreceptor via the cGMP gated cation channels in the photoreceptor outer

segment, whence they can diffuse through the cilium into the inner segment. ATP dependent channel pumps present in the inner segment pump Na^+ out into the IPM, whilst allowing K^+ to enter the photoreceptor (McBee et al. 2001). Ion exchangers in the outer segment prevent total depolarisation by returning Ca^{2+} and K^+ to the IPM in exchange for Na^+ (McBee et al. 2001). In the light, the transduction cascade results in a decrease in cGMP, outer segment channel closure and cell hyperpolarisation. The following paragraphs describe the transduction cascade.

1.3.2. The phototransduction cascade

In a dark-adapted state, the membranous discs of the rod outer segments all contain high concentrations of visual pigment, rhodopsin. These pigment molecules are composed of the protein opsin covalently bound to the chromophore 11-cis-retinal (Lamb and Pugh 2004). Light absorption triggers the photoisomerisation of 11-cis-retinal, turning it into all-trans-retinal within the pigment molecule. The photoisomerisation of the chromophore transforms the photopigment to all-trans-retinal and opsin via the photo-intermediaries metarhodopsin II and III (Pepe 2001). Being enzymatically active, metarhodopsin triggers the phototransduction cascade by converting the protein transducin into its active form (Lamb and Pugh 2004). Transducin activates the enzyme phosphodiesterase, catalysing the degradation of the intracellular messenger cGMP. As cGMP breaks down, the gated ion channels close and the cell hyperpolarises, resulting in less glutamate being released at the photoreceptor synapse. This leads to a change in the polarisation of the 2^{nd} order neurons, signalling a visual response.

Transducin is continuously converted by metarhodopsin II until its inactivation by rhodopsin kinase and arrestin (Lamb and Pugh 2004). This inactivation stops the degradation of cGMP, re-opening the gated ion channels, allowing the cell to gradually regain its depolarised state, ending the visual response (Lamb and Pugh 2004).

1.3.3. The retinoid cycle

The process of converting inactive visual pigment molecules back to their active state, the retinoid cycle, has been well characterised (Lamb and Pugh 2004). This process differs for rod and cone visual pigments, as shown in Figure 1.10 and Figure 1.11.

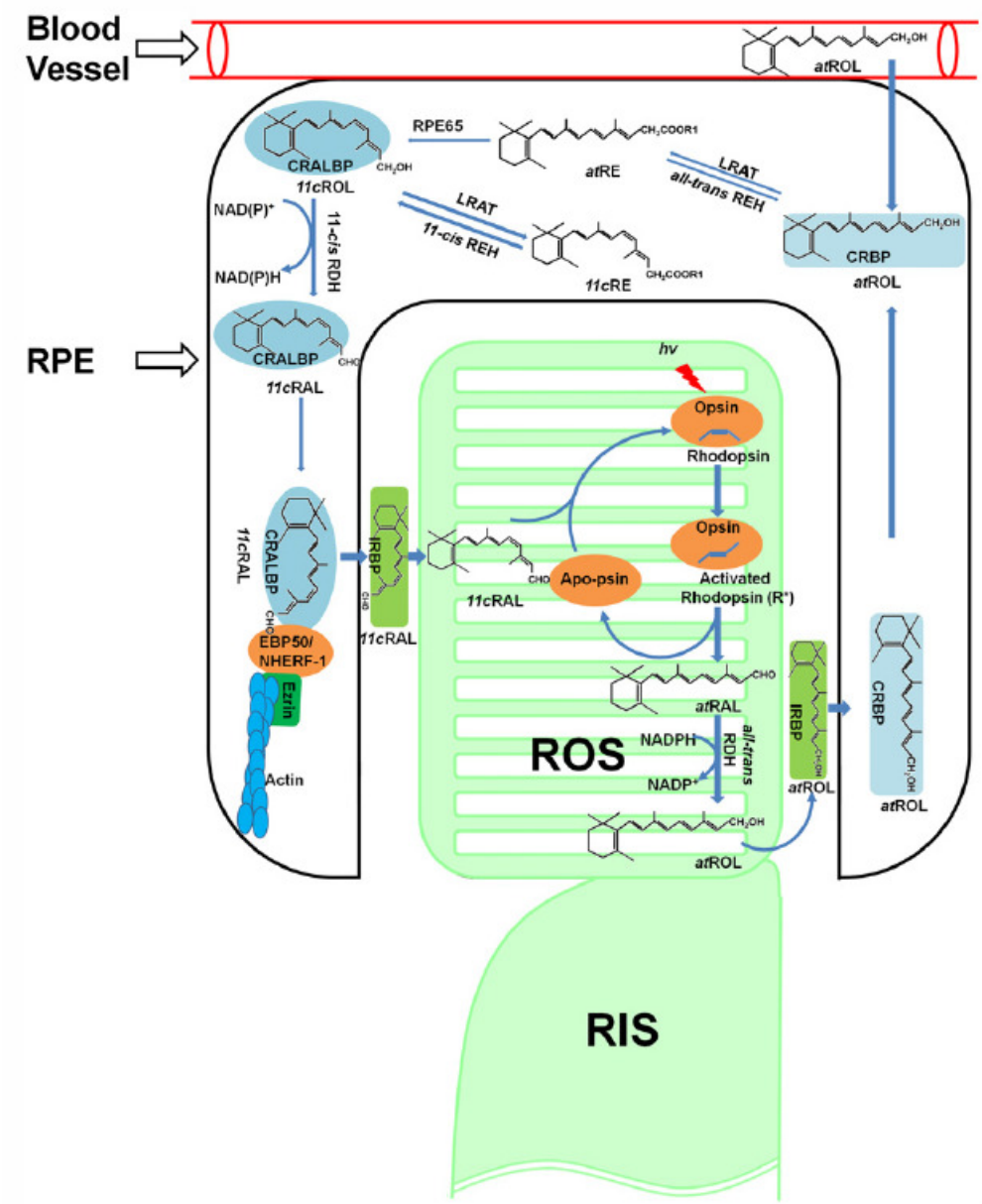

Figure 1.10 An illustration of the biochemical processes involved in the rhodopsin retinoid cycle (Wang and Kefalov 2011). See text in Section 1.3.3.1 for details.

1.3.3.1. Rhodopsin regeneration

The regeneration of rhodopsin largely takes place within the RPE (McBee et al. 2001). Once separated from opsin, all-trans-retinal is reduced to all-trans-retinol by all-trans-retinal dehydrogenase. The inter-photoreceptor binding protein (IRBP) facilitates the removal of all-trans-retinol from the outer segment of the photoreceptor into the RPE cell cytoplasm, with the lone opsin molecule remaining

in the outer segment (Lamb and Pugh 2004). Within the RPE, the enzyme retinyl ester isomerohydrolase causes the isomerisation of all-trans-retinol to 11-cis-retinol, this is then oxidised into the 11-cis-retinal form by 11-cis retinol dehydrogenase. In a separate pathway, direct photo-isomerisation of all-trans-retinol to 11-cis-retinal by the G-protein-coupled receptor provides a minor contribution to the 11-cis-retinal stock. IPRB then facilitates the return of 11-cis-retinal to the photoreceptor outer segments where it binds to a lone opsin molecule, recreating a photo-labile rhodopsin molecule (McBee et al. 2001). This last step is thought to be the rate limiting step in the regeneration of visual pigment, and is dependent on the rate-limited supply of 11-cis retinal from the RPE to the photoreceptor outer segments (Lamb and Pugh 2004; Mahroo and Lamb 2004).

1.3.3.2. Photopsin regeneration

The time constant of visual pigment regeneration is much shorter for cone (~100 seconds) than rod visual pigments (~400 seconds) (Alpern 1971). The speed of cone regeneration, combined with the biochemical limits of the RPE mediated retinoid cycle to support cone vision in bright illumination, points to an alternative cone regeneration pathway (Mata et al. 2002; Lamb and Pugh 2004; Wang and Kefalov 2011). This theory is supported by the identification of the enzymes required to convert all-trans-retinol to 11-cis retinol within the Müller cells and the ability of cone cells to perform the last step of converting 11-cis-retinol to 11-cis retinal within their outer segments (Mata et al. 2002; Wang and Kefalov 2011).

Wang and Kefalov (2011) provide an account of the cone-specific retinoid cycle (see Figure 1.11). All-trans-retinal is reduced to all-trans-retinol, which is transported to the Müller cells, possibly chaperoned by IRPB. Within the Müller cells, all-trans-retinol binds to the cellular retinol binding protein (CRBP) and is directly isomerised to 11-cis-retinol by Isomerase II (Mata et al. 2002; Wang and Kefalov 2011). IRBP is thought to aid the transport of 11-cis-retinol to cone photoreceptor inner segments, where it moves to the outer segment. Once within the outer segment, reduction to 11-cis-retinal is either by oxidisation by an unidentified 11-cis retinal dehydrogenase, or by coupling to all-trans-retinal reduction (Wang and Kefalov

2011). 11-cis-retinal is then free to bind with a free opsin molecule. This proposed pathway has yet to be fully confirmed, but appears to run in parallel with the established rod retinoid cycle (Wang and Kefalov 2011).

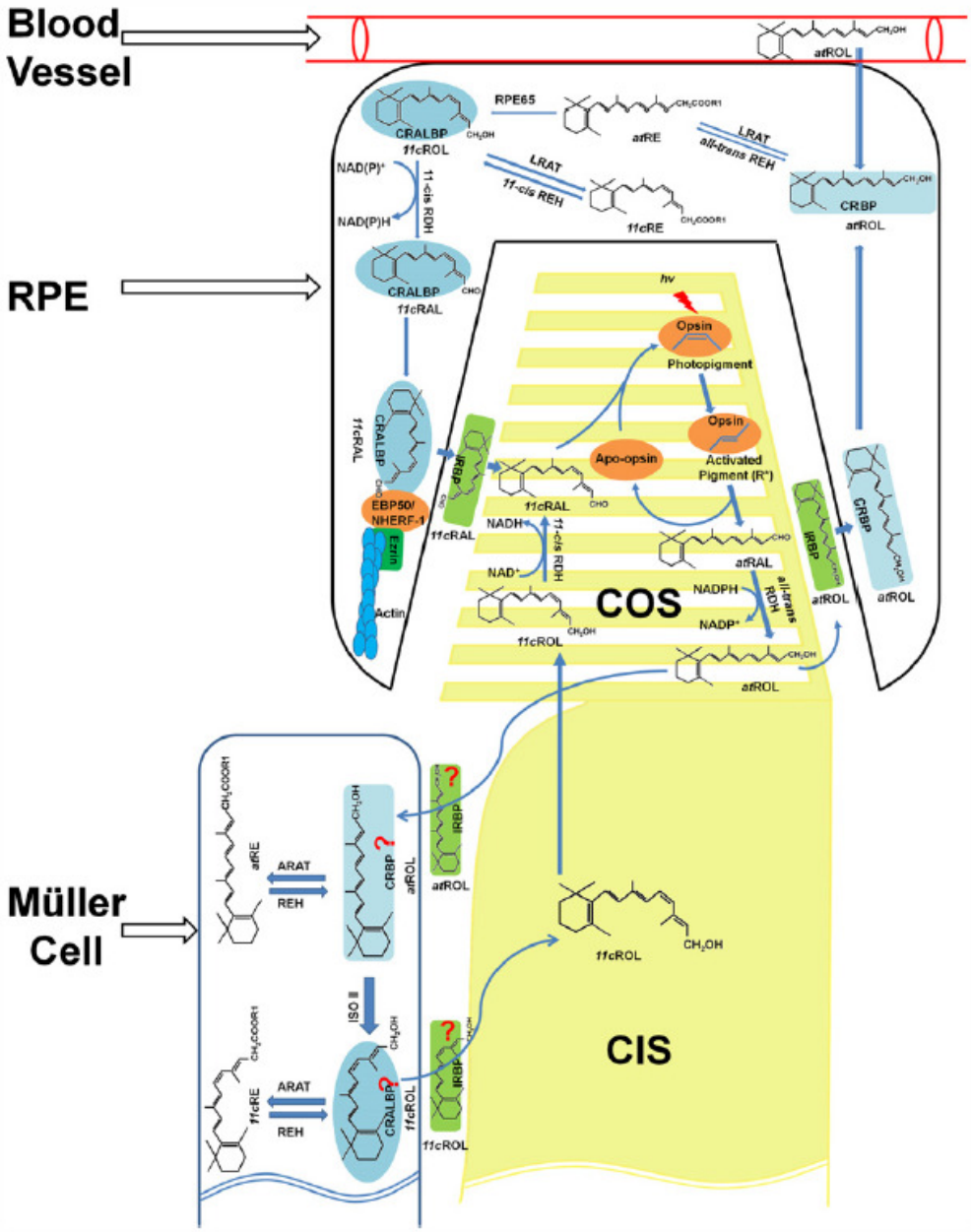

Figure 1.11 An illustration of the biochemical processes involved in the photopsin retinoid cycle (Wang and Kefalov 2011). See text in Section 1.3.3.2 for details.

1.4. Assessment of visual pigment kinetics

As the phototransduction cascade and retinoid cycle drive the visual system, techniques capable of the *in vivo* assessment of visual pigment kinetics could provide clinicians with vital information on visual functionality. These processes are dependent on the photoreceptors and associated structures (RPE, Bruch's membrane and choroid). Hence, the mapping of visual pigment kinetics has the potential to aid diagnosis and improve monitoring of any outer retinal disease; such as age related macular degeneration (AMD) and retinitis pigmentosa (Liem et al. 1996). For comparison, techniques currently available for the clinical assessment of outer retinal function will be discussed here. The relative merits of each technique are highlighted in Table 1.1.

1.4.1. Dark adaptometry

Dark adaptation refers to the recovery of visual threshold following exposure to a bright light. In 1937 the first detailed psychophysical investigation of dark adaptation showed striking results, seen in Figure 1.12 (Hecht et al. 1937). It was noted that there was a change in threshold exceeding 8 log units as the eye recovered to its dark-adapted state after a substantial bleach of photopigment. As threshold dropped, the data fell into two parts, highlighting the different kinetics of rod and cone regeneration discussed in Section 1.3. Finally, it was apparent that the recovery of light sensitivity is a lengthy process. Whilst early work suggested that the recovery of rod and cone thresholds each followed a single exponential time-course (Hecht et al. 1937), more recently it has been demonstrated that the rod branch of recovery may be modelled using two linear functions reflecting different components of rod photopigment regeneration (Lamb and Pugh 2004). An additional, first component of rod recovery occurs during the early part of the dark adaptation process whilst cones continue to determine threshold, and so is masked by the cone branch of the adaptation function (Hecht et al. 1937).

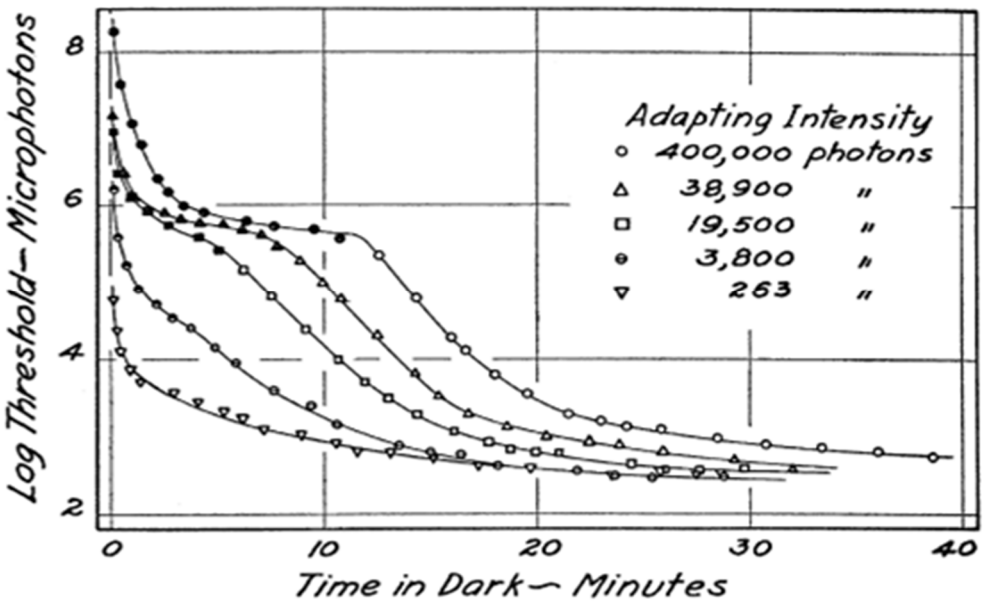

Figure 1.12 Classic dark adaptation measurements, from psychophysical techniques (Hecht et al. 1937). This shows the reduction with time of the minimum stimulus intensity seen by a participant.

The recovery of visual function during dark adaptation is largely dependent on the regeneration of the visual pigments. Hence this technique provides an indirect, subjective assessment of photoreceptor kinetics. The technique and its limitations are discussed in 1.4.1.1.

1.4.1.1. Limitations

The psychophysical assessment of dark adaptation is a simple technique, with little more needed than a variable light source of known wavelength. However, whilst providing an insight into photoreceptor kinetics, any psychophysical test reflects the activity of the entire visual pathway. The measured threshold is modified by the amplification of the visual response; thresholds measured by psychophysics remain raised by 3 log units after the majority of visual pigment has regenerated (Hecht et al. 1937; Alpern 1971). In conjunction with this, assessment of the regeneration of rhodopsin requires a long testing protocol, with normal subjects requiring at least 30 minutes to reach absolute threshold after a substantial proportion of photopigment has been bleached (Hecht et al. 1937). The measurement duration must be extended further for those suffering from slowed regeneration e.g. people with AMD (Gaffney et al. 2012). Although the long test duration of up to 60 minutes has

previously made this technique unviable for use in routine clinical practice, recent work on the AdaptDx dark adaptometer has shown that it is possible to differentiate between people with early AMD and healthy controls within as little as 6.5 minutes, as shown in Figure 1.13A (Jackson et al. 2014). However, in the longitudinal evaluation of visual function, such as when monitoring treatment outcomes, it is necessary to obtain an actual value for the time taken to dark adapt as opposed to recording a failure to reach a criterion state of dark adaptation within a pre-determined timeframe. In order to obtain these data, a prolonged recording time is still required with the AdaptDx adaptometer (see Figure 1.13B).

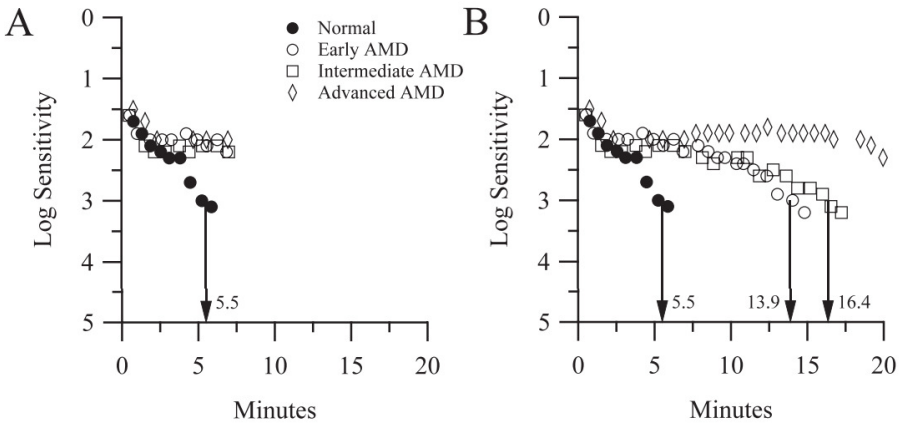

Figure 1.13 Showing results from the AdaptDx device and the time taken for individuals with AMD and age similar controls to reach a criterion threshold (the 'rod intercept') within the second component of rod recovery. A) Showing results from the truncated test of 6.5 minutes where healthy controls reached the rod intercept within the timeframe, whilst people with AMD did not. B) Showing the extended test of 20 minutes, demonstrating the increase in the rod intercept with advancing disease severity (Jackson et al. 2014).

1.4.2. Electrophysiology

Electrophysiology is an objective technique for studying the electrical properties of biological cells and tissues, a detailed description of electrophysiology is given by Perlman (2012). Evoked potentials are assessed by measuring the voltage change after stimulation across the structure being investigated. The measurement of retinal evoked potentials is referred to as electroretinography. Unlike dark adaptometry, the electroretinogram (ERG) does provide an objective measure of retinal activity.

The ERG has been used in several ways to investigate photoreceptor kinetics. In particular, the leading edge of the a-wave has been used as a surrogate measure of photopigment regeneration (Paupoo et al. 2000; Mahroo and Lamb 2004,2012). For example, Mahroo and Lamb (2004,2012) assumed the amplitude of the photopic ERG a-wave, measured at 14-15ms post flash, was an indication of the concentration of cone visual pigment present and showed it to be linearly related to bleaching intensity (Mahroo and Lamb 2004). They demonstrated that the change in a-wave amplitude after a bleach followed a time course which could be described by a rate-limited model of photopigment regeneration. It is possible that the a-wave recovery was also influenced by adaptation occurring in other retinal layers however, the time course of the change corresponded well to the published densitometric measurements of photopigment regeneration, as shown in Figure 1.14 (van Norren and van de Kraats 1989b; Mahroo and Lamb 2012). A similar approach was used by Thomas and Lamb (1999) to evaluate the regeneration of pigment in rod photoreceptors.

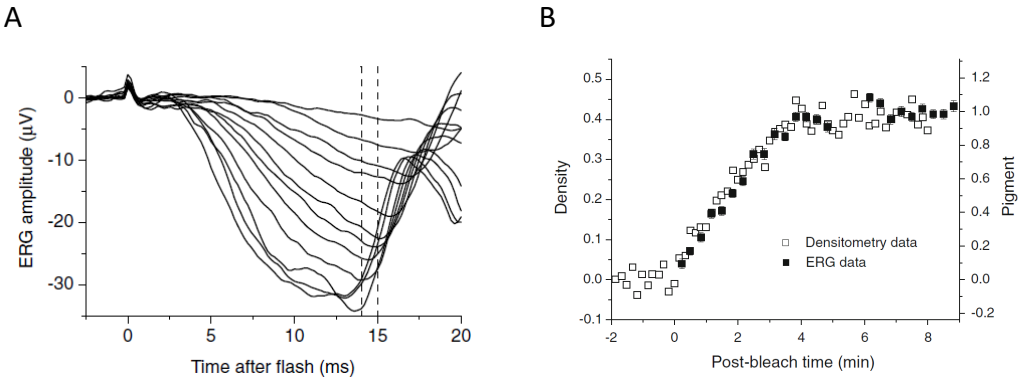

Figure 1.14 A) Showing a family of a-waves obtained after bleaches of increasing intensity (Mahroo and Lamb 2004). B) A comparison of regeneration rates recorded using electrophysiology (right hand axis) and densitometry (left hand axis) (Mahroo and Lamb 2012).

A pragmatic alternative is to evaluate the recovery of amplitude of the steady state 41Hz ERG after exposure to an adapting light (Binns and Margrain 2005). As data are continuously collected, this allows the time course of recovery to be assessed after a single bleaching exposure. Although this signal has principally been attributed to bipolar cell activity (Kondo and Sieving 2002), the recovery of the amplitude of the first harmonic of this response following a bleach mirrors that of cone photopigment

regeneration (Binns and Margrain 2005). This 'ERG photostress test' has been used to investigate outer retinal pathology, such as AMD (Binns and Margrain 2005; Binns and Margrain 2007; Wood et al. 2011).

As with dark adaptometry, there are some practical limitations to electroretinography.

1.4.2.1. Limitations

Electrophysiology is a complex technique which, due to the time-consuming nature of the recording and minimally invasive electrode placements, requires both a high level of participant co-operation and clinician training. Even so, substantial between-subject and between-session variability in amplitude has been noted (Grover et al. 2003; Fishman et al. 2005).

With respect to the evaluation of outer retinal function, whilst electrophysiology provides a certain measure of isolation of activity from specific groups of retinal cells, the peaks and troughs measured represent the summed activity of different neurone groups. Hence, the a-wave is not an uncontaminated measure of visual pigment kinetics, but shaped by signals from the bipolar cells and the inner retina as well as the photoreceptors (Granit 1933; Brown 1968; Miller and Dowling 1970). Recent work by Robson (2014) suggests that mathematical modelling of the leading edge of the a- wave may be used to isolate photoreceptoral responses. However, whilst this modelling approach has shown success (Robson and Frishman 2014), it is yet to be widely employed and the convention remains the measurement of the peaks and troughs of visible subcomponents (McCulloch et al. 2015). The simultaneous recording of isolated responses from the rod and cone systems is not possible using this conventional approach.

A further limitation of the full-field ERG is the lack of spatial resolution i.e. the measured signal is a sum of all activity across the whole retina (Hood 2000). Rod and cone photoreceptors can be isolated topographically using a focal ERG. However, the substantial averaging required to provide an optimal signal-to-noise ratio limits spatial resolution. The multifocal ERG does provide some spatial resolution, limited

to either 63 or 103 retinal loci (Hood 2000). However, as this response is derived by mathematical processing, its retinal origins are less well understood than the full-field flash ERG (Hood 2000).

1.4.3. Retinal densitometry

Optical density defines the degree to which any light absorbing pigment attenuates transmitted light. As pigments have specific light absorption properties dependent on wavelength, the optical density is wavelength dependent, resulting in a characteristic absorption spectrum for each pigment. The calculation of optical density is a relatively simple concept, describing how well a material absorbs light as the ratio between incident and transmitted light.

Retinal densitometry is an objective technique comparing the reflectance of the light and dark-adapted retina to quantify the optical density of visual pigments *in vivo*, either at a single time point or during pigment regeneration. As such, it has been used to directly measure visual pigment kinetics since the 1950s (Campbell and Rushton 1955; Rushton 1956a). It is an objective technique (Rushton 1956a), capable of investigating rod and cone kinetics separately (Rushton 1956b,1963a) with spatial resolution (Faulkner and Kemp 1984). As densitometry is not currently used as a clinical technique, there is no 'standard' device or technique available, instead a myriad of different optical designs and techniques have been used to evaluate visual pigment kinetics.

Densitometry perhaps owes its lack of widespread application in clinical and research fields to technological limitations. These limitations will be discussed in detail later, but deserve a brief mention here. Firstly, there is the small signal being measured, for example, reported rhodopsin optical density measurements are in the region of 0.2 (Ripps and Weale 1969b; Liem et al. 1996), further discussed in Chapter 2. Secondly, there is the low signal-to-noise ratio, difficult to overcome as incident light must be kept to a minimum to facilitate pigment regeneration (Rushton 1956a), further discussed in Chapter 2. Compounding these factors is the density of other

ocular absorbing layers and the light attenuating effect of internal stray light (van de Kraats et al. 1996), further discussed in Chapters 6, 7 and 8.

However, densitometry holds several advantages over electrophysiological and psychophysical techniques; these are highlighted in Table 1.1. Key advantages are the objective nature of the technique, the direct evaluation of the visual pigment and the potential for the simultaneous, spatially resolved assessment of rod and cone regeneration across the retina.

Table 1.1 Highlighting the relative benefits of visual pigment densitometry

	Dark Adaptation	Electrophysiology	Densitometry
Cheap	X		
Simple equipment	X		
Established data base	X	X	
Objective		X	X
High sensitivity		X	X
High specificity			X
High spatial resolution			X
Direct assessment of visual pigment			X

1.4.3.1. Clinical applications

These advantages outlined in Section 1.4.3 make retinal densitometry suitable for investigations into any disorder where the function of the outer retina is compromised. Despite the current limitations preventing the clinical application of the technique densitometry has been used to successfully investigate a wide variety of outer retinal disorders in a research setting, these include; retinitis pigmentosa (Perlman and Auerbach 1981), Ushers syndrome (Fulton and Hansen 1987), acute posterior multifocal-placoid pigment epithelium (Keunen et al. 1989) and myotonic dystrophy (Bruggen et al. 1992). A detailed description of these investigations is given in Section 2.6.4.

One outer retinal pathology not yet investigated is age-related macular degeneration (AMD). It has been shown that slowed visual pigment regeneration is a key bio-marker, allowing the early diagnosis of the disease (Jackson et al. 2014), see

Section 1.4.1. As such, it seems prudent to develop a clinical device capable of objectively assessing visual pigment regeneration rates across the central retinal region most commonly affected by AMD. The development and evaluation of the densitometer described in this thesis marks a crucial stepping stone in this research.

1.5. Attenuation of incident light

Retinal densitometry evaluates the reflectivity of the retina in its bleached and unbleached state. However, whilst visual pigment is an important absorber within the eye, the structures of the eye described in Section 1.2 all absorb light to varying degrees. This section will outline the absorption characteristics of these structures. For a more detailed characterisation of the spectral absorption characteristics of these structures, the reader is referred to Section 9.3.

These absorption characteristics protect the eye from harmful radiation and optimise its functional abilities. This attenuation of light passing through the eye has a considerable effect upon the measured retinal reflectance. Viewing the fundus depends upon light which has passed through the ocular structures twice, once upon entering and once upon leaving the eye. Whilst many clinical techniques can circumvent this issue by increasing the intensity of incident light, measurement of visual pigment regeneration must take place under minimal light conditions. Therefore, this light attenuation not only has a considerable effect on the measured retinal reflectance but reduces the signal-to-noise ratio.

The ocular components which attenuate incident light will be discussed here in anatomical order, from anterior to posterior. Those structures whose primary purpose is the transmission of light will be discussed in terms of transmission, whilst the pigmented layers whose primary purpose is absorption will be discussed in terms of absorption.

1.5.1. Ocular media

The tissues anterior to the retina comprise the cornea, aqueous humour, crystalline lens and the vitreous humour, known collectively as the ocular media. The ocular media are often thought of as being optically transparent. However, light incident on the retina is attenuated to some extent by these structures. Transmission across these structures is shown for healthy eyes (age range 4 weeks – 75 years) in Figure 1.15.

The cornea absorbs strongly below 300nm, transmitting between 80 and 95% of the visible wavelengths between 400 – 950nm, with transmission increasing monotonically across this range (Boettner and Wolter 1962). Transmission between 950nm and 1300nm, whilst decreasing, remains high, with two local minima at 1000nm and 1200nm. Beyond 1300nm transmission reduces to nil at 1940nm. A 3rd local minimum is present at 1450nm. Transmission of the cornea has been shown to decrease with age, with proportionally greater effect on wavelengths shorter than 500nm.

Being similar in structure, the aqueous and vitreous will be discussed together. Whilst transmission is almost nil at wavelengths shorter than 300nm, it is 90-95% and spectrally independent from 420nm to 900nm (Boettner and Wolter, 1962; Smith and Baker, 1981, van de Kraats et al, 2008). Like that of the cornea, the transmission of these structures exhibits 2 local minima at 1000nm and 1200nm before reducing to zero at 1500nm. Transmission of the aqueous decreases faster than that of the vitreous with increasing wavelength, but shows a local maximum at 1650nm, where transmission from the vitreous is nil. There is no evidence of any changes in transmission with age (Boettner and Wolter 1962).

The crystalline lens transmits little light at wavelengths shorter than 370nm, although a local maximum of 7% transmission is seen at 330nm (Boettner and Wolter 1962). Transmission swiftly increases from nil at 370nm to 93% at 475nm (Boettner and Wolter 1962). Across the wavelengths 475nm to 900nm, transmission of light through the crystalline lens is 93-95% and shows minimal spectral variation

(Boettner and Wolter 1962). Beyond 900nm transmission decreases rapidly to nil at 1500nm, with 2 local minima at 1000nm and 1200nm (Boettner and Wolter 1962). A final slight increase in transmission is seen at 1650nm. Like the cornea, transmission through the lens shows a significant reduction with age, most noticeable at the shorter wavelengths (Boettner and Wolter 1962; Norren and Vos 1974; Weale 1988). In young lenses (<25 years old) the local maximum at 330nm is more prominent, transmitting more light at this short wavelength (Boettner and Wolter 1962). The benefit of the short wavelength absorption by the lens is two-fold; the attenuation of the eye's chromatic aberrations improves the quality of the retinal image, whilst absorption of ultra-violet light (UV) has a protective effect. As such, the UV 'window' at 330nm in young eyes may be of critical importance regarding risk of retinal damage (Behar-Cohen et al. 2014). Absorption characteristics within an individual are also dependent upon the shape and thickness of the lens, which varies with accommodative status (Boettner and Wolter 1962).

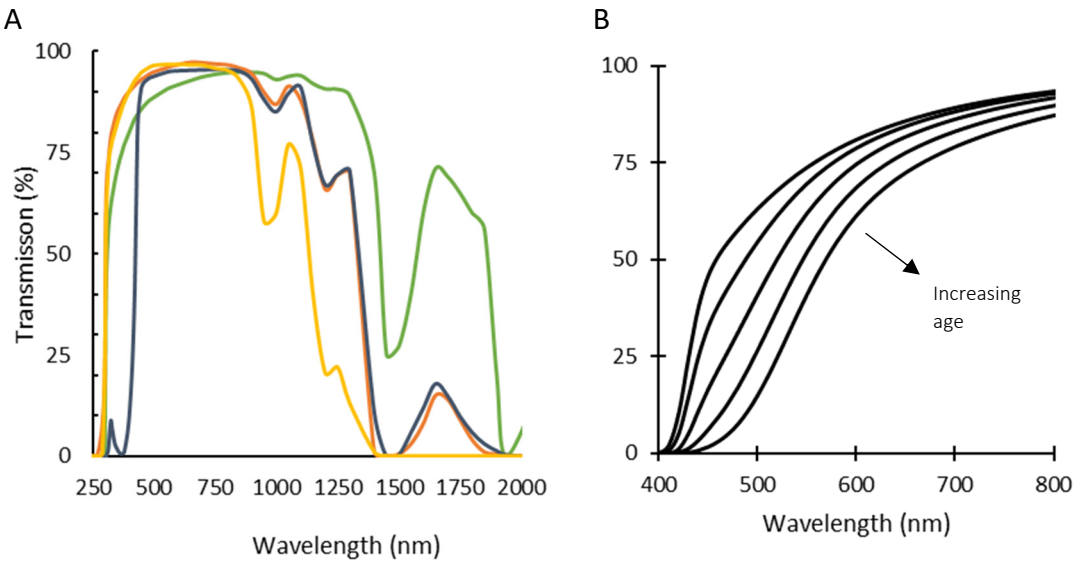

Figure 1.15 A) Spectral transmission of the human cornea (green), aqueous humour (orange), lens (dark blue) and vitreous humour (yellow) (Boettner and Wolter 1962). Across the visible spectrum, transmission is high with minimal spectral variation. B) Combined ocular media transmission across the visible spectrum for ages 10,30,50,70 and 90. Calculated using a model described by van de Kraats & van Norren (2007).

From 200 to 2000nm the components of the ocular media present varying transmission characteristics, becoming an interesting topic in their own right (Figure

1.15). Transmission across the visible spectrum has been modelled for, amongst other purposes, retinal reflectometry. Most recently, an accurate model has been provided by van de Kraats and van Norren (van de Kraats and van Norren 2007), which models the corneal, aqueous, lenticular and vitreous transmission as one, including an age varying component (van de Kraats and van Norren 2007).

1.5.2. Macular pigment

Composed of lutein, zeaxanthin and meso-zeaxanthin, macular pigment is a strongly absorbing blue light filter located within the central 2^{o} of the retina, peaking at the fovea (Bone et al. 1988; Kilbride and Keehan 1990; Bone et al. 2007). Macular pigment absorbs light between 390nm to 540nm with an optical density peak at 460nm (Wyszecki and Stiles 1982). The absorption spectrum is independent of age (Bone et al. 1988; Demarco et al. 1992). Peak optical density measurements vary with age and between individuals (Bone et al. 1988; Demarco et al. 1992). In healthy subjects, the optical density of macular pigment ranges from 0.21 to 0.54 (Brindley and Willmer 1952; van Norren and Tiemeijer 1986; Delori and Pflibsen 1989). The ability of macular pigment to absorb blue light and quench free radicals suggests its purpose may be to reduce photochemical light damage, as well as optimising image quality (Reading and Weale 1974; Khachik et al. 1997; Landrum et al. 1997; Wooten and Hammond 2002).

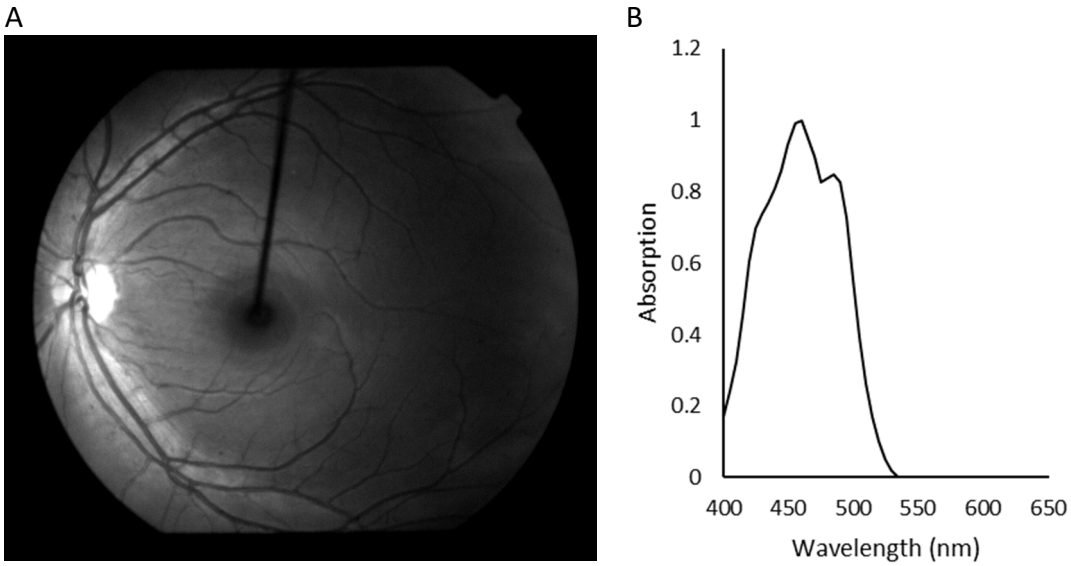

Figure 1.16 A) A retinal image (LE), obtained from the research densitometer described in this thesis, using 470nm light, vertical bar is the fixation target. The central region of macular pigment absorption can be seen. B) Showing the absorption spectra for macular pigment, data obtained from Wyszecki and Stiles (1982).

1.5.3. Visual pigments

As discussed in Section 1.2.4, cone and rod photoreceptors contain different visual pigments, allowing both colour discrimination and usable vision across a large range of light conditions. Any densitometric investigation into the distribution or kinetics of a single visual pigment type will require differentiation between rhodopsin, S-, M- and L- wavelength sensitive cone pigments. According to *in vitro* studies rhodopsin has a maximal absorption of light at 496nm (±2.3nm), whilst the absorption of cone pigments peak at 419nm (±3.6nm), 531nm (±3.5nm) and 558nm (±5.2nm) for the short, medium and long wavelength specific pigments, respectively, as in Figure 1.17 (Dartnall et al. 1983). As these data are based on *in vitro* analysis, they are independent of interactions with other ocular absorbers. Subtle variations in the structure of M- and L- wavelength sensitive opsins are responsible for minor differences among individuals with normal colour vision, with a combined spectral range peaking between 530-563nm (Neitz et al. 1991).

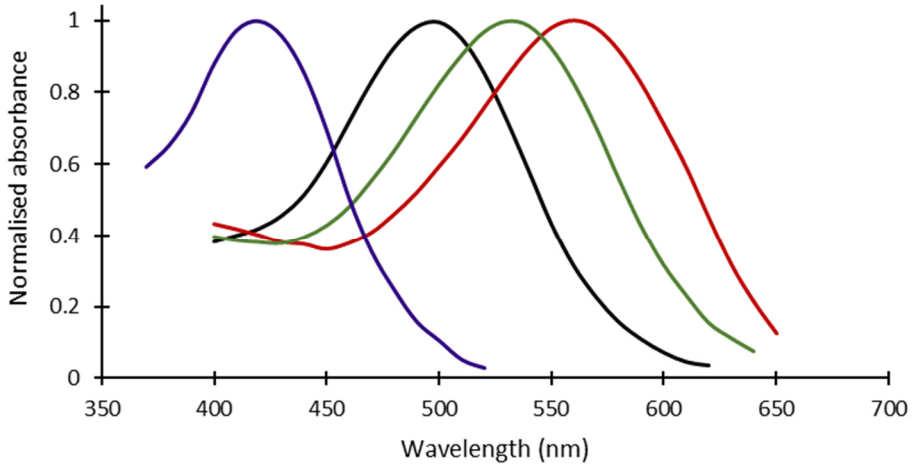

Figure 1.17 Absorbance spectra for each of the four visual pigments (S-cones, rhodopsin, M- and L- cones; blue, black, green and red respectively), obtained using *in vitro* methods. (Dartnall et al. 1983).

1.5.4. Photo-intermediaries

In a review of the rod phototransduction cascade, the presence of photo-intermediaries was highlighted (Pepe 2001). This is of relevance to densitometry as the optical density of photo-intermediaries varies with incident light intensity. Their absorbance spectra are of importance as it has been suggested their presence may contaminate reflectometry results after exposure to a flash bleach (Ripps and Weale 1969b; Rushton et al. 1969). Metarhodopsin II has an absorption peak at 380nm, whilst metarhodopsin III has an absorption peak near 460nm (Figure 1.18A) and has been shown to be present in the data for a period of minutes (Figure 1.18B presents the time course of decay) following exposure to a flash bleach (Ripps and Weale 1969b).

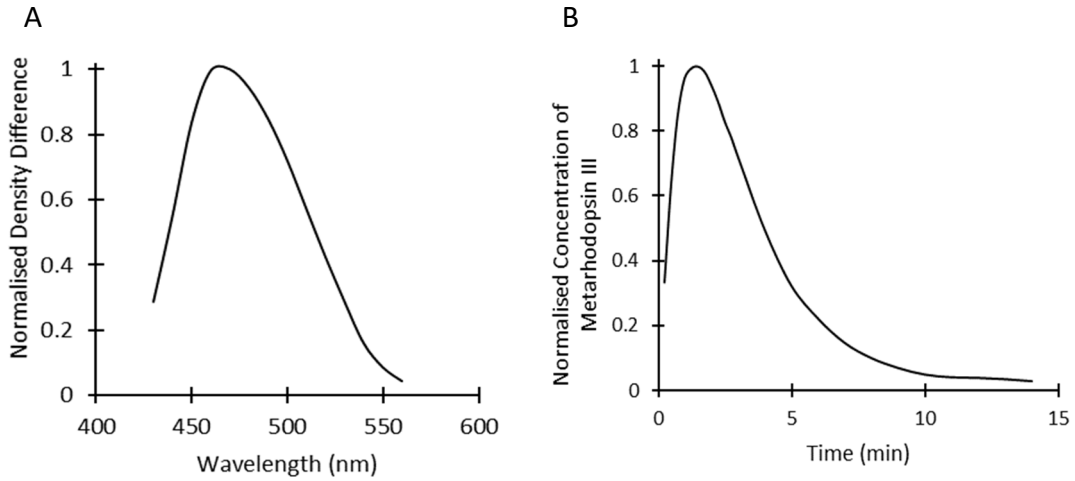

Figure 1.18 The absorption characteristics of metarhodopsin III. A) Presents the absorption spectra and B) the time course of decay. Adapted from Ripps and Weale (1969b)

In vitro studies have shown the transformation of peak absorption from 380-460nm over time after exposure to light; which has been attributed to the decay of metarhodopsin II to form metarhodopsin III (Lewis et al. 1997). Little is known about the absorption characteristics of the photo-intermediaries photorhodopsin, barthorhodopsin and lumirhodopsin, and no reference has been made to them in the literature in relation to reflectometry measurements. Their potential effect on absorption is limited by the brevity of their presence.

1.5.5. Haemoglobin

The absorption spectrum of haemoglobin varies greatly across wavelengths between 250nm and 600nm, furthermore, the absorption spectra differ for oxygenated and deoxygenated blood, as shown in Figure 1.19 (van Assendelft 1970). Within the visible spectra, note the local maxima of absorption at 416nm, 542nm and 577nm for oxygenated blood and 559nm for deoxygenated (van Assendelft 1970).

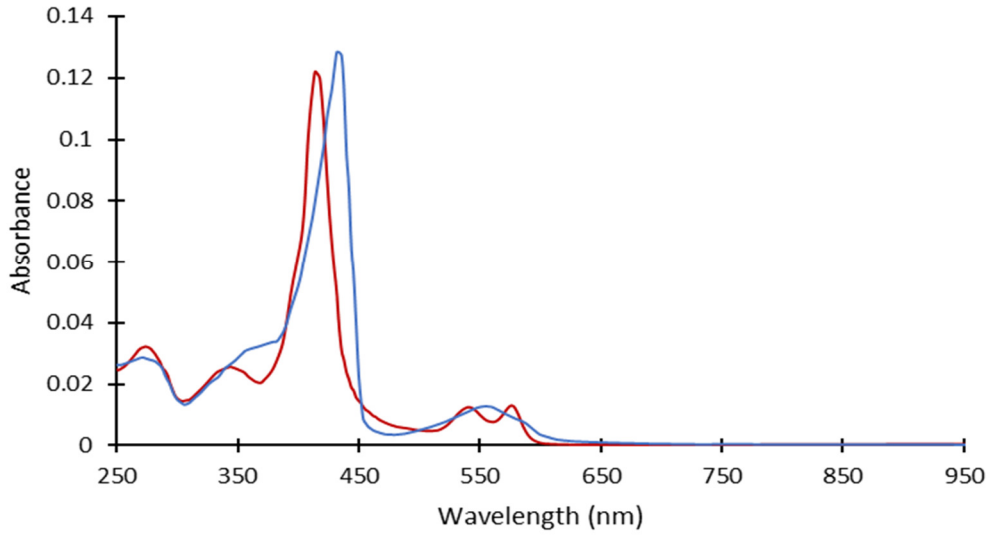

Figure 1.19 The absorption spectra of haemoglobin for both oxygenated (red) and de-oxygenated conditions (blue), assuming a thickness of 1µm (van Assendelft 1970).

The dual vascular system creates two layers of haemoglobin; firstly, within the inner retinal vessel and capillary network and, secondly, in the much larger choroidal system. Blood in both the inner retinal and choroidal circulations is assumed to be 95% oxygenated (van de Kraats et al. 1996). Whilst haemoglobin in the retinal vessels absorbs strongly, its presence in the retinal capillary network has a minimal effect upon light due to the tiny vessel diameter of 1.5µm. The overall effect of absorbance by haemoglobin in the retinal layers is dependent upon the location of the measurement, i.e. whether a vessel is present. The choroid presents a denser layer of blood around 272µm, ±81µm SD (Manjunath et al. 2010), with minimal topographical variations (Wood et al. 2011). The optical density of the haemoglobin present in the retina is therefore dependent upon the thickness of this layer (Delori and Pflibsen 1989; van de Kraats et al. 1996).

1.5.6. Melanin

Melanin is present posterior to the retinal layers, in the RPE and choroid, where it acts as a light absorber, reducing intra-ocular scatter (Weiter et al. 1986). Melanin has a peak absorbance at 335nm and, although decreasing to near transparency at the far infra-red, it is a strong absorber throughout the visual spectrum, as seen in Figure 1.20 (Kollias 1995). There is significant topographical variation; choroidal

melanin concentration increases from the posterior pole to the periphery, whilst RPE melanin concentration decreases (Weiter et al. 1986). The macula shows the greatest concentration of melanin (Weiter et al. 1986). As melanin in the deeper ocular layers is not replaced, a decline in density with age is seen (Weiter et al. 1986).

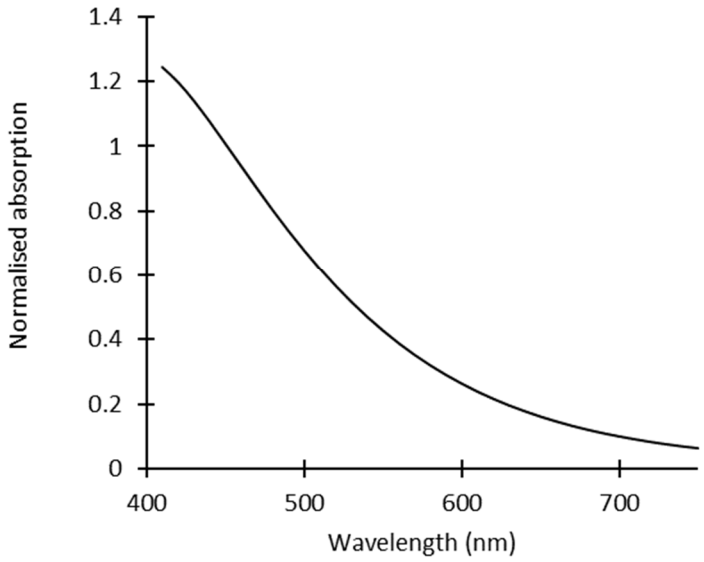

Figure 1.20 Melanin absorption spectrum, as published by Gabel (1978). Normalised to 450nm.

1.6. Summary

Section 1.1 provided a brief background, highlighting the relevance of retinal densitometry as a potentially useful clinical tool and giving an overview of the structure of the investigations reported in this thesis. Section 1.2 provided a summary of the structures of the eye, with detail placed on those deemed pertinent to densitometry. Section 1.3 discussed the physiological processes driving the bleaching and regeneration of visual pigments which facilitate the measurement of pigment density through retinal densitometry. Section 1.4 described the techniques that have been used to measure these processes, highlighting the relative benefits of retinal densitometry. The ocular tissues were revisited in Section 1.4.3.1, where the absorption characteristics of each ocular pigment were discussed in turn.

A systematic review of the literature on densitometry devices, techniques and capabilities is presented in the next chapter, followed by the relevant aims and hypothesis.

Chapter 2 - Systematic Review

2.1. Background

Using an ophthalmoscope to look into the eyes of anesthetised crocodiles and fish, Abelsdorff (1897) was the first to visualise the kinetics of visual pigments. He noted the purple colour of the retina could be reduced with a bright light and that the original colour only returned once the light source was removed. The white tapetum in these animals increases reflections making this type of observation easier, whilst the pigmented choroid and RPE found in humans increases the difficulty of this observation in man (Abelsdorff 1898).

Brindley and Willmer (1952) first reported that a quantitative measure of reflectance could be made, in this case measuring the absorption spectrum of human macular pigment. Their device, based on the optics of a retinoscope, split the fundus reflection into a portion from the macula and one from the peripheral retina. A neutral density wedge allowed the subjective evaluation of reflectance to be equalised in the two regions. Whilst measurement of the relative reflectance of the central and peripheral light adapted fundus was possible, attempts to measure the absorption spectrum of rhodopsin using the same device resulted in a 'surprisingly small' (and unspecified) measurement (Brindley and Willmer, 1952). The intensity of the light source used (not specified in the publication) was almost certainly the cause of this and the addition of a photomultiplier in subsequent reflectometers allowed a light source of lower intensity to be used, resulting in the first successful *in vivo* measurements of rhodopsin density in humans being reported (Rushton and Campbell 1954; Campbell and Rushton 1955).

The publication of 9 papers in quick succession demonstrated the interest and potential value of ocular densitometry (Rushton and Campbell 1954; Campbell and Rushton 1955; Rushton 1956a,b,1961b,a,1963a,b,c). These publications initially

detailed the optical density of both rhodopsin and iodopsin in man and, subsequently, the rate of regeneration of these pigments. Developments since the 1960s have included wide field imaging (Kilbride et al. 1989) and use of scanning laser ophthalmoscope (SLO) devices (van Norren and van de Kraats 1989a).

2.2. Aims

The aims of this systematic review were to:

1. consolidate the literature regarding past and current developments in densitometry methods;
2. document results for both human visual pigment optical densities and regeneration time constants; and,
3. identify current limitations in the technique.

2.3. Methods

Eligibility criteria for the included studies were that the study must:

1. involve *in vivo* visual pigment measurement in humans;
2. describe the use of retinal densitometry;
3. have been published between January 1950 and May 2017 (this timeframe includes the first publications on visual pigment densitometry); and,
4. be written in the English language.

Studies assessing only lutein, macular pigment and conference abstracts were excluded.

Potentially eligible studies were identified using the search engines 'Web of Knowledge' and 'PubMed' with the following terms; "Reflectom* OR Densitom*" AND "retina" and "Regeneration OR Density" AND "Human".

All potentially relevant abstracts were assessed by the author against the inclusion criteria and the full article obtained for those which appeared eligible. Further papers were then identified by hand searching the reference lists of all included studies and two previous review papers (Liem et al. 1996; Berendschot et al. 2003). Information from all included studies was collated into a data extraction table, which forms the basis of the summary of included studies (see Appendix A). No formal evaluation of the quality of included studies was carried out. However, any potential limitations in study design are highlighted in the text of the review.

2.4. Results

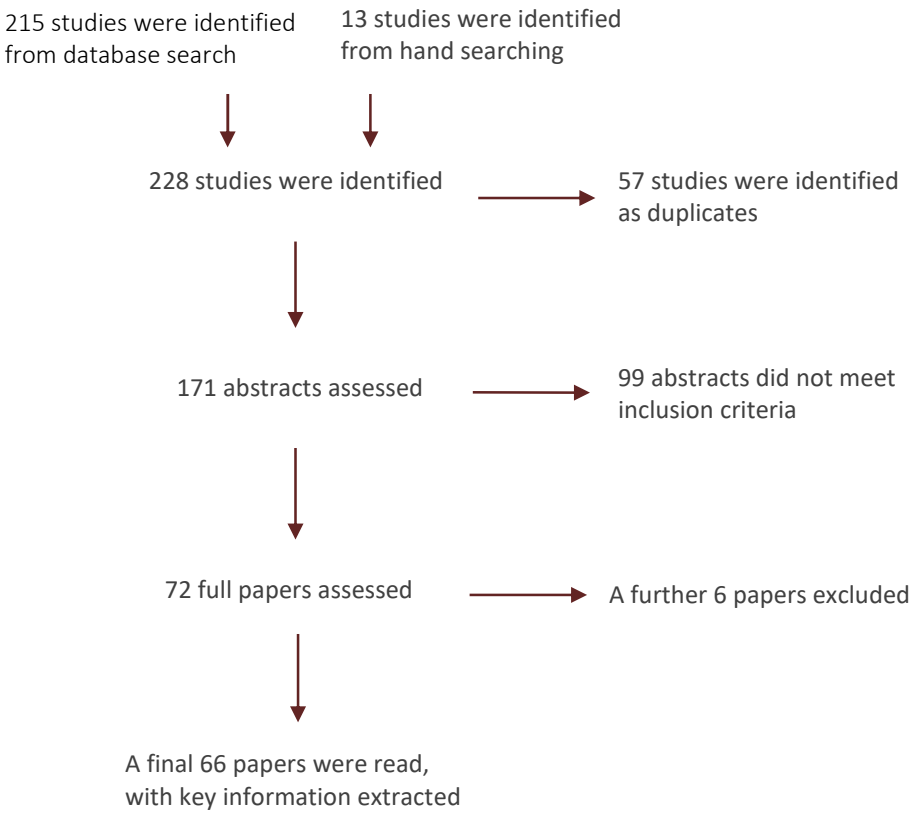

Figure 2.1 Flow diagram of study selection. Common exclusion criteria included the investigation of either macular pigment or oximetry alone, or purely animal studies.

The initial search was conducted on the 10/10/13 and concluded on 29/05/17 and the above terms returned 215 potentially relevant papers from the two databases. Hand searching the literature added a further 13 papers. These papers were entered into EndNote where 57 were immediately identified as duplicates. After reading the abstracts, a further 99 were excluded, either failing to meet eligibility criteria or by being duplicates not identified by EndNote. Full manuscripts were obtained for the remaining 72 studies. Upon reading the full article a further 6 were excluded, bringing the final total to 66.

2.5. Past and present technology

This section of the review concentrates on the technological development of retinal densitometry since the 1950s.

There are two distinct varieties of densitometry device; spot devices and wide-field imaging devices. Spot densitometers measure reflectance from a specific retinal locus, usually between 1° and 6° in diameter; the retina within this field is assumed to be topographically homogenous. Imaging, or wide field, densitometers are capable of extracting reflectance information over a relatively large retinal area, for example 25° x 25° (Faulkner and Kemp 1984) with varying degrees of spatial resolution. Spectral resolution is possible within both types of device and enables retinal reflectance data to be extracted across the spectrum. In addition, some devices are capable of temporal resolution, although as yet, no device has performed all functions simultaneously.

The densitometry literature may be delineated according to the device used. These devices will now be discussed in detail.

2.5.1. Early densitometers

The initial research in human retinal densitometry was carried out using two spot devices, developed by Rushton, which provided all the human densitometry data published prior to 1963 (Rushton and Campbell 1954; Campbell and Rushton 1955; Rushton 1956a,b,1961b,a,1963a,b,c). These devices were based upon the optical design originally described by Brindley and Willmer (1952), with the addition of a photomultiplier (Figure 2.2). The measurement process required a subjective comparison of the output from the reflected measuring beam (usually green) with that of the reference beam (usually deep red).

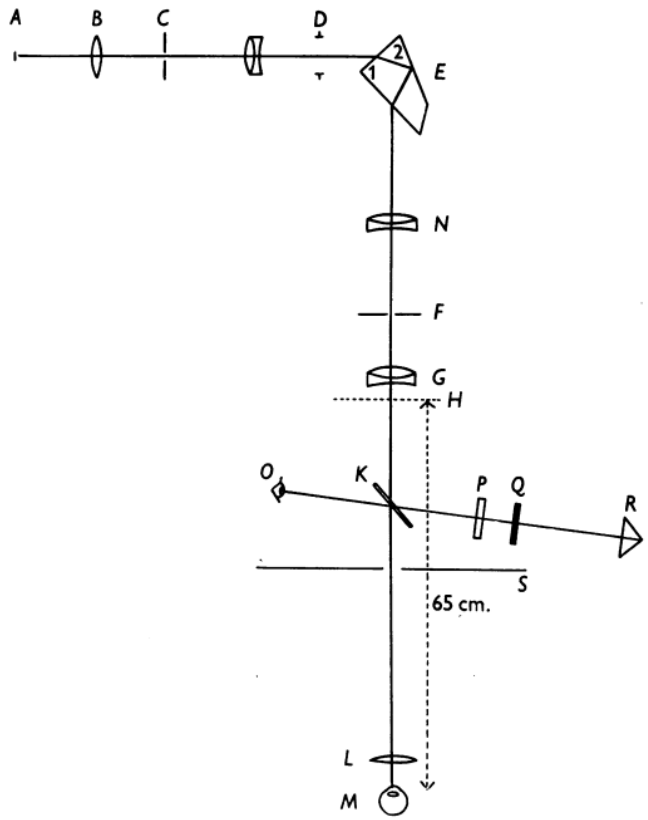

Figure 2.2 A schematic of the retinal reflectometer described by Brindley and Willmer (1952). Light from a ribbon filament source (A) passed through various optics, to be split at slide (K) before reaching the participants eye. Returning light passed through K to reach the observers eye. A prism (R) located the two beams side by side, whilst the neutral density filters (P, Q) were adjusted to equalise the two beams.

It was assumed that the reflectance of the reference beam was unaffected by visual pigment bleaching, due to the insensitivity of visual pigment to light of long wavelength. Therefore, any variations in reflectance of the reference beam throughout the recording were attributed to artefacts e.g. eye movements and drifts. These would have a comparable effect on the reflectance of the measurement and reference beams. Therefore, by subjectively matching the output from the two beams, it was possible to use the reference beam to correct for these artefacts. This use of a reference beam was a common feature of many densitometry devices.

Notably, results included the first published optical density (OD) for rhodopsin (OD 0.15) and chlorolabe (OD 0.35) in humans (Rushton 1956a; King-Smith 1973b). Perhaps of more importance were Rushton's efforts in proving that the data

obtained corresponded to rhodopsin and iodopsin, establishing retinal densitometry as a viable investigative technique in humans (Campbell and Rushton 1955; Rushton 1956b,1963b,c). Despite its relative success as a research tool, the device suffered from two significant limitations; measurements were only obtainable from a single wavelength and were dependent upon a subjective input.

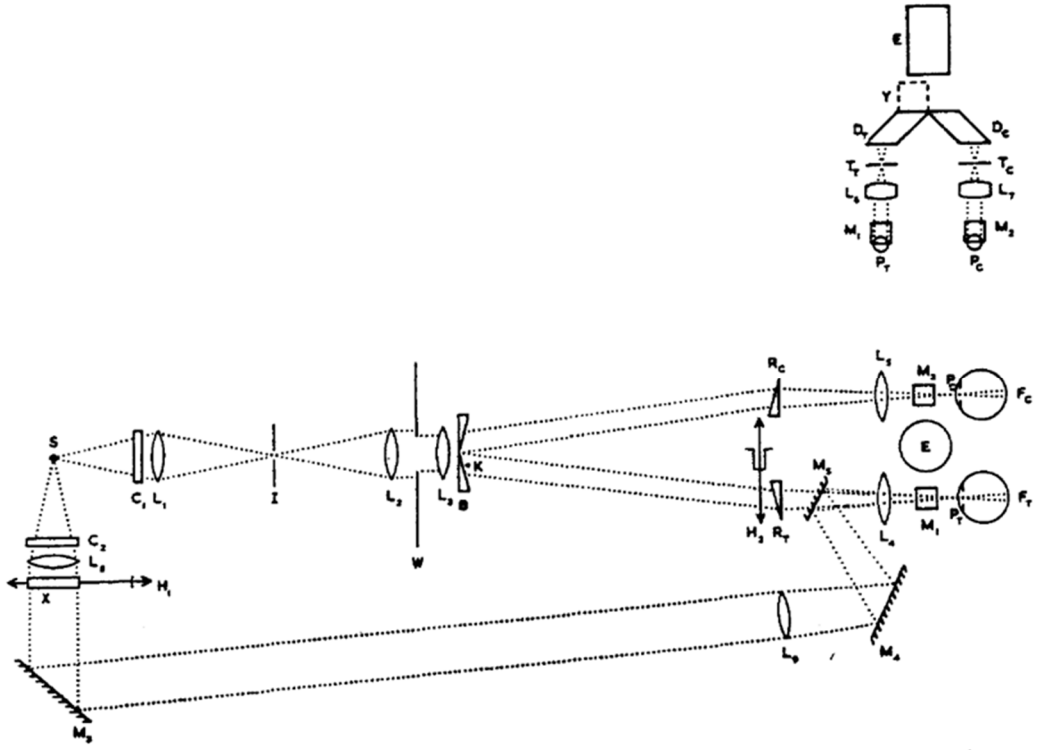

Figure 2.3 The densitometer developed by Ripps and Weale (1963); a more complex design than that described in Figure 2.2. The major differences were the inclusion of a control eye (Pc) and the filter wheel (X).

Ripps and Weale (1963), recognising the limitations of a single wavelength, developed their device (Figure 2.3) around a rotating wheel containing 20 bandpass filters, allowing more detailed investigation of cone pigments. Their design removed the subjectivity from the measurement procedure, sped up the routine and provided enough spectral resolution to investigate the absorption spectra of 2 cone photopigments (Ripps and Weale 1963,1965,1969a). The design of this device was later emulated by the Utrecht densitometers. The second major difference was the use of the participant's fellow eye as a control for the reference beam. It seems

unlikely that the use of the fellow eye added much to the design, as its use has been little replicated since.

2.5.2. Florida device

Developed by Hood and Rushton in 1971, the Florida Densitometer (Figure 2.4) was a refinement of that used by Rushton in the 1950's. The main differences were a circular polarizer (P_r), a rotating mask (D), the addition of two photocathodes (PC1, PC2) and a bleaching source. These changes improved the speed and accuracy with which a measurement could be taken, however, the measurement process remained subjective.

The basic optical design of the Florida densitometer is shown in Figure 2.4. Light from source A was split into two beams; one passed through the band width filter, λ, to become the measuring beam whilst the other passed through the deep red filter, R, to become the reference beam. A neutral density wedge, W_1, provided control over the intensity of the reference beam. These two beams were perpendicularly polarized, allowing the recombined beam to be alternated in a sinusoidal fashion by a circular polarizer, P_r. This beam was focussed upon the nasal aspect of the subject's pupil, with reflected light leaving the eye via the temporal side of the pupil. The separation of the two pupils reduced any contamination of the reflected beam. The iris stop (S_3) could be manually adjusted to control the field of view reaching the photocell, PC1. Bleaching was provided by the light source B, a tungsten filament, it was recombined with the measuring beam and focussed upon the pupil by lens two, L2. To prevent contamination of the reflected camera signal by the bleach, it was masked out during the measurement procedure by rotating mask, D. The spectral output and intensity of the bleach were controlled by filters and a neutral density wedge.

Due to the rotation of the circular polarizer, the measurement beam was 90^o out of phase with the reference beam. Thus, the signal received was a measurement of reflection from the measuring beam followed by the reflection from the reference beam. After dark adaptation, the position of the neutral density wedge (W_1) was set

to equalise the amplitude of each signal, resulting in a flat line when the reference and measuring beam were superimposed. As the amplitude of the measuring beam increased following exposure to a bleaching source, the position of W_1 was adjusted to re-equalise the amplitudes of the measuring and reference beams. Therefore, the change in position of W_1 was directly related to the optical density. Initially developed with a single measuring beam, the spectral output could be modified to suit individual research questions.

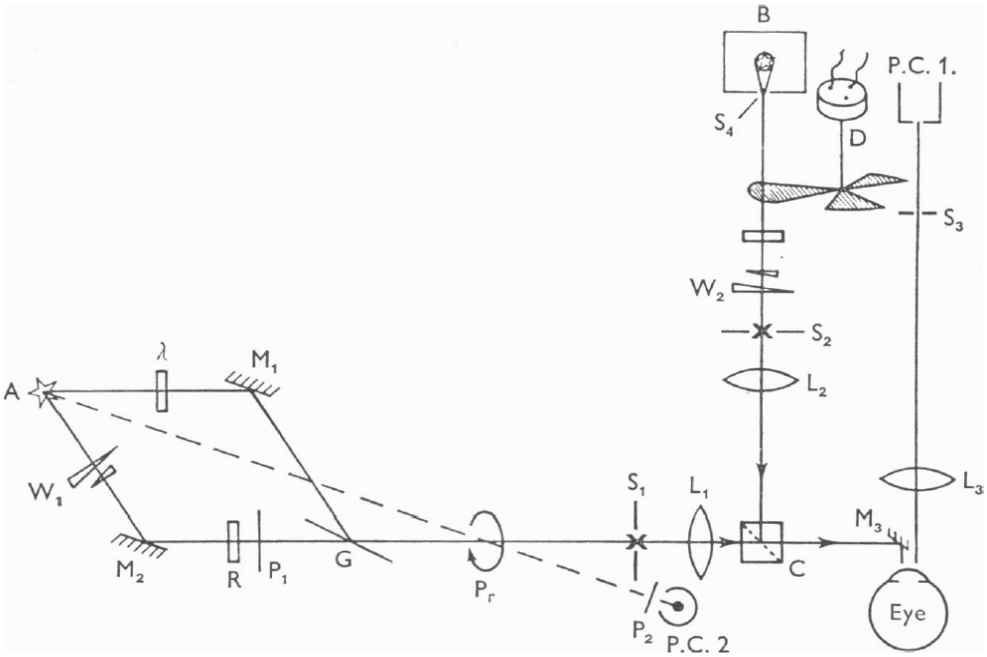

Figure 2.4 Diagram of Florida device taken from Hood and Rushton (1971). See text for details.

Although an improvement on earlier devices, the Florida device had its own limitations. As the position of the wedge was adjusted subjectively, measurements were difficult to master. Only a single wavelength could be investigated at one time and the temporal resolution was approximately 20 seconds, making the assessment of cone OD changes relatively difficult (van Norren and van de Kraats 1981).

Another, subtler, limitation related to the field of illumination. The iris stop, S_3, in the optics of the reflected beam controlled the area of retina measured, ranging from a diameter of 1.4° to 15.2° (Alpern and Pugh 1974; Baker et al. 1991), but it is unclear how the illumination field was controlled and what effect, if any, it had on

superficial stray light. Although most papers discussed the size of the bleach beam, none mentioned limiting the area of retina illuminated by the measuring beam. In addition, there appears to have been no capability to adjust the focus for any refractive error.

Despite these limitations, the Florida device has been used in many studies of rhodopsin and its kinetics (Alpern 1971; Alpern and Pugh 1974; Pugh 1975; Perlman and Auerbach 1981; Fulton and Hansen 1988; Baker et al. 1991; Sieving et al. 1995; Bone et al. 2007).

2.5.3. Utrecht device

The Utrecht device was developed by van Norren and van de Kraats (1981). Like the Florida device it was a spot densitometer, but with the several crucial differences in design. The addition of a microprocessor and photon counting device facilitated the automation of the measurement procedure and the use of a modified fundus camera simplified the alignment procedure (van Norren and van de Kraats 1981). The entry and exit pupils were given greater separation than in the Florida device, reducing the contamination of the imaging beam. The transition from wedge measurements to electronic processing of the photomultiplier output provided a twofold benefit; reducing the effect of human error on the results and allowing for continuous recording of reflectance from the eye.

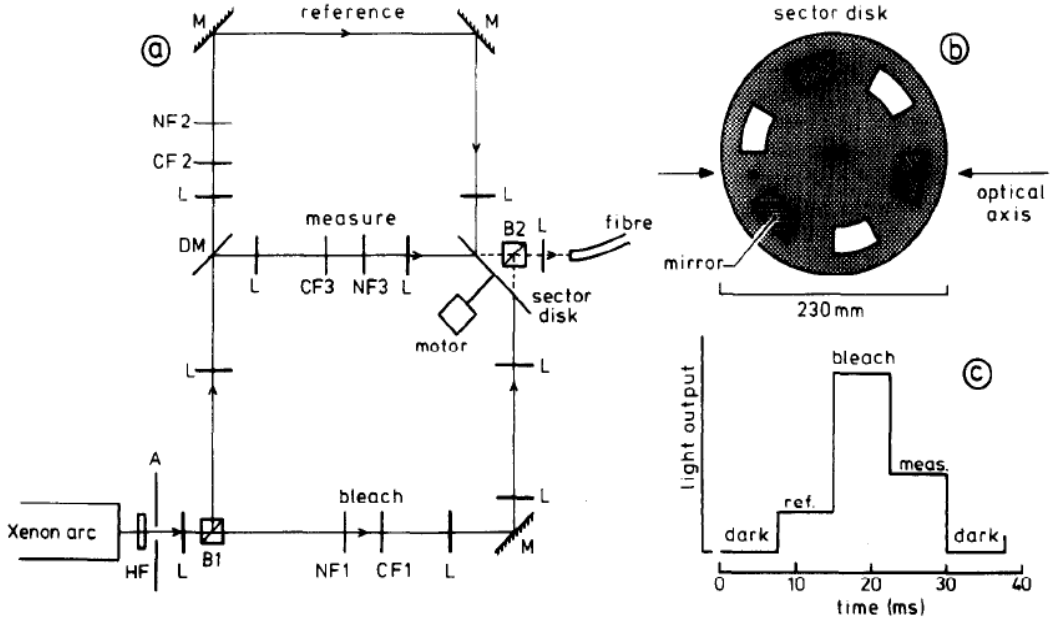

Figure 2.5 Showing A) a schematic of the Utrecht densitometer addition to a fundus camera, B) the sector disk controlling transmission to the fundus camera and C) the light output transmitted to the fundus camera. (van Norren and van de Kraats 1981). See text for details.

The schematic is shown in Figure 2.5. Light from a xenon arc lamp was split into two beams (B1). The first became the bleaching beam, the intensity of which was adjusted using neutral density filters. The second was split by a dichroic mirror (DM); which passed light beyond 650nm into the reference beam and reflected shorter wavelengths into the measuring beam. The deep red beam was further truncated by an interference filter (711nm) whilst the measuring beam passed through a wheel containing 16 interference filters, evenly spaced across the visible spectrum. All three beams converged on the rotating sector disk before being joined by a beam splitter (B2). Rotation of the disc sequentially presented a dark period, the reference beam, the bleaching beam and measuring beam into the incident pathway. A fibre optic passed the incident beam into the modified Zeiss camera. The reflected beam returned by the same path.

The entrance and exit pupils of the machine were 1.3mm each, allowing them to be positioned in close proximity, increasing the depth of focus (van Norren and van de Kraats 1981). The proximity of the beams enabled by the small exit pupil (as opposed to the large exit beams found on the Florida and Weale devices) made best

use of the Stiles-Crawford effect, perhaps the cause for the slightly higher optical density measurement, see Section 1.4 (King-Smith 1973a; van Norren and van de Kraats 1981). In addition to expediting the measurement process, the Utrecht device also boasted an increased range of wavelength options over the Florida device. Both modifications facilitated the assessment of cone kinetics (van Norren and van de Kraats 1981; Keunen et al. 1989; van Norren and van de Kraats 1989b; Bruggen et al. 1992; Berendschot et al. 1996b).

In comparison to the Florida device, the measuring beam was presented to the eye with increased regularity. To compensate for potentially increasing the light exposure on the visual pigments, 'dark periods' were introduced into the measurement cycle and the intensity of the measuring beam was decreased to 630 trolands to minimise bleaching throughout the procedure. The lower incident light resulted in a decrease of the signal to noise ratio. However, with electronic processing, the Utrecht device could record continuously, with temporal averaging used to reduce the impact of the relatively low signal to noise ratio.

2.5.4. Imaging devices

In their investigation into the effect of Oguchi's disease on OD, Carr and Ripps (1967) identified the lack of spatial information in the early densitometers as a major limitation. Obtaining OD measurements across the retina, in a systematic manner, was a major undertaking until Faulkner and Kemp (1984) published a description of the first imaging densitometer.

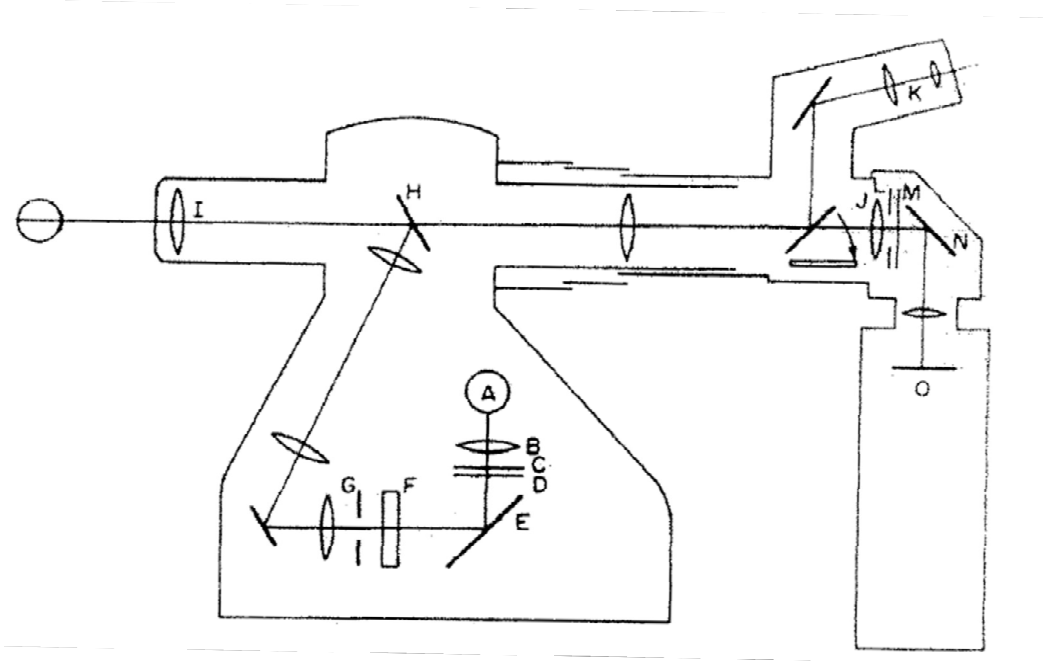

Figure 2.6 Schematic of a wide field imaging densitometer, utilising a commercial fundus camera. See text for details. (Faulkner and Kemp 1984).

Developed around a commercial fundus camera, this imaging device was the first to provide topographical information on the OD of rhodopsin (Faulkner and Kemp 1984). However, the large entrance pupil used for the technique increased stray light in the measurement, limiting the ability of the device to provide estimates of OD comparable to the spot designs. Stray light introduces a 'red shift' in the absorption spectrum by preferentially attenuating the optical density measured at shorter wavelengths. In addition, the amount of stray light present is not constant, being highly dependent upon the accurate alignment of the device within the participant's pupil (Faulkner and Kemp 1984).

2.5.5. Scanning laser ophthalmoscope devices

Scanning laser ophthalmoscope (SLO) devices have been adapted for the purposes of spatially-resolved densitometry. The raster scanning of the retina by lasers reduces the effect of superficial stray light, but wavelengths are limited to those found in commercial SLOs; the 488nm or 514nm of an Argon laser are used as the measuring beam and 633nm or 790nm of a helium-neon (HeNe) laser as the reference. Van de Kraats and van Norren (1989a) were the first to develop their own

device. Whilst several SLO devices capable of reflectometry measurements have been described, only the 1989 (van Norren and van de Kraats) device was designed specifically for this purpose. All other systems were based upon commercially available SLOs, employing a mirror to redirect the reflected beam to a photomultiplier (Elsner et al. 1992; DeLint et al. 1996; Tornow et al. 1999; Theelen et al. 2008; Sekiryu et al. 2009; Morgan and Pugh 2013). The van de Kraats and van Norren (1989a) device is described below.

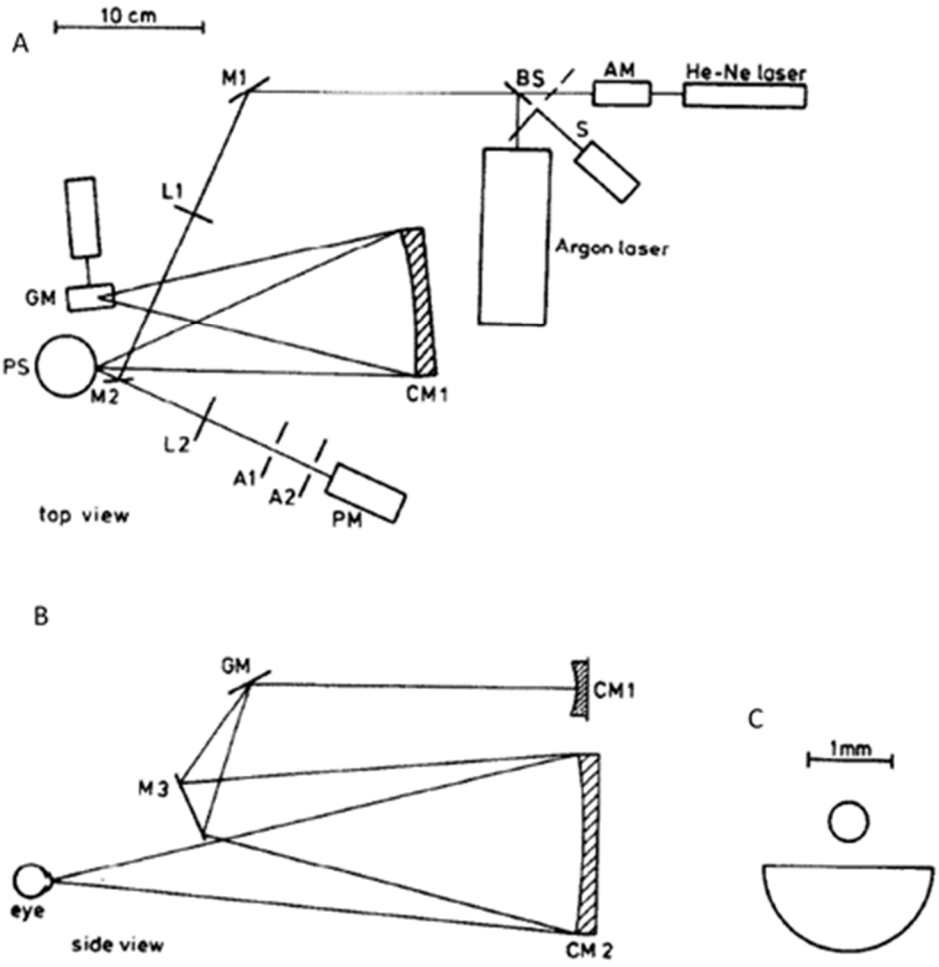

Figure 2.7 Shows the schematic optics for the van de Kraats and van Norren (1989a) confocal SLO densitometer (a) plan view (b) side view and (c) visualisation of the entry and exit pupils. See text for details.

Figure 2.7 shows the optics of the van Norren & van de Kraats (1989a) SLO densitometer in both horizontal (a) and vertical (b) planes, it also describes the entrance and exit pupils (c). The beam was composed of an Argon laser (514nm) and a He-Ne laser (633nm), the shutter (S) and beam splitter (BS) controlled the beam

transmission. The laser was then deflected into the eye via several mirrors (M1, M2, CM1, GM, M3 and CM2) and a polygon scanner (PS) was used to create the raster scan. The reflected beam followed the same path to M2 where light from the lower half of the pupil could pass, reaching the photomultiplier (PM) via a lens (L2). Exit pupil dimensions were controlled by the semi-circular aperture A2. The entrance pupil diameter was 0.5mm.

The raster motion of the SLO device allowed a relatively large retinal image to be captured. The incident light beam (0.9^{o} diameter) was used to generate an image that covered 23^{o}x18.5^{o} (van Norren and van de Kraats 1989a). However, spatial averaging resulted in image resolution dropping, creating individual pixels subtending 5.4^{o} x 4.3^{o} of visual angle. The advantage of the SLO approach was twofold. Firstly, stray light was minimal, and secondly, the raster method of laser presentations lowered the steady state bleaching levels during recording periods. It is difficult to quantify the extent of the benefit conferred by these factors, due to the other differences between the imaging densitometry systems and the lack of recorded stray light measurements. However, since the first published use of SLO densitometry in 1989, only 1 published study has used an imaging based device whilst 9 have used an SLO based system, suggesting the superiority of the technique (van Norren and van de Kraats 1989a; Elsner et al. 1992; Elsner et al. 1993; DeLint et al. 1996; Elsner et al. 1998; Sandberg et al. 1999; Tornow et al. 1999; Theelen et al. 2008; Sekiryu et al. 2009; Ojima et al. 2011; Morgan and Pugh 2013). In comparison, 5 have used the Utrecht device and 4 the Florida device during the same timescale.

Despite the improved optics, some limitations remain. The spectral capacity of these devices is determined by available lasers, with only 3 capable of providing useable wavelengths within the visible spectrum. This means that it has not been possible to obtain OD measurements with the spectral resolution required for the simultaneous isolation of visual pigments. Whilst commercial devices have been adapted for densitometry purposes, they lack the adaptability of a purposely designed device.

2.6. Densitometry results

In this section, published data on human visual pigment OD and regeneration rates obtained via densitometry are presented and compared.

2.6.1. Optical density of rhodopsin

Table 2.1 summarises the range of *in vivo* rhodopsin OD measurements obtained using densitometry. Results obtained using the Florida densitometer provide an OD for rhodopsin spanning a range from 0.13 to 0.35 (Perlman and Auerbach 1981; Fulton and Hansen 1987). The variation may be due to the retinal location tested, wavelength used or the variable effect of stray light. The OD of 0.35 stands as the highest recording of rhodopsin optical density to date (Alpern and Pugh 1974; Perlman and Auerbach 1981). Perlman and Auerbach (Perlman and Auerbach 1981) tested a greater number of retinal locations within an individual than usually measured with a spot densitometer. Thus, they are more likely to have measured optical density at its maximum concentration and minimised stray light through many repeated alignment procedures. The published rhodopsin optical densities of 0.16 and 0.18-0.21 measured with the Utrecht device (Liem et al, 1991; van Norren and van de Kraats 1989) show a narrower range than those measured using the Florida device, indicating a reduced error in the measurement technique

Results from the TV based systems provided greater spatial information, however the optical densities recorded with these devices were considerably lower (0.06) than those from the spot densitometers. However, this result was recorded using a 560nm measurement source. Results at 500nm were not reported, possibly due to metarhodopsin III contamination (Ripps and Weale 1969a; Faulkner and Kemp 1984). The low rhodopsin OD was attributed to increased stray light within the eye, caused by the larger entrance pupil and area of retina illuminated (Section 5.3.2). Furthermore, the measurement of 0.06 was taken at an eccentricity of 30^{o}; whilst most other rod OD measurements were from 18^{o} in the temporal retina where rod photoreceptors are at their highest concentration.

Table 2.1 Rhodopsin optical density values from the literature. The mean OD reported in the literature is 0.21 (±0.093SD)

	Early Devices	Florida	Utrecht	Wide field TV	SLO
Rushton (1956a)	0.15				
Ripps and Weale (1963)	0.17-0.19				
Alpern and Pugh (1974)		0.35			
Perlman and Auerbach (1981)		0.35			
Faulkner and Kemp (1984)				0.06	
Fulton and Hansen (1987)		0.16			
van Norren & van de Kraats (1989b)			0.16		
Liem et al. (1991)			0.18-0.21		
Sieving et al. (1995)		0.16			
Bone (2007)				0.20	
Morgan and Pugh (2013)					0.32

Rhodopsin optical density measurements from SLO devices have been poorly documented. Only Morgan and Pugh (2013) obtained a comparable measurement to Perlman and Auerbach (1981) with a rhodopsin OD of 0.32. Comparison to other devices shows this result was much higher than many previous experiments; however only the ODs measured by Perlman & Auerbach (1981) and Alpern & Pugh (1974) were higher. This is likely to be attributable to the lower levels of stray light with the SLO devices.

2.6.2. Optical density of iodopsin

The Florida densitometer was used to investigate the optical density of erythrolabe in three publications, all by King-Smith (King-Smith 1971,1973a,b), who reported the OD of erythrolabe to be approximately 0.40. Although no other results from the Florida device have been published on erythrolabe to confirm King-Smith's results, it does correspond with Rushton's work on the other foveal pigment, chlorolabe, where he estimated a stray light corrected OD of 0.35 (Rushton 1963a; King-Smith 1973a,b). However, mixed cone pigment OD has been measured more recently by Fulton & Hansen (1987) and Baker (1989; 1991), all publications reporting OD values of 0.20 or lower.

Table 2.2 Iodopsin optical density values from the literature. The mean OD reported in the literature is 0.29 (±0.104SD).

M- denotes medium cone pigment, L- long cone pigment, unspecified mixed cone pigment measured at the fovea.

	Early devices	Florida	Utrecht	Wide field TV	SLO
Rushton (1963b)	0.13 (M-)				
Villermet and Weale (1966)	0.20				
King-Smith (1971)		0.42 (L-)			
King-Smith (1973a)		0.40 (L-)			
King-Smith (1973b)		0.42 (L-)			
van Norren & van de Kraats (1981)			0.29		
Smith et al., (1981)			0.30		
Kilbride (1983)				0.28	
Kilbride et al. (1986)				0.24	
Fulton and Hansen (1987)		0.10			
Keunen et al. (1987)			0.32		
van Norren and van de Kraats (1989b)			0.49		
van Norren and van de Kraats (1989a)					0.35
Baker et al. (1989)		0.20			
Baker et al. (1991)		0.17			
Bruggen et al. (1992)			0.38		
Elsner et al. (1992)					0.2
Elsner et al. (1993)					0.30
Berendschot (1996b)			0.44 0.31 (L-) 0.35 (M-)		
DeLint et al. (1996)					0.28
Sandberg et al. (1999)				0.19	
Tornow et al. (1999)					0.35
Bone et al. (2007)				0.30	
Theelen et al. (2008)					0.11
Sabeson et al. (2015)					0.32 (L-) 0.34 (M-)

Measurement of foveal optical density and visual pigment regeneration was facilitated by the development of the Utrecht densitometer. The increased number of wavelengths and the ability to continuously record data allowed more accurate measurement of the swift foveal visual pigment recovery. Published foveal cone optical densities range from 0.29 to 0.49, with both extremes recorded by van

Norren and van de Kraats (van Norren and van de Kraats 1981,1989b). The higher OD was recorded with the Utrecht II. Berendschot (1996b) measured the OD of chlorolabe and erythrolabe using dichromats, finding a lower foveal optical density than that of trichromats. His individual chlorolabe and erythrolabe measurements of 0.35 and 0.31, respectively, are in-line with Rushton's chlorolabe findings, but low compared to King-Smith's erythrolabe findings (Rushton 1963a; King-Smith 1973a; Berendschot et al. 1996b).

Whilst cone optical densities measured with a wide-field imaging device remain on the low side, they show better agreement with other devices than the rod pigment optical density. The mean foveal optical density measurements from normal subjects of 0.19, 0.24 (Table 2.2) (Kilbride et al. 1986; Sandberg et al. 1999) are all below the lowest foveal OD's reported using the Utrecht device (van Norren and van de Kraats 1981). However, lower cone OD values have been recorded with both the Florida (Fulton and Hansen 1987) and the early Rushton device (Villermet and Weale 1966).

Results from 5 of the 6 papers reporting data on foveal OD from SLO systems compare very well, see Table 2.2. The outlying dataset, Theelen (2008), gives a low optical density of 0.11, measured using a 488nm laser. This wavelength is not readily absorbed by foveal visual pigments and thus would be expected to give a low foveal optical density. Of the 5 optical density measurements that do compare well, 4 different SLO systems and 2 different wavelengths were used – 514nm (van Norren and van de Kraats 1989a; DeLint et al. 1996; Tornow et al. 1999) and 594nm (Elsner et al. 1992; Elsner et al. 1993). Given the variation between the procedures, to get such consistent results is testament to the advantages of an SLO system. All foveal optical density measurements recorded using an SLO system have been conducted with colour normal participants (trichromats).

2.6.3. Pigment kinetics

Pioneering work by both Rushton (Rushton et al. 1969) and Alpern (Alpern 1971) in the 1970's established the time constant of regeneration (τ) which, assuming first

order kinetics, can be described by (Equation 2.1 (Alpern 1971; Thomas and Lamb 1999). (Equation 2.1 enables calculation of the proportion of pigment present, p, following exposure to a light source of known intensity, I (trolands), presented for a duration, t (seconds). The half bleach constant, I_{Rh}, is the intensity (trolands) required to achieve a 50% photopigment bleach. The time constant of regeneration for rhodopsin, τ_{Rh} (seconds), is the time taken for the proportion of rhodopsin to return to approximately 63.3% (i.e. ~$1 - {}^{1}/_{e}$) of its maximum value,

$$p = \left(\frac{I}{I + I_{Rh}}\right) \cdot \left\{1 - e\left(-\left(1 + \frac{I}{I_{Rh}}\right) \cdot \frac{t}{\tau_{Rh}}\right)\right\}$$

(Equation 2.1).

The time-constant of regeneration (τ_{Rh}) has been investigated extensively using the Florida device (Table 2.3). Rhodopsin regeneration times reported using the Florida device vary from 288 seconds to 386 seconds (Alpern 1971; Alpern and Pugh Jr. 1974; Baker et al. 1991; Coile and Baker 1992; Sieving et al. 1995). These variations are largely due to the bleaching light used; pigment regeneration occurs more rapidly after a flash bleach (70 seconds) than an equilibrium bleach (140 seconds) of the same magnitude (Hollins and Alpern 1973; Smith et al. 1983). Coile and Baker's (1992) investigation into the effect of stray light found little effect on the time constant of regeneration for cones.

As the time constant of regeneration has been shown to be unaffected by stray light (Coile and Baker 1992), there is less variation between the devices than for optical density measurements. This can be seen when comparing τ values for both rods and cones across all the densitometer types (Table 2.3 and Table 2.4). Even the wide field TV densitometer, with its elevated levels of stray light, produced results for cone tau (118 seconds) (Sandberg et al. 1999) and rod tau (240 seconds) (Faulkner and Kemp 1984) comparable to those reported using the Utrecht and Florida systems (Baker et al. 1991).

Table 2.3 Estimates of the time constant of rod pigment regeneration (seconds)

	Early devices	Florida	Utrecht	Wide field TV	SLO
Campbell and Rushton (1955)	458				
Rushton (1961a)	302				
Ripps & Weale (1969a)	240				
Alpern (1971)		386			
Hollins and Alpern (1973)		374			
Faulkner and Kemp (1984)				240	
van Norren and van de Kraats (1989b)			300		
Baker et al. (1991)		302			
Sieving et al. (1995)		288			
Morgan and Pugh (2013)					420

Table 2.4 Estimates of the time constant of cone pigment regeneration (seconds)

	Early Devices	Florida	Utrecht	Wide field TV	SLO
Smith et al. (1983)			140		
Fulton and Hansen (1987)			115		
Keunen et al. (1987)			99		
van Norren and van de Kraats (1989b)			100		
Bruggen et al. (1992)			69		
Coile and Baker (1992)		96			
Sandberg et al. (1999)				118	
Horio et al. (1999)		163			

Recovery time is affected by the bleaching intensity, as shown by Bruggen (1992) who found the shortest τ with the lowest intensity bleach of 5.6 log photopic trolands. Liem et al (1996) reported the greatest inter-subject variation of rhodopsin regeneration across 44 normal subjects, from a low near 200s to the longest close to 600s (515nm). This variation was found to be significantly related to age, with a 28 second increase/decade. A smaller effect of 12 second increase/decade was noted by Coile and Baker (1992) when evaluating the effect of age on cone adaptation using the Florida device.

2.6.4. Effect of ocular pathology

As one of the few techniques lending itself to the investigation of outer retinal function, densitometry has been used to study various ocular pathologies. These studies are discussed below.

Due to the lack of spatial resolution, spot densitometers do not lend themselves to pathological investigations, however some attempts have been made. Perlman and Auerbach (1981) used the Florida system to assess how rod optical density was affected by retinitis pigmentosa (RP). They found a large variance, with OD being ~1/3 lower for all retinitis pigmentosa subjects than controls and showing no topographical variance (Perlman and Auerbach 1981). Fulton and Hansen (1987) also used the Florida device in their investigations of cone pigment OD and kinetics within individuals with Ushers syndrome. Little change in OD was found, but the τ slowed in a manner suggestive of other cross linked retinal dystrophies, suggesting that densitometry could make a clinically useful tool for this type of pathology (Fulton and Hansen 1987).

Likewise, only a few investigations into a limited number of pathologies (acute posterior multifocal placoid pigment epitheliopathy, myotonic dystrophy and retinitis pigmentosa) have taken place using the Utrecht and Utrecht II densitometers (Keunen et al. 1989; Bruggen et al. 1992; Berendschot et al. 1996a). The results have been inconclusive due to fixation difficulties, stray light and limitations in spatial resolution – but all suggest that if the technologies and techniques could be developed further, densitometry may be a useful clinical tool.

Imaging densitometers can complement OD measurements with contour maps showing spatial variations. For example, Figure 2.8 shows the effect of RP on rhodopsin distribution. It can also be seen from Figure 2.8 that if a traditional spot reading was taken at a specific locus (marked with a cross) there would be little to differentiate between the normal subject and the one suffering from retinitis pigmentosa. This emphasises the diagnostic limitations of spot densitometers and the relative capability of imaging densitometers (Carr and Ripps 1967; Faulkner and

Kemp 1984; van Meel et al. 1993). Along with reducing rhodopsin OD, retinitis pigmentosa has been shown to increase the foveal time constant of regeneration by about 46% (Faulkner and Kemp 1984; Sandberg et al. 1999), which Sandberg (1999) suggests could prove to be clinically diagnostic.

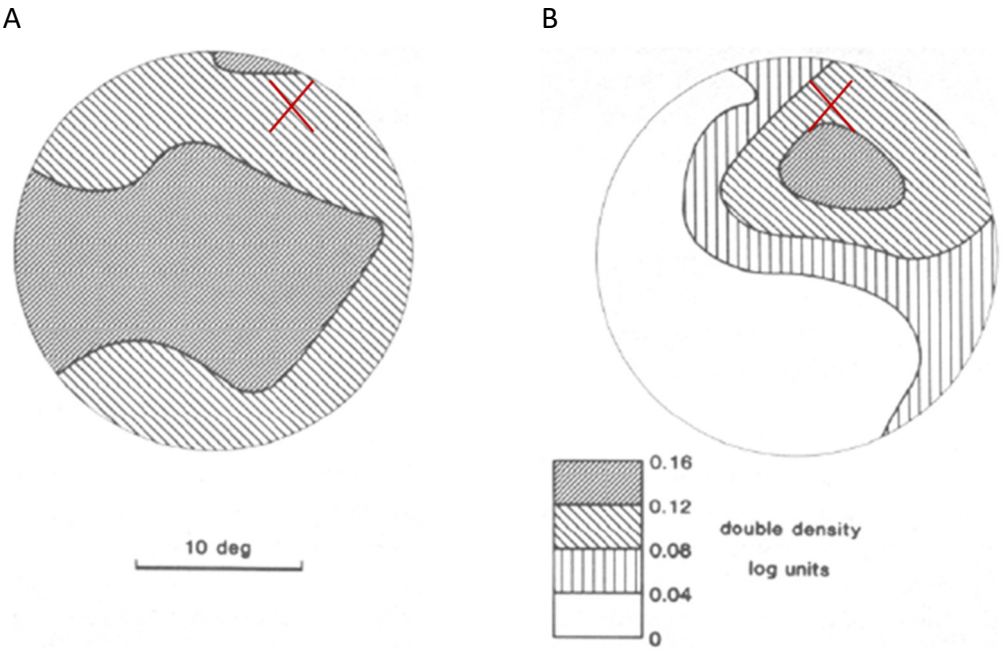

Figure 2.8 Contour map showing spatial variation across a 10° retinal locus, at 30° temporal eccentricity. A) Shows a healthy participant and B) shows a participant with retinitis pigmentosa. The crosses show how sampling with a spot densitometer may miss signs of retinal dystrophies. Modified from Faulkner and Kemp (1984).

Kemp (1988) investigated how vitamin A affects the impact of biliary cirrhosis and Crohn's disease on rhodopsin function. Optical density across the retina was found to be within the normal range in people with these conditions, but the τ was reduced. Treatment with vitamin A serum was shown to return τ to normal.

Likewise, SLO based densitometer systems may be useful in assessing the optical density of visual pigments in certain retinal pathologies. Retinal tears and detachments, unexplained VA loss, retinal dystrophies and central serous chorio-retinopathy have all been investigated (Elsner et al. 1992; Berendschot et al. 1996a; Theelen et al. 2008; Ojima et al. 2011).

2.7. Limitations of current technology

The technology used to measure optical density has advanced since Rushton and Campbell's (1955) initial investigations. Many sources of error have been removed and modern systems are capable of improved spatial or spectral resolution, and in some cases, both (Sandberg et al. 1999; Berendschot et al. 2010; Morgan and Pugh 2013). Still, many of the limiting factors facing Rushton remain; in particular the high absorbance and low reflectance (less than 1% below 500nm) of the human eye. Scatter has a larger effect upon the readings from the wider field imaging-based systems than the spot devices, although this effect has been reduced with the SLO systems. Finally, accurate alignment has proven crucial for all devices, often necessitating the use of a dental bite bar.

2.7.1. Low signal and photon shot noise

Due to the high levels of light attenuation within the structure of the eye (see Section 1.4.3.1, Chapter 1), a low signal count, and related poor signal to noise ratio, is physiologically unavoidable. The simplest way to increase reflected light would be to increase the incident light (the measuring beam), however increased light initiates visual pigment bleaching, reducing measured optical density. A more sensitive photon measuring system would be desirable, allowing a lower intensity measuring beam to be used. However, all photon measuring systems are limited by shot noise which results because of the discrete nature of the photon. Shot noise can be quantified by Equation 2.2 where *SNR*, is the signal to noise ratio present in the measurement and *P*, is the photon count reaching the retina,

$$SNR = \frac{P}{\sqrt{P}}$$

(Equation 2.2).

As such, shot noise is of greater proportion when the signal is low, and is the limiting factor to all retinal densitometry devices.

2.7.2. Stray light

Few papers attempt to quantify the stray light present in devices used for their experiments and within those that do there is a great variation. For example, when Baker et al (1991) assessed the effect of stray light present at 589nm in a modified version of the Florida system, it was found to reduce the OD measurement by 0.15. In contrast, Perlman and Auerbach (1981) found a reduction in the OD measurement of only 0.08 (at 560nm) attributable to stray light, even though they were measuring over a larger retinal area than Baker et al (1991). In addition, there appears to be a topographical aspect to stray light. Alpern and Pugh (1974) concluded that the higher peripheral OD they found was due to reduced stray light, with increased reflections from the nerve fibre reducing the central measured OD.

Since Rushton identified stray light as having an adverse effect upon optical density measurement, a variety of reflectance models have been published to account for this (Rushton 1965; van Blokland and van Norren 1986; van Norren and Tiemeijer 1986; Delori and Pflibsen 1989; Hodgkinson et al. 1994; van de Kraats et al. 1996). Although very detailed, none has been universally accepted. Another limiting factor for the application of these models is the topographical variation within the retina. The models are either rod or cone specific, whereas devices capable of imaging deal with data from rod and cone photoreceptors simultaneously. Stray light from surfaces anterior to the retina has minimal effect on spot devices. SLO devices have improved on this further, as laser measuring beams are even less affected by this stray light component (van Norren and van de Kraats 1989a). However, the wide measuring beams found on imaging based devices are affected by superficial stray light, as evidenced by the differences in maximum iodopsin optical density found with a spot device and wide-field imaging device, 0.49 and 0.24 respectively (Kilbride et al. 1986; van Norren and van de Kraats 1989b). Furthermore, Kilbride (1986) notes difficulty in defining optical density below 560nm, possibly due to superficial stray light having a greater effect upon the shorter wavelengths.

2.7.3. Participant alignment

All the densitometers described here share a common limitation, the need for stable fixation and posture throughout the recording procedure. This is not only to ensure the same region of retina is being investigated, but also to reduce alignment artefacts and maintain a stable reflected signal. The significance of this limitation increases with the duration of the experiment and is a probable reason why fewer investigations into regeneration rates have been undertaken compared to investigations into optical density. Whilst it is possible to partially overcome this limitation either by using a participant bite bar, data correction by a reference beam, or both, there are problems with each method. The use of a bite bar is a sensible approach in the research setting. However, if retinal densitometry is to realise its clinical potential, a bite bar is not a feasible solution for a diagnostic technique in regular clinical use. Furthermore, the use of a long wavelength reference beam has recently been questioned, with evidence of intrinsic retinal signals measurable after a significant pigment bleach in the deep red visual spectrum (Masella et al. 2014).

2.8. Summary

Non-invasive evaluation of visual pigment kinetics could be a useful clinical tool. To this end, ocular densitometry has progressed from physiological investigations, such as those by Rushton and Weale in the 50's and 60's, to attempt to characterise visual pigment characteristics in specific retinal diseases (Perlman and Auerbach 1981; Faulkner and Kemp 1984; Keunen et al. 1989; Bruggen et al. 1992; Elsner et al. 1992; Berendschot et al. 1996b; DeLint et al. 1996; Theelen et al. 2008; Ojima et al. 2011). Yet, despite its clinical attractiveness and potential sensitivity to ocular pathology, the technique remains in relative obscurity and has never been used in a clinical trial.

There are several potential explanations for this. Firstly, to get the most out of the technique requires spectral, spatial and temporal resolution which, whilst possible separately on the devices described, are not resolved simultaneously by any single

device. Secondly, a clinical technique needs to be fast and simple to use. Although there are several systems based upon clinically available SLO devices (e.g. the Spectralis OCT - Heidelberg Engineering Inc, Franklin), the measurement process remains time consuming and complicated. Finally, densitometry has helped increase understanding of the disease mechanism of many 'pre-diagnosed' retinal diseases, but due to its low specificity will generally require the use of a second technique such as an ERG or visual fields to aid differential diagnosis (Berendschot et al. 2003).

The wide field imaging devices (TV and SLO based designs) offer the highest spatial resolution to the clinician with regards to clinical data. However, both design variations have major limitations. TV imaging devices can provide a high degree of spatial and spectral resolution, but are dependent upon a large entrance pupil, introducing stray light and errors in the measurement. Whilst having greater spatial resolution, the SLO devices are limited in spectral resolution with few suitable wavelengths available.

If these limitations could be overcome, there is little doubt as to the potential usefulness of spatially resolved densitometry in the early diagnosis of many retinal diseases and the objective monitoring of retinal response to treatment. Berendschot (2003) suggests 'a user friendly (and affordable) version of such an apparatus might open new roads for clinical reflectometry' adding that many applications of densitometry are still to be developed. This is a positive outlook, and one that could be improved upon further if investigation times could be reduced and the device made user friendly, to both patient and operator.

2.9. Rationale for the study

This review has both highlighted the ability of densitometry to probe *in vivo* photopigment characteristics in healthy and diseased retinas and identified a number of limitations. Significantly, recent work has emphasised slow pigment regeneration as being a leading functional biomarker for early age-related macular degeneration (AMD) (Dimitrov et al. 2008; Owsley 2011; Gaffney et al. 2012; Jackson

et al. 2014) and therefore, retinal densitometry may have a role in the diagnosis and monitoring of early and intermediate AMD.

The devices reviewed in this chapter could be split into two distinct variants; the first able to process reflection data across the visible spectrum at a single retinal location, the second capable of spatially resolving monochromatic retinal images (Rushton 1956b; Morgan and Pugh 2013). To date there have been no publications describing a densitometry device that can simultaneously capture spatial, temporal and spectral data. For the effective assessment of early and intermediate AMD in a clinical setting a combination of spectral, spatial and temporal resolution is likely to be vital.

The work described in this thesis relates to the development and evaluation of a novel multispectral, imaging densitometer, developed during a collaboration between Cardiff University and United Kingdom Astronomy Technology Centre (UKATC). Technological advances of the last decade may help overcome some of the limitations highlighted in this review. The densitometry device described and used in this thesis was used as a platform to investigate some of the challenges associated with imaging densitometry, with the overarching aim of aiding the development of a clinic ready device.

2.10. Aims

The overarching objective of the work described in this thesis was to understand some of the key challenges associated with imaging densitometry, by addressing the following aims:

1. To isolate the rod and cone spectra and regeneration kinetics.
2. To compare the *in vivo* experimental results with values published in the literature.

3. To quantify the ability of a scattered light correction to bring the *in vivo* visual pigment absorption spectra into alignment with published *in vitro* data.

4. To produce topographical maps of rod and cone photopigment optical density.

2.11. Hypotheses

On the basis of the literature review, it is hypothesised that:

1. It will be possible to quantify rod and cone photopigment density across the central retina and characterise their differing regeneration kinetics.

2. For each photopigment, the measured peak optical density and regeneration kinetics will be broadly in line with previously published results.

3. The measured absorption spectra will show a red shift in comparison to the published *in vitro* data, with the absorption spectra for rod and cone photopigments being affected to the same extent.

4. Metarhodopsin III will not be measurable in the post bleach absorption spectra.

5. It will be possible to correct for any spectral shift present in the data by making an adjustment for intraocular light scatter.

6. Through the application of this correction, it will be possible to produce physiologically plausible maps of photopigment optical density.

The following chapter describes the novel multispectral densitometer, built in collaboration between Cardiff University and UKATC, that can capture reflectance data over space and time.

Chapter 3 - General Methods

3.1. Introduction

Chapter 2 discussed the development of retinal densitometry, paying particular attention to both past and present technology. The devices reviewed could be split into two distinct variants; the first able to process reflection data across the visible spectrum at a single retinal location, the second capable of spatially resolving monochromatic retinal images (Rushton 1956b; Morgan and Pugh 2013). To date there have been no publications describing the simultaneous capture of spatial, temporal and spectral data. This chapter describes a novel multispectral densitometer, built in collaboration between Cardiff University and UKATC, that can capture reflectance data over space and time.

3.2. Device description

The densitometer used to collect the data in this thesis is a 2nd generation device and will be referred to from here as the Mark II device. It is shown in Figure 3.1. The Mark II has been built around the optics of a non-mydriatic retinal camera, a Topcon TRC-50 IX. A basic description of the original camera and the modifications made by UKATC are given below, and a schematic is provided in Figure 3.3.

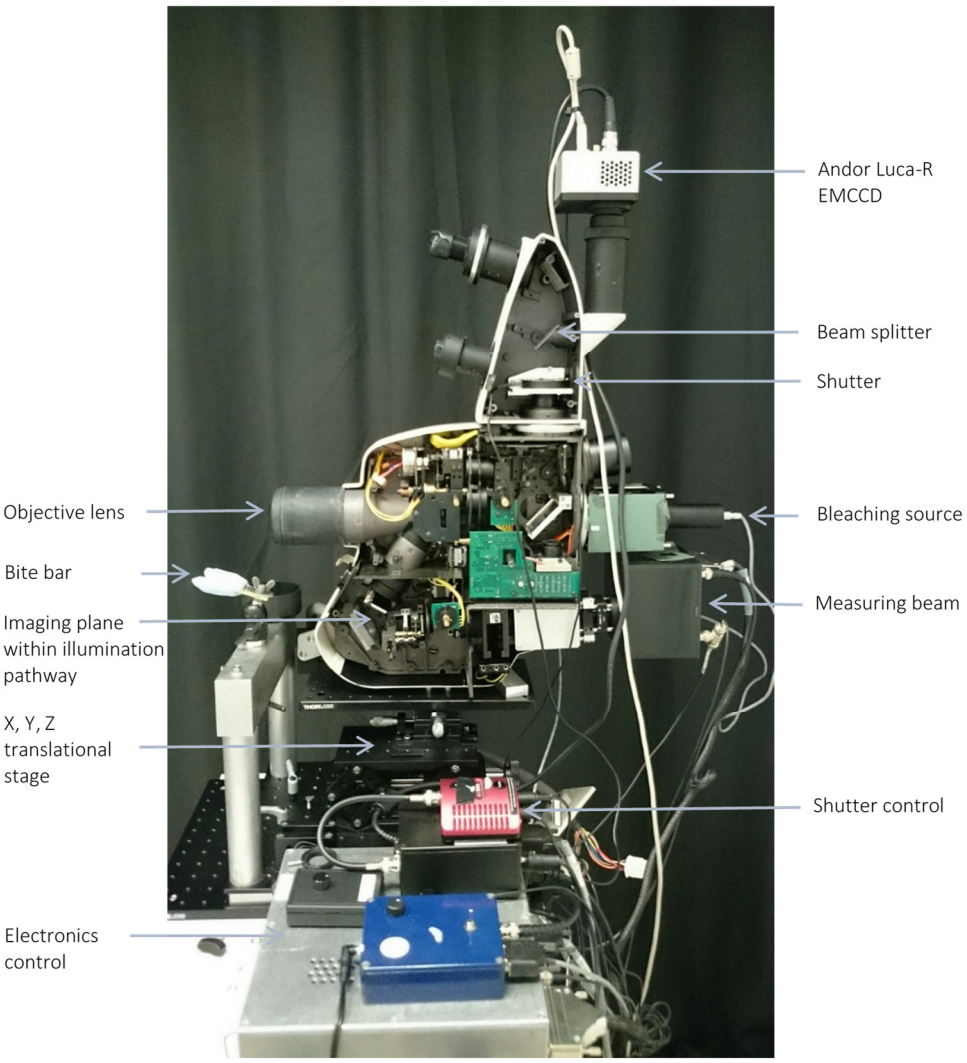

Figure 3.1 Showing the internal construction of the Mark II device and the peripheral control hardware, with key components labelled.

The camera was modified in several ways to facilitate imaging densitometry:

1. The xenon flash was replaced with an integrating sphere and light emitting diodes (LEDs) covering the visible spectrum; 450, 470, 500, 545, 590, 620, 650, 680, 710 and 740nm (nominal wavelengths). Further details are provided in Section 3.2.3.

2. The original camera was replaced with an electron multiplying charged coupled device (EMCCD), the Luca-R (Andor Technology Ltd, UK). A ‘fire’ pulse generated by the camera synchronised the LEDs with the camera’s frame rate.

3. A secondary light source facilitated photopigment bleaching. This bleaching light source consisted of a white light LED (LEDWE-50, Thorlabs Incorporated, USA) and an optional longpass filter with a 475nm cut off (to attenuate blue light) and 92% transmission (Schott AG, Germany).

4. The device was mounted on an X, Y, Z vernier stage to facilitate accurate alignment, while a dental impression secured the participant's head.

The optical pathways of the illumination and imaging beams will be discussed briefly, before a more detailed description of each vital component.

The measuring beam comprised 12 LEDs, activated sequentially and mounted in an integrating sphere to produce a uniform illumination beam. The sequence, duration of exposure and intensity of the LEDs were controlled by an external circuit board. The illumination beam passed through a pupil stop and was reflected into the objective lens relay by a flat mirror via an imaging plane containing the fixation target.

Figure 3.2 A schematic of the illumination beam (green annulus) and imaging beam (orange circle) as seen in the pupil plane. The illumination annulus has an outer diameter of 6.7mm, inner diameter or 4.7mm and the imaging beam has a diameter of 3.2mm.

Focussed on the pupil plane, the illumination beam, shaped into an annulus by the pupil stop, entered the eye via the cornea and periphery of the crystalline lens, as shown in Figure 3.2. Light reflected from the retina returned through the centre of the pupil. A focussing wheel (LW1) corrected the participants' refractive error and

an optional magnification lens (LW2) defined the field of view (20º, 35º or 50º) before the imaging beam reached the CCD. The bleaching light source shared the same optical pathway as the imaging beam. An additional electronic shutter (S) prevented light from the beaching source from striking the CCD.

Manual switches on the camera body controlled various filters, the pupil stop, image focus (LW1) and imaging field size (LW2), (Figure 3.3). Unless otherwise stated, these were set to the largest pupil stop, the correct focus for the participant, 50º image field and no filters in the illumination pathway.

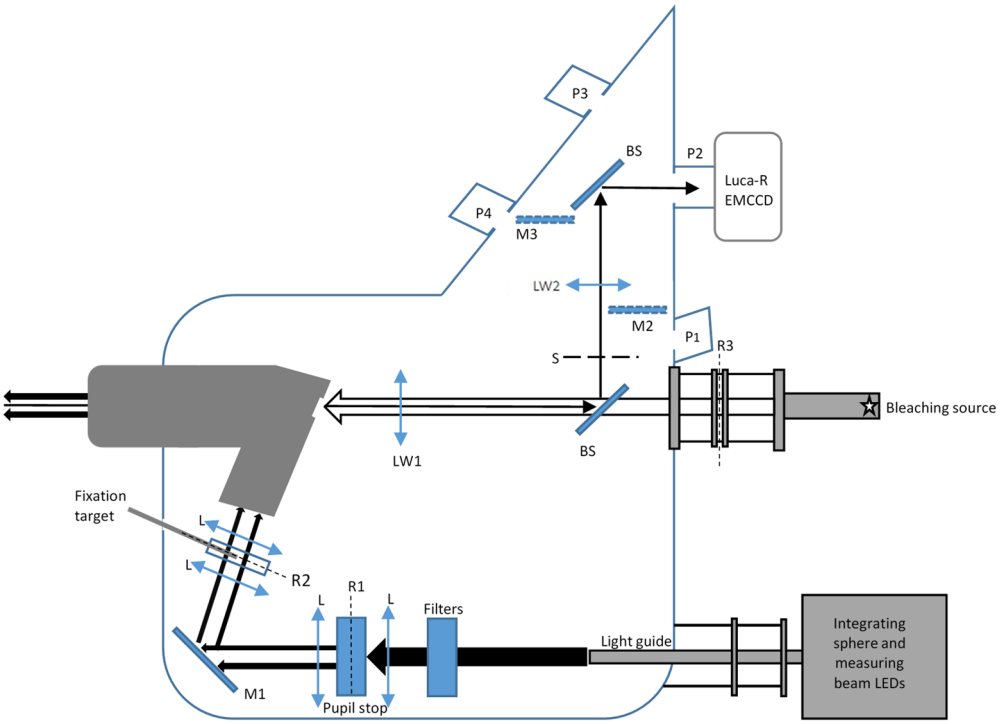

Figure 3.3 A schematic of the Mark II device. Abbreviations, BS = beam splitter, L = lens, LW = lens wheel, M = mirror, ND = neutral density block, P = optical ports, R = planes imaged upon retina, S = electronical shutter. Additional details of the modifications are within the text. The optics immediately behind the objective lens are those from the original TRC-50IX retinal camera. Not to scale. See text for more detail.

3.2.1. Camera

The replacement of the original 35mm film camera with the Andor Luca-R, an electron multiplying charge coupled device (EMCCD), was the most significant

addition to the system, facilitating continuous and efficient photon capture across the image at low light levels. The Luca-R was developed for, and is capable of, detection of single photon events within short time periods. The EMCCD is split into an image area and a storage area, separated by an opaque mask, facilitating its frame transfer capability. The benefit of this is the electronic transfer of the photon count from the light sensitive image area to the light insensitive storage area prior to readout, allowing continuous image acquisition without the need for a shutter.

A further benefit of the Andor Luca-R, is the capability for on-chip binning, which consists of combining the detected charge from 2 or more pixels prior to readout (e.g. 1x2 pixel binning). This spatial summation increases the signal detected, whilst retaining much lower readout noise when compared to performing the same procedure in computer memory, where the read-out noise of each pixel is summated into the detected signal. On-chip binning is defined into vertical and/or horizontal binning and the charge from up to 8 pixels in each direction can be summed together. When both horizontal and vertical binning is combined, the EMCCD becomes a matrix of large 'superpixels':

- 1x1 binning = 1004 x 1002 pixels,
- 8x8 binning = 125 x 125 pixels; superpixels are 64x more sensitive to a photon episode.

Unless otherwise stated, the data collected in this PhD thesis were recorded with 8x8 binning - maximising sensitivity whilst sacrificing spatial resolution. For an eye with no refractive error and an axial length of 24mm, an 8 x 8 pixel is equivalent to 0.48^{o} x 0.48^{o} or 138µm x 138µm (Stephen Todd, UKATC).

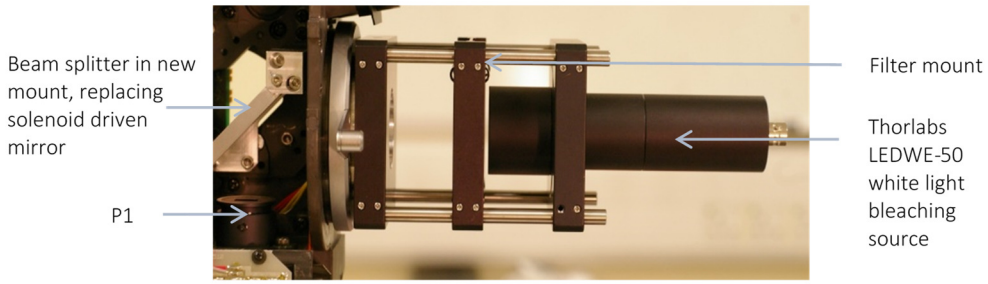

Figure 3.4 Detail of the bleaching module and attachment point to the main device.

3.2.2. Bleaching source

The bleaching source module was attached to the bayonet mount port on the rear of the main housing, shown in Figure 3.4. This mount was originally used to record patient details upon the image, via a solenoid driven mirror. For densitometry measurements, there is no benefit in driving a mirror to use the bleaching source and this was replaced with a fixed position beam splitter (Edmund Optics 80%R:20%T). A Thorlabs 60mm cage plate was used to mount the bleaching module upon the optical axis of the camera system. The bleaching module itself was constructed entirely from standard Thorlabs components, combined with the bayonet mount from the original camera body and a simple mount for a BNC power supply. Illumination was provided by a white LED (LEDWE-50, Thorlabs Incorporated, USA), collimated by a single lens; the spectral output is shown in Appendix C. The fundus camera optics then formed an image of this on the pupil of the eye. A “filter mount”, positioned at R3 (Figure 3.3) allowed 50.8mm square components to be placed at the focal plane for selective bleaching of retinal areas.

3.2.3. Measurement beam

The original flash bulb and filament bulb were removed from the illumination system of the fundus camera and replaced by twelve LEDs, the spectral output of which are given in Table 3.1. The LEDs and filters were bonded into custom made mounting components, the schematics are given in Figure 3.5A. The LEDs were mounted into two ports of a three-inch integrating sphere to achieve uniform illumination over the full field of view. Light from the integrating sphere was fed into

the densitometer via a 6mm diameter light guide. The entire unit is shown in Figure 3.5B.

A

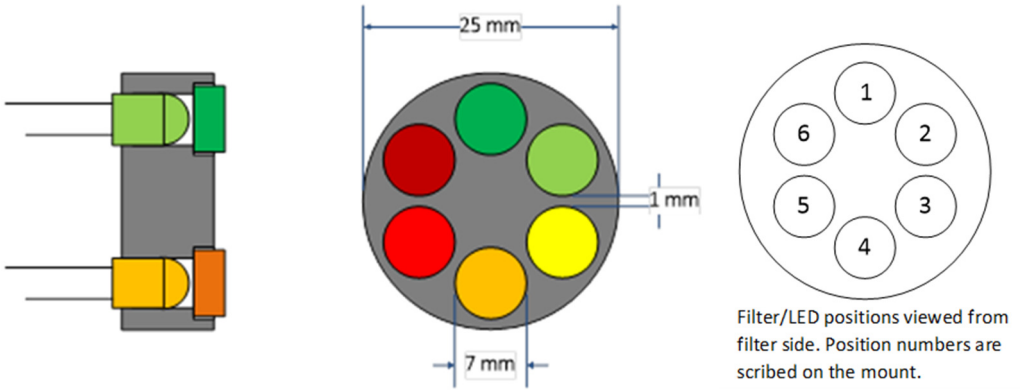

B

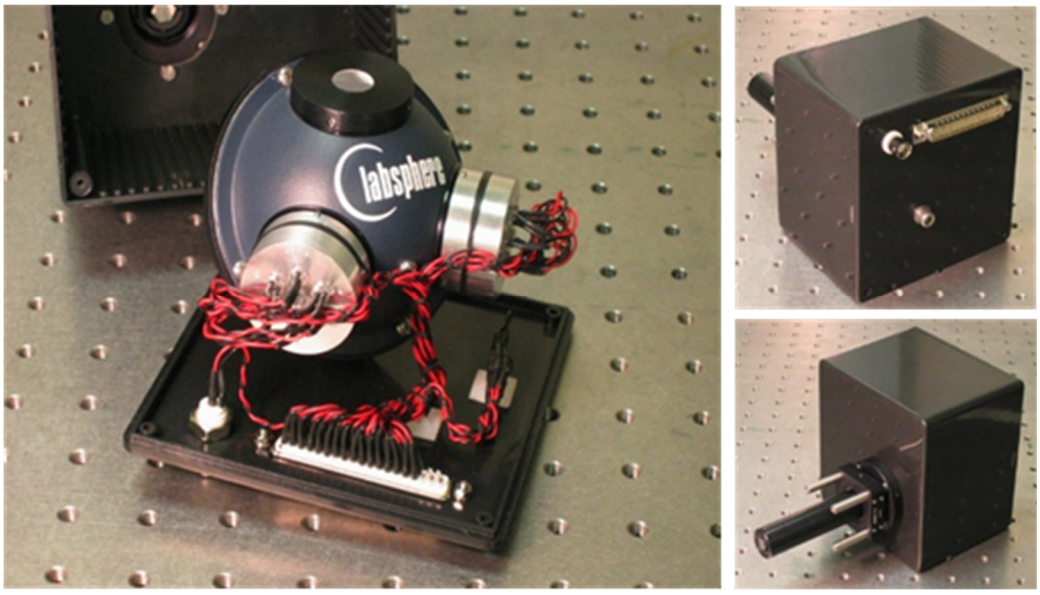

Figure 3.5 A) Construction of the LED and bandpass filter ports, each containing 6 LEDs (Stephen Todd, UKATC). B) Showing the integrating sphere with connected LEDs, alongside the enclosed unit with light guide and electronic connections.

3.2.4. Densitometer mount

The Mark II was mounted onto an external shell plate, supported by two 6mm vernier stages providing 6mm of lateral and translational range and a lab jack providing 56mm of vertical range (Thorlabs, USA). A securely fastened bite bar on an adjustable ball socket minimised head movement (shown in Figure 3.1). A unique

dental impression was created for each participant using Aquasil soft putty (Dentsply, USA), and attached to the bite bar. The bite bar maximises the stability of the participant's head during recording, and was positioned such that the participant's left eye was aligned with the objective lens. The vernier stage was used to align the image with the participant's pupil plane, creating a Maxwellian view optical system.

3.2.5. Electronics

A custom-built control box, separate to the main densitometer body, determined the user defined protocol via a LabVIEW GUI interface.

3.3. Calibration

Before any densitometric measurements of the visual pigments could be made, calibration was required. Of particular importance were the luminance and spectral output of both the measuring and bleaching beams.

3.3.1. Spectral output

Table 3.1 LED calibration data

LED	Nominal output (nm)	Peak output (nm)	Bandwidth (nm) at FWHM	Retinal illuminance (photopic trolands)
1	450	449	10.84	20.42
2	470	469	13.10	65.73
3	500	503	19.63	216.96
4	545	541	12.77	371.39
5	590	589	9.92	201.65
6	620	620	10.20	116.14
7	650	653	11.65	20.04
8	680	678	12.89	0*
9	710	707	13.11	0*
10	740	743	25.79	0*

* LEDs 680 to 740 show a retinal illuminance of 0 photopic trolands as outside the visible spectrum, i.e. these wavelengths do not bleach iodopsin.

The spectral output of all the LEDs was measured using a Jeti Specbos 1201 spectroradiometer. The results are given in Table 3.1 and Appendix C. Note that all but LED 10 have a full width half maximum (FWHM) of less than 20nm.

3.3.2. Luminance

Retinal illuminance, for both the measuring and bleaching sources, was calibrated using an ILT1700 research radiometer (certificate number 607057219, date 07.06.2016), corrected to C.I.E. human eye response by the Y29295 filter (International Light Technologies).

3.3.2.1. Measuring beam

The user defined measuring beam intensity determined both the retinal illuminance and camera signal. To accurately characterise retinal reflectance across wavelengths, the intensity of each of the measuring beam LEDs was adjusted so that the measured camera signal from a spectrally flat surface was equal across all wavelengths. Initially, this was done by obtaining images of a Munsell neutral grey target (20%), and altering the LED intensity in an iterative manner until the signal recorded was equal across all wavelengths. Retinal illuminance at this LED setting was then calculated using the methods described by Westheimer (1966) as shown in Appendix D.

Over the 16.6 minute post bleach recording period (outlined in Section 3.5.2.3) the time averaged retinal illuminance was 97 photopic trolands, equivalent to 558 scotopic trolands. At this setting, bleaching levels were predicted as 2.01% and 0.32% for rod and cone visual pigments respectively (Alpern 1971). Unless otherwise stated, the measuring beams were run at the intensities shown in Table 3.1 for all measurement types.

3.3.2.2. Bleaching beam

Instead of full field illumination, the area of retina bleached was defined by a mask inserted into the filter mount, highlighted in Figure 3.3. This mask had the dual purpose of providing a fixation target during the bleach and leaving a portion of

retina, corresponding to the location of the fixation rod, unbleached, allowing steady fixation to be maintained during the bleach recovery measurement. With the bleaching mask in place, the retinal illuminance was measured in the same manner as above. At 60% intensity, it provided a retinal illuminance of 5.4 log photopic trolands and 6.4 log scotopic trolands. It was calculated that a 120 second bleach at this intensity provides a 91% cone bleach and 99% rod bleach (Alpern 1971). This bleaching period was preceded by a 'ramping' up phase, of 30 seconds each at 5% and 30% making the final 60% bleach more comfortable. Unless otherwise stated, this was the standard bleaching procedure used.

3.4. Functionality

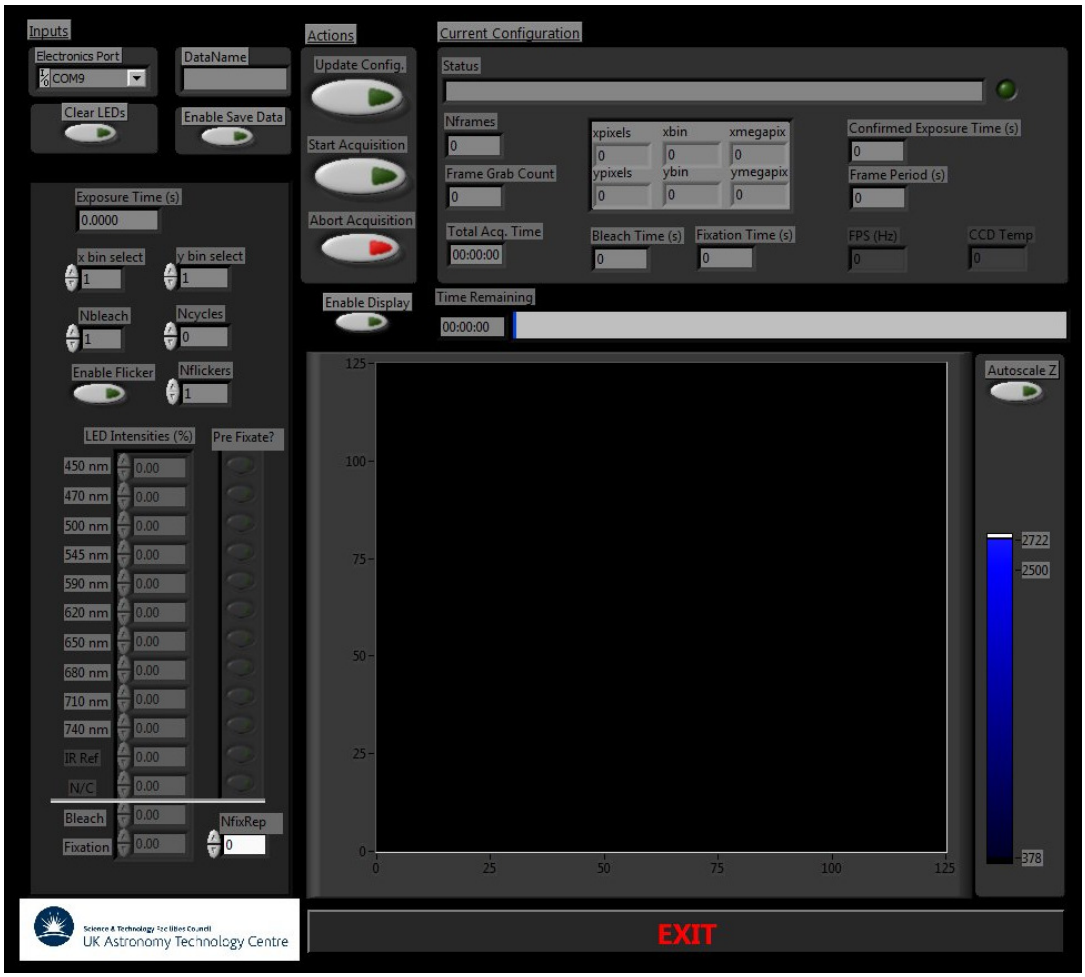

Figure 3.6 A screenshot of the LabVIEW GUI used to define image acquisition protocol.

The device modifications and the electronic control GUI (LabVIEW (National Instruments, Austin)) provide an exquisite amount of control over the use of the device. The GUI and electronics present in the Mark II densitometer were programmed and designed by David Atkinson (UKATC) The functionality of the device is discussed below.

3.4.1. Exposure time

A 'fire' pulse generated by the camera synchronised LED illumination to the camera exposures. The exposure time (in seconds) can be any continuous number. A compromise was made between the larger signal obtained for longer exposure times, and the temporal resolution. Unless otherwise stated, the frame rate was set to 5Hz. One benefit of reducing exposure time to 200ms was the ability to reduce motion blur caused by eye movements. Another was that blinks, which could also corrupt the data, only affected one or two adjacent frames.

3.4.2. Measuring beam duty cycle

Whilst the presentation order of the measuring beams was determined by wavelength (short to long) the choice of LEDs to present and their intensity was fully controllable. Unless otherwise stated, all 10 LEDs were presented sequentially using the pre-determined luminance levels in Table 3.1 and an exposure of 0.2 seconds; a single cycle through all LEDs was 2 seconds.

3.5. Experimental procedure

3.5.1. Participant preparation and device set up

All participants were given an information sheet and written consent was obtained before participation. As determined by the diameter of the pupil stop in the optics, pupil dilation of over 7mm was required for all participants. This was achieved by instilling two drops of 1% tropicamide, separated by 5 minutes, and one drop of 2.5% phenylephrine. Whilst the pupils were dilating, a dental impression was created for each participant and attached to the bite bar. This procedure took place

in subdued lighting conditions. Once pupil diameter exceeded 7mm, the densitometer was aligned and focussed on the centre of the left pupil, using the 500nm LED set at 100% intensity. The right eye was occluded. Participants were required to fixate upon the tip of the fixation rod within the illumination pathway, using their bite bar to aid stability. The device was aligned by hand using the X, Y, Z vernier stage, ensuring the retinal image was focussed and contained no image ghosting or veiling luminance. Once aligned at 500nm, image quality was assessed using 450nm and 590nm LEDs and, if poor, the focussing/alignment procedure was repeated - ensuring a clear image across the spectrum. The alignment procedure would usually be completed within 10 minutes. Due to the sensitivity of the EMCCD, this procedure took place under very low levels of room illumination, with a blackout curtain isolating the device.

3.5.2. Standard recording protocol

Once the densitometer was aligned, and satisfactory images were obtained with all three wavelengths, the participant left the bite bar for a 15 minute dark adaptation period, during which time a 'background' reference image series was collected (see 3.5.2.1). Following this, the participant returned to the bite bar for the recordings; a dark adapted (3.5.2.2) and a bleach recovery series (3.5.2.3). For all recordings, the measuring beams were set to their pre-calibrated intensities, 8x8 pixel binning and a 5 Hz frame rate. The number of frames captured with each LED (or ncycles) was altered for each time series. The recordings were viewed in real time and saved onto the PC hard drive. This allowed assessment of participant compliance, artefacts and alignment/focussing issues.

3.5.2.1. Background reference

This data series was collected in total darkness, a piece of black felt positioned 60cm from the objective lens was used to absorb the light from the measuring beam. With no reflected light present in the image, camera signal comprised EMCCD bias levels and light scatter from within the instrument. The final background reference signal comprised the average of 10 wavelength cycles; the recording taking 20 seconds. In

the background reference images, the signal recorded by any given pixel S_0 (x, y co-ordinates) in the frame illuminated by wavelength λ is described by (Equation 3.1,

$$S_0(\lambda, x, y) = (C + X) \cdot E$$

(Equation 3.1),

where C is the bias level of the EMCCD for any pixel and wavelength, X is the background light levels within the instrument for any pixel and wavelength and E is the quantum efficiency of the CCD.

These factors were present in all recordings. Hence, the background reference image for the appropriate wavelength was subtracted from each image in the dark adapted and bleach recovery time series in order to correct for camera bias and light levels within the instrument.

3.5.2.2. Dark adapted series

Participant preparation usually lasted 30 minutes and took place in subdued lighting, followed by a 15 minutes period of adaptation in absolute darkness. In this dark-adapted state, the photoreceptors contain the maximum amount of pigment, so reflectance is minimal. The measuring beam cycled through all wavelengths 60 times; the whole recording taking 120 seconds. The signal recorded ($S_{DA}(\lambda, x, y, t)$) is described by (Equation 3.2,

$$S_{DA}(\lambda, x, y, t) = (R_{DA}(\lambda, x, y, t) + C + B + X) \cdot E$$

(Equation 3.2),

where $R_{DA}(\lambda, x, y, t)$ is the contribution of the dark adapted retinal reflectance to the final camera signal at any wavelength and time, retinal location and time point and B is back scattered ocular light.

3.5.2.3. Bleach recovery series

This was recorded following exposure to the bleaching source. Following the bleach, the measuring beam cycled through all wavelengths 500 times; the whole recording

taking 16.6 minutes. The signal recorded ($S_B(\lambda, x, y, t)$) is described by (Equation 3.3,

$$S_B(\lambda, x, y, t) = (R_B(\lambda, x, y, t) + C + B + X) \cdot E$$

(Equation 3.3),

where $R_B(\lambda, x, y, t)$ is the contribution of the bleached retinal reflectance to the final camera signal at any wavelength, retinal location and time point. Note that, if visual pigment regeneration is complete by the end of the bleach recovery series, the magnitude of the signal S_B in the final frames of the series should equal S_{DA} (the dark-adapted signal).

3.5.3. Image processing

The dark and bleached time stacks were processed according to the steps outlined in the Figure 3.7. The dataset used to outline the image processing steps was recorded using the methods described in Section 3.5.

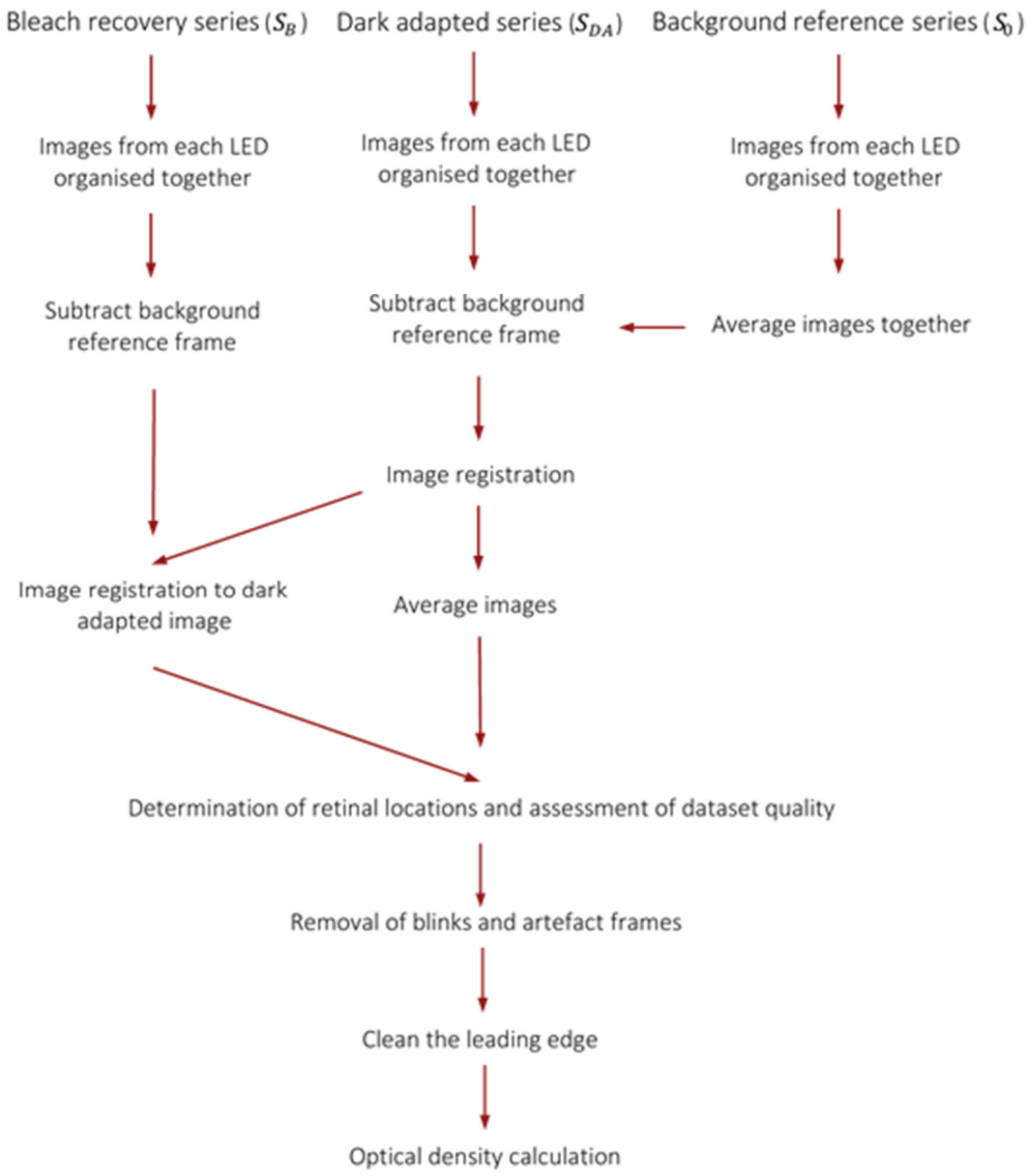

Figure 3.7 Flow diagram summarising the key steps taken during image processing, see text for further detail.

Data analysis began with the opening of the raw densitometry images. These were stored on the computer paired with the Mark II, each recording created a single folder with all images in the acquisition in time sequence and an additional config file (an example config file is provided in Appendix E). Each image was saved consecutively as a .DAT file. Initial processing of these images was performed using a

series of routines written by Stephen Todd (UKATC), in the information data language (IDL) programming language (Exelis Visual Information Solutions, Boulder).

The images were loaded into IDL, using the config file to organise images according to time (t) and wavelength (λ), creating 10 image stacks. For each dataset, there were 'bleach', 'dark' and 'background' image stacks. For each LED the 'background reference' image stacks, containing only CCD bias and internal light scatter, were averaged together (for an example, see Figure 3.9) and subtracted from all dark and bleached images.

All retinal images were corrected for the spatial variation in CCD bias and internal stray light, using (Equation 3.4,

$$S_{n,C}(\lambda, x, y) = S_n(\lambda, x, y) - S_0(\lambda, x, y)$$

(Equation 3.4),

where S_C is the corrected camera signal, S is the raw image and S_0 is the background camera signal for all wavelengths (λ), pixel locations (x, y) and any bleaching conditions (n).

A B

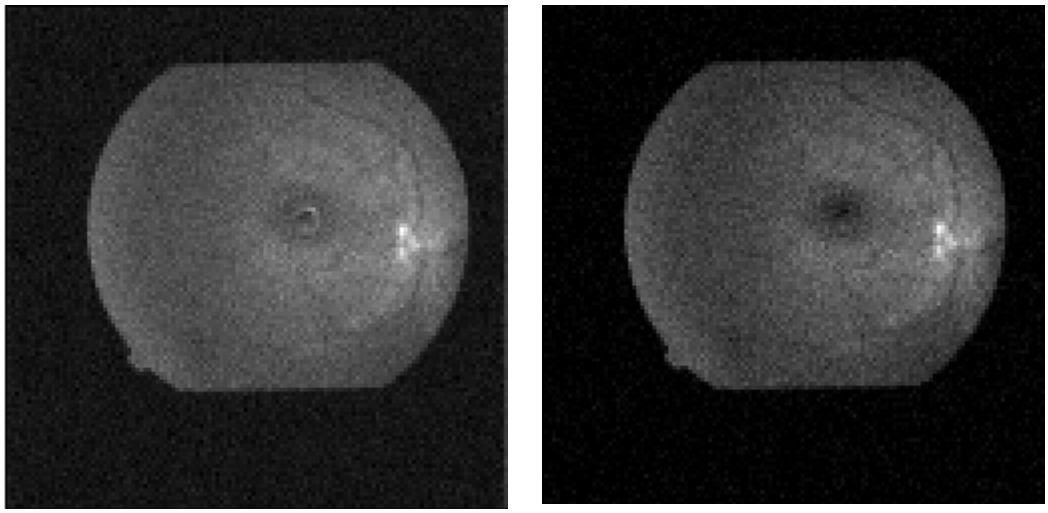

Figure 3.8 Showing retinal images obtained with the retinal densitometer at 450nm. A) Displaying the raw image; note the central artefact. B) Displaying the same image following background subtraction; note the central artefact is no longer present.

A raw image (450nm) is shown in Figure 3.8, where a central artefact is visible, with the background subtracted image shown alongside for comparison.

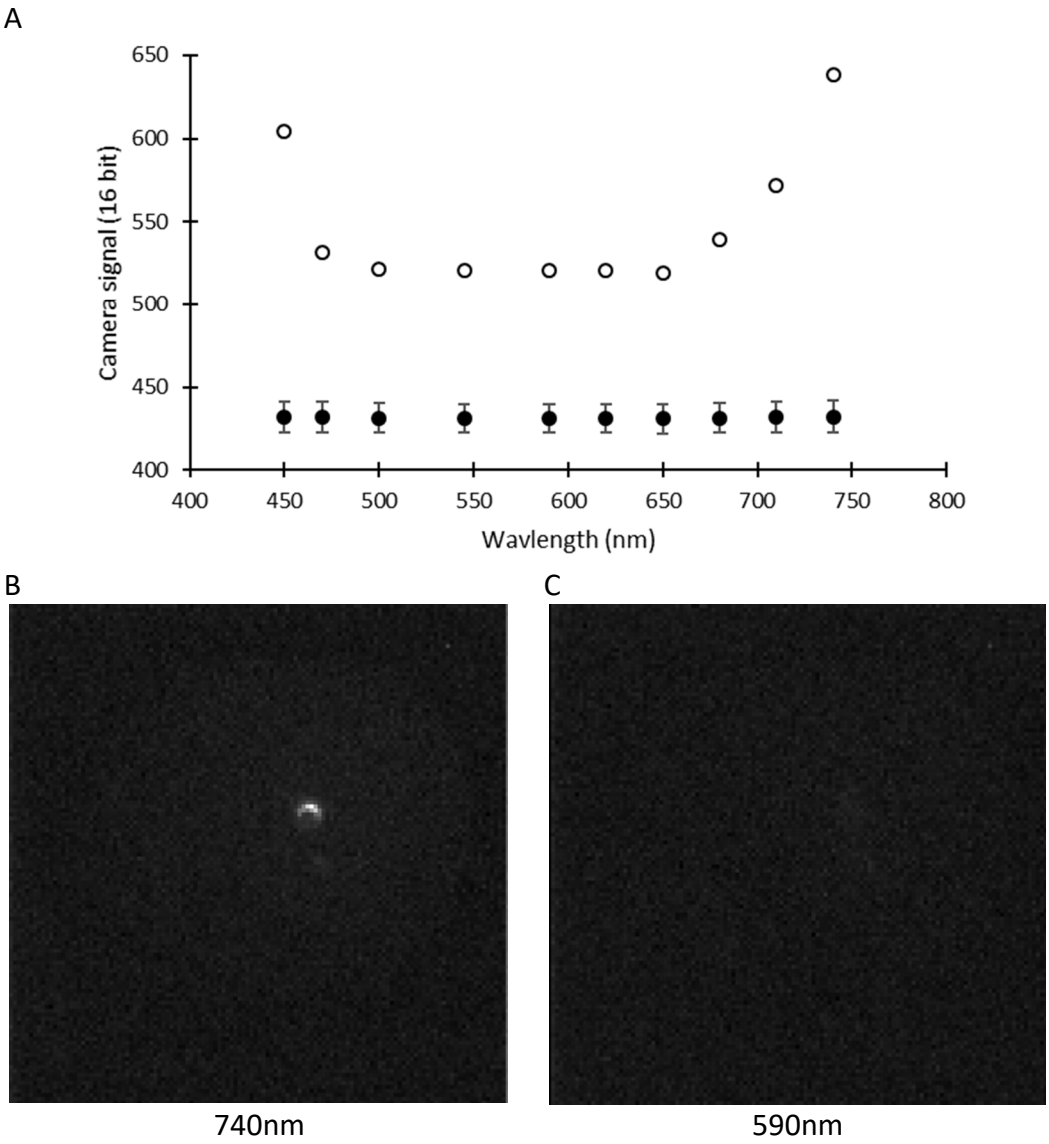

Figure 3.9 Spectral variation of camera signal in the background measurement, data points taken from the median of all 10 frames recorded per wavelength. A) The mean camera signal (closed circles) with standard error bars as measured across the entire frame. The spectral dependence of the peak camera signal within the image is highlighted (open circles). The spatial distribution of the camera signal is shown for the wavelengths with the highest (740nm) (B) and lowest (590nm) (C) measured camera signal.

3.5.3.1. Image registration

Image registration was used to superimpose all retinal images. This was necessary to account for small eye movements which occurred during the recording of the dark or bleach data sets.

The image registration algorithm employed located the high contrast borders in each retinal image and compared them to a reference image (the 10th image from the dark-adapted series). A Laplacian filter was applied to the data to enhance the contrast of small scale features (e.g. blood vessels) and reduce the effect of large scale features (e.g. uneven illumination). The difference in x, y coordinates (the offset) was measured using a fast Fourier transformation (FFT) routine. This searches for the cross correlation of each image by rotating and translating the images in comparison to the reference image. A mask was used to remove the image borders and fixation rod shadow from the correlation routine.

3.5.3.2. Artefact removal

Several artefacts were present in the recordings. In particular, the initial frames were prone to mis-alignment artefacts as the participants fixation was affected by the bleaching source. The extent of these varied between individual recordings, so each dataset was viewed, and a judgement made as to how many frames should be removed from the recording. If more than the initial 3 frames for a single wavelength were affected, the dataset was discarded. Blinks were simpler to identify and remove as they caused a spike in reflectance signal, allowing effective removal via a MATLAB routine; all data points one standard deviation above the average of the time series were removed, this was repeated three times. Figure 3.10 shows example blink artefacts. As these artefacts were readily identifiable, the blink removal algorithm was shown to be accurate by comparison to a dataset where the blinks had previously been identified visually.

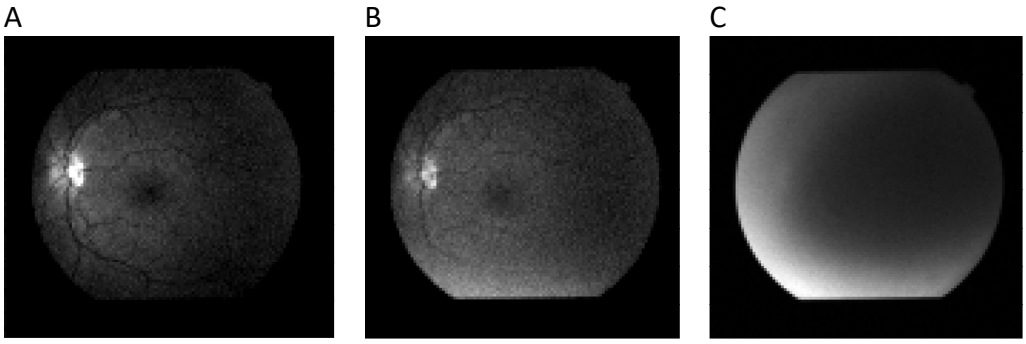

Figure 3.10 Showing three retinal images, captured using the 545nm LED during a single acquisition sequence (dark adapted). A) Shows an unaffected retinal image, B) a partial blink and C) a complete blink.

3.5.3.3. Retinal location

Preliminary investigations required data from isolated rod and cone photoreceptors only. This was easily achieved by exploiting the physiological variation in rod and cone distributions across the central retina (see Section 1.2.41.2.4, Chapter 1). The retinal areas investigated were the fovea and an area 10^{o} temporal to the fovea (the limit of the bleached retina). The foveal region was located subjectively by eye from the image registered time series and the parafoveal region was a location 20 pixels temporal to this, along the horizontal mid line. All data in the following results section refers to these retinal locations as shown in Figure 3.11.

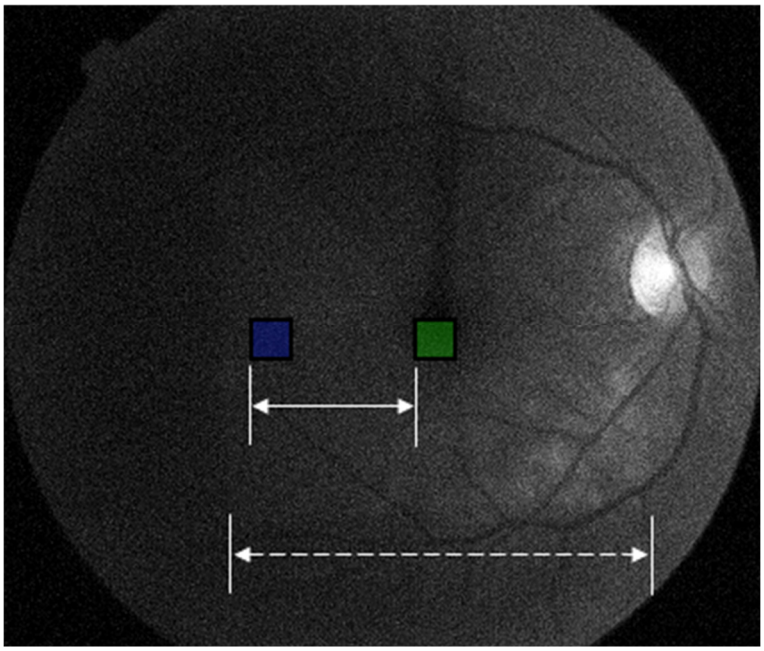

Figure 3.11 A high definition, 1x1 pixel binning, retinal image taken immediately post bleach. The dashed arrow represents the extent of bleached retina (25°). The solid arrow represents the separation of 9.6° between the foveal (green) and parafoveal (blue) retinal locations. Boxes enlarged for clarity.

Figure 3.12 demonstrates the data correction procedures, described above, applied to the raw camera signal for a regeneration and a dark-adapted time sequence obtained from a foveal location. The final panel (D) is logged and used to calculate optical density; subtle differences are noticeable in the quality of the final corrected data (D) compared to the raw data (A); the 'blink' spikes have been removed from the time series, the CCD bias has been removed and image registration has reduced the temporal noise.

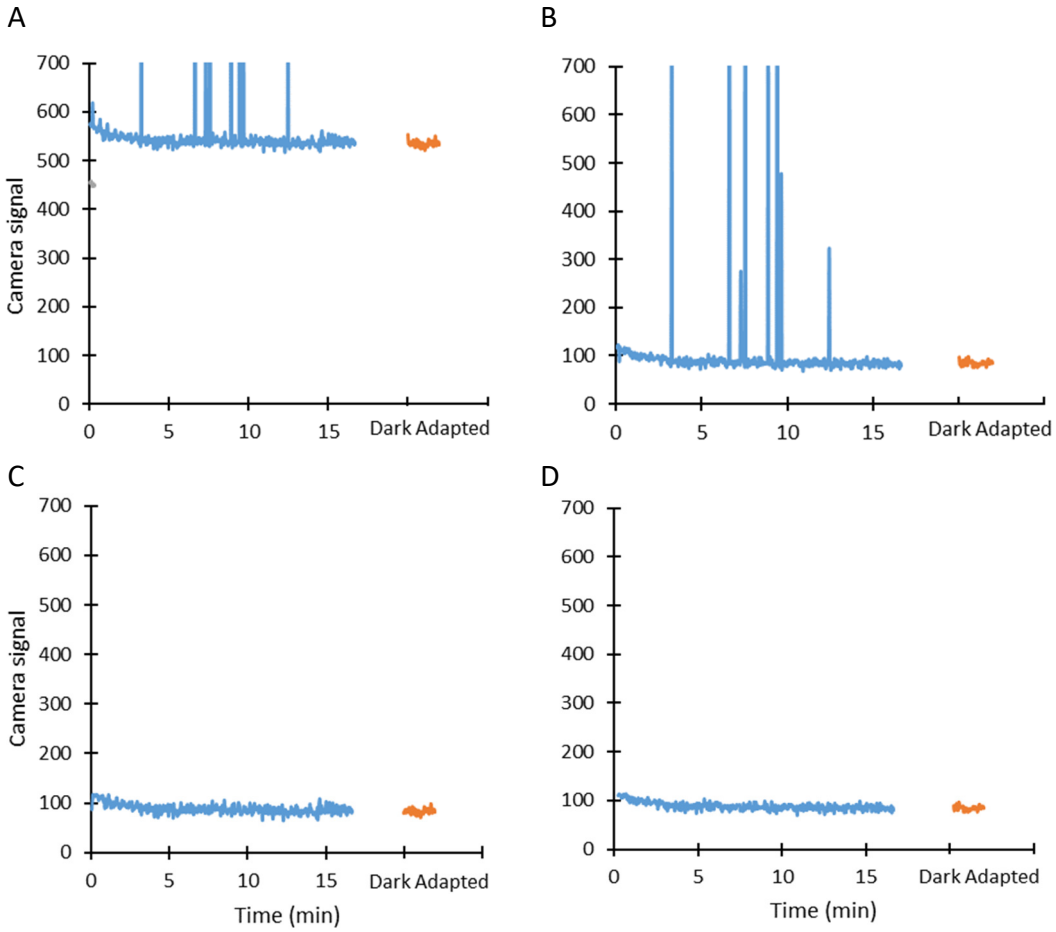

Figure 3.12 Examples of foveal camera signal from one participant (AB) at a highly absorbing wavelength (545nm). Each panel represents a stage in the data correction procedure. A) Represents the raw data, B) the data has been image registered and had the CCD bias removed, C) follows blink removal and D) shows the removal of the first frame and represents the final data used for optical density calculation.

3.6. Summary

This chapter has outlined the development of a novel densitometer which was designed to measure visual pigment density, over space, time and wavelength.

The ultimate aim of this device development was to enable production of repeatable spatially resolved maps of visual pigment optical density and regeneration. However, at the outset it was recognised that the Mark II device would likely be susceptible to some of the issues which beset previous investigations, namely, stray light and a low signal-to-noise ratio. Therefore, the first step was to evaluate the performance of the Mark II densitometer against some reference standard, e.g. published data on

human visual pigments. Whilst the exact optical density and regeneration rates of the visual pigments are open to debate, the *in vitro* absorption spectra have been well characterised (Dartnall et al. 1983; Kraft et al. 1993; Stockman and Sharpe 2000). Hence, the next chapter presents spectral results from preliminary experiments and compares them to the known *in vitro* absorption spectra and *in vivo* regeneration kinetics for rhodopsin and cone pigments.

Chapter 4 - Pilot Investigations

4.1. Introduction

The previous chapter described the Mark II densitometer in detail. Retinal densitometry provides one of the few means to obtain *in vivo* measurement of visual pigment density and regeneration rates (for other techniques see Section 1.4, Chapter 1). This chapter presents the results from pilot experiments and a preliminary analysis.

The exact optical density and absorption spectrum of the visual pigments measured using *in vivo* techniques have not been established with certainty, with results being dependent upon the device and methods employed (Section 2.6.1 and Section 2.6.2, Chapter 2). However, the absorption spectra measured using *in vitro* techniques are well established, providing a suitable benchmark for comparison (Dartnall et al. 1983; Stockman and Sharpe 2000). The rate of visual pigment regeneration following exposure to a bleaching source can only be measured using *in vivo* techniques. Unlike optical density, regeneration rates are largely consistent across available devices (Section 2.6.3, Chapter 2). Whilst first order kinetics have traditionally been used to model densitometry regeneration measurements and provide a good working approximation for rhodopsin regeneration (Alpern 1971; Thomas and Lamb 1999). Elegant modelling by Mahroo, Lamb and Pugh (Lamb and Pugh 2004; 2004) has demonstrated visual pigment regeneration to be well described by a rate limited model (abbreviated to the MLP model). Along with providing a good fit for both rhodopsin and cone pigment regenerations, rate limited Michaelis-Menten models have long been used to accurately describe enzyme reactions similar to those seen in the retinoid cycle (Mahroo and Lamb 2012).

The purpose of these pilot investigations was to evaluate the performance of the Mark II densitometer by determining the absorption spectra, optical density and

regeneration rates of rod and cone photoreceptors using the device and comparing these values to previously defined and published data.

Section 2.7.2 (Chapter 2) highlighted the possibility of ocular stray light confounding the absorption spectra reported from previous densitometry investigations. Given this, it seemed prudent for the experimental absorption spectra to be compared with those obtained by both *in vitro* (Dartnall et al. 1983) and *in vivo* methods (Rushton 1956b; Ripps and Weale 1963; Faulkner and Kemp 1984; Kilbride et al. 1986; van Norren and van de Kraats 1989b; Kilbride and Keehan 1990; Liem et al. 1991; van de Kraats et al. 1996).

Given the many influential publications describing regeneration rates through the application of first order kinetics and measured using densitometry (Ripps and Weale 1969b; Alpern 1971; Rushton and Powell 1972; Hollins and Alpern 1973), the regeneration data obtained in the pilot studies were modelled using first order kinetics and compared with those discussed in Section 2.6.3 (Chapter 2) and presented in Table 2.3 and Table 2.4. Finally, a comparison was made between the ability of the traditional exponential model and the physiologically plausible MLP model to describe the experimental regeneration data presented here.

4.2. Aims

1. To measure the rod and cone visual pigment absorption spectra and compare to published values obtained via both *in vivo* and *in vitro* techniques.

2. To compare the rod and cone optical density to published *in vivo* values.

3. To measure visual pigment regeneration kinetics and evaluate models of visual pigment regeneration.

4.3. General methods

The three aims stated above were addressed using the methodology described in Chapter 3. Unless otherwise specified, the apparatus, procedures, image processing used in the following study were as described in Section 3.5 (Chapter 3).

Table 4.1 Participant characteristics

Participant	Age	Gender	LOCSIII grade	Ocular History
AB	36	F	1	-7.50DS
AW	28	M	1	-5.50DS
TM	48	M	1	Plano / Protanope
CJ	25	M	1	Plano

Four participants took part in this study. All had corrected visual acuities of 6/6 (0.0 LogMAR) or better in the test eye, refractive errors within ±7.50DS and no diagnosis of ocular pathology; the optical media had a LOCS III grade of 1 or less for all categories (Chylack et al. 1993). One participant was a protanope, aiding the characterisation of foveal cone visual pigments. All participants were experienced with the use of the device. Age, gender and ocular history for each participant are provided in Table 4.1.

4.4. Investigation of visual pigment absorption spectra

Each visual pigment has a unique absorption spectrum. Using a multi spectral imaging device, such as the Mark II device, it should be possible to characterise these absorption spectra. Comparison of the isolated visual pigment spectra to previously published spectra was undertaken in order provide a method of bench-marking the spectral capabilities of this device. This study addressed the first aim of the chapter, to measure and compare the isolated visual pigment absorption spectra with previously published *in vivo* and *in vitro* data.

4.4.1. Methods

The Mark II is capable of imaging 50° on the retina at a resolution of 0.48°. The dimensions of the two regions of interest investigated were 0.96° x 0.96°. These preliminary investigations required data from isolated rod and cone photoreceptors. Isolation was obtained by exploiting the variation in both the topographical photoreceptor density, Section 1.2.4 (Osterberg 1935; Curcio et al. 1990) and visual pigment regeneration rates, Section 1.3 (Rushton 1963b; Ripps and Weale 1969a).

The foveal region of interest was located subjectively by eye from the image registered time series and a parafoveal region was located 10° temporal to this point, along the horizontal mid line, as shown in Figure 3.11 (Chapter 3).

4.4.1.1. Isolating the cone spectrum

To isolate the cone spectrum, the fovea was selected as the region of interest as rod density is zero at this location. Equation 4.1 was used to estimate the isolated cone ΔOD for all wavelengths (λ) and at time (t) following cessation of the bleach,

$$\Delta OD(\lambda, t) = log\left(\frac{S_B(\lambda, t)}{S_{DA}(\lambda)}\right)$$

(Equation 4.1),

where S_B represents the post bleach camera signal measured for each wavelength (λ) and the time following bleach cessation (t) represents the mean camera signal 0-10 seconds after bleach cessation. S_{DA} represents the average camera signal obtained for each wavelength, following the dark adaptation period.

4.4.1.2. Isolating the rod spectrum

An area approximately 10° temporal to the fovea was used to extract rod data as the field of view of the bleaching source was limited (25°, see Chapter 3) and histological data suggest that cone density is reduced to approximately 6% of all photoreceptors at this location (Curcio et al. 1990). Compared to cone photopigment regeneration, rod pigment regeneration is a lengthy process. This difference in recovery rate was

exploited to isolate the rod absorption spectrum. If a 1% cone contribution can be regarded as negligible, the rod absorption spectrum could therefore be determined when cone pigment is 80% regenerated, i.e. about 180 seconds after bleach cessation (Mahroo and Lamb 2004). The isolated rod ΔOD was therefore calculated for all wavelengths using Equation 4.1 at the parafoveal region of interest, using data captured 180 to 280 seconds after bleach cessation.

For comparison with published absorption spectra, the average experimental rod and cone absorption spectra for each participant were normalised to their peak ΔOD values. The peak ΔOD was also used for comparison to the published *in vivo* optical density values for both rod and cone photoreceptors.

4.4.2. Results

Figure 4.1 and Figure 4.2 show the mean normalised experimental spectra for all participants. Figure 4.1 shows the absorption spectrum measured at the foveal location and Figure 4.2 the parafoveal region. The experimental absorption spectra obtained were largely consistent between the participants for the separate locations, with the greatest variability seen at the foveal region, where peak absorption was seen at either 590nm or 620nm (Figure 4.1 A, B, C). Foveal data collected from the protanope participant (Figure 4.1 D) showed a marked variation from the group, with an absorption peak at 550nm. The greatest variation in optical density was seen in the data collected using the 450nm LED, ranging from -0.05 to 0.2 between participants.

The absorption spectra obtained in the parafoveal region showed more consistency. Absorption was seen to peak at 545nm for three of the four participants (Figure 4.2 A, C, D), while one participant exhibited a slightly different shape for their parafoveal spectrum (Figure 4.2 A), with peak pigment density at 500nm with low standard error. Like in the foveal location, the largest variation in measured optical density was seen in the data collected using the 450nm LED, across all participants.

At both locations, whilst the mean absorption spectra showed many similarities, there appeared to be a variation in the quality of the data collected. For example,

the standard error around the foveal absorption spectrum shown in Figure 4.1 B was greater than in the other plots. This was repeated at the parafoveal location, with higher standard error seen in Figure 4.2 B and C. In addition to the variability seen in optical density measured with 450nm, several participants showed higher than expected optical density measurable in wavelengths 650nm and beyond, most evident in Figure 4.1 D and Figure 4.2 B.

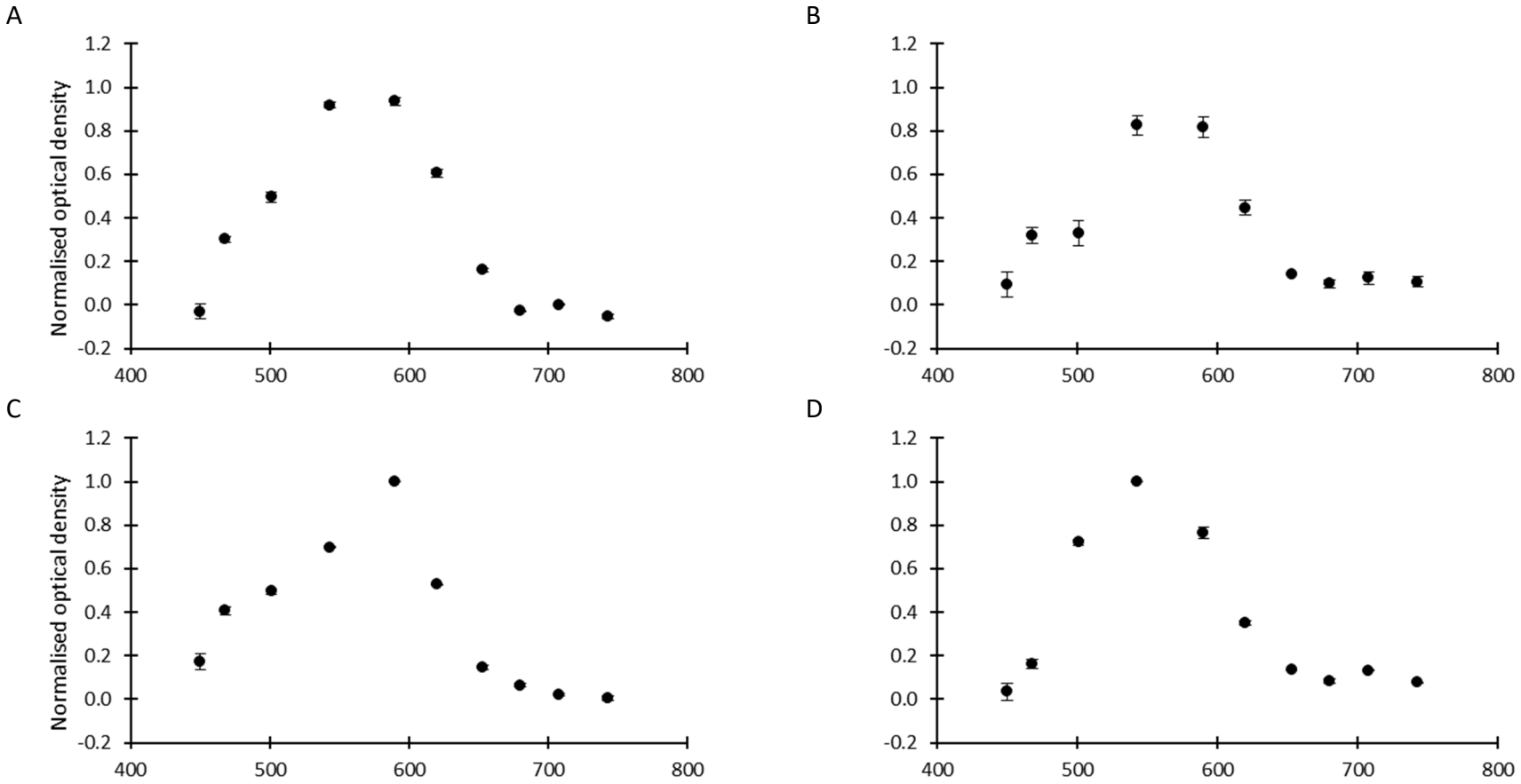

Figure 4.1 Comparison of the experimental cone absorption spectra for each participant (A) AB, B) AW, C) CJ and D) TM) normalised to peak. Circles represent the mean of three recordings (standard error bars).

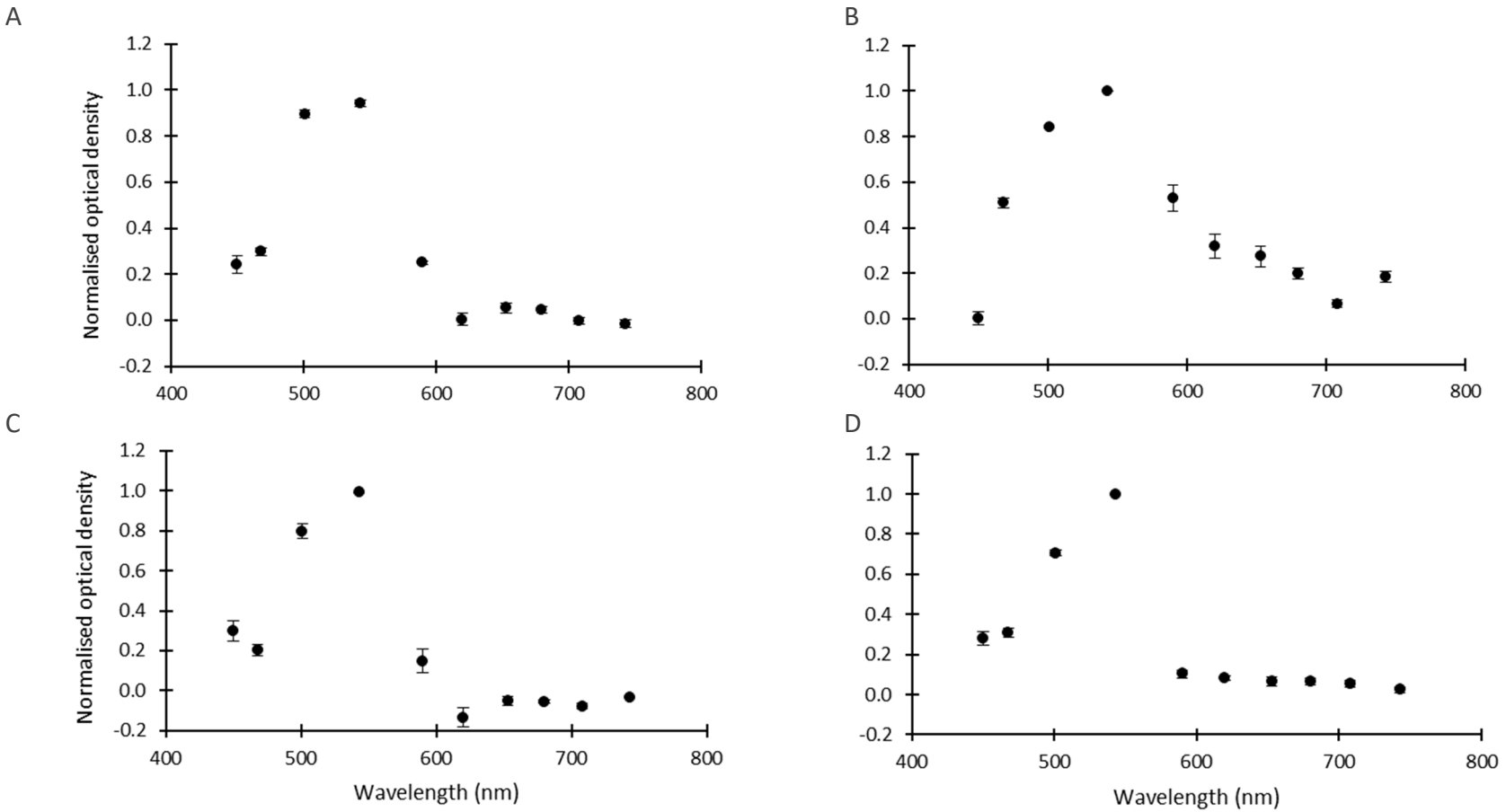

Figure 4.2 Comparison of the experimental rod absorption spectra for each participant (A) AB, B) AW, C) CJ and D) TM), normalised to peak. Circles represent the mean of three recordings (standard error bars).

The normalised absorption spectra in Figure 4.3 corresponds well with *in vitro* data (Dartnall et al. 1983) in terms of shape. However, both rod and cone experimental absorption spectra exhibit a spectral shift to the longer wavelengths. This red shift can be seen to vary with retinal location, being more pronounced in the parafoveal location (Figure 4.3C) than at the foveal location. Data collected from the foveal region showed minor attenuation in optical density below 545nm and a peak between 590nm and 545nm, creating a narrower spectral profile compared to the combined M- and L- cone *in vitro* spectra. Absorption spectra for colour normal participants closely followed L- cone absorption spectra (Figure 4.3A). Conversely, data from the protanope participant can be seen lie between the known M- and L- cone absorption spectrum, with a small red shift at the shorter wavelengths (Figure 4.3B).

The previously published absorption spectra, obtained using retinal densitometry is also presented in Figure 4.3 as grey open symbols; Panel A shows mixed cone (Ripps and Weale 1963; Kilbride et al. 1986; van Norren and van de Kraats 1989b; Kilbride and Keehan 1990; van de Kraats et al. 1996), Panel B isolated M- cone (Rushton 1963a) and Panel C rhodopsin spectra (Rushton 1956a; Faulkner and Kemp 1984; van Norren and van de Kraats 1989b; Kilbride and Keehan 1990; Liem et al. 1991). In general, the published *in vivo* spectra show a similar red shift to the experimental data presented here. However, in most cases, the published *in vivo* spectra lie closer to the *in vitro* data than the experimental data collected during this pilot study. This phenomenon is most noticeable for the rhodopsin spectrum, where peak *in vivo* optical density appears to centre around 525nm, compared to 496nm (±2.3nm) obtained from *in vitro* studies (Dartnall et al. 1983). There is a greater range in the published mixed cone *in vivo* spectral data, some of which compare favourably with the pilot data collected here.

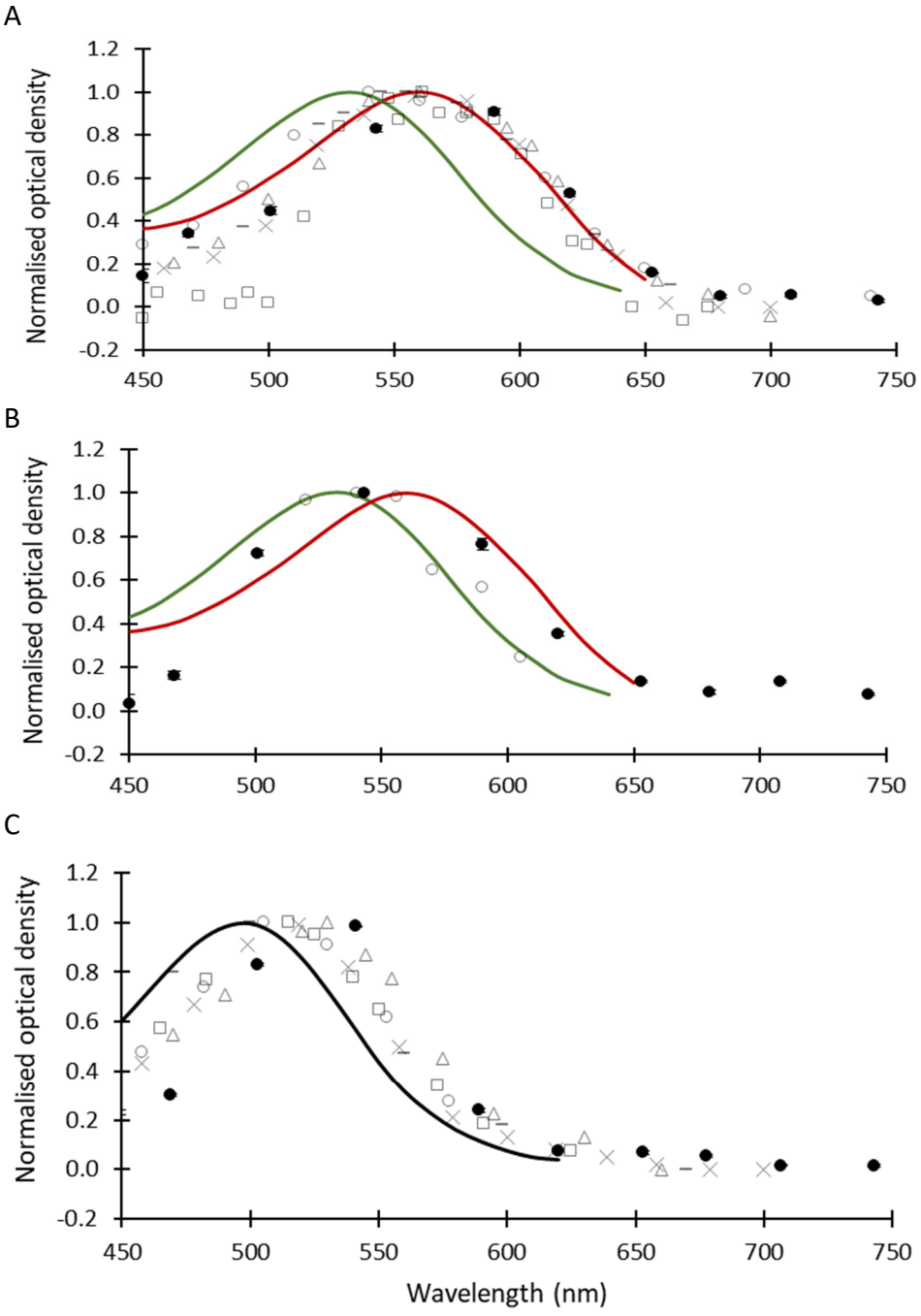

Figure 4.3 Comparison of the normalised experimental data (filled symbols, standard error bars) with published *in vivo* spectra (open symbols) and *in vitro* spectra (solid lines). A) Presents the mean mixed cone spectra from 3 colour normal participants, B) the M- cone spectra obtained from a protanope participant and C) the mean rod spectra from 4 participants. Continuous coloured lines show known *in vitro* spectra from Dartnall et al (1983); black presents rhodopsin, green presents M- cone, red presents L- cone. The grey symbols represent the previously published *in vivo* absorption spectra obtained via retinal densitometry. A) presents the mixed cone spectra (Ripps and Weale 1963; Kilbride et al. 1986; van Norren and van de Kraats 1989b; Kilbride and Keehan 1990; van de Kraats et al. 1996), B) presents an isolated M- cone pigment (Rushton 1963a) and C) presents the rhodopsin spectra (Rushton 1956a; Faulkner and Kemp 1984; van Norren and van de Kraats 1989b; Kilbride and Keehan 1990; Liem et al. 1991). Of note is the spectrum collected by an imaging densitometer (x) in panels A and C (Kilbride and Keehan 1990).

4.4.3. Discussion

This investigation addressed the first aim of the pilot study; to measure and compare the isolated visual pigment absorption spectra with previously published *in vivo* and *in vitro* data.

The methodology exploited the topographical variation in photoreceptor distribution and knowledge of cone visual pigment regeneration kinetics to isolate the rod and cone absorption spectra. The observation that these absorption spectra are a good match with published data suggests this approach was successful.

The shift in absorption spectra from the published *in vitro* data to longer wavelengths was partially expected (Figure 4.3). This effect has been described previously (Faulkner and Kemp 1984) and has been attributed to ocular straylight and attenuation of the short wavelength light by the optical media (Ripps and Weale 1965; Rushton 1965). However, the red shift seen in Figure 4.3C is larger (~30nm) for the presented experimental data than the published *in vivo* absorption spectra, the measurement of which should have been affected by the ocular media in the same manner. What then, could be the cause of the variation in absorption spectra from the *in vivo* data collected using the same technique? Considering the mixed cone spectra only (Figure 4.3A), it would be straightforward to attribute the discrepancy from the *in vivo* data to the varying ratio of M:L cones in the photoreceptor matrix of different individuals (Roorda and Williams 1999). However, the data in Figure 4.3B defies this explanation as the isolated M- cone pigment obtained from a single protanope also varies from the *in vivo* spectra. Further, the rhodopsin spectrum (Figure 4.3C) should also have been free from contamination by other pigments, yet it too shows a significant variation from the published data.

Perhaps then, the kinetics of visual pigment regeneration are the cause of the discrepancy? Only affecting *in vivo* recordings, the dynamic presence of photo-intermediaries (discussed in Section 1.5.4) following exposure to a bleaching source are known to affect the measured spectra (Rushton 1956a; Ripps and Weale 1969a). Of the known rhodopsin photo-intermediaries only 2, barthorhodopsin and

photorhodopsin, could contribute to the red shift seen in the experimental spectra with peak absorptions of 543nm and 558nm respectively. However, their presence is so transient – photorhodopsin and barthorhodopsin being present for a mere 2.2 picoseconds following bleach cessation (Birge and Hubbard, 1981) – that it is not possible they have contributed to the measured absorption spectra. This leads to the consideration of metarhodopsin III. However, as a strong absorber in blue wavelengths (peak 460-480nm) its presence would increase absorption in this region of the spectrum, which would be expected to produce a slight blue shift. Further, the rhodopsin spectrum was collected from data ~5 minutes after exposure to the bleaching source, by which point metarhodopsin III is expected to have decayed to negligible levels (Ripps and Weale 1969a). Despite this, contamination of the spectra by metarhodopsin III has previously been reported (Rushton 1956a; Ripps and Weale 1969a) and as such this should be assessed further (see Section 5.4.1, Chapter 5).

Hence, stray light seems the most likely explanation for the red shift observed in this pilot data. Rushton (1965) was among the first to attempt to quantify ocular stray light. He showed that light scatter from the pre-receptoral retinal layers was likely to be a source of error in densitometry, altering the shape of the *in vivo* absorption spectrum. Therefore, consideration must be given to variations between the densitometry devices. Excluding data obtained from Kilbride and Keehan (1990), depicted by an X in Figure 4.3, the published *in vivo* absorption spectra were obtained from spot densitometers. In terms of stray light control, spot densitometers are superior to their imaging counterparts due to the relatively limited amount of light entering the eye. This may explain why the red shift observed in these pilot data (e.g. in Figure 4.3C) was greater than that observed in previously published datasets.

However, there remains a discrepancy between the data obtained with the imaging densitometer described here and that used by Kilbride and Keehan (1990). There are two crucial differences between the Kilbride and Keehan (1990) data and the experimental data presented here. Firstly, the field of view (50^{o}) of this device is relatively larger than the 20^{o} field used by Kilbride and Keehan (1990). Secondly,

Kilbride and Keehan (1990) studied a location at a greater retinal eccentricity (20^{o} temporal) than the parafoveal location (10^{o} temporal) studies here. These factors are significant because a larger field of view may induce a higher proportion of stray light and the retinal thickness of the two regions is subtly different. It seems possible that the discrepancy between the pilot data presented here and published spectra is related to an increased stray light effect.

The effect of scattered light is likely to be greatest at short wavelengths for two reasons. Firstly, intraocular light scattering has been shown as wavelength dependent, with a significant proportion present in the short wavelengths (Ginis et al. 2013). Secondly, as ocular reflectance is much lower in the short wavelength region of the spectrum (e.g. <2% at 500nm, in comparison to >10% above 680nm (Delori and Pflibsen 1989; van de Kraats et al. 1996)), the effect of any scattered light is more pronounced in this region of the spectrum.

A final thought should be given to some unusual characteristics observed in this data. Intra- participant variation could be seen in the normalised absorption spectra, most noticeable in Figure 4.1 B, C, and Figure 4.2 B, D. This was expected at the short wavelengths due to the low signal to noise ratio, however beyond 650nm the recorded camera signal increased, achieving a high signal to noise ratio and variation around the mean would be expected to be small. There have been recent investigations into the possibilities of an 'intrinsic' retinal signal (Schallek et al. 2009a; Schallek et al. 2009b; Tsunoda et al. 2009; Masella et al. 2014), measurable in the far-red spectrum after cessation of a significant bleach. Whilst there is no conclusive proof such a signal is measurable in humans, it is possible this affected the results seen in Figure 4.1 and Figure 4.2.

4.5. Investigation of visual pigment regeneration kinetics and optical density

The two classes of visual pigment (rhodopsin and iodopsin) have specific regeneration rates. Visual pigment regeneration rates have been described by first order equations (Alpern 1971) for many years and, more recently, by rate limited kinetics (Lamb and Pugh 2004; Mahroo and Lamb 2004).

The measurement of the visual pigment regeneration rates in this study provided a method for bench-marking the temporal capabilities of this device. Further, the two models of regeneration could be evaluated. This study therefore addressed the second and third aims of this chapter; to compare the rod and cone optical densities to published *in vitro* and *in vivo* values and to measure visual pigment regeneration kinetics and evaluate models of visual pigment regeneration.

4.5.1. Methods

The optical density at any time (t) and location (x, y) can be described through the summation of rod and cone density, as in Equation 4.2,

$$\Delta OD(x, y, \lambda, t) = OD_r(t) \cdot N_r(\lambda) + OD_c(t) \cdot N_c(\lambda)$$

(Equation 4.2),

where $OD_r(t)$ and $OD_c(t)$ represent the total optical density of rod and cone visual pigment present at the given location and time. The previous results reported the normalised absorption spectra for both rhodopsin $N_r(\lambda)$ and cone visual pigments $N_c(\lambda)$.

To determine the density of rod (OD_r), and cone (OD_c), visual pigment at each timepoint during the regeneration process, optical density data $\Delta OD(\lambda, t)$ were fitted with the normalised rod and cone spectra $N_r(\lambda)$ and $N_c(\lambda)$, as described in

Figure 4.3. In practice this was achieved using the *fminsearch* function in MATLAB (see Appendix K).

The solution to the *fminsearch* routine returned both rod and cone visual pigment regeneration time series for each retinal location. For the purposes of investigating visual pigment kinetics, the rod trace from the parafoveal region and cone trace from the foveal region were selected.

The spectrally resolved time sequence for each visual pigment was fit with both the MLP rate limited model, (Lamb and Pugh 2004; Mahroo and Lamb 2004) ((Equation 4.3) and an exponential model (Alpern 1971) (Equation 4.4), using a least squares paradigm (Solver function, Excel),

$$\Delta OD(t) = \left(1 - K_m \cdot W\left\{\frac{OD(0)}{K_m} \cdot e\left[\frac{OD(0)}{K_m}\right] \cdot e\left[-\frac{1+K_m}{K_m} \cdot r \cdot t\right]\right\}\right) \cdot \sigma$$

(Equation 4.3),

where t is time after bleach cessation in seconds, K_m is the Michaelis constant, W is the Lambert-W function, r is the initial rate of regeneration after a total bleach and σ is the asymptotic density of the pigment. The parameters σ and r were allowed to vary whilst K_m was fixed to a value of 0.2, as described in Lamb and Pugh (2004),

$$\Delta OD(t) = 1 - \left\{e\left(\frac{-t}{\tau}\right)\right\}$$

(Equation 4.4),

where, the time constant of regeneration, τ (seconds), is the time taken for the proportion of visual pigment to return to approximately 63.3% (i.e. ~$1 - {}^{1}/_{e}$) of its maximum value. Time after bleach cessation, t, is in seconds.

4.5.2. Results

Figure 4.4 shows an example of the model fit for both an MLP rate limited and exponential model to cone visual pigment regeneration, for a single dataset. A full

breakdown of the rate of regeneration and τ for all participants is given in Table 4.2. Both the MLP and rate limited models provided an equally good description of the data, with the mean RMSE value across the group being 0.022 (±0.003), for each model. Whilst the RMSE was similar for both models, viewing the data suggested that the rate limited model may have provided a better description of the data over the initial period of regeneration, with the exponential model showing a greater deviation from the data between 2 and 5 minutes.

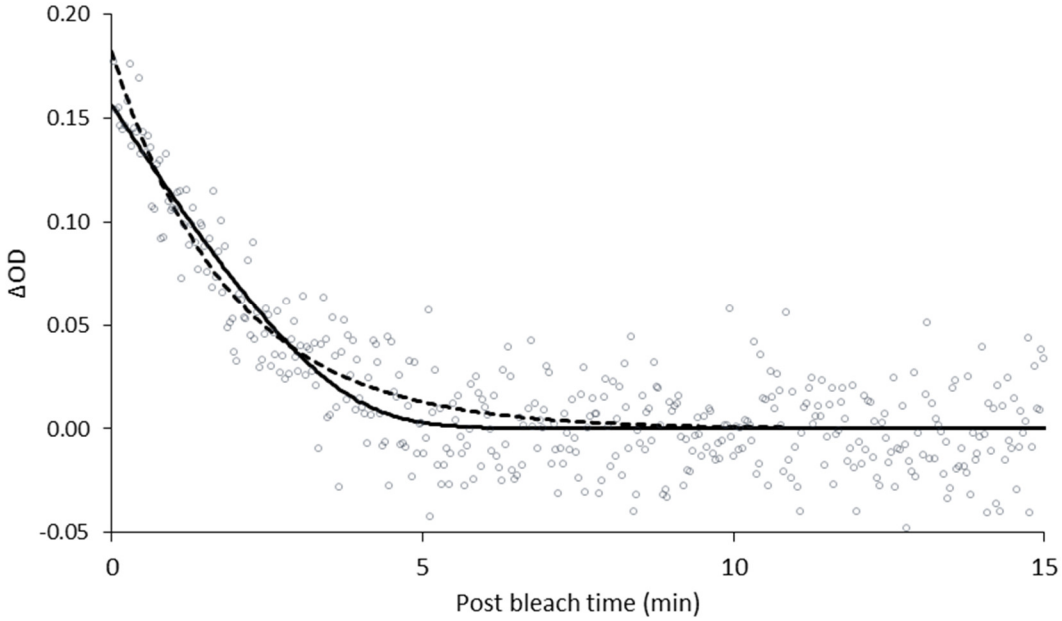

Figure 4.4 The MLP rate limited (solid line) and an exponential (interrupted line) model fit to the isolated cone visual pigment regeneration for a single participant (circles).

AB dataset 3 - r 0.30min^{-1}, ΔOD 0.016, RMSE 0.019, τ 113 seconds, ΔOD 0.18, RMSE 0.019.

The average rate of regeneration and τ obtained for all participants was 0.29min^{-1} (±0.09 SD) and 128 seconds (±71 SD), respectively.

Table 4.2 The regeneration kinetics for all datasets and participants, for the isolated cone pigment.

Participants	r (min^{-1})	τ (seconds)
AB dataset 1	0.35	71
AB dataset 2	0.30	113
AB dataset 3	0.17	124
AW dataset 1	0.22	157
AW dataset 2	0.27	125
AW dataset 3	0.28	118
CJ dataset 1	0.43	69
CJ dataset 2	0.39	87
CJ dataset 3	0.23	149
TM dataset 1	0.12	335
TM dataset 2	0.35	97
TM dataset 3	0.34	93
Mean	0.29 (±0.09SD)	128 (±71SD)
Mean RMSE	0.022 (±0.003SD)	0.022 (±0.003SD)

Figure 4.5 shows an example of the model fit for both an MLP rate limited and exponential model to rod visual pigment regeneration, for a single dataset (colour normal). A full breakdown of the rates of regeneration and τ for the peak wavelengths, across all participants is given in Table 4.3. Both the MLP and rate limited models provided a good description of the data, again with identical RMSE values of 0.017 (±0.003SD). The average rate of regeneration and τ obtained for all participants was $0.12min^{-1}$ (±0.02 SD) and 372 seconds (±78 SD).

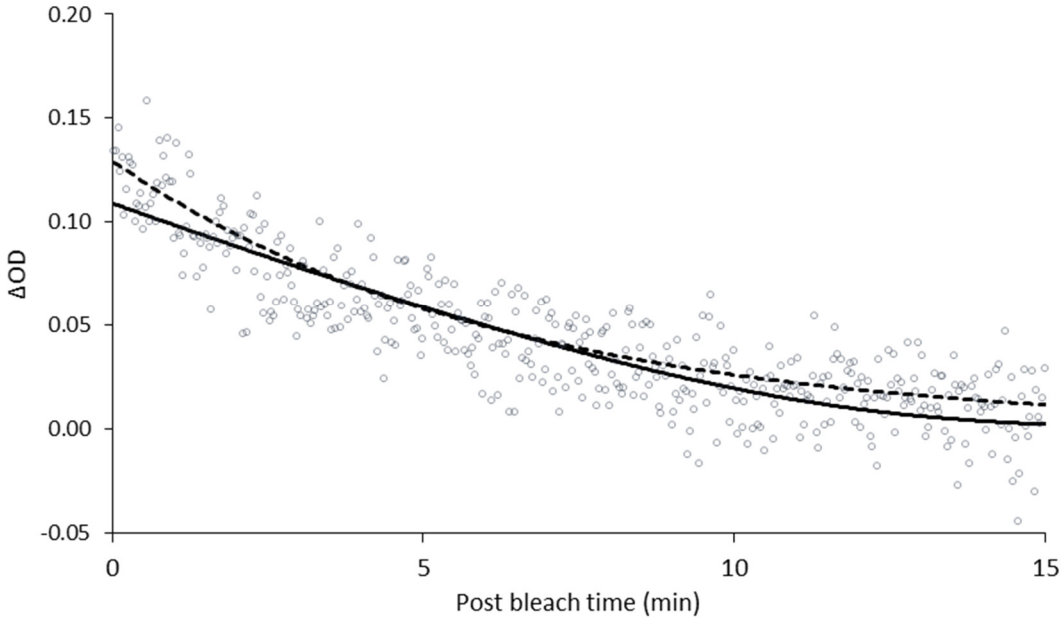

Figure 4.5 The MLP rate limited (solid line) and an exponential (interrupted line) model fit to the isolated rod visual pigment regeneration for a single participant (circles).

AB dataset 2 - r 0.10min^{-1}, ΔOD 0.11, RMSE 0.018, τ 413 seconds, ΔOD 0.13, RMSE 0.018.

Table 4.3 The regeneration kinetics for all datasets and participants, for the isolated rod pigment. Modelling of the mean $\Delta OD(t)$ provided the group fit for all participants.

Participant	r (min^{-1})	τ (seconds)
AB1	0.11	373
AB2	0.12	383
AB3	0.10	413
AW1	0.11	467
AW2	0.15	207
AW3	0.14	294
CJ1	0.12	360
CJ2	0.13	385
CJ3	0.15	326
TM1	0.10	498
TM2	0.13	328
TM3	0.11	427
Mean	0.12 (±0.02SD)	372 (78 SD)
Mean RMSE	0.017 (±0.003SD)	0.017 (±0.003SD)

Whilst the RMSE was identical for both models, there was a proportionately greater range for the value of τ, than there was for the rate. In addition, whilst the MLP

model appeared to underestimate the ΔOD, the exponential appeared to provide an overestimation of ΔOD.

The mean rod $\Delta ODmax$ for all participants was measured as 0.09 (±0.023 SD). The cone $\Delta ODmax$ was measured as 0.16 (±0.047 SD) for the colour normal participants and a substantially lower cone $\Delta ODmax$ of 0.04 (±0.046 SD) was measured for the protanope. These values were obtained from the rate limited model fit of the modelled rod and cone regeneration traces.

4.5.3. Discussion

This set of pilot experiments set out to address three aims (Section 4.2). The measurement and comparison of the isolated rod and cone visual pigment absorption spectra was addressed in Section 4.4. The remaining aims, the measurement of visual pigment regeneration kinetics and optical density and evaluation the MLP and exponential models of regeneration, have been addressed using the data presented in section 4.5.2.

The mean rate of regeneration obtained from for both cone (0.29min^{-1}, ±0.009 SD) and rod (0.12min^{-1}, ±0.02SD) visual pigments compare well with those published in the literature. Using a very different method, Mahroo and Lamb (2004,2012) suggest cone visual pigment regeneration can be well modelled using rates of between 0.32min^{-1} and 0.39min^{-1}, comparable to the measured rate of 0.29min^{-1}. Lamb and Pugh (2004) obtained a rate of 0.085min^{-1} for rhodopsin kinetics, again comparable to the experimental value of 0.12min^{-1} observed here. The τ values obtained at the foveal (128 seconds ±71SD) and parafoveal (372 seconds ±78SD) locations, also correspond well with the values from the literature (see Table 2.3 and Table 2.4). Interestingly, while both models provide a good fit in terms of RMSE, values for τ suggest faster initial regeneration rates than obtained through the MLP model. This is particularly evident when viewing the cone model fits (Figure 4.4), where the exponential model can be seen to overestimate ΔOD in comparison to the MLP model, particularly in the first few minutes of regeneration.

Whilst there are similar published values for the peak ΔOD obtained in this pilot study, the rod and cone ΔOD of 0.09 (±0.023 SD) and 0.16 (±0.047 SD), respectively, remain on the low side when compared to published data (Section 2.6.1 and Section 2.6.2, Chapter 2). However, whilst below the published average, ΔOD of 0.21 (rod) and 0.29 (cone), the experimental values presented here are similar to those previously published by wide field imaging densitometers (see Tables 2.1 and 2.2), in particular Faulkner and Kemp (1984) published a peak rod OD of 0.06, whilst Fulton and Hansen (1987) published a peak cone OD of 0.1.

It is possible the bleaching source in the Mark II densitometer did not provide the photopigment bleach expected. Extensive calibrations with the ILT1700 research radiometer (International Light Technologies Incorporated, USA), itself calibrated to ISO/ISEC 17025 standard by International Light Technologies Incorporated (USA) suggested the bleaching source was capable of reaching the required intensity. However, whilst the equations used to estimate photopigment bleaching used in this study have been implemented by many investigators, being based on first order kinetics, their accuracy is questionable and, despite technological advancements in the techniques, have remained un-repeated in peer reviewed literature since the 1970's.

4.6. Summary

The data presented here show that the Mark II densitometer can capture information about the visual pigments.

Whilst the absorption spectra measured in this experiment undoubtedly relate to the visual pigments, they do vary from the known literature, displaying a small but definite 'red shift'. For example, the measured cone spectra do not compare directly to the known M- and L- cone spectra, this is exemplified in the spectra recorded from the protanope participant.

Investigation into the photopigment kinetics suggest that both the exponential and MLP models of regeneration kinetics provide a good description of the data with

neither model superior in terms of goodness of fit. However, the exponential model shows a greater variability in τ and peak OD, which corresponds to the faster regeneration rates obtained through this method. In addition, the MLP model has been accepted as a more physiologically robust description of visual pigment regeneration. As such, it seems prudent to employ the MLP model of visual pigment kinetics to describe the regeneration data collected using this device.

The spectral shift seen in Figure 4.3 presented an obstacle to the use of the well characterised *in vitro* visual pigment spectra to separate the contributions from the three common visual pigments; rods M- and L- cones. However, prior to investigating the causes of the spectral shift seen in Figure 4.3, it was essential to fully understand the more unexpected features of the data. The studies described in the following Chapter investigated these inconsistencies. A priority was to explore the possible impact of metarhodopsin III. Then, the accepted constant which describes the bleaching of visual pigments was re-assessed using the Mark II densitometer, which was capable of measuring visual pigment optical density independent of a long red wavelength reference source. Furthermore, given the recent report of reflectance changes at long wavelengths following photopigment bleaching (Masella et al. 2014), it was also of interest to quantify changes in long wavelength reflectivity following photopigment bleaching in humans.

Chapter 5 - Effect of Metarhodopsin III, I_{Rh} and Long Wavelength Reflectance

5.1. Introduction

Chapter 4 described the optical density, absorption spectra and rate of regeneration for rods and cones using data obtained from the Mark II densitometer. Whilst the rate of regeneration was comparable to values from the published literature, the optical density and absorption spectra showed some discrepancies. The experimental optical density measured for rod and cone visual pigments was lower than had previously been reported (Alpern and Pugh Jr. 1974; Morgan and Pugh 2013). Furthermore, the absorption spectra for some participants showed variation at wavelengths shorter than 500nm and longer than 620nm. This was unexpected for two reasons; firstly, there is no known cause of interparticipant variation in the rhodopsin spectra and, secondly, rhodopsin does not absorb light beyond 620nm (Dartnall et al. 1983). These unusual results, discussed in Sections 4.4.3 and 4.5.3 (Chapter 4), invited further investigation.

Contamination of the data by metarhodopsin III, a time dependent, short wavelength absorbing pigment was considered as this may have impacted the short wavelength data. Ripps and Weale (1969b) demonstrated the absorption spectra they obtained immediately following a photoflash bleach to be made up of two pigments, rhodopsin and metarhodopsin III, with a differing time course of decay. Figure 5.1 shows that as time after bleach cessation progresses, the shape of the difference spectra changes, with a shift in peak wavelength from around 470nm at 0.5 minutes to 510nm at 10 minutes. This change in the spectral shape provides the evidence for a secondary non-rhodopsin pigment, with a differing rate of decay.

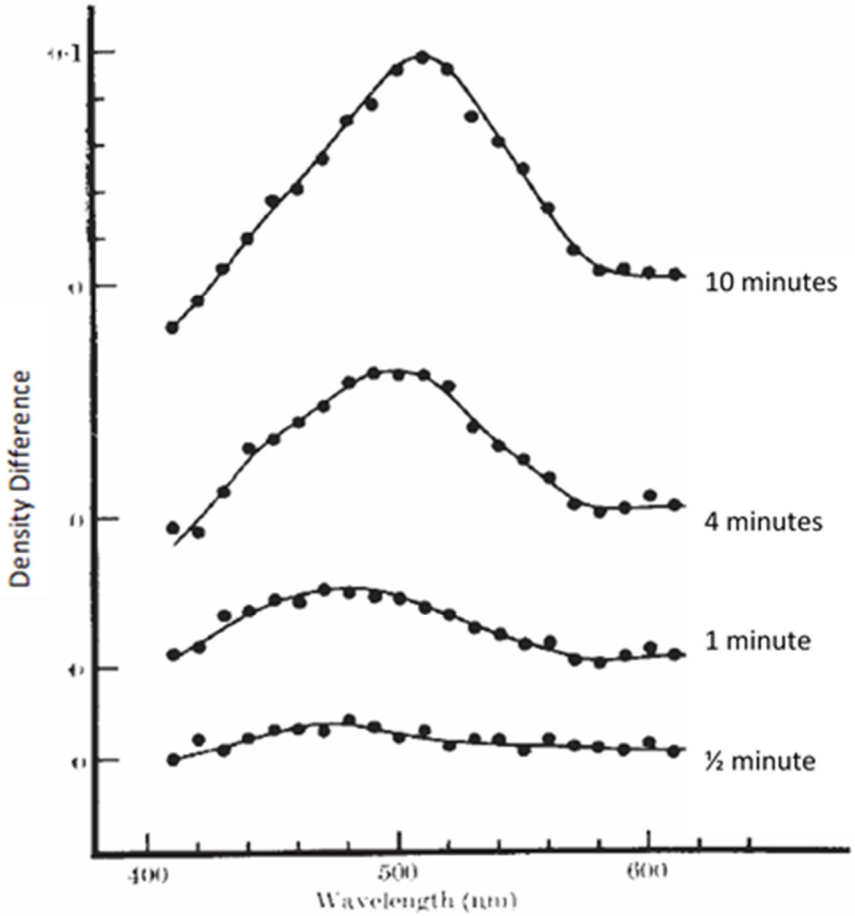

Figure 5.1 Density difference at 0.5, 1.0, 4.0 and 10 minutes after bleach cessation. Average results from 3 participants, with the density difference on the y-axis and the post bleach time on the right-hand side. Plots separated vertically for clarity. Reproduced from Ripps and Weale (1969b).

If a similar pattern is shown to be present in the data obtained in Chapter 4, then contamination of the visual pigment spectra by metarhodopsin III is a likely possibility. However, there are two distinct differences between the methodology used in Chapter 4 and that used by Ripps and Weale (1969b). Their data were collected immediately after a flash bleach (<0.8ms in duration) of 7.1 log scotopic trolands. The bleach employed in Chapter 4 was an equilibrium bleach of 6.2 log scotopic trolands, with a duration of 120 seconds. In addition, a 'ramping' period of 60 seconds during which the participant was exposed to a gradually increasing light source was used prior to this. Secondly, the proportion of pigment bleached was different for each study; Ripps and Weale (1969b) estimated a 68-78% rhodopsin

bleach, whilst the bleach described in Chapter 4 was an estimated 99% bleach of the rhodopsin present. These two differences may play a role in determining whether the data collected for Chapter 4 were influenced by metarhodopsin III to a meaningful extent. Firstly, the time since bleaching began (and metarhodopsin III was initially produced) was 3 minutes longer in the equilibrium bleach utilised in Chapter 4 than the flash bleach described by Ripps and Weale (1969b). It is possible that metarhodopsin III may have decayed to negligible levels during this time. Secondly, the lower intensity light combined with the higher proportion of pigment bleached may have affected the metarhodopsin to rhodopsin ratio. Even so, it is prudent to contemplate the possibility of the data having been contaminated by metarhodopsin III.

Returning to the question of the low optical density measurement and long wavelength variations, seen in Chapter 4, it is possible these two unusual results are related. Retinal reflectance in the long wavelength region of the spectrum has traditionally been considered stable. Indeed, this assumption was fundamental to the design of early retinal densitometers (Section 2.5.1), where measurements were based on the direct comparison between a relatively short wavelength measuring source and a long wavelength reference source (Rushton et al. 1969; Alpern 1971; Hood and Rushton 1971; Sieving et al. 1995).

However, there is evidence to indicate systematic changes in retinal reflectance at long wavelengths, at both foveal (DeLint et al. 2000) and parafoveal (Masella et al. 2014) locations, this raises some doubt over the methodology used in these key papers defining rhodopsin kinetics (Ripps and Weale 1969a; Alpern 1971; Rushton and Powell 1972). For example, Masella et al (2014) showed that long wavelength retinal reflectivity increases following exposure to a substantial light source (over 7 log scotopic trolands), the effect measurable for a period of at least 15 minutes. Whilst these fluctuations raised doubts regarding results obtained from early densitometers (Masella et al. 2014), recent investigations (Morgan and Pugh 2013) have found that τ_{Rh} values measured independent of red light are broadly similar to the original values (Alpern 1971; van Norren and van de Kraats 1989b). Although

these publications suggest the estimates of τ_{Rh} are correct, the accuracy of the half bleach constant, I_{Rh} for equilibrium bleaches remains an open question. This is particularly pertinent considering the relatively recent work by Morgan and Pugh which suggested that, following a flash bleach, the constant I_{Rh} may be higher than the previously established value (Alpern 1971; Morgan and Pugh 2013). It Is possible this could be the same for longer duration equilibrium bleaches, impacting on the accuracy of any photobleaching calculation. Therefore, the relatively low optical density recorded in Chapter 4 may have been due to insufficient bleaching.

Understanding the relationship between light intensity and photopigment bleaching is the starting point for robust evaluation of dark adaptation kinetics. Whilst elegant modelling by Mahroo and Lamb (2004) demonstrated rhodopsin regeneration to be well described by a rate limited model, it was seen in Chapter 4 that first order kinetics (Alpern 1971) provide a good working approximation and were therefore used to derive the constants τ_{Rh} and I_{Rh} in the investigations described here. Furthermore, this would allow direct comparison to the historically calculated values (Ripps and Weale 1969a; Alpern 1971; Rushton and Powell 1972). Based on first order principles, Equation 5.1 (Alpern 1971) enables the calculation of the proportion of pigment present, p, following exposure to a light source of known intensity, I (trolands), presented for a duration, t_B (seconds). The half bleach constant, I_{Rh}, is the intensity (trolands) required to achieve a 50% photopigment bleach. The time constant of regeneration for rhodopsin, τ_{Rh} (seconds), is the time taken for the proportion of rhodopsin to return to $1 - {}^{1}/_{e}$ (i.e. approximately 63.3%) of its maximum value,

$$p = \left(\frac{I}{I + I_{Rh}}\right) \cdot \left\{1 - e\left(-\left(1 + \frac{I}{I_{Rh}}\right) \cdot \frac{t_B}{\tau_{Rh}}\right)\right\}$$

(Equation 5.1).

With increasing bleach duration, a point is reached where the rate of photopigment bleaching equals the rate of its regeneration. Thereafter, extending the duration of the bleach has no further effect upon the proportion of rhodopsin present. Under

these equilibrium conditions, Equation 5.1 can be simplified to Equation 5.2 (Alpern 1971),

$$P_{eq} = \left(\frac{I}{I + I_{Rh}}\right)$$

(Equation 5.2).

The value of I_{Rh} is established in the literature as 4.44 log scotopic trolands and is commonly used to calculate rhodopsin bleaches (Paupoo et al. 2000; Pianta and Kalloniatis 2000). A value of 372 seconds for τ_{Rh} was obtained during the preliminary experiments and corroborated by the published literature, (Section 4.5.3) (Alpern 1971; Sieving et al. 1995). Therefore, this value was used in the calculation of the half bleach constant. Table 5.1 summarises the parameters used in equations in Chapter 5.

Table 5.1 Parameters used in Chapter 5

Parameter	Definition
p	Proportion of visual pigment present after exposure to a light source of known intensity (I) and duration (t_B). Calculated using Equation 5.1.
P_{eq}	Proportion of visual pigment present after exposure to an equilibrium bleach. Calculated using Equation 5.2.
t	The proportion of visual pigment present at a given time (t) after cessation of the bleaching source. Calculated using Equation 5.3.
I	Intensity, in scotopic trolands, of the bleaching source.
I_{Rh}	Intensity, in scotopic trolands, required to bleach 50% of the rhodopsin present in a fully dark adapted, healthy retina.
t_B	Duration of the bleach, in seconds.
τ_{Rh}	Time taken for rhodopsin to return to $1 - {}^{1}/_{e}$ (i.e. approximately 63.3%) of it maximum value.
$\Delta OD(t)$	The experimental optical density (double pass) measured at a given time (t) after cessation of the bleaching source. Calculated using Equation 4.1.
$\Delta ODmax$	The theoretical optical density present after a 100% visual pigment bleach.
$\Delta DD(\lambda)$	Density difference (double pass), calculated using Equation 5.3
$S_o(\lambda)$	Camera signal immediately after bleach cessation (for all wavelengths)
$S_t(\lambda)$	Camera signal at any given time following bleach cessation (for all wavelengths)

The studies described here investigated the inconsistencies between the published densitometry literature and the experimental data presented in Chapter 4. A priority was to explore the possible impact metarhodopsin III may have had upon the

experimental data. Then, the accepted value for I_{Rh} was re-assessed using the Mark II densitometer, which was capable of measuring visual pigment optical density independent of a long red wavelength source. It was also of interest to quantify changes in long wavelength reflectivity following photopigment bleaching in humans.

5.2. Aims

The specific aims of the investigations described here were:

1. To explore the temporal characteristics of the difference spectra to determine if metarhodopsin III could be contaminating the data.
2. To establish the value of I_{Rh} using the Mark II densitometer which allows the measurement of visual pigment optical density independent of a long red wavelength source.
3. To calculate the proportion of visual pigment bleached, using the white light LED as described in Chapter 4.
4. To investigate long wavelength (740nm) data collected in Chapter 4 with regard to variation in reflection following a bleach.

5.3. Methods

5.3.1. Investigating the potential impact of metarhodopsin III

The data evaluated were those collected in Chapter 4 (Section 4.4.1), i.e. 3 full 16-minute bleach regeneration recordings from 4 participants. The same parafoveal retinal locus was investigated i.e. a 2x2 pixel (1^ox1^o) region, 10^o temporal to the fovea.

The raw data were processed as described in Section 3.5 (Chapter 3). Briefly, the EMCCD reference and internal stray light signal was subtracted, the images registered to a common frame and any blinks removed,

$$\Delta DD(\lambda) = log\left(\frac{S_o(\lambda)}{S_t(\lambda)}\right)$$

(Equation 5.3).

The camera signal for each wavelength was averaged over 30 second periods. The initial time point (i.e. the average of the first 30 seconds following bleach cessation) became the reference post-bleach data, $S_0(\lambda)$. Equation 5.3 calculated the density difference (ΔDD) for all subsequent time points, $S_t(\lambda)$. The density difference obtained at 5 time points, spread throughout the series, was compared for any notable change in spectral shape.

5.3.2. Establishing the half bleach constant (I_{Rh})

5.3.2.1. Participants

Four healthy participants were studied (ages 25, 27, 31 and 48) each providing informed, written consent. Ethical approval was obtained from the School of Optometry and Vision Sciences and adhered to the tenets of the Declaration of Helsinki. All participants had corrected visual acuity of LogMAR 0.0 (6/6) or better in the test eye, refractive errors within the range of the device (±7.50 DS) and no diagnosis of ocular pathology. In particular, the optical media had a LOCS III grade of <1, for all categories (Chylack et al. 1993). One participant was a protanope, all others had normal colour vision. All participants were experienced with the procedures and device used in these experiments.

5.3.2.2. Device modifications

Whilst modifications (described below) to the bleaching and illumination apertures of the retinal densitometer were required for this study, unless stated, the device was as described in Chapter 3.

A circular 12° diameter mask, centered 18° temporal to fixation was positioned in R2 (Figure 3.1, Chapter 3). This retinal location combines the maximum rod photoreceptor density with a negligible cone photoreceptor density (Curcio et al. 1987). A 15° mask defined the bleached region. This mask was inserted in position R3 (Figure 3.1, Chapter 3) and centred over the 12° measuring field. This left the fovea unbleached, allowing accurate fixation throughout the measuring procedure. A longpass filter, with 95% transmission from 500 - 740nm (475nm Schott Glass filter; Schott AG, Germany) was placed in front of the bleaching source for this study.

5.3.2.3. Data collection

Data were collected using the 500nm measuring beams at a frame rate of 2.5Hz, providing a time-averaged retinal illuminance of 2.95 log scotopic trolands.

The eye was exposed to the bleaching source for 300 seconds followed by a 120 second post bleach recording. The bleach/record procedure was repeated for all bleaching intensities. Each subsequent bleaching episode increased retinal illuminance by approximately 0.3 log scotopic trolands; beginning at 2.90 and increasing to 5.50 log scotopic trolands. As bleaching intensity increased incrementally, there was no need to repeat the dark adaptation process between each recording.

5.3.2.4. Data analysis

The median camera signal from the central 5° of the illuminated region was obtained and Equation 4.1 (Chapter 4) was used to calculate the optical density, for all time points and bleaching conditions, $\Delta OD_n(t)$.

The proportion of visual pigment present following cessation of the bleaching source, $p_n(t)$, was calculated for all bleaching episodes using Equation 5.4. $\Delta ODmax$ was the theoretical optical density change following a complete rhodopsin bleach,

$$\mathrm{p_n}(t) = 1 - \left(\frac{\Delta \mathrm{OD_n}(t)}{\Delta ODmax}\right)$$

(Equation 5.4).

For each bleaching procedure, n, the proportion of rhodopsin present immediately before, $p_{n-1}(120)$, and immediately after, $p_n(0)$, each bleach was determined using linear regression. The amount that would be present at equilibrium, $P_{eq\ n}$, was calculated using Equation 5.2. Knowledge of these values along with the regeneration rate, τ_{Rh} (372 seconds, Section 4.5.2, Chapter 4), and bleaching duration, t_B (300 seconds), allowed the proportion of pigment present following a bleach of any intensity, *B*, to be calculated, using Equation 5.5 (Alpern 1971),

$$\mathrm{p_n}(0) = \mathrm{P_{eq\ n}} + \left(\mathrm{p_{n-1}}(120) - \mathrm{P_{eq\ n}}\right) \cdot \mathrm{e} - \frac{\mathrm{t_B}}{\tau_{\mathrm{Rh}} \cdot \mathrm{B}}$$

(Equation 5.5).

Putting the measured values of $p_n(0)$ and $p_{n-1}(120)$ from each of the n recordings into Equation 5.5 gave a set of n equations. A least squares optimisation algorithm was used to solve Equation 5.5 simultaneously with Equation 5.4 and Equation 5.2 to obtain both variables in question, i.e. I_{Rh} and $\Delta ODmax$ (Solver function, Excel).

The proportion of pigment present following the bleach employed in Chapter 4 (i.e. a 120 second bleach of 6.4 log scotopic trolands) was then calculated using Equation 5.1, where τ_{Rh} was 372 seconds and I_{Rh} was the mean value found using the method described above.

5.3.2.5. Investigating long wavelength ocular reflectance

The data evaluated were those collected in Chapter 4 (Section 4.4.1), i.e. 3 full 16-minute bleach regeneration recordings from 4 participants. The same parafoveal retinal locus was investigated i.e. a 2x2 pixel (1°x1°) region, 10° temporal to the fovea.

The raw data were processed as described in Section 3.5 (Chapter 3). Briefly, the EMCCD reference and internal stray light signal were subtracted, the images registered to a common frame and any blinks removed.

Signal levels for all frames post-bleach were normalised to the median dark-adapted level, providing a normalised reflectance change following bleach cessation, with a temporal resolution of 2 seconds. The mean normalised reflectance was obtained for all 12 data sets presented in Chapter 4 and the 95% confidence limits calculated.

5.4. Results

5.4.1. Investigating the impact of Metarhodopsin III

Figure 5.2 presents the mean density difference absorption spectra at several time points following bleach cessation. The only data point exhibiting any temporal variation was that obtained from the 450nm LED.

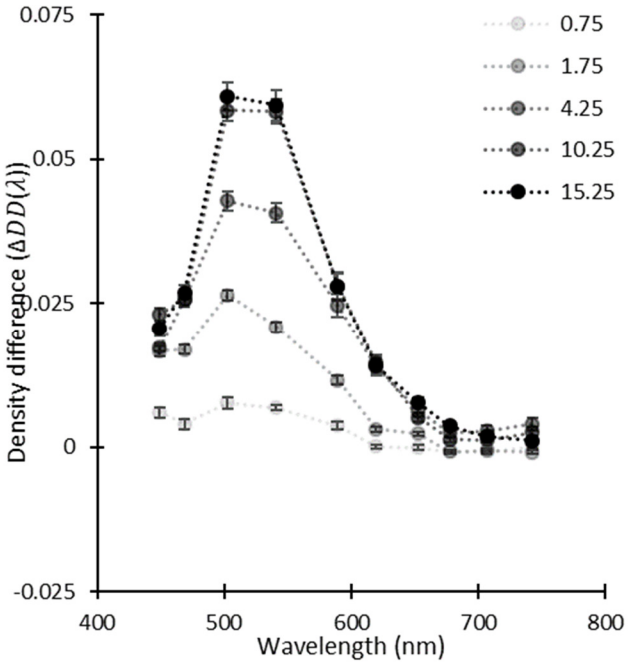

Figure 5.2 The mean density difference ($\Delta DD(\lambda)$) for all participants, measured at 5 time points with a similar temporal distribution to those in Figure 5.1. The distinctive shift in peak wavelength from 470nm to 510nm observed by Ripps and Weale (1969b) is not evident in the experimental data presented here, the peak wavelength is repeatable at 500nm. Error bars describe the standard error, lines interpolated for clarity.

The 450nm data point was comparatively higher at both 0.75 and 1.75 minutes than for the all subsequent difference spectra, with an inflection point at 470nm for the same time points. The remaining difference spectra, collected at 4.25, 10.25 and 15.25 minutes all showed a repeatable shape. Throughout the time-series, the peak of the absorption spectra remained at 500nm.

5.4.2. Establishing the half bleach constant (I_{Rh})

Figure 5.3 shows the optical density change measured following the 2.90 log scotopic trolands bleach (open symbols) and a 5.50 log scotopic trolands bleach (closed symbols) with linear regression trendlines (dotted lines), from one participant. The open symbols show that there was no obvious change in optical density when camera signal immediately post bleach was compared to the dark-adapted recording. This is reflected in the fact that there was no detectable change in optical density during the 120 second bleach regeneration recording period, indicating that there was no measurable photopigment bleach at these light intensities. However, the closed symbols show that there was a change in optical density of 0.17, measurable immediately following bleach cessation.

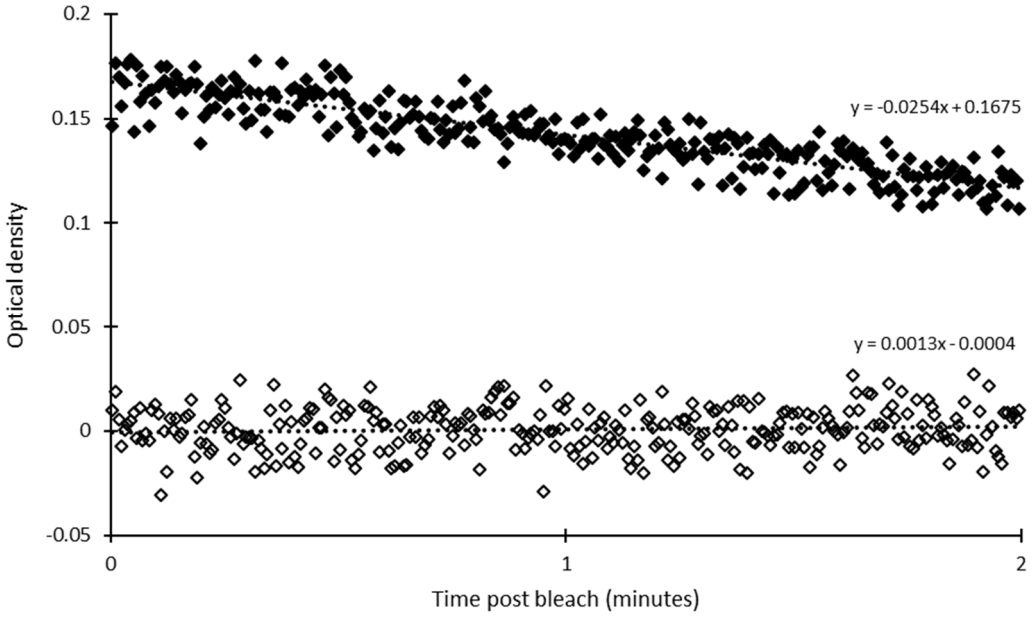

Figure 5.3 Change in optical density over 2 minutes, following a 2.90 (open symbols) and a 5.50 (closed symbols) log scotopic troland bleach, for participant CJ. The optical density change relative to the dark-adapted recording for this participant was 0.00 and 0.17 respectively.

Table 5.2 Values obtained from the modelling procedure for all participants

	CJ	JF	NC	TM	*Average*
$\Delta ODmax$	0.19	0.21	0.17	0.21	*0.20*
I_{Rh}	4.54	4.65	4.66	4.59	*4.62*

Table 5.2 presents the values obtained for I_{Rh} and $\Delta ODmax$. The average value for I_{Rh} was 4.62 log scotopic trolands (± 0.02 SE). The value of $\Delta ODmax$ was found to be consistent within the participant group, with an average value of 0.20 (± 0.01 SE).

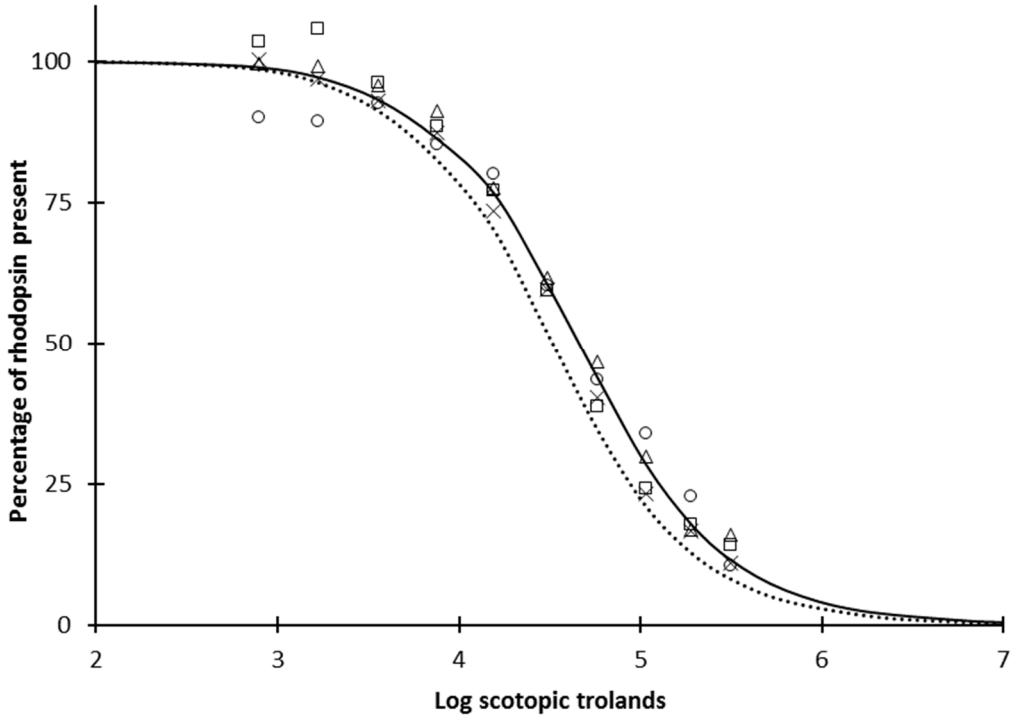

Figure 5.4 Effect of increasing retinal illuminance upon the percentage of visual pigment present, as measured after 300 seconds; data for all participants (each symbol type represents a participant) are shown against the average I_{Rh} = 4.62 log scotopic trolands (solid line). The dashed line was obtained using the I_{Rh} value of 4.44 log scotopic trolands, as originally proposed by Alpern (1971).

Figure 5.4 shows the proportion of photopigment present at each bleaching intensity. This figure effectively represents the photosensitivity of rhodopsin to light. For all four participants, the proportion of photopigment present declined monotonically as bleaching intensity increased. The model fit was excellent, with a RMSE of 0.027 (± 0.09 SD) across the participants. It can be seen that the data were consistent between individuals; although some discrepancies were seen at the lower bleaching levels where, due to lower optical density measurements, noise had a greater effect on trend line analysis. The data points did not meet the y-axis at the highest bleaching intensities, indicating that a 100% bleach of photopigment was not achieved.

The half bleach constant (I_{Rh}) values obtained for individual participants are shown in Table 5.2. Figure 5.4 also presents the modelled bleach (Equation 5.1) using the

average I_{Rh} value of 4.62 log scotopic trolands obtained from the experimental data (solid line) alongside the model fit obtained using the value of 4.44 log scotopic trolands for I_{Rh}, as suggested by Alpern (1971) (dashed line). A minor discrepancy was evident at the higher bleaching levels. However, using a value of 4.62 log scotopic trolands for I_{Rh}, the proportion of pigment present following a 120 second bleach of 6.4 log scotopic trolands (as employed in Chapter 4) was calculated as 0.02, i.e. a 98% bleach.

5.4.3. Investigating long wavelength ocular reflectance

No systematic changes in retinal reflectance following bleach cessation were observed when measured with 740nm light. For all participants, retinal reflectance at this wavelength was seen to be stable and comparable to pre-bleach reflection levels, shown in Figure 5.5.

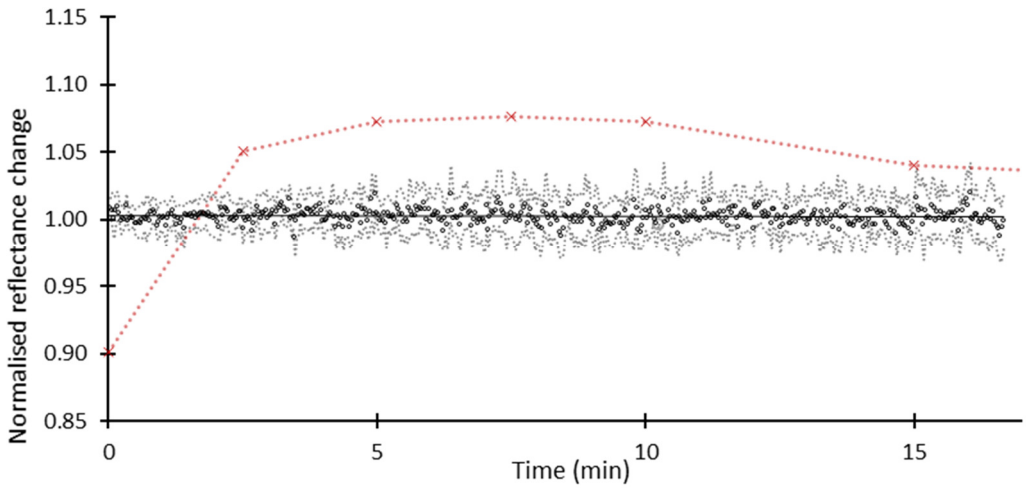

Figure 5.5 Change in reflectance measured using a 740nm light source in the peripheral retina following exposure to an equilibrium bleach of 6.2 log scotopic trolands. Solid line shows a linear fit through the data, satisfied by the Equation $y = -8 \cdot 10^{-05} \cdot t + 1.003$. Mean data from 12 experiments (4 participants, 3 repeats), the dashed lines to either side of the data describe the 95% confidence limits. The crosses describe the data from Masella et al (2014), measured with 794nm light source, following a 2 second flash of 7.6 to 7.9 log scotopic trolands.

5.5. Discussion

The three studies described in this Chapter addressed some of the questions raised by the data shown in Chapter 4. Firstly, the possible contamination of the short wavelength data by metarhodopsin III was investigated. Then the half bleach constant (I_{Rh}) was re-assessed. Finally, the long wavelength data were investigated for changes in retinal reflectance following a bleach.

By examining the shape of the difference spectra over time it was possible to determine if metarhodopsin III could be contaminating the data. Figure 5.1 presents the density difference measured following a visual pigment bleach at several time points. The data were repeatable for all the time points, with low SEM across the spectrum. However, the clear shift in the spectral shape reported by Ripps and Weale (1969b) was not evident in the experimental data (Figure 5.2). In fact, the experimental peak density difference remained stable at 500nm throughout the time series. What is evident is a relative decrease in the density difference measured at 450nm as the time series progresses. It is possible that a transient short wavelength absorber may be affecting the 450nm data point. Due to the relatively long time course and given the 'red shift' seen in the parafoveal location (Figure 4.3, Chapter 4) it is more likely that change at 450nm was related to a small contribution from the S- cones, rather than metarhodopsin III. However, there is little evidence for contamination of the key wavelengths of 470nm to 620nm, where the bulk of the density difference was measured. Therefore, the consequence on the measured absorption spectra is likely to have been negligible.

The half bleach constant (I_{Rh}) was investigated using a technique independent of any long wavelength reference source to determine if any variation in this constant could account for the relatively low ΔOD reported in Chapter 4, i.e. was the bleaching source bright enough. A modest discrepancy between the experimental I_{Rh} values reported here and those found in the literature (Alpern 1971) was observed. The best fitting models of the data from these four participants had a

mean I_{Rh} of 4.62 log scotopic trolands (± 0.02SE), a value slightly higher than that of 4.44 log scotopic trolands reported previously (Alpern 1971), with low inter-individual variability. This finding indicates that a higher than anticipated retinal illuminance was required to bleach 50% of the rhodopsin. However, at the high intensities used throughout this thesis the discrepancy in I_{Rh} has negligible effect on the calculation of pigment present. Crucially, at the intensity and duration used in Chapter 4 the pigment bleach was estimated at 98%. A minimal difference when compared to the original estimation of 99%, using the value suggested by Alpern (1971). Hence, the low OD results observed in Chapter 4 were not due to insufficient bleaching.

In the simultaneous solution of the Equation 5.2, Equation 5.4 and Equation 5.5 to acquire a value for the half bleach constant and a theoretical value for the rhodopsin optical density measured following a 100% bleach, $\Delta ODmax$, was returned. The average $\Delta ODmax$ (0.20, ± 0.01SE) was consistent with the current literature (Faulkner and Kemp 1984; van Norren and van de Kraats 1989b; Liem et al. 1991; Masella et al. 2014). Minor inter-participant variations in optical density, such as those seen in our data (Table 5.2), have also been reported previously (Kilbride and Keehan 1990).

The methods used to investigate the half bleach constant and obtain the $\Delta ODmax$ in two crucial ways from those described in Chapter 4. The first was the bleaching procedure and the second was the field of illumination, could either of these account for the relatively high theoretical rhodopsin optical density reported here?

The bleaching procedure was estimated to result in a lower pigment bleach than that employed in Chapter 4. As such, this is an unlikely source for increase in the theoretical rhodopsin density. To ensure the rigor of the calibration of the bleaching and imaging sources used the ILT1700 research radiometer (International Light Technologies Incorporated, USA) was calibrated by International Light Technologies Incorporated, USA to the ISO/ISEC 17025 standard at the outset. Hence, every confidence can be had in the bleaching intensity measured.

The field of illumination was reduced from 50° to 12° and centred on the peak rod density (18° temporal), facilitating the direct investigation of rhodopsin kinetics immediately following bleach cessation. The effect of this on optical density measurement may be two-fold. As the investigation took place over the peak rod density, it may simply be that there was a greater density of rhodopsin present. At the 10° eccentricity used in Chapter 4, rod density is around 75% of that at 18° (Curcio et al. 1987). Accounting for this, the expected rhodopsin density at 10° would be in the region of 0.15, not 0.09 as reported in Chapter 4. It is likely then, that the reduction in the field of illumination itself played a role in the increased $\Delta ODmax$. It is known that spot densitometers, with a smaller field of illumination are less prone to any additional stray light than their wider field counterparts (Faulkner and Kemp 1984; van Norren and van de Kraats 1989b; Berendschot et al. 2003).

The 8% increase in long wavelength (794nm) retinal reflectance recently observed by Masella et al (2014) lasted for several minutes after bleach cessation. The duration of this change corresponds to the time period used to collect optical density data during the original investigations into rhodopsin kinetics (Ripps and Weale 1969a; Alpern 1971; Rushton and Powell 1972) and could have led to erroneous bleach constant values. More specifically, the increase in reflectivity at longer wavelengths would result in an over-estimation of the true optical density change.

To determine whether a similar effect was found in the current study, the 740nm data collected in Chapter 4 were investigated for temporal variations after bleach cessation. In contrast to the findings of Masella et al (2014), fluctuations in long wavelength retinal reflectance were not observed. However, the stable reflectance measurements at 740nm (Figure 5.5) were consistent with the data published by DeLint et al (2000), who measured retinal reflectance at 790nm following exposure to a comparable equilibrium bleach (5.9 log scotopic trolands) and found no temporal changes in the peripheral location studied. What then explains the differences in these two sets of observations? The bleach used by Masella et al

(2014) was of a shorter duration (2 seconds) and significantly greater intensity (7.6 to 7.9 log scotopic trolands) than that used here. The discrepancy between our observations and those of Masella et al (2014) could suggest the dynamics of the intrinsic retinal signal differ when measured following exposure to a short flash or longer equilibrium bleach, in a similar way to photopigment regeneration (Rushton et al. 1969; Alpern 1971; Lamb and Pugh 2004). Given that the proposed source of the intrinsic signal is a variation in the light scattering properties of the outer retinal structures in response to the photopigment regeneration processes (DeLint et al. 2000; Tsunoda et al. 2009; Masella et al. 2014), it is reasonable to hypothesise that altered regeneration dynamics could affect these properties. It is also possible the processes which result in the intrinsic retinal signal measured by Masella et al (2014) have stabilised under the equilibrium bleach conditions used in this study.

5.6. Summary

The post bleach density difference spectra changed little over time. The modest change observed at 450nm was quite unlike that observed by Ripps and Weale (1969b). Although it is possible that a photo-intermediary (likely metarhodopsin III) affected the density difference measured at 450nm data point, another explanation is modest S- cone contamination.

The value of I_{Rh} was re-assessed using the Mark II densitometer independent of any long wavelength reference source. At 4.62 log scotopic trolands, the average I_{Rh} established here was approximately 0.2 log scotopic trolands higher than that previously reported in the literature (4.44 log scotopic trolands) (Alpern 1971). In support of the estimate presented here, Morgan and Pugh (2013) recently reported a value 0.2 log scotopic trolands higher than the classical half bleach constant following a flash bleach of rhodopsin (Alpern 1971), this was later confirmed by Masella et al (2014). This suggests that a little more light is needed to bleach a given amount of photopigment than was previously expected.

Whilst the impact of the reported value for I_{Rh} is negligible at the high intensities used in this research, at the bleaching levels often used in clinical settings for dark adaptation studies (around 5.5 log scotopic troland for instruments such as the Goldmann-Weekers Dark Adaptometer (Gaffney et al. 2011)), the discrepancy is considerable at about 10%. Hence future investigators should consider the values reported here to yield a more accurate estimate of bleaching levels.

The study re-examining the half bleach constant for rhodopsin suggested that insufficient bleaching was not the cause of the relatively low OD values observed in Chapter 4. Having ruled out this possibility, the most likely explanation is the scattered light created by the 50^{o} imaging field. Hence the effect of stray light is examined in the following chapter.

Chapter 6 - A Correction for Back Scatter

6.1. Introduction

Spectral data from the Mark II densitometer showed a pronounced 'red-shift' or short wavelength attenuation, when compared to the known spectral absorption characteristics of photopigments obtained *in vitro* (Dartnall et al. 1983; Kraft et al. 1993; Stockman and Sharpe 2000). The difference is highlighted in Figure 4.3 (Chapter 4).

The original intention was to extract the optical density of the three major visual pigments (rod, M- and L- cone) by fitting the experimental data with the *in vitro* spectral data of Dartnall et al. (1983). However, the application of this approach was thwarted by the 'red-shift' demonstrated in Chapter 4 (Figure 4.3). As discussed in Section 4.4.3, the observed attenuation is likely to be caused by light that has not traversed the retina e.g. light back scattered from the optical media (Rushton 1965). Correcting for this should result in both an increased optical density measurement and reduced red shift, thus facilitating accurate pigment fitting.

It should be noted that the 'red-shift' observed here is similar to that produced by other densitometers (Rushton 1956a; van Norren and van de Kraats 1989b; Kilbride and Keehan 1990) but, this is not a universal finding (Rushton 1963a; van de Kraats et al. 1996). Figure 6.1 highlights variations in the profile of the cone spectra obtained in different studies.

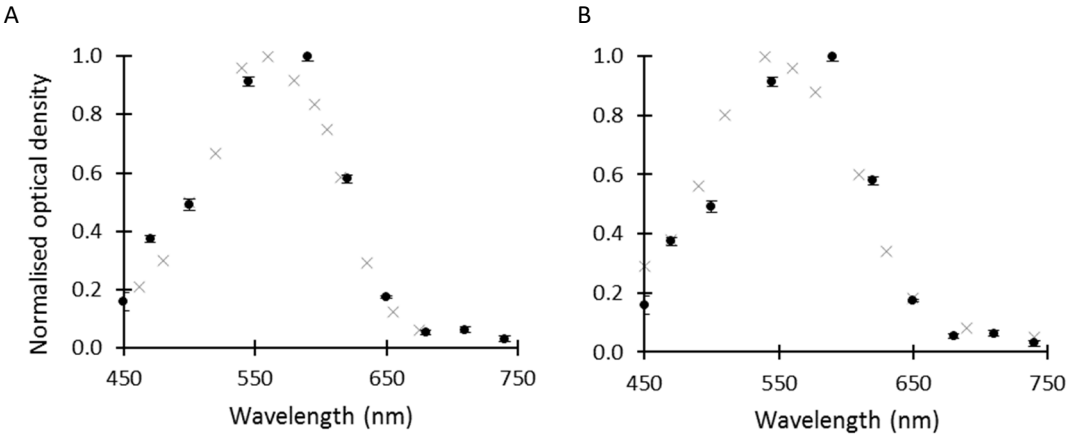

Figure 6.1 Comparison of normalised experimental foveal cone spectrum (3 participants, as described in Chapter 4 – filled circles, standard error bars) with published foveal cone spectra obtained from two contrasting densitometry techniques (grey crosses). The peak wavelength of the experimental spectrum is found at 590nm. A) Presents the comparison against the spectrum from an imaging densitometer (Kilbride et al. 1986), with a peak wavelength of 560nm. B) Presents the comparison of the spectrum from a narrow field spot densitometer (van de Kraats et al. 1996), with a peak wavelength of 540nm. The experimental spectrum is comparable to that from the alternate imaging device, yet shows a greater red shift when compared to the spot device.

Inter-study differences may be attributed to the optical design of the densitometer. In particular, the field of illumination used. An examination of the data presented in the literature suggests that densitometers with a small field of illumination (e.g. spot densitometers) show a relatively limited 'red-shift' (van Norren and van de Kraats 1989b; Berendschot et al. 2003) while those with a larger field of illumination (e.g. imaging densitometers) show a more pronounced 'red-shift' (Faulkner and Kemp 1984; Kilbride et al. 1986; Berendschot et al. 2003). Similar differences in overall ocular reflectance have also been observed. For example, in some studies of ocular reflectance (Brindley and Willmer 1952; Charman 1980; van Blokland and van Norren 1986; Delori and Pflibsen 1989) short wavelength ocular reflectance (<500nm) has been estimated to be less than 1% whilst others (Vos et al. 1965; Fowler et al. 1977) have reported a reflectance significantly higher than this, about 3-5%. When considering that Fowler et al (1977) obtained their values using a fundus imaging camera, these differences may be attributed to the optical design and the field of illumination of the instrument.

Thus, a possible explanation for the 'red-shift' observed with the experimental spectra is back scattered light from surfaces anterior to the photoreceptor outer segments, e.g. the optical media (Delori and Pflibsen 1989). The measured OD is attenuated by the addition of stray light, according to Equation 6.1,

$$\Delta OD(\lambda) = log\left(\frac{R_B(\lambda) + SL(\lambda)}{R_{DA}(\lambda) + SL(\lambda)}\right)$$

(Equation 6.1),

where $R_B(\lambda)$ is the bleached retinal signal, $R_{DA}(\lambda)$ the dark adapted retinal signal and the parameter $SL(\lambda)$ is the signal attributable to stray light.

If the wavelength dependent 'scatter' parameter ($SL(\lambda)$) could be accurately quantified, it would be possible to correct the spectral data from the Mark II densitometer. To this end, a first step was to use Equation 6.1 to quantify the 'scatter' parameter required to bring the rod and M-cone data from the Mark II into alignment with the *in vitro* data. This was achieved by manually altering the value of $SL(\lambda)$ in Equation 6.1 to bring the normalised experimental spectra (presented in Figure 4.2) into register with the *in vitro* data from Dartnall et al. (1983). Figure 6.2 summarises the results.

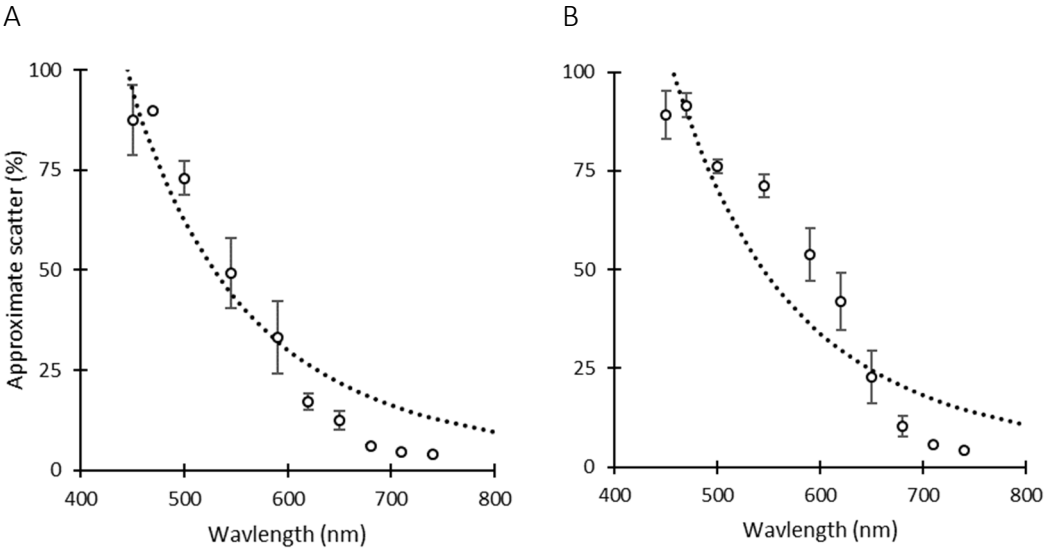

Figure 6.2 Magnitude of the 'scatter' parameter, $S(\lambda)$, in Equation 6.1 as a function of wavelength for rods, with standard error bars. A) Showing an example of the stray light required to register the experimental rod spectrum (presented in Figure 4.2A) from a single participant (AB). B) Shows an example of the stray light required to register the experimental M- cone spectrum (presented in Figure 4.1D) from a protanope participant (TM). The dotted line in each plot describes a Rayleigh scatter curve for comparison.

A visual inspection of the curves in Figure 6.2 suggests there is significant short wavelength back scatter within the Mark II densitometer. There is minimal difference in the magnitude of back scatter between the scatter observed for M-cones and for the rods. The overall shape is suggestive of Rayleigh scattering but the fit is far from perfect, with the Rayleigh function overestimating long wavelength scatter for both pigments. Both the fitted scatter parameters and Rayleigh function suggest that about 90% of the signal in the shorter wavelengths is comprised of scattered light. What could be the origin of this scatter?

Due to the large area of illumination (50^{o}) one potential source for the back scattered light is the optical media and, in particular the crystalline lens. Scatter from the crystalline lens is -believed to be dominated by the 7-14nm diameter of lens proteins, producing a Rayleigh scattering effect (Wooten and Geri 1987; Jacques 2013). If some of this scattered light were contaminating the imaging path this could explain the attenuation observed.

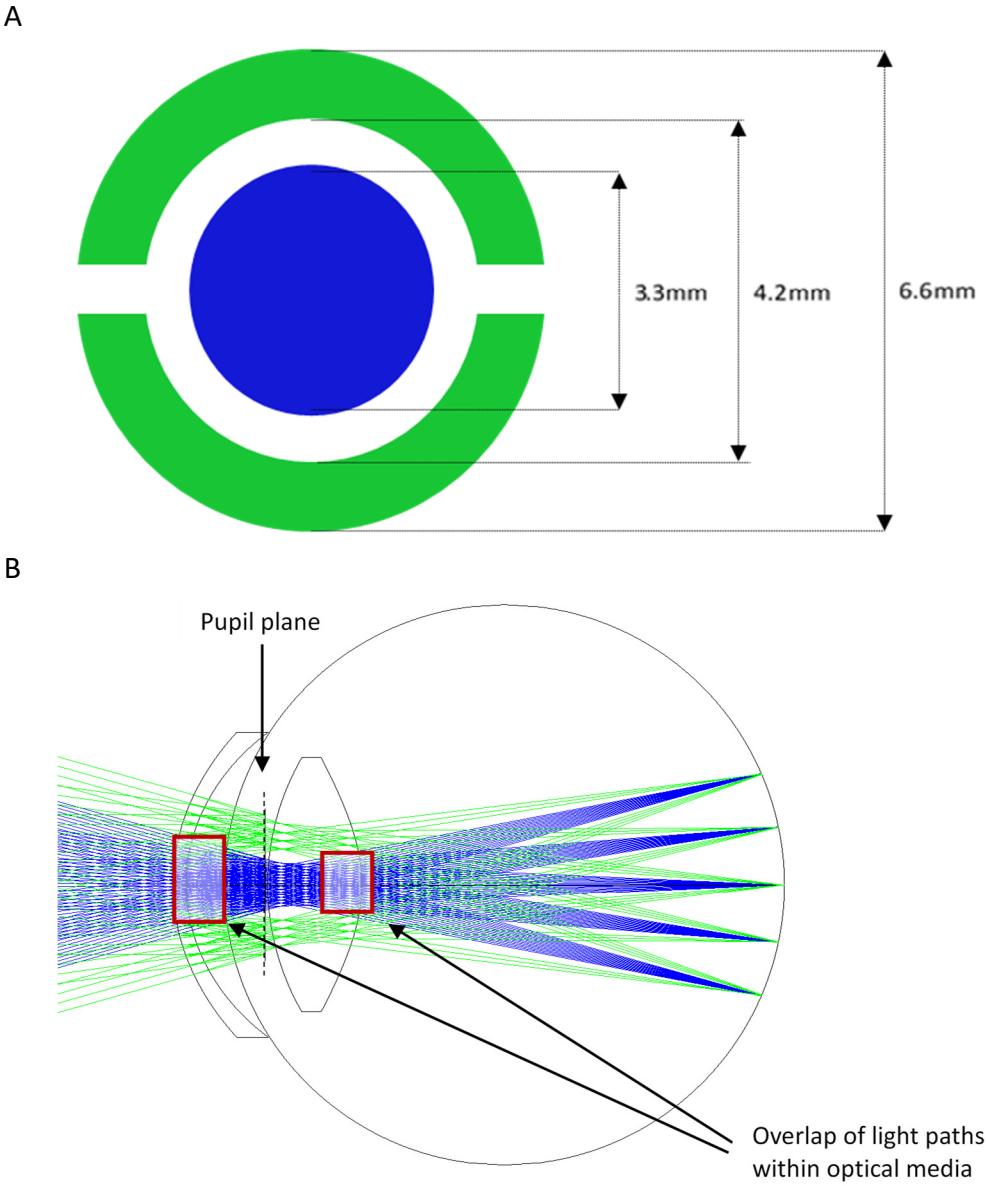

Figure 6.3 A) Showing a cross section of the illumination (green) and imaging (blue) beams, as seen at the pupil plane. B) Showing a ray diagram showing interaction of the imaging (green) and illumination (blue) beams in the human eye. Ray diagrams created in Zemax (Zemax LLC, Seattle) by Stephan Todd (UKATC).

Figure 6.3 shows the cross section of the illumination and imaging beams at the pupil plane. In Maxwellian view optical systems, such as the device used here, the pupil plane of the instrument is aligned with the eyes pupil (Figure 6.3). Figure 6.3 also shows significant overlap of the light paths in the crystalline lens and cornea and this could be a potential source of contamination of the imaging beam.

There are several design options which can limit the overlap of the light paths:

1. Decreasing the dimensions of the illumination annulus and/or imaging pupil,

2. Additional central obscuration introduced in the illumination beam conjugate to the surface of the crystalline lens,

3. Reduction of the field of illumination.

We will now consider each option, regarding the device used for this work. The first two options require substantial, delicate and permanent hardware alterations, which would not have been possible to achieve in the lab.

However, the third option could be implemented through the addition of a simple variable aperture which would allow constriction of the field of illumination. By increasing the separation of the illumination and imaging pathways anterior and posterior to the pupil it should be possible to reduce contamination of the imaging beam. With less stray light captured by the imaging beam, the resulting signal count would reduce, therefore amplifying the ratio between the bleached and dark-adapted retina (see Equation 4.1). When the measured signal no longer decreases with field of illumination this would indicated the pathways no longer overlapped.

The experiment described in this chapter set out to quantify the wavelength dependent back scatter independently of the measurement of visual pigment. It was hoped that this data could be used to correct the experimental spectra presented previously (Figure 4.3, Chapter 4).

The approach taken was based on the observation, from the literature, that back scatter appears to vary according to the field of illumination. More specifically, that back scatter is directly proportional to the area of retina illuminated.

6.2. Aims

The experiments presented here set out to test the hypothesis that a measurable back scatter correction can be applied to the experimental spectral data in order to

align the *in vivo* rod and cone spectra with the established *in vitro* functions. To that end, this experiment had 3 specific aims:

1. To explore the relationship between wavelength dependent camera signal and the field of illumination.

2. To estimate the back scatter for the 50^{o} field of illumination used in the Mark II device.

3. To correct the *in vivo* rod and cone spectra accordingly and determine agreement with published *in vitro* data.

6.3. Methods

6.3.1. Participants

Two experienced participants (AB, TM) took part in this study. Both had corrected visual acuity of 6/6 or better in the test eye, refractive errors within ±7.50DS mean sphere and no diagnosis of ocular pathology; in particular, clear ocular media i.e. a LOCS III grade of 1 or less (Chylack et al. 1993). Both participants were experienced with this device. Further details of age, gender and ocular history for each participant are given in Table 6.1.

Table 6.1 Participant Characteristics

Participant	Age	Gender	LOCSIII grade	Ocular History
AB	36	F	1	-7.50DS
TM	50	M	1	Plano, Protanope

Further, both participants provided absorption spectra in the investigations presented in Chapter 4 (Figure 4.2). Thus, any stray light correction could be applied directly to participant specific data.

6.3.2. Apparatus

To explore the relationship between measured back scatter and field of illumination it was necessary to modify the Mark II densitometer to accommodate a variable aperture in the imaging plane.

The Mark II has the capability to adjust the imaging field of view using a lens wheel, however this does not adjust the illumination beam. Given the accessibility of the imaging plane in the Mark II (which usually contains the fixation marker), the field of illumination was reduced by inserting a variable aperture at this location. That is, the fixation rod was replaced with a Thorlabs adjustable aperture wheel (D5OSZ) and a central fixation target. Figure 6.4 shows the aperture wheel and its location in the imaging plane.

A B

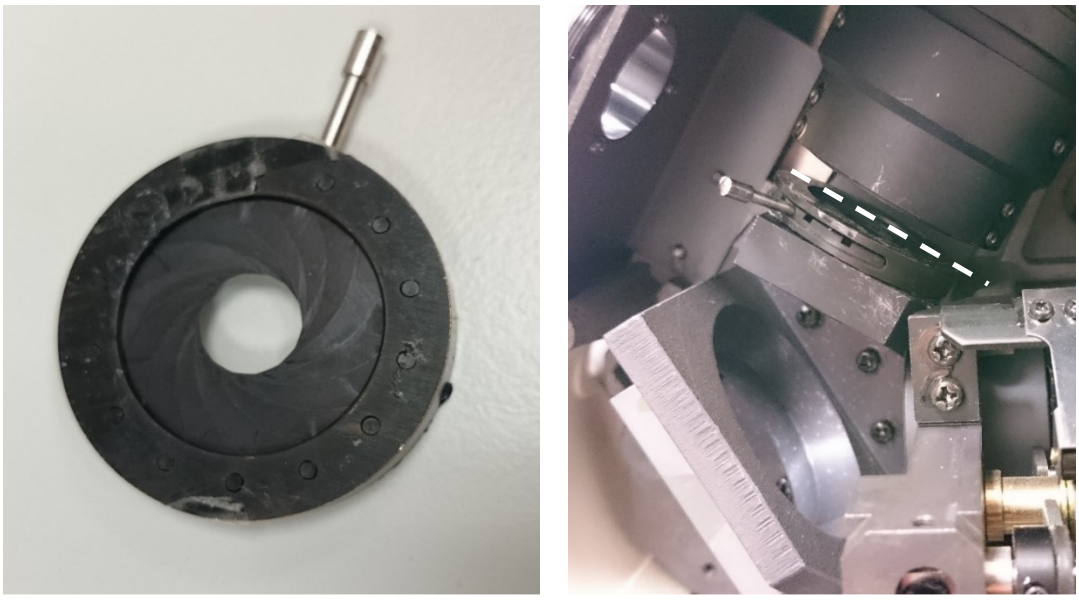

Figure 6.4 A) The Thorlabs variable aperture, without fixation target. B) The imaging plane in the Mark II densitometer (located by white dashed line). The fixation rod was removed, and the aperture wheel positioned securely to the lower lens mount.

The aperture wheel was continuously variable, with no ‘scale markings’, and therefore required manual adjustment whilst live images showing the area of retina illuminated were observed. Hence, the exact retinal area illuminated could only be estimated at the time and had to be determined more precisely post hoc via retinal image analysis.

To maximise the signal to noise ratio for this study, the intensity of all LEDs was increased to 100%. At this intensity, it was estimated that 0.35% of iodopsin and 0.49% of rhodopsin would be bleached during the acquisition period. All measurements were recorded following a 20 minutes period of dark-adaptation. Four measurements of 30 frames each (60 seconds), were recorded, the size of the aperture reduced between each. In addition, a reference frame, containing CCD bias and internal stray light, was recorded for each aperture setting.

6.3.3. Data analysis

The size of the aperture used for each recording was determined post hoc on the basis of the intensity profile across the horizontal midline of the images obtained from the 500nm source. The aperture positions and approximate field sizes are shown in Table 6.2.

Table 6.2 The field of illumination for each aperture position

Aperture position	Measured field of illumination (AB)	Measured field of illumination (TM)
Position 1	50°	50°
Position 2	25°	29°
Position 3	18°	22°
Position 4	10°	14°

The data from each aperture position were processed in the same manner as the dark-adapted recording, described in Chapter 3. That is, the images were registered, blinks were removed, and the final set of images were used to create an average. To quantify back scatter the camera signal was extracted from a 2x2 pixel region from the centre of the image as a function of wavelength. Regression analysis was then used to determine the relationship between camera signal and measured field of illumination. Importantly, the camera signal with an infinitely small field of illumination could be predicted in this way.

The fraction of light attributable to back scatter $SL(\lambda)$ was determined using (Equation 6.2,

$$SL(\lambda) = \left(\frac{50^o(\lambda) - 0^o(\lambda)}{50^o(\lambda)}\right)$$

(Equation 6.2),

where $50^o(\lambda)$ was the camera signal obtained with the full field of illumination and $0^o(\lambda)$ was the theoretical camera signal estimated for a field size of zero degrees obtained via linear regression analysis.

Thus, Equation 6.3 describes how the contribution of backscattered light could be removed by modifying Equation 6.1 to obtain a more accurate optical density value ($\Delta OD_{adj}(\lambda)$),

$$\Delta OD_{adj}(\lambda) = log\left[\frac{R_B(\lambda) - \left(R_{DA}(\lambda) \cdot SL(\lambda)\right)}{R_{DA}(\lambda) - \left(R_{DA}(\lambda) \cdot SL(\lambda)\right)}\right]$$

(Equation 6.3).

6.4. Results

Figure 6.5 shows example retinal images obtained from a single participant using the 500nm LED, for each of the apertures listed in Table 6.2.

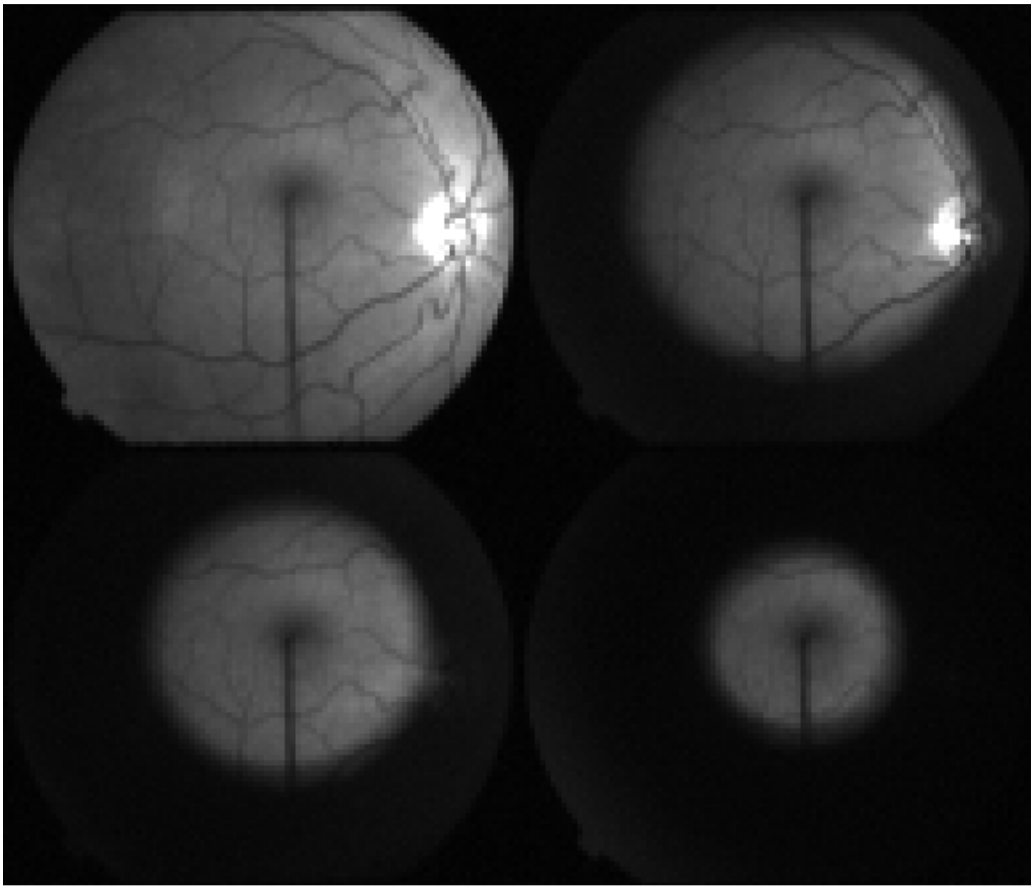

Figure 6.5 Example images from participant TM. Averaged 500nm images (corrected for CCD bias, stray light and blinks) for each aperture size. Image brightness scaled to the 50° image. Top: L-R 50°, 29°. Bottom L-R: 22°, 14°.

Image J (National Institutes of Health, Maryland) was used to extract the camera signal along the horizontal meridian. These data are presented Figure 6.6 and shows the camera signal as a function of retinal eccentricity for each field of illumination listed in Table 6.2. Note the spike in the data around 15 degrees corresponding to the position of the optic nerve head and the relatively gentle slope leading away from the illuminated area.

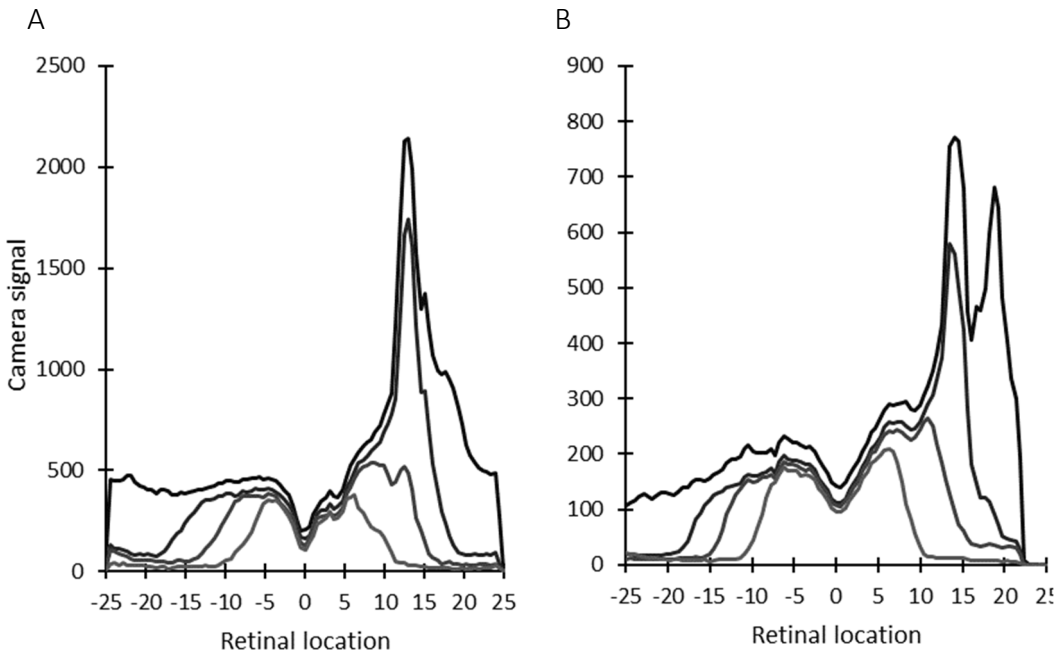

Figure 6.6 Camera signal measured at 500nm for all aperture positions along the horizontal midline for participant AB (A) and TM (B). The large spike in reflectance around 15° is related to the optic disc, the notch in panel B related to a major blood vessel, the central dip present around 0° in both panels highlights the foveal region. Aperture positions from black to light grey are 1, 2, 3, 4 (Table 6.2 shows the exact field of illumination).

The camera signal at the centre of the image, over an area of 2x2 pixels, was extracted and plotted as a function of the field of illumination (see Figure 6.7 below). Regression lines were used to predict the theoretical camera signal that would have been obtained with a field size of zero degrees. As expected, for all wavelengths, camera signal reduced monotonically with reducing field of illumination. Indeed, the linear regression provides a good description of the data.

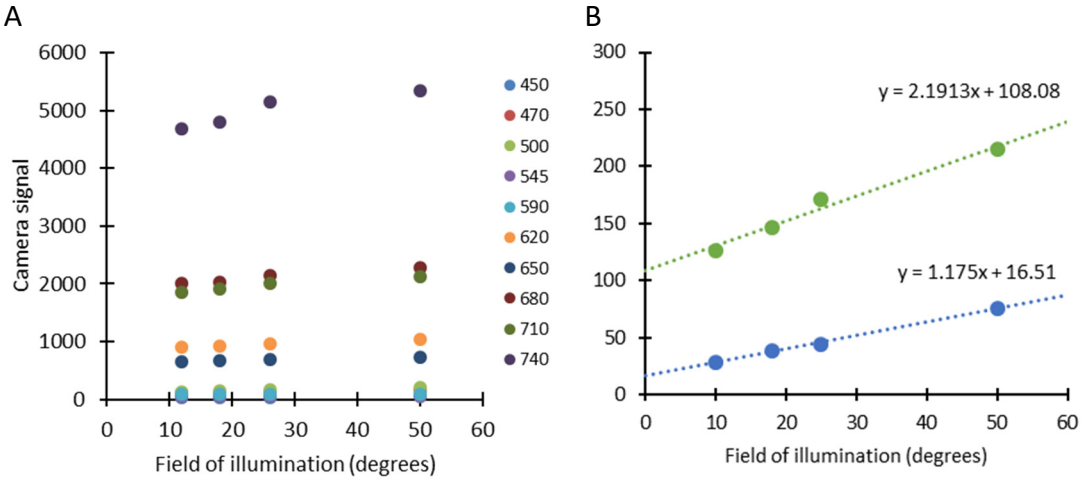

Figure 6.7 Camera signal in the central retina (2x2 pixel area) for participant AB. A) Presents camera signal as a function of field of illumination for each wavelength. This is exemplified in B) using the 500nm (green) and 450nm (blue) data, where an intercept of 108.08 and 16.51 was observed respectively.

The results of this evaluation are presented in Table 6.3 and Table 6.4 for the individual participants. The percentage of the camera signal resulting from back scattered light reduced with increasing wavelength. Further, the scatter present in the images obtained with the shorter wavelengths (<545nm) was substantial.

Table 6.3 Results of the regression analysis showing the predicted camera signal with a small field of illumination (FoI) and the results of the scatter calculation (AB).

	FoI 0° (camera signal)	FoI 50° (camera signal)	Scatter (camera signal)	Scatter (%)	Regression slope
450	16.51	75.63	59.12	78.17	1.17
470	86.26	177.39	91.13	51.37	1.82
500	108.08	214.91	106.83	49.71	2.19
545	44.30	56.71	12.41	21.88	0.26
590	91.21	101.73	10.51	10.33	0.22
620	869.99	1051.15	181.16	17.23	3.63
650	632.16	737.12	104.96	14.24	2.12
680	1934.13	2283.12	348.99	15.29	7.15
710	1803.37	2135.17	331.81	15.54	6.86
740	4568.99	5333.36	764.37	14.33	16.31

Table 6.4 Results of the regression analysis showing the predicted camera signal with a small field of illumination (FoI) and the results of the scatter calculation (TM).

	FoI 0° (camera signal)	FoI 50° (camera signal)	Scatter (camera signal)	Scatter (%)	Regression slope
450	3.71	89.63	85.92	95.86	1.71
470	29.24	114.91	85.66	74.55	1.70
500	37.66	94.17	56.51	60.01	1.14
545	65.28	110.79	45.51	41.07	0.93
590	130.11	182.86	52.75	28.85	1.09
620	324.79	410.69	85.90	20.92	1.80
650	541.75	650.69	108.94	16.74	2.34
680	805.42	993.24	187.82	18.91	4.26
710	1161.96	1420.71	258.75	18.21	5.71
740	3309.30	3615.68	306.38	8.47	6.27

In fact, the percentage of scatter present was wavelength dependent, reminiscent of Rayleigh scattering. To aid this comparison, Figure 6.8 plots the scatter data as a function of wavelength.

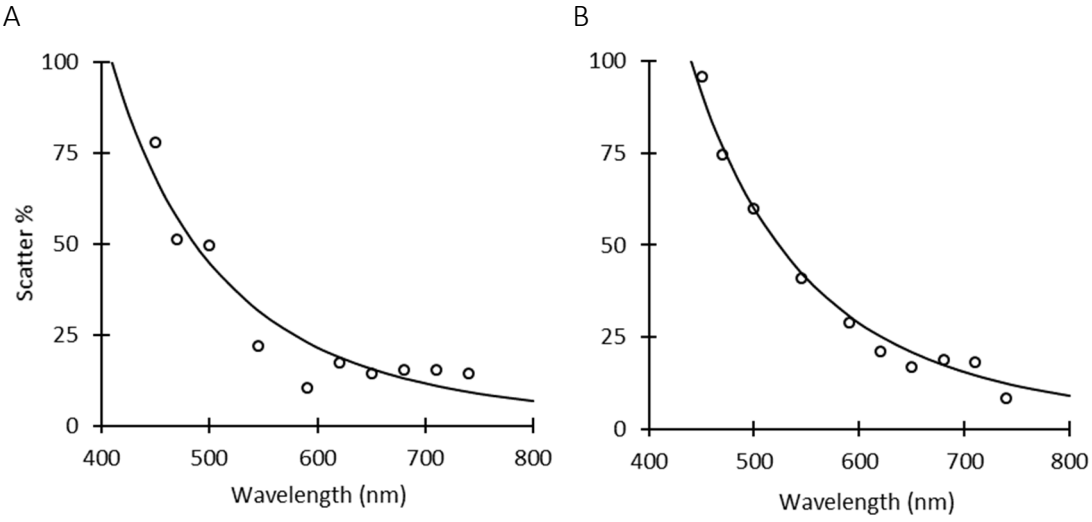

Figure 6.8 Percentage scatter as a function of wavelength. The solid line is a Rayleigh scattering function fitted using a least squares algorithm (Solver, Excel). Panels A and B present data from AB and TM, respectively.

The stray light component was removed from the raw absorption spectra, originally presented in Figure 4.1D and Figure 4.2A, using Equation 6.3 and the values presented in Table 6.3 and Table 6.4. The adjusted absorption spectra are presented

in Figure 6.9 for both foveal and parafoveal locations, *in vitro* and unadjusted spectra are also shown for comparison.

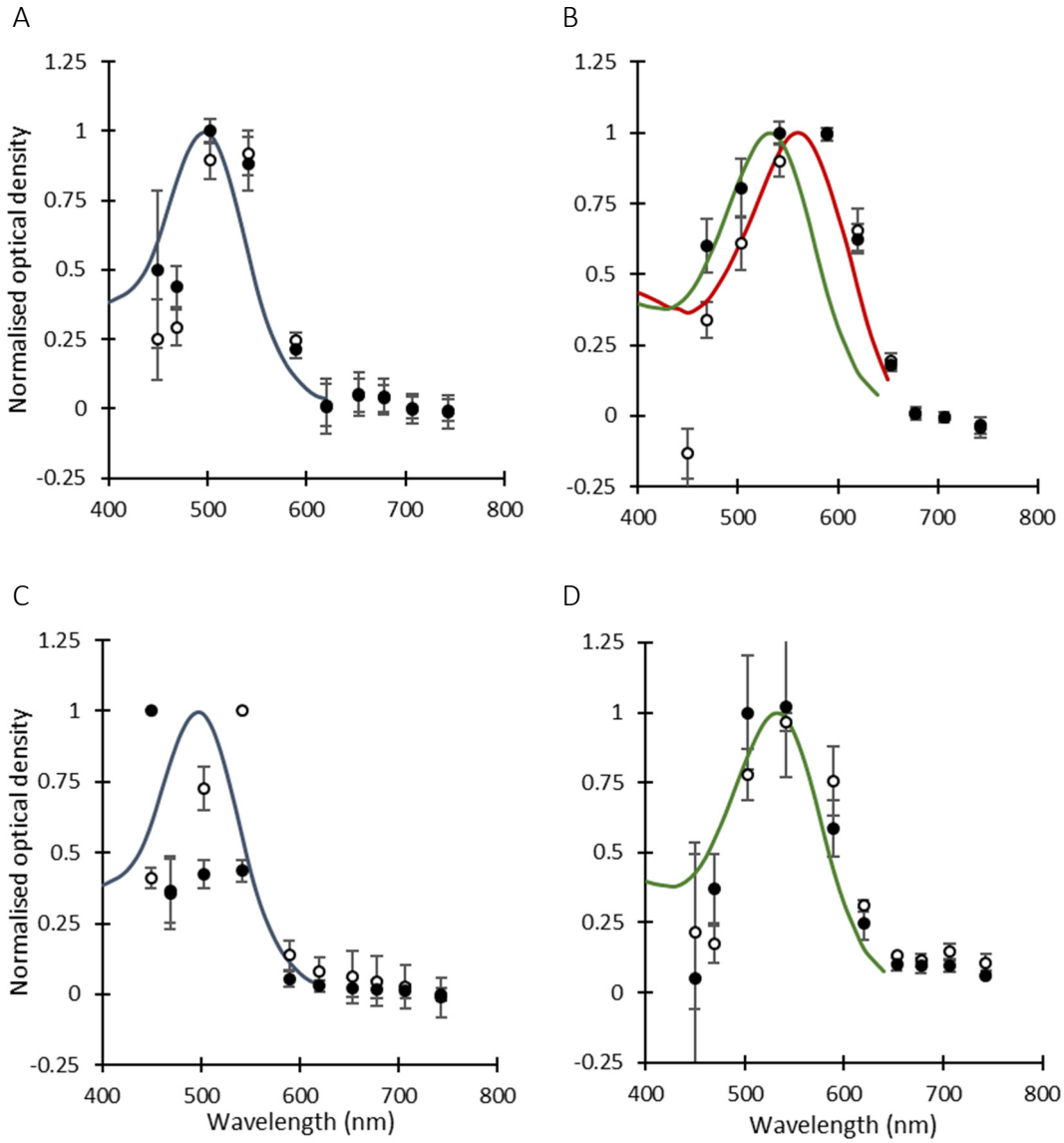

Figure 6.9 The adjusted (filled circles) and unadjusted (open circles) normalised absorption spectra for both subjects, as described in Chapter 4 (standard error bars). A) Presents correction of the rhodopsin spectra (AB), B) correction of the mixed cone foveal spectra (AB), 450nm normalised OD = -0.4, C) correction of the rhodopsin spectra (TM) and D) correction of the M- cone spectra from a protanope (TM). Solid lines represent the relevant *in vitro* absorption curves (Dartnall et al. 1983).

From Figure 6.9 it may be seen that the adjusted spectra were shifted to the shorter wavelengths and more like the *in vitro* counterparts than the unadjusted data. However, excluding the rod correction in panel A, all spectra were affected by an over or under-correction, particularly at 450nm, with the adjusted cone spectra

returning a value of -0.4 for AB and the adjusted rod spectrum returning a value of 1 for TM.

6.5. Discussion

The hypothesis that a measurable 'stray' light correction can be applied to align the experimental rod and cone absorption spectra with established *in vitro* functions was tested by addressing three specific aims.

The first was simply to explore the relationship between camera signal and field of illumination, with the expectation that a reduction in the field of illumination would result in a lower camera signal. This is demonstrated in Figure 6.7, with all wavelengths showing a reduction in measured signal as the aperture size decreased. Further, the relationship between the field of illumination and camera signal was shown to be well described by a linear function, allowing estimation of the camera signal that would be measured from an infinitely small field of illumination. However, as the number of photons illuminating a region is directly proportional to the area illuminated, that the relationship between the diameter of the illumination field and the camera signal was linear was unexpected. This suggests that the relationship between illumination and camera signal is more complex than originally thought.

The second aim was to quantify the amount of additional light present in the 50^{o} field of illumination of the described device. Calculating the camera signal from a theoretical 0^{o} field of illumination (Table 6.3 and Table 6.4), the application of (Equation 6.2 provided the fraction of additional light present in the 50^{o} image, or $SL(\lambda)$. Figure 6.8 demonstrates the wavelength dependence of $S(\lambda)$, and the similarities to Rayleigh scattering suggest this additional camera signal was dominated by internal stray light from within the crystalline lens. Whilst the estimated scatter function (Figure 6.2) showed strong resemblance to the measured scatter function (Figure 6.8), it is interesting to note that the estimated scatter function did not decrease monotonically. In Figure 6.2 the peak scatter was at

470nm, not 450nm. The systematic departure from the Rayleigh curve in Figure 6.2 matches the visual pigments investigated (i.e. the largest difference is seen at 500nm in Figure 6.2A and at 545nm in Figure 6.2B). If the experiment described in this chapter had been undertaken in a bleached, rather than a dark-adapted state, would there be a similar discrepancy in the results?

Finally, an attempt was made to correct the extracted rod and cone spectra using Equation 6.3. Overall, the adjusted spectra (Figure 6.9) showed greater resemblance to the published *in vitro* spectra than their unadjusted counterparts. The correction for the foveal cone spectrum was particularly convincing for both participants. Indeed, Panels A, B and D (Figure 6.9) corroborate the published *in vitro* rod, mixed- and M- cone spectra. The correction for the rod spectrum in panel A showed improvement on the unadjusted spectrum, however the 470nm wavelength showed insufficient correction. In contrast, the rod spectrum in panel C was too severe, being dominated by the 450nm wavelength. Whilst an improvement on the unadjusted spectra, exclusion of this wavelength did not register the spectrum with the *in vitro* data (not shown).

The corrected and normalised 450nm data showed a range from 0.5 to 1 for rod optical density and a range of -0.4 to 0.05 for cone optical density. Perhaps this broad range can be explained by the substantial subtraction implemented in Equation 6.3. At 450nm the proportion of stray light was calculated at 94% (TM) and 79% (AB). This equated to a mean camera signal of 133 ±3.3 SEM (TM) and 102 ±3.4 SEM (AB) at the parafoveal location. When the difference in camera signal between the bleached and dark-adapted measurements with this wavelength is considered (7.5 ±0.2 SEM and 5.4 ±3.4 SEM for TM and AB respectively) it is of little surprise that the results were somewhat volatile.

The second issue related to the assumption that stray light is uniform across the image. With the expectation that any stray light would be uniform across the image, a single foveal location was investigated. Yet, as can be seen in Figure 6.9, the replication of the *in vitro* cone spectrum is superior when compared to the partial correction of the rhodopsin spectrum, for both participants, suggesting that the

stray light measured from the central region is not representative of that from the entire retina. This could well be explained by the presence of additional reflective layers which lie anterior to the photoreceptor layer. The excellent review by Berendschot (2003) highlights the reflective surfaces present within the eye. Of interest are the inner retinal structures of the ILM and the RNFL. The ILM has been shown to provide both diffuse and specular reflections, and hence is wavelength independent (Gorrand et al. 1984; van de Kraats et al. 1996). As a structure, the ILM thickness is uniform across the peripheral retina, with a decrease in thickness at the fovea (Matsumoto et al. 1984; Henrich et al. 2012). The intensity of the measured reflectance from the ILM has been shown to be dependent upon: retinal curvature, ocular orientation, the location of the device's exit pupil and the orientation of the incident light (Gorrand et al. 1984). However, no relationship between reflectivity and ILM thickness has been shown (Berendschot et al. 2003). ILM reflectance may show inter-participant variation, dependent upon the individual retinal curvature. However, accurate alignment of the device controls for the other factors, eliminating these sources of intra-participant variation. With little evidence of topographical variation in ILM reflectance, it is unlikely to account for the differences seen between the adjusted rod and cone spectra.

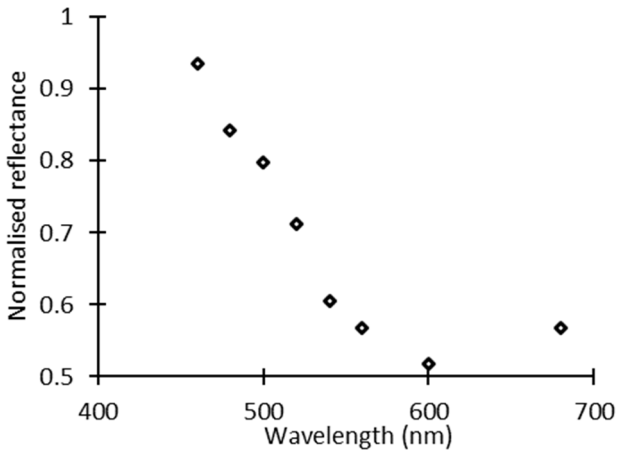

Figure 6.10 The wavelength dependent characteristics of the retinal nerve fibre layer, taken from Knighton et al (1989) and normalised to 450nm.

The RNFL has been shown to have spectrally dependent reflectance, reducing in intensity with increasing wavelength, as shown in Figure 6.10 (Knighton et al. 1989).

Reflectivity of the RNFL has also been shown to increase in proportion with thickness (Knighton et al. 1989). RNFL thickness is known to vary in thickness from a maximum depth near the optic nerve head to negligible thickness in the foveal region. Therefore, the RNFL could contribute to topographical differences in back scatter.

The final issue was that the approach described here required several steps to obtain a partial solution. Whilst it may be possible to follow this line of experimentation to an exact conclusion, the requirement for several methodological steps complicates the measurement process. With the ultimate aim of developing a user friendly, clinical technique a simpler method must be sought.

6.6. Summary

The relationship between the field of illumination and camera signal was determined and used to predict the likely fraction of stray light present in a 50^{o} image. It is likely that the only source of stray light accounted for in this experiment, was from the ocular media. This is suggested by the description of the scatter function, $SL(\lambda)$, as a Rayleigh curve, and corroborated by a review of the spectral templates which comprise light scattering and absorption within the ocular media (van de Kraats and van Norren 2007).

However, the measured contamination only provides a partial correction of the spectra, suggesting that the 'stray light' estimation undertaken here was only partially correct. Another potential source of 'stray light' affecting the retinal images collected here is the RNFL, which shows both a strong wavelength dependent reflection and significant topographical variation.

Many ocular reflection models have been described, perhaps the application of a similar approach will allow the full correction of the spectra without compromising the recording technique (Rushton 1965; van Norren and Tiemeijer 1986; Delori and Pflibsen 1989; van de Kraats and van Norren 2008). However, accurate modelling of ocular reflectance requires knowledge of absolute retinal reflectance.

The following chapter describes the construction of a novel model eye, which was used to calibrate the system and permit the measurement of absolute reflectance across the retinal image. This, in turn, enabled the topographical modelling of retinal reflections, including those arising from the RNFL and additional ocular tissues.

Chapter 7 - The Cardiff Model Eye

7.1. Introduction

The *in vivo* measurement of visual pigment absorption spectra showed a red shift compared to the absorption spectra obtained using *in vitro* techniques. Based on the assumption that back scatter from the ocular media was responsible for the results identified in Chapter 4 (Figure 4.3), Chapter 6 attempted to address this red shift. However, the experiments were only partially successful, so it was decided that an ocular reflection modelling approach may be more effective.

The desire to accurately characterise the optical properties of the ocular tissues has led to the development of several detailed ocular reflection models (van Norren and Tiemeijer 1986; Delori and Pflibsen 1989; van de Kraats et al. 1996; van de Kraats and van Norren 2008). The application of these models all require calibrated ocular reflectance measurements. However, to date these models have only been applied to reflection data obtained from spot densitometers, where a simple flat field surface provides a sufficiently accurate calibration method (van Norren and Tiemeijer 1986; van de Kraats et al. 1996).

The wide field of view of an imaging densitometer complicates the calibration procedure. To facilitate retinal imaging the focal plane of the device must follow retinal curvature, the use of a flat field calibration system would therefore be inaccurate. Secondly, any irregularities in the uniformity of either the measurement or imaging pathway will manifest as artificial changes in ocular reflectance, hindering attempts to model the effect of human ocular tissues. Although the measuring beam of the device originates from an integrating sphere to provide uniformity, it is unlikely that the optics of the device are perfect.

Calibration of ocular reflectance across the field of view of the Mark II densitometer required the construction of an accurate model eye, which provided the means to

replicate the interaction between the device optics and the human eye and ensure robust calibration procedures.

7.2. Aims

The aim of the work described in this Chapter was to evaluate a model eye capable of accurately replicating the interaction between the human eye and a relatively wide field imaging device (i.e. the densitometer), in order to facilitate ocular reflectance modelling. To that end, three aims were identified.

1. To construct a model eye capable of calibrating ocular reflectance.
2. To characterise the spatial distribution of retinal illumination using the model eye, thereby facilitating a flat field calibration.
3. To validate the flat field ocular reflectance calibration using data from human eyes and compare the result with published ocular reflectance data.

7.3. The Cardiff model eye

The following section describes the optical design and construction of the Cardiff Model Eye used to calibrate ocular reflectance. Table 7.1 defines all parameters used throughout Chapter 7.

Table 7.1 Parameters used Chapter 7

Parameter	Definition
$GS(\lambda, x, y)$	Camera signal measured from the grey calibration surface, for all wavelengths and pixel locations.
$WS(\lambda, x, y)$	Camera signal measured from the white calibration surface ($BaSO_4$), for all wavelengths and pixel locations.
$GR(\lambda, x, y)$	Reflectance of the grey surface, calculated using Equation 7.1.
$S_{ME}(\lambda, x, y)$	Camera signal measured from the model eye measuring surface, for all wavelengths and pixel locations.
$S_{ME}100(\lambda, x, y)$	Camera signal measured from the model eye measuring surface scaled up to a surface of 100% reflectance using Equation 7.3, for all wavelengths and pixel locations.
$S_{DA}(\lambda, x, y)$	Camera signal measured from a dark-adapted retina, for all wavelengths and pixel locations.
$OR(\lambda, x, y)$	Ocular reflectance calculated using Equation 7.4, for all wavelengths and pixel locations.

7.3.1. Optical design of the Cardiff model eye

Many theoretical and optical model eyes exist in the literature, highlighted in a review by de Almeida and Carvalho (2007), ranging from a simplified single lens model first described by Emsley, a description of which is given by Pedrotti and Pedrotti (1998) to a complex multi surface approach incorporating chromatic aberration, spherical aberration and accommodation (Escudero-Sanz and Navarro 1999). The most widely used model being the full model developed by Gullstrand in 1911, a description can be found in Tunnacliffe (1993). However, the aspherical cornea and use of 4 refractive surfaces to describe the crystalline lens alone mean the construction of such an eye is not trivial. The Cardiff Model Eye was based on the Simple Gullstrand Eye with 5 parameters defining the radius of curvature, refractive index and central thickness of the cornea, anterior chamber, crystalline lens, posterior chamber and the retinal radius of curvature. Table 7.2 provides the values defining these parameters, alongside the values used in the construction of the Cardiff Model Eye.

Due to practical restrictions in the construction of the model eye the values defining the parameters vary slightly from those in the Simple Gullstrand Eye. A well-established contact lens firm (Jack Allen, Enfield) manufactured the replica cornea and crystalline lens from a material with a refractive index of 1.4. Whilst, the human retina doesn't have a single radius of curvature and is better fit by an oblate

ellipsoid, the central 60° has been shown to be accurately modelled by a single radius of -12mm (Escudero-Sanz and Navarro 1999). The slight adjustments to the radii of curvature (r_2) and central thickness of some parameters accounted for these alterations. Modelling of the proposed optical design was done using Zemax (Zemax LLC, Seattle) by Dr James Fergusson (Cardiff University) to quantify the total axial length (23.1mm), focal length (15.9mm) and power of the optics (62.9DS).

Table 7.2 Physiological and schematic values describing the ocular structures and model eye optics

	The Simplified Gullstrand Eye (Tunnacliffe 1993)			The Cardiff Model Eye		
	Radii of curvature (mm)	Refractive index (n)	Central Thickness (mm)	Radii of curvature (mm)	Refractive index (n)	Central Thickness (mm)
Cornea	r1 = 7.8 r2 = 6.8	1.38	0.5	r1 = 7.8 r2 = 6.7	1.4	0.5
Aqueous humour	N/A	1.34	3.1	N/A	1.33	3
Lens	r1 = 10.0 r2 = -6.0	1.41	3.6	r1 = 10.0 r2 = -8.0	1.4	4.5
Vitreous humour	N/A	1.34	17.2	N/A	1.33	15.8
Retina	r1 = -17.2	N/A	N/A	r1 = -12	N/A	N/A

7.3.2. Assembly of the Cardiff model eye

Figure 7.1 shows the components of the model eye. James Fergusson (Cardiff University) designed the housing of the model eye using CAD software (Onshape, Cambridge). MEC manufacturing (Cardiff School of Engineering, Cardiff) printed the unit to a resolution of 0.1mm (tolerance of 1%).

A

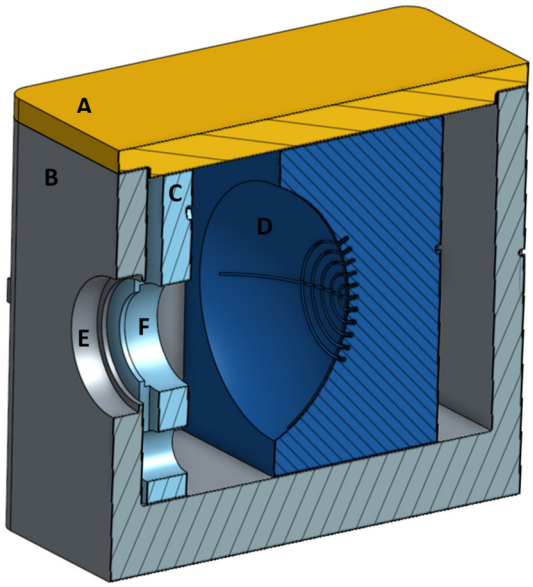

B

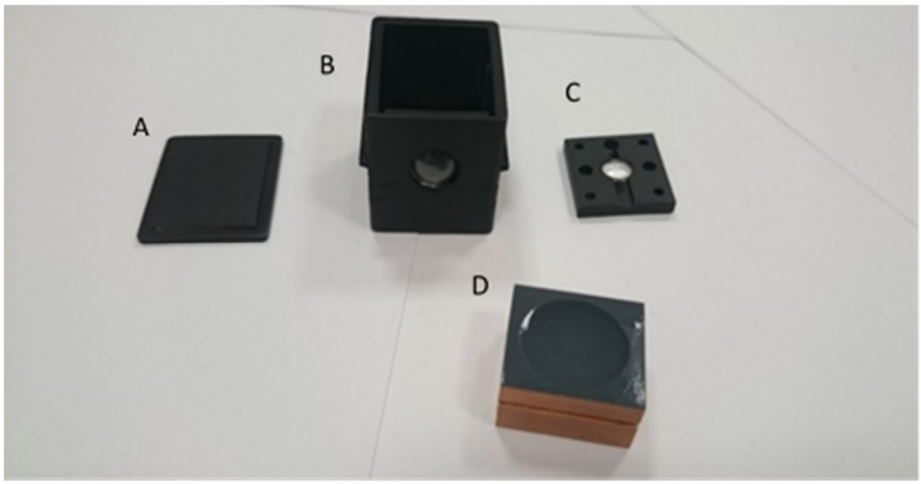

Figure 7.1 A) presents a cross section of the model eye and assembled components where; A is the cover; B the outer casing; C the iris pupil stop; D the imaging surface; E the location of the replica cornea and F location of the replica crystalline lens. B) Presents an image of the model eye and components (dis-assembled). Appendix F present the full schematics, including dimensions.

The housing comprised of 4 separate components; the cover (A, Figure 7.1), main body (B, Figure 7.1), iris pupil stop (C, Figure 7.1) two retinae, one printed with a smooth imaging surface, the other with a graticule imaging surface (D, Figure 7.1). The design facilitated the assembly, removal and cleaning of the components. A recess on the front external surface of the body of the model eye (E, Figure 7.1) accepted the cornea. The iris pupil stop had a similar groove (F, Figure 7.1) for the artificial crystalline lens. The iris pupil stop fitted flush against the front internal

surface of the main body, with correct alignment of the crystalline lens ensured through fitting guides. A groove on one side of the imaging surface (D, Figure 7.1) interlocked with a positive ridge inside the body of the model eye, locating the surface in the emmetropic position. Two grooves on the opposite side of the imaging surface allowed simulation of either a +5.00DS or -5.00DS refractive error. The cover prevented external light contaminating the image during use (A, Figure 7.1). To achieve emmetropia and minimise specular reflections, the anterior and posterior spaces were filled with distilled water (n = 1.334).

7.3.3. Spectral characteristics of the imaging surface

Accurate ocular reflectance calibrations require the knowledge of the reflectance of the imaging surface. Barium sulphate ($BaSO_4$) provides a spectrally flat Lambertian surface with a reflection of 99.4% (Weidner et al. 1985) and has long been used for this purpose in both industry and research (Budde 1976). However, as a water-soluble powder, $BaSO_4$ cannot be used to coat a submerged surface. An additional issue with using $BaSO_4$ in this model eye was that, when positioned 15.8mm from the pupil plane the highly sensitive CCD chip in the Mark II would saturate under most imaging conditions.

As ocular reflections range from <1% to ~12% (Delori & Pflibsen, 1989) the ideal finish for the imaging surface within the model eye would have reflective properties within this range, be spectrally flat and a Lambertian reflector, i.e. the intensity of reflectance is independent of viewing angle. A dark grey matt paint (Modelmates UK, #49101), meeting these requirements, was applied to the imaging surface. Calibration against the well-known reflectance properties of $BaSO_4$ allowed characterisation of the imaging surface reflectance, facilitating the determination of absolute ocular reflectance for all imaging conditions.

A pilot study was carried out which aimed to characterise the reflectance properties of the paint used against the well-known reflectance properties of $BaSO_4$.

7.3.3.1. Data Collection

A flat calibration surface was coated with identical paint (Modelmates UK, #49101). To replicate the submersion of the imaging surface, the calibration surface was wetted with distilled water prior to calibration. Positioning the calibration surface at a slight angle prevented coupling of the specular reflections, created by the air/water interface, into the measuring beam. The centre of the surface was positioned at a distance, d, from the objective lens of the retinal densitometer. $GS(\lambda, x, y)$ defined the camera signal measured at the centre of rotation of the grey calibration surface. A second flat surface coated in $BaSO_4$ was positioned in the same plane, at the same distance, d, from the objective lens of the retinal densitometer. The camera signal obtained from the centre of the white surface ($BaSO_4$) was given as $WS(\lambda, x, y)$. CCD bias and internal stray light were quantified and subtracted from both image sets. Equation 7.1 allowed the wavelength dependent reflectance of the grey surface, $GR(\lambda, x, y)$, to be calculated, assuming $BaSO_4$ reflected 99.4% of light at all wavelengths (Weidner et al. 1985),

$$GR(\lambda, x, y) = \frac{GS(\lambda, x, y)}{\left({}^{WS(\lambda, x, y)}/_{0.994}\right)}$$

(Equation 7.1).

7.3.3.2. Results

Figure 7.2 shows example images (500nm only) obtained for calculating the reflectivity of the grey paint used to coat the imaging surface of the model eye. The mean camera signal for both $BaSO_4$ (Figure 7.2A) and the grey paint (Figure 7.2B) obtained along the axis of rotation (highlighted) was used to calculate the reflectivity of the paint (Figure 7.2C) using Equation 7.1.

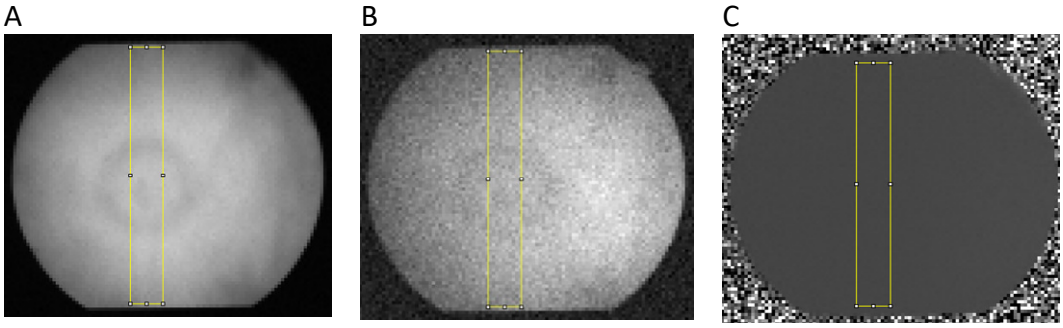

Figure 7.2 A) The camera signal from the $BaSO_4$ at 500nm. B) The camera signal from the grey surface at 500nm. C) The reflectance from a grey surface at 500nm, calculated using Equation 7.1. The highlighted region corresponds with the axis of rotation. Pixels within this region were averaged (median) to characterise the spectral reflectance of the paint when wet.

That there is a pattern visible in Figure 7.2A and B suggests that there is some spatial variation present at 500nm. The reflectivity of the paint decreased from 10.17% at 450nm to 6.57% at 740nm, as seen in Figure 7.3. Equation 7.2 uses a power law to describe the wavelength dependent characteristics of the reflectance from the model eye,

$$GR(\lambda) = 21.15 \cdot \lambda^{-0.87}$$

(Equation 7.2).

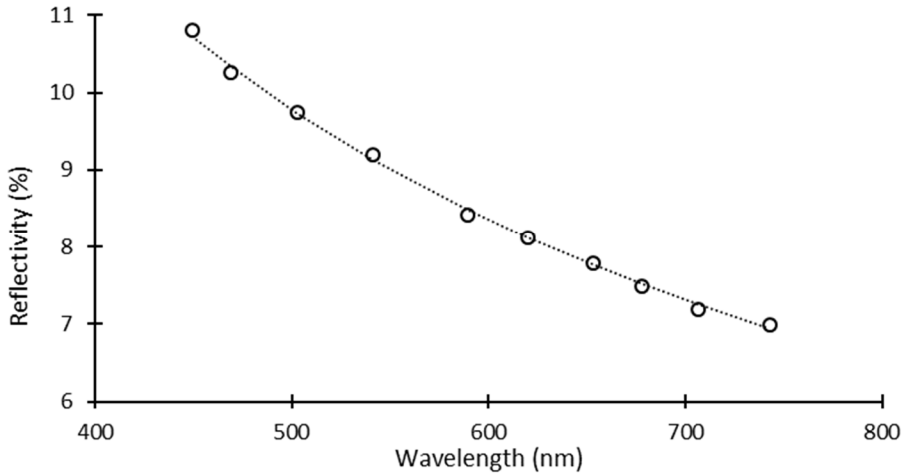

Figure 7.3 Spectral reflection characteristics of the grey paint applied to the model eye retina (open circles), dashed line represents a power model, defined by Equation 7.2

7.4. Characterising spatial uniformity

The aim of the following section was to characterise the spatial distribution of retinal illumination using the model eye. Knowledge of this distribution facilitates the flat field correction required to accurately calibrate ocular reflectance.

7.4.1. Data Collection

The investigation of the spatial characteristics of the illumination optics required images collected from the model eye imaging surface.

Alignment of the imaging system to the model eye followed a similar procedure as that described in Section 3.5.1. Using the 500nm LED, alignment of the device took place with the graticule imaging surface (Label D, Figure 7.1B) set in the emmetropic position, mimicking the participants refractive error. Following alignment, the graticule imaging surface was replaced with the Lambertian grey imaging surface and a series of images recorded (ncycles 30). Chapter 3 (Section 3.5.2) describes the imaging protocol, i.e. the pre-determined levels which defined LED intensity (Table 3.1, Chapter 3), binning was set to 8x8 and an exposure time of 0.2 seconds was used. A subsequent reference series was obtained (Section 3.5.2.1).

7.4.2. Data Analysis

Following subtraction of the reference series (CCD bias and internal stray light) from the model eye images, the median camera signal of the data set was extracted for each wavelength and location, $S_{ME}(\lambda, x, y)$. Knowledge of the reflectivity of the imaging surface ($GR(\lambda)$) allowed the camera signal to be scaled to a value that would have been achieved had the reflectance been 100% ($S_{ME}100(\lambda, x, y)$), shown in Equation 7.3,

$$S_{ME}100(\lambda, x, y) = \frac{S_{ME}(\lambda, x, y)}{GR(\lambda)}$$

(Equation 7.3).

The spatial distribution of the illumination beam was investigated across a central region of interest (30^o x 5^o), taken along the horizontal midline. Within this region of interest, the median of the y pixels (10 pixels) was taken, providing a resolution of 30 pixels x 1 pixel.

7.4.3. Results

The images obtained from the model eye lacked spatial uniformity, as shown in Figure 7.4. For all wavelengths, camera signal was lower in the periphery of the image, increasing to a peak in an annulus near the centre of the image. Localised regions of increased camera signal are present in the peripheral regions, most noticeably on the left and right of the image.

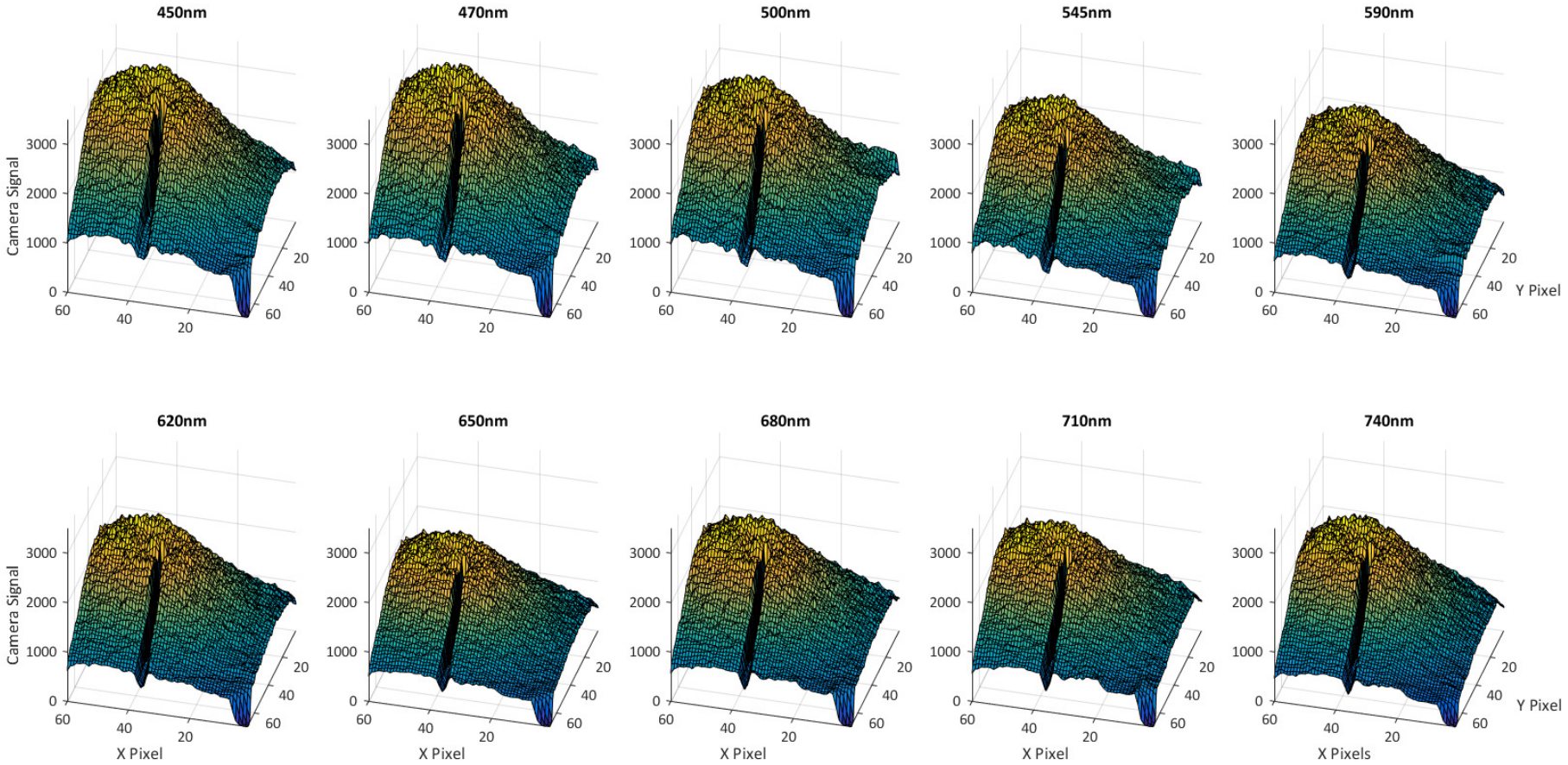

Figure 7.4 Unadjusted camera signal obtained from model eye imaging surface, for all wavelengths. Central 30°.

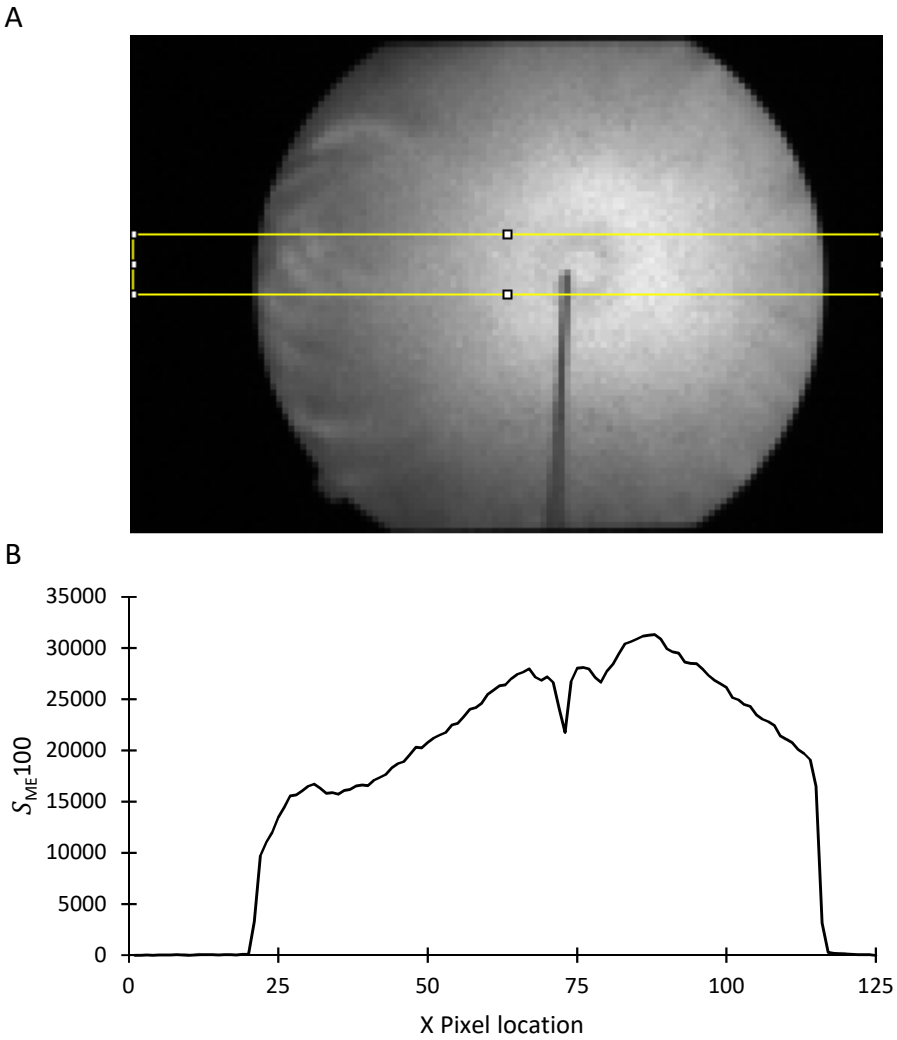

Figure 7.5 A) A raw 500nm image. Within the region of interest shown, camera signal at each x location was taken as the mean of the y pixels (height, 10 pixels). B) Camera signal measured from the above image, corrected to $S_{ME}100(500, x)$ using Equation 7.3.

Figure 7.5 shows a representative image collected with the 500nm LED. The peripheral distortions and central annulus can be seen.

7.5. Calibration of ocular reflectance

The aim of the following study was to validate the flat field ocular reflectance calibration obtained from the Cardiff Model Eye using data from human eyes and comparing the result with published ocular reflectance data.

7.5.1. Data collection

The calibration of ocular reflectance required the collection of fundus images.

Chapter 3 describes the imaging device, set up and alignment procedures used to obtain images from a human participant. As there was no interest in visual pigment optical density or regeneration in this investigation, image collection followed a 20-minute dark-adaptation process, as described in Section 3.5.2 (ncycles = 30). A subsequent reference series was obtained, as described in Section 3.5.2.1.

7.5.2. Data analysis

Subtraction of CCD bias and internal stray light from the raw images provided the unadjusted time series. Equation 7.4 calibrated the ocular reflectance $OR(\lambda, x, y)$ of each image ($S_{DA}(\lambda, x, y)$) in the unadjusted time series,

$$OR(\lambda, x, y) = \frac{S_{DA}(\lambda, x, y)}{S_{ME}100(\lambda, x, y)}$$

(Equation 7.4).

Once calibrated to fractional ocular reflectance ($OR(\lambda, x, y)$), the images were registered to a single reference frame, blinks removed, and the median obtained. The ocular reflectance was extracted from four regions for investigation; a vertical midline through the fovea (2° x 30°), a horizontal midline through the foveal (30° x 2°), the central 30° x 30° retinal area and a small parafoveal location (2.5° x 2.5° region, 10° temporal, positioned on the horizontal midline). This final region of interest was similar in size and retinal location to that used by Delori and Pflibsen (1989), allowing direct comparison between the two studies. Normalisation of the images to the pixel of highest intensity allowed a direct comparison between the unadjusted camera signal ($S_{DA}(\lambda, x, y)$) and calibrated ocular reflectance ($OR(\lambda, x, y)$) at all wavelengths.

7.5.3. Results

Figure 7.6A shows the camera signal variation across the central 30° of the 500nm model eye images. A region of higher intensity, around 15° in diameter, was centred slightly superior-nasal to the centre of the image.

A

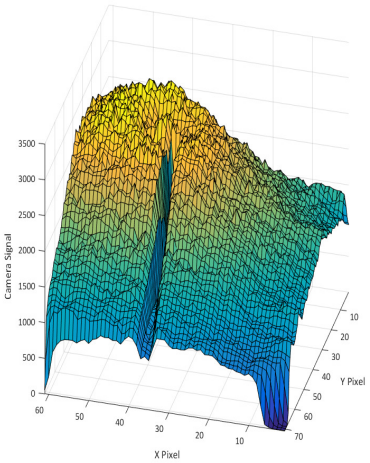

B

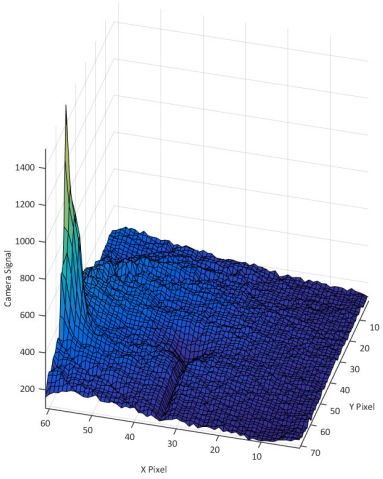

C

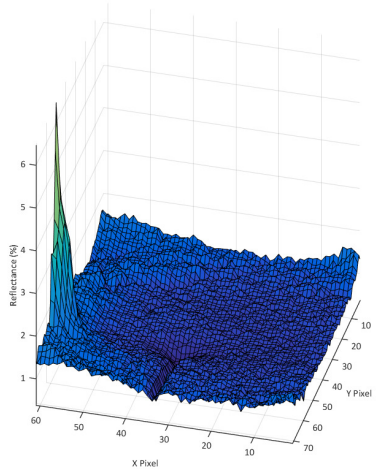

Figure 7.6 Calibrating for ocular reflectance across the central 30°, at 500nm. A) Camera signal measured from the model eye. B) Unadjusted camera signal measured from the human fundus. C) Calibrated ocular reflectance. Appendix G provides this information across all the wavelengths.

Figure 7.6B shows the central 30° obtained from the unadjusted retinal images. This corresponds with the intensity profile measured using the model eye (Figure 7.6A) in both size and location, demonstrating the effect measuring beam uniformity has upon the retinal images. The calibrated ocular reflectance

(calculated using Equation 7.4) is shown for 500nm in Figure 7.6C and across all wavelengths in Appendix G.

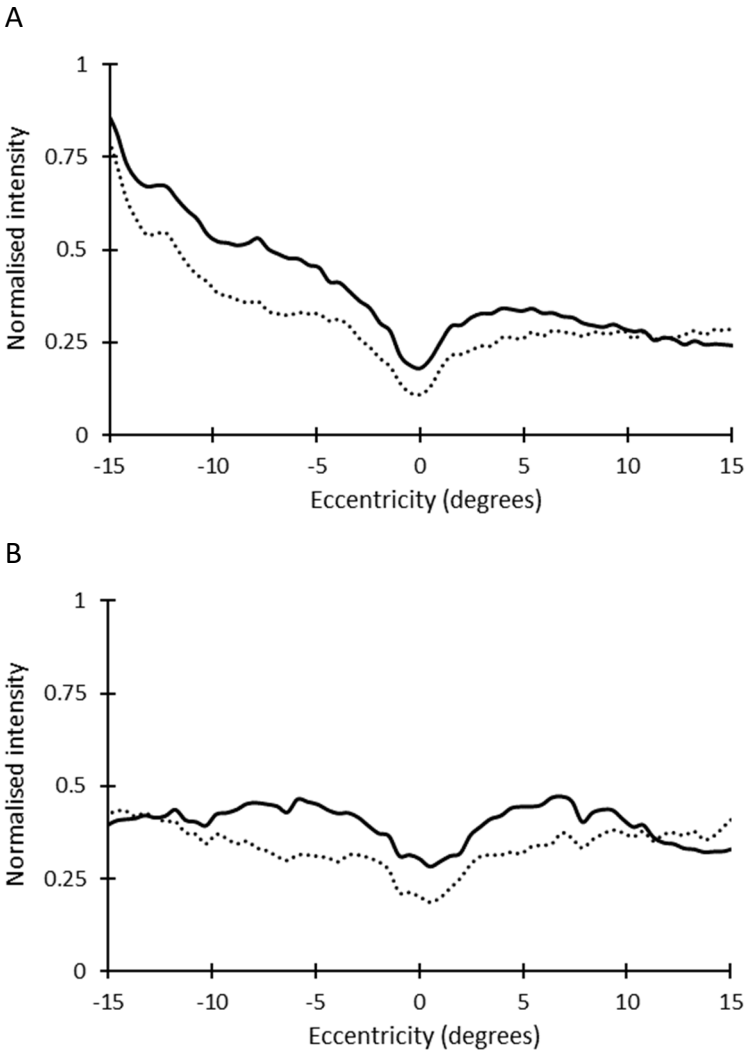

Figure 7.7 Normalised intensity along A) the horizontal midline and B) vertical midline for the unadjusted camera signal (solid line) and calibrated ocular reflectance (interrupted line).

The profile across the centre of the ocular reflectance images (Figure 7.6) present a uniform appearance. This is a substantial change from the unadjusted retinal images, which can clearly be seen in Figure 7.7. The unadjusted images exhibited a temporal to nasal intensity decrease and a central region of raised intensity, this pattern was consistent with the illumination pattern seen in the model eye (Figure 7.6A). The flattening of intensity was present at all wavelengths, but most noticeable in the longer wavelengths.

Figure 7.7 shows the normalised intensity profile along the horizontal and vertical midline at 500nm, comparing the unadjusted camera signal to the calibrated ocular reflectance. Along the horizontal midline of the unadjusted image there was a distinct trend of decreasing intensity from left to right across the image (Figure 7.7A). This trend was not present in the calibrated reflectance image, although a slight increase near the ONH was present. A similar trend was seen in the vertical midline, with the unadjusted image showing a central intensity increase which wasn't present in the more uniform reflectance image.

7.5.3.1. Comparison with published data

Having converted camera signal to retinal reflectance, it was possible to compare the retinal reflectance obtained with the Mark II densitometer to that published in the literature (Delori and Pflibsen 1989).

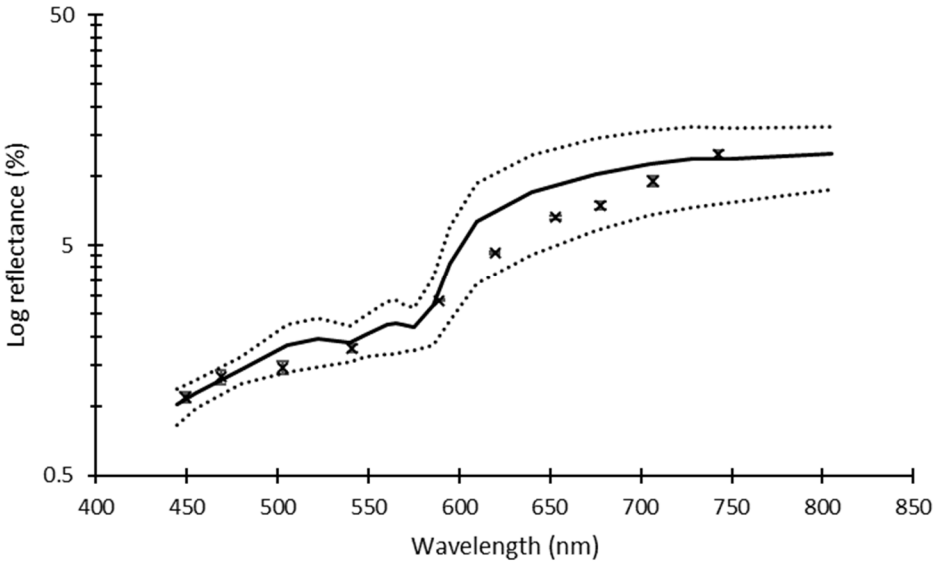

Figure 7.8 Parafoveal ocular reflectance from a 2.5x2.5° region 14° temporal to the fovea (crosses, standard error bars), compared to the average ocular reflectance from Delori and Pflibsen (1989) (solid line), upper and lower boundaries (dotted lines) are 1 standard deviation from the mean.

The calibrated ocular reflectance obtained from the peripheral location was seen to rise monotonically with wavelength. The data were a good match with the peripheral reflectance data published by Delori and Pflibsen (1989), as shown in Figure 7.8.

7.6. Discussion

This chapter describes the design and evaluation of a model eye developed to calibrate ocular reflectance measurements. In the process, a lack of spatial and spectral uniformity in the optical system of the Mark II densitometer was identified. The model eye facilitated the correction of the retinal images for both these spatial and spectral variations. Whilst vital to the accurate calculation of ocular reflectance as shown here, the model eye could also serve as a useful calibration device across all modalities of retinal imaging.

The intensity profile of the illumination beam was shown to dominate the spatial profile of the unadjusted images, as seen in both the model eye (Figure 7.4) and the human retina (Figure 7.6B). The peak of this profile was centred nasal and inferior to the fovea, resulting in a wavelength dependent, artefactual variation in camera signal across the retinal images. This can be seen in Figure 7.4 (model eye camera signal) and Figure 7.6B (retinal camera signal). Equation 7.3 describes the use of the model eye camera signal to calculate ocular reflectance. Following this correction, the ocular reflection images showed minimal variation in signal across the central 30^{o} for each wavelength (Figure 7.7), which is consistent with expected results from a homogenous retinal region. Visibly, the macula, nerve fibre layer and blood vessels were more prominent and defined after correction.

When imaging the human retina, peripheral edge artefacts were visible. This was more apparent in the calibrated reflection data. Differences between the model eye and human eye may explain these artefacts. A probable cause of these artefacts lies with pupil misalignment during acquisition of the retinal images. The pupil used on the model eye was larger (8mm diameter) than the dilated human pupil (7.5mm diameter) (Ratanapakorn et al. 2006). Furthermore, the human eye is prone to involuntary fixational eye movements affecting the perfect alignment (Rolfs 2009), despite the use of a bite bar during retinal

imaging. As these artefacts are not present in the model eye images they remain uncorrected following calibration by the model eye, thus accentuating their presence.

7.7. Summary

The model eye provided a method of measuring the reflectivity of an imaging surface, the same shape and location as a human retina. Imaging of the model eye provided information on the spatial and spectral uniformity across all images collected with the device. This facilitated the simultaneous calibration of retinal images to their true reflectance values and the topographical correction for lack of uniformity. The central 30^{o} of retina was accurately corrected, providing a true ocular reflectivity comparable to that published by Delori and Pflibsen (1989), as demonstrated by Figure 7.8. However, increased intensity present in the periphery of the unadjusted retinal images was not corrected by the model eye images. Therefore, this artefact was attributed to the interaction between the optics of the human eye and the imaging device, with misalignment and peripheral aberrations the most likely source.

Chapter 8 - Ocular Reflection Modelling

8.1. Introduction

Visual pigment spectra measured *in vivo* are different to those obtained with the *in vitro* methods, with those obtained *in vivo* all showing a 'red shift' to a greater or lesser extent (Ripps and Weale 1965; Faulkner and Kemp 1984; Kilbride and Keehan 1990; van de Kraats et al. 1996). This has been attributed to the interaction of the optical properties of the human eye with those of the instrument, generating wavelength dependent stray light and diluting the measured optical density (Rushton 1965; Delori and Pflibsen 1989; Kilbride and Keehan 1990; van de Kraats and van Norren 2008). The experiments described in Chapter 6 attempted to quantify stray light directly. Although the investigation was partially successful, it was evident that pre-receptor retinal contributions to stray light had been underestimated (Section 6.5).

Consequently, this indicated the need for a way of accurately describing the reflection characteristics of pre-photoreceptor ocular components. Accurate modelling of ocular reflectance may allow the 'red shift', seen in Figure 4.3 (Chapter 4), to be corrected, thereby facilitating accurate characterisation of rod, M- and L- cone spectra (Dartnall et al. 1983). At the outset of the following investigations, the expectation was that an accurate ocular reflectance model would facilitate the identification of retinal layers based on their spectral signatures alone. Thus, allowing the mathematical removal of the contributions from ocular layers anterior to the visual pigments and a more accurate assessment of visual pigment optical density (see Equation 6.1, Chapter 6).

8.2. Aims

The aims of the investigations discussed in this Chapter were to:

1. Identify any ocular reflection models from the literature which may be able to isolate outer retinal reflectance from the experimental data obtained with the densitometer.

2. Evaluate the ability of relevant ocular reflection models to characterise the ocular reflection data obtained with the densitometer.

8.3. History of ocular reflection modelling

Many ocular reflection models have been described and a detailed overview can be found in the review paper by Berendschot (2003). The following paragraphs provide a critique of each model (Ripps and Weale 1965; King-Smith 1973a; van Blokland and van Norren 1986; van Norren and Tiemeijer 1986; Delori and Pflibsen 1989; van de Kraats et al. 1996; Hammer and Schweitzer 2002; van de Kraats and van Norren 2008).

Ripps and Weale (1965) presented the first description of the light path through the intra-photoreceptor matrix. Their hypothesis was that the distribution of photoreceptors within the interphotoreceptor matrix caused the break-down of the Beer-Lambert law (which states absorbance is directly proportional to the path length and concentration of any given pigment), resulting in an underestimation of the true optical density value. King-Smith (1973a) built on the description of light transmission through the inter-photoreceptor matrix with the introduction of directional light and the Stiles-Crawford effect. However, the reflective properties of the ocular tissues were not included in this analysis. A single, wavelength independent surface, corresponding to the sclera, provided the only reflective layer in both these early models. While photoreceptor spacing could account for the underestimation of visual pigment

density *in vivo*, it could not explain the 'red shift' nor accurately describe the large range in ocular reflectivity observed across the spectrum. In an attempt to account for this, van Blokland and van Norren (1986) further developed the existing models by introducing a secondary reflecting source placed directly behind the photoreceptors. They came to two pertinent conclusions. Firstly, that light scatter in the inter-photoreceptor matrix was strongly influenced by the presence of visual pigment and, secondly, that other sources of reflection are likely to contribute to the total reflectance profile.

When describing the bleached retina, no visual pigment is present in the photoreceptor layer. As such, the modelling of light pathways through the inter-photoreceptor matrix is of less importance in the bleached retina (van Blokland and van Norren 1986). Van Norren & Tiemeijer (1986) proposed an ocular reflection model with the RPE and sclera as reflective layers and introduced four ocular absorbing layers; the lens, macular pigment, melanin and blood. The combination of these absorbing layers and reflective surfaces provided a relatively good description of ocular reflectance (Section 9.3.1 and 9.3.2, Chapter 9, show the spectral profiles of these layers). Delori & Pflibsen (1989) noted the failure to describe both inner retinal reflections and forward light scatter from both the media and choroid as limitations in previous models. They proposed a more complex model that included both light loss from the optical media and reflection information from a surface replicating the inner limiting membrane through the solution of a secondary fit (Delori and Pflibsen 1989). However, the main focus of their work was an attempt to describe the complex absorbance and scattering properties of the choroidal layer through the application of Kubelka-Munk scattering coefficient equations (Kubelka and Munk 1931; Delori and Pflibsen 1989). The resulting model contained 11 free parameters. To improve parsimony, 5 of these were constrained to a fixed value. A model published by Hammer and Schweitzer (2002) assumed similar ocular layers to the two preceding models, describing inner retinal reflectance through the use of a fixed parameter. However, their approach could not be solved

analytically but rather relied on the adding-doubling method, a lengthy iterative process, to obtain results (Hammer and Schweitzer 2002).

Arguably, the most complete model of retinal reflectance was that proposed by van de Kraats et al (1996). Their model provided a similar description of the ocular absorbers and reflectors to that proposed by van Norren & Tiemeijer (1986). However, they applied a complex theory to describe the light guide effect of the cones, stray light within the foveal intracellular matrix and reflections from the outer segment discs. For this approach, the Stiles-Crawford effect was an essential factor in the solution of the 11 free parameters, utilising measurement of both on and off axis reflectance to estimate photoreceptor directionality in both dark adapted and bleached retinal states. van de Kraats and van Norren (2008) have since updated the description of the optical media and choroidal thickness. Whilst primarily a model to describe foveal reflectance, through modelling at 5 discrete locations across the retina, Berendschot et al. (2010) had some success using the updated model to describe parafoveal reflections using 11 parameters. However, the methods remained dependent upon the Stiles-Crawford effect.

To facilitate reliable modelling of reflections across the retina, a physiologically plausible model with high parsimony was required. Further, the published literature regarding ocular reflection models highlights the interaction between reflective surfaces and absorbing layers (van Norren and Tiemeijer 1986; Delori and Pflibsen 1989; van de Kraats et al. 1996; Berendschot et al. 2003). These requirements preclude the use of the models which fail to account for light absorption by the ocular tissues (Ripps and Weale 1965; King-Smith 1973a; van Blokland and van Norren 1986). The models of a more complex nature exclude themselves because they contain so many free parameters that multiple fits can be obtained i.e. there is no single solution to curve fitting. The method proposed by van de Kraats and van Norren (van de Kraats et al. 1996; van de Kraats and van Norren 2008) relies upon the measurement of on and off axis reflectance to

account for the Stiles-Crawford effect, an approach that was not possible due to the configuration of the illumination and imaging cones of the Mark II device.

In presenting a description of ocular reflections in terms of both reflection and absorption of the various tissues, with minimal free parameters and on the basis of a single bleached recording, the models proposed by van Norren and Tiemeijer (1986) and Delori and Pflibsen (1989) are of greatest interest here and will be discussed further. These models are referred to as Model I and Model II, respectively, for the remainder of this Chapter.

8.4. Description of Models I and II

The following section considers the two ocular reflection models in more detail with Figure 8.1 providing a schematic representation of the models for comparison.

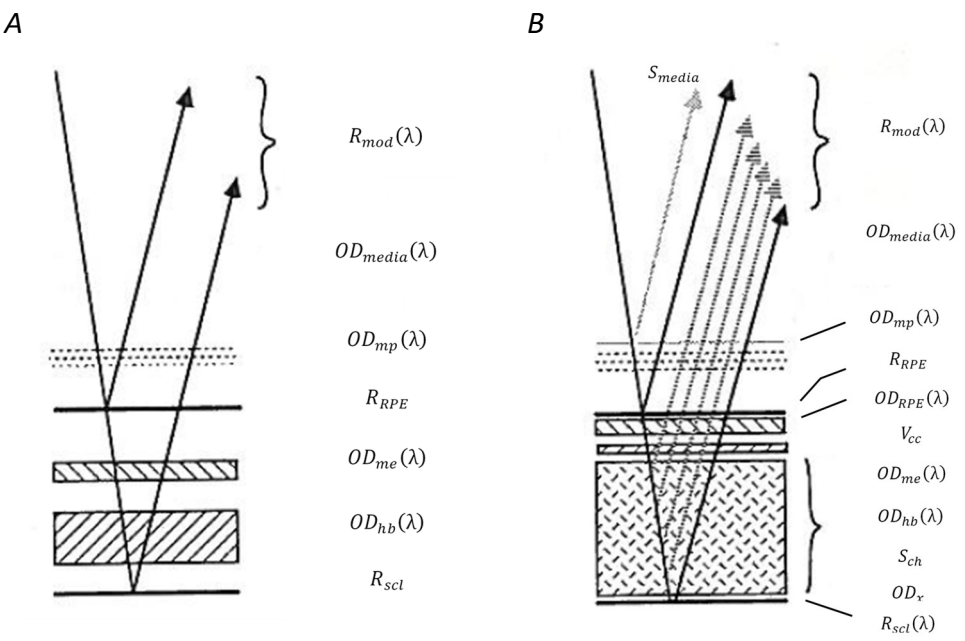

Figure 8.1 A) Schematic of the ocular layers used to describe model I (van Norren and Tiemeijer 1986). B) Schematic of the ocular layers used to describe model II (Delori and Pflibsen 1989). Figure modified from (Delori and Pflibsen 1989).

8.4.1. Model I

Model I (van Norren and Tiemeijer 1986) provides a relatively simple description of 6 ocular layers shown Figure 8.1A, all parameters used are defined in Table 8.1.

The absorption characteristics of the ocular media, $OD_{media}(\lambda)$, macula pigment $OD_{mp}(\lambda)$, melanin, $OD_{me}(\lambda)$ and choroidal haemoglobin, $OD_{hb}(\lambda)$ along with wavelength independent reflections from the RPE, R_{RPE} and sclera R_{scl} are included in this model. The solution of Equation 8.1 provides the modelled ocular reflectance, $R_{mod}(\lambda)$,

$$R_{mod}(\lambda) = \left\{R_{RPE} \cdot 10^{-\left[2\cdot\left((OD_{media}(\lambda)\cdot V_{media})+(OD_{mp}(\lambda)\cdot V_{mp})\right)\right]}\right\} + \left\{R_{scl} \cdot 10^{-\left[2\cdot\left((OD_{media}(\lambda)\cdot V_{media})+(OD_{mp}(\lambda)\cdot V_{mp})+(OD_{me}(\lambda)\cdot V_{me})+(OD_{hb}(\lambda)\cdot V_{hb})\right)\right]}\right\}$$

(Equation 8.1),

where V_{media}, V_{mp}, V_{me}, V_{hb} are variable scaling factors for the wavelength-dependent absorbing layers and R_{RPE} and R_{scl} are variable scaling factors for the wavelength-independent reflecting layers. Table 8.1 summarises the parameters and variables used in this model.

Table 8.1 Parameters used in Model I

Parameter	Definition
$OD_{media}(\lambda)$	Spectral shape defining the light absorbed by the human ocular media. Data obtained from Vos and van Norren (1974).
$OD_{mp}(\lambda)$	Spectral shape defining the light absorbed by human macula pigment. Data obtained from Snodderly et al. (1984).
$OD_{me}(\lambda)$	Spectral shape defining the light absorbed by human melanin. Data obtained from Gabel (1978).
$OD_{hb}(\lambda)$	Spectral shape defining the light absorbed by the haemoglobin present in the choroid (haemoglobin assumed to be 95% oxygenated). Data obtained from van Assendelft (1970).
R_{RPE}	Wavelength independent reflections from a surface positioned behind the photoreceptors.
R_{scl}	Wavelength independent reflections from a surface positioned behind the choroid.
V_{media}	A scaling factor, defining the amount of light absorbed by the human ocular media.
V_{mp}	A scaling factor, defining the amount of light absorbed by macula pigment.
V_{me}	A scaling factor, defining the amount of light absorbed by melanin.
V_{hb}	A scaling factor, defining the thickness (µm) of the haemoglobin layer present within the choroid.

8.4.2. Model II

Delori & Pflibsen (1989) developed Model II to better describe the long-wavelength reflections in an attempt to reduce the variability of the results. A schematic of the model is shown in Figure 8.1B and the additional parameters are defined in Table 8.2. Figure 8.2 outlines the optical characteristics of the parameters used for both models.

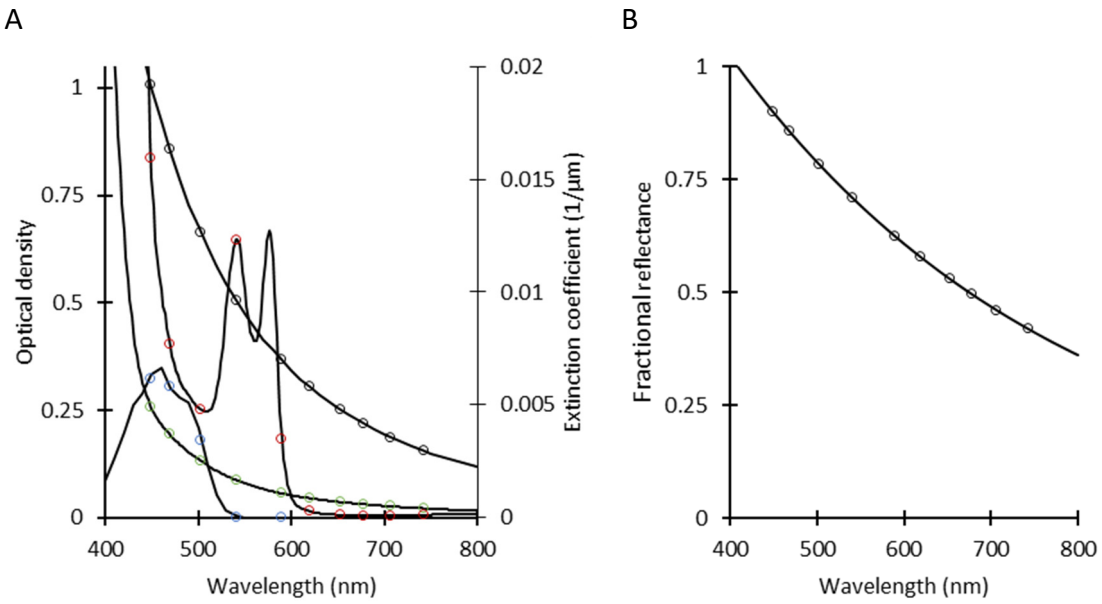

Figure 8.2 A) Absorption characteristics of the ocular pigments as described in Delori & Pflibsen (1989). Solid lines show the data extracted from the literature and the open circles highlight the specific values used in the model, which correspond to the measuring beams in the Mark II densitometer. $OD_{mp}(\lambda)$ (blue circles) has been obtained from Snodderly et al (1984), $OD_{media}(\lambda)$ (green circles) is from van Norren & Vos (1974) and $OD_{me}(\lambda)$ (black circles) has been taken from Gabel et al (1978). $OD_{hb}(\lambda)$ (red circles) is shown on a secondary axis and taken as 1µm of 95% oxygenated haemoglobin from van Assendelft (1970). B) Reflectance of the sclera normalised to 50% at 675nm used in model II (1989).

This model adds separate parameters defining absorption of the choriocapillaris and the main choroidal space to replace the choroidal haemoglobin layer from Model I. The haemoglobin spectrum, $OD_{hb}(\lambda)$, defines the characteristics of both components. An additional wavelength-independent parameter, OD_x, describes unknown light loss within the choroid. S_{media} and S_{ch} define wavelength-independent light loss from the optical media and choroid. Equation 8.2 defines the wavelength dependent scleral reflectance, $R_{scl}(\lambda)$ (shown in Figure 8.2B),

$$R_{scl}(\lambda) = 0.5 \cdot e^{[-0.00261 \cdot (\lambda - 675)]}$$

(Equation 8.2).

Equation 8.3 defines the modelled ocular reflectance obtained using Model II, $R_{mod}(\lambda)$,

$$R_{mod}(\lambda) = \left\{R_{RPE} \cdot 10^{-\left[2\cdot\left((OD_{media}(\lambda)\cdot V_{media})+\left(OD_{mp}(\lambda)\cdot V_{mp}\right)\right)+S_{media}\right]}\right\} + \left\{R_{ch}(\lambda) \cdot 10^{-\left[2\cdot\left((OD_{media}(\lambda)\cdot V_{media})+\left(OD_{mp}(\lambda)\cdot V_{mp}\right)+(OD_{RPE}(\lambda)\cdot V_{RPE})+(OD_{hb}(\lambda)\cdot V_{cc})\right)\right]}\right\}$$

(Equation 8.3).

Where V_{RPE} is a scalar for melanin present in the RPE layer and V_{cc} defines the thickness of the blood layer OD_{hb} within the choriocapillaris. Equation 8.4 defines the choroidal reflection, $R_{ch}(\lambda)$, which is in turn dependent upon the Kubelka-Munk theory, described through solution of Equation 8.5 and Equation 8.6. For a full description of the Kubelka-Munk Theory see Kubelka and Munk (1931),

$$R_{ch}(\lambda) = \frac{\left(1 - R_{scl}(\lambda)\right)\cdot(a - b\,coth\,b\cdot S_{ch}\cdot t_{ch})}{a + b\,coth\,b\cdot S_{ch}\cdot t_{ch} - R_{scl}(\lambda)}$$

(Equation 8.4),

$$a = 1 + \frac{[(OD_{me}(\lambda)\cdot V_{me}) + (OD_{hb}(\lambda)\cdot V_{hb}) + OD_x]\,log\,e}{s_{ch}\cdot t_{ch}}$$

(Equation 8.5),

$$b = (a^2 - 1)^{1/2}$$

(Equation 8.6).

Having described the two most relevant reflection models, the following section describes the experimental methods used to obtain the reflectance data that were used to evaluate them.

Table 8.2 Additional parameters used in Model II

Parameter	Definition
OD_x	Describing spectrally neutral light loss within the choroid of unknown origin.
S_{media}	Forward scattered light loss from the optical media.
$OD_{RPE}(\lambda)$	Spectral shape defining the light absorbed by human melanin. Data obtained from Gabel (1978).
S_{ch}	Forward scattered light loss from within the choroid.
$R_{scl}(\lambda)$	Wavelength dependent scleral reflectance, defined by Equation 8.2.
t_{ch}	Thickness of the choroid (μm), non-haemoglobin portion.
V_{cc}	Thickness of the choriocapillaris (μm).
$R_{ch}(\lambda)$	Wavelength dependent reflectance from the choroid, defined by the simultaneous solution to Equations 8.4 – 8.6.

8.5. Methods

8.5.1. Participants

Five healthy participants were studied. Each provided informed, written consent with Ethical approval obtained from the School of Optometry and Vision Sciences. All procedures adhered to the tenets of the Declaration of Helsinki. All participants had corrected visual acuity of LogMAR 0.0 (20/20) or better in the test eye, refractive errors within the range of the device (±7.50 DS) and clear ocular media, i.e. LOCS III, grade ≤1 (Chylack et al. 1993). One participant was a protanope, all others had normal colour vision. Table 8.3 summarises participant characteristics. All participants were experienced with the lengthy procedures and the device used.

8.5.2. Apparatus

The densitometer has been described in Chapter 3, with minor changes to the bleaching source and illumination pathway as described here.

The bleaching mask, described in Chapter 3, protected the superior retina from the light source, aiding fixation by preventing photopigment bleaching in this region. Enlarging the bleaching source to a full 25^o aperture, with a central fixation spot, facilitated optical density investigation across the central retina.

During retinal imaging, a large cross hair replaced the fixation target previously used. This provided a peripheral target for fixation immediately after bleach cessation, before regeneration allowed the centre of the target to be accurately fixated.

The model eye was used to calibrate the data collected from the densitometer, as described in Chapter 7.

8.5.3. Procedure and analysis

Dark adapted, bleach regeneration and reference images were collected following the protocol described in Section 3.5 and the model eye reference images were collected as described in Section 7.4.1.

As previously described, reference images containing CCD bias and scattered light within the instrument were subtracted from all retinal images, camera signal values were converted to ocular reflectance according to light distribution in the model eye, images were registered to a reference frame and blink artefacts were removed. The foveal and parafoveal regions of interest were a 2x2 pixel region located on the fovea and a 2x2 pixel region located 10^{o} temporal to the fovea, respectively. The median reflectance of the initial 30 seconds (15 frames) of the bleach regeneration recording defined ocular reflectance at each retinal location.

8.5.4. The fitting routine

A least squares optimisation algorithm (Solver, Excel) was used to fit the two models to the logged experimental reflectance values obtained from the parafoveal and foveal locations, for each participant. The experimental reflectance was logged to avoid fitting bias toward the longer wavelengths where reflectance was significantly higher. No constraints were imposed on any of the variables.

8.6. Results

Table 8.3 presents the individual characteristics for each participant. The refractive error for 4 out of 5 participants was near plano, the 5th participant had a refractive error of -5.50DS. The mean age was 34.2, with a standard deviation of 10.1.

Table 8.3 Participant characteristics

Participant	Age	Gender	LOCSIII grade	Ocular History
HM	29	F	1	+0.25DS
AW	32	M	1	-5.50DS
JF	30	M	1	Plano
TM	52	M	1	-0.50DS / Protanope
CJ	28	M	1	-0.25DS

8.6.1. Results obtained with Model I

Figure 8.3 presents an example of the model fit from each retinal location for participant CJ. Appendix H presents the model fit from each retinal location for all participants. Table 8.4 presents the average value for each parameter.

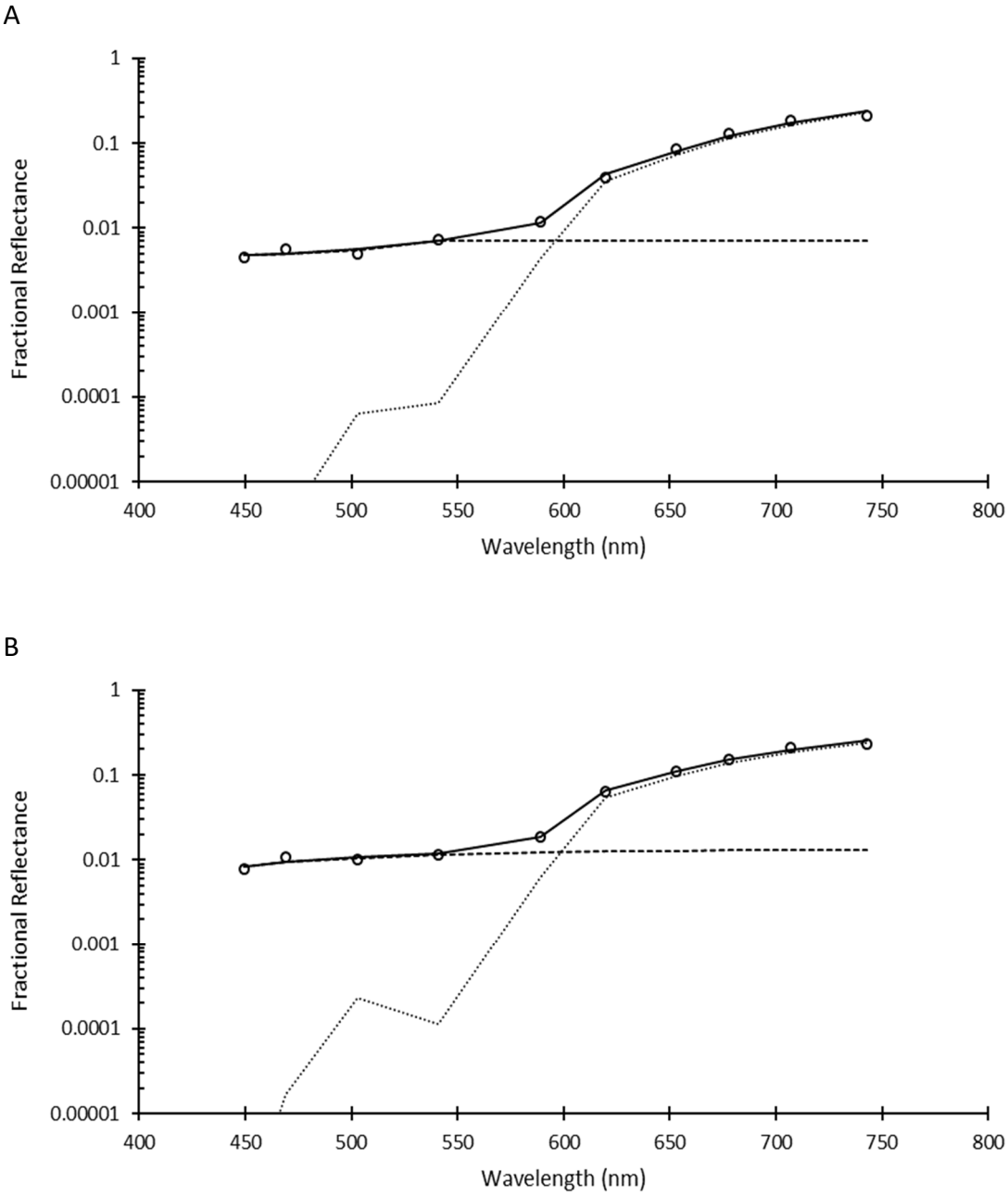

Figure 8.3 Example results showing fit of Model I to the data from participant CJ at two locations. Circles are experimental data, solid lines represent the model fit, the dashed line describes the contribution from the RPE reflection and the dotted line the contribution from the scleral reflection.

A) Foveal fit described by parameter values of V_{media} = 0.00, V_{mp} = 0.09, V_{me} = 2.31, V_{hb} = 170.5µm, R_{RPE} = 0.7% and R_{scl} = 64.1%. RMSE = 0.0045.

B) Parafoveal fit described by parameter values of V_{media} = 0.11, V_{mp} = 0.00, V_{me} = 1.74, V_{hb} = 197.3µm, R_{RPE} = 1.4% and R_{scl} 54.7%. RMSE = 0.0027.

Table 8.4 Results for Model. Showing group mean and standard deviation.

	Fovea	Parafovea
V_{media}	0.05 (±0.07)	0.13 (±0.03)
V_{mp}	0.04 (±0.04)	0.00 (±0.00)
V_{me}	2.03 (±0.35)	1.55 (±0.25)
V_{hb} (μm)	147 (±65)	155 (±54)
R_{RPE} (%)	0.8 (±0.1)	1.6 (±0.3)
R_{scl} (%)	49.4 (±12.9)	41.7 (±12.7)
RMSE	0.0063 (±0.0034)	0.0023 (±0.0016)

Model I (van Norren and Tiemeijer 1986) provided a good description of ocular reflectance in both the foveal and parafoveal locations, with low RMSE values of 0.0063 (±0.0034SD) and 0.0023 (±0.0016SD) respectively. The RPE contribution dominated the short- to mid-wavelength reflectance, with the scleral reflection having more impact upon the spectral shape for wavelengths beyond 590nm (where blood is nearly transparent). All parameters showed variation between the two retinal locations. V_{me}, V_{mp} and R_{scl} returned higher values in the fovea, while V_{hb}, R_{RPE} and V_{media} returned higher values in the parafovea. There was some uncertainty around the mean values for both V_{media} (0.05 ±0.07SD) and V_{mp} (0.04 ±0.04SD) in the foveal location, where the standard deviation was of an equivalent magnitude to the mean.

8.6.2. Results obtained with Model II

Figure 8.4 presents an example of the model fit from each retinal location for participant CJ, following the free fit of all variables. Appendix H presents the model fit from each retinal location for all participants. Table 8.5 presents the average value for each parameter.

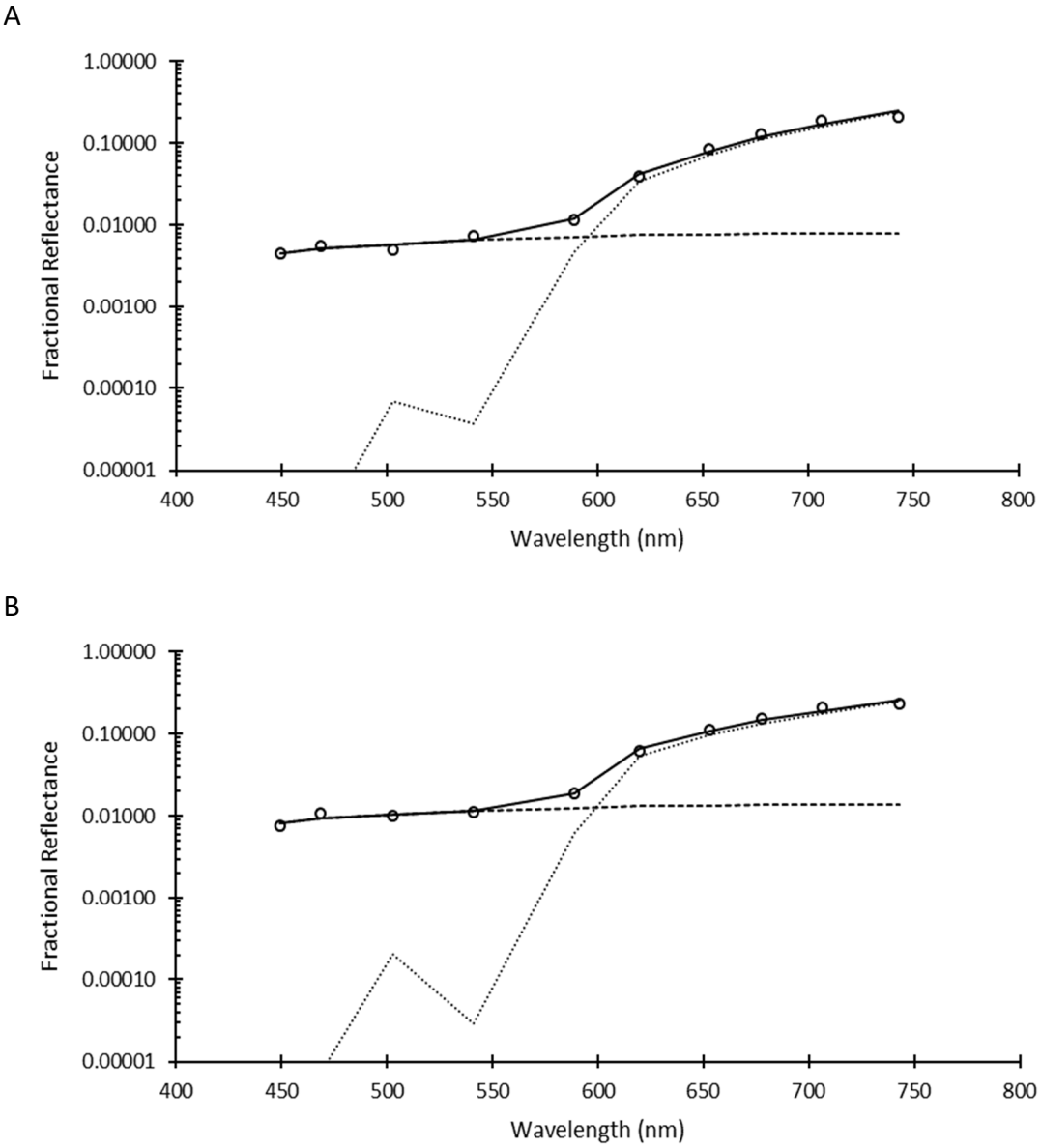

Figure 8.4 Example results showing fit of Model II to the data from participant CJ at two locations. Circles are experimental data, solid lines represent the model fit, the dashed line describes the contribution from the RPE reflection and the dotted line the contribution from the scleral reflection.

A) Foveal fit described by parameter values of V_{media} = 0.118, V_{mp} = 0.005, V_{me} = 0.04, V_{hb} = 113µm, V_{RPE} = 2.47, V_{cc} = 63 µm, OD_x = 0.01, R_{RPE} = 1.1%, S_{ch} = 5.8, S_{media} = 0.17 and t_{ch} = 334 µm. RMSE = 0.006

B) Parafoveal fit described by parameter values of V_{media} = 0.12, V_{mp} = 0, V_{me} = 0.04, V_{hb} = 144µm, V_{RPE} = 1.89, V_{cc} = 82µm, OD_x = 0.02, R_{RPE} = 2.4%, S_{ch} = 4.75, S_{media} = 0.12 and t_{ch} = 316µm. RMSE = 0.003

Table 8.5 Results for Model II. Showing group mean and standard deviation.

	Fovea	Parafovea
V_{media}	0.05 (±0.05)	0.13 (±0.03)
S_{media}	0.11 (±0.05)	0.09 (±0.03)
V_{mp}	0.08 (±0.06)	0.000 (±0.000)
R_{RPE} (%)	1.3 (±0.4)	2.6 (±0.88)
V_{RPE}	2.37 (±0.08)	1.60 (±0.36)
V_{cc} (µm)	54.8 (±41.8)	64.7 (±27.9)
V_{me}	1.38 (±1.71)	1.37 (±1.63)
V_{hb} (µm)	334.5 (±196.7)	355.3 (±247.7)
t_{ch} (µm)	176.6 (±128.0)	151.8 (±135.1)
S_{ch}	0.62 (±0.37)	0.45 (±0.028)
OD_x	1.91 (±1.75)	2.96 (±1.92)
RMSE	0.0046 (±0.0034)	0.0020 (±0.0014)

Model II (Delori and Pflibsen 1989) provided a convincing description of the retinal reflectance at both the foveal and parafoveal locations, with low group RMSE values of 0.0046 (±0.0034SD) and 0.0020 (±0.0014SD) respectively.

8.7. Discussion

Of the many ocular reflection models in the published literature (Ripps and Weale 1965; King-Smith 1973a; van Blokland and van Norren 1986; van de Kraats et al. 1996; Hammer and Schweitzer 2002; van de Kraats and van Norren 2008), only two were deemed appropriate for evaluation in this chapter (van Norren and Tiemeijer 1986; Delori and Pflibsen 1989).

Table 8.4 and Table 8.5 provide the returned parameter values and the RMSE values for both models. That both models returned such low RMSE values (0.0023 and 0.0020 for the parafoveal region for Models I and II, respectively) demonstrates their ability to describe the ocular reflection profile. The good visual fit (Figure 8.3 and Figure 8.4, Appendix H) provided by both models further corroborates this. Furthermore, the results in Table 8.4 are comparable with the data presented by both previous publications using this model, suggesting the model was implemented correctly (van Norren and Tiemeijer

1986; Delori and Pflibsen 1989). Similarly, the results in Table 8.5 present findings that are in close agreement with those of Delori and Pflibsen (1989) for many parameters. However, there are some differences in the parameters defining the choroidal layers and the additional stray light components. The experimental haemoglobin thickness is consistently thicker than that suggested by Delori and Pflibsen (1989), for example the mean modelled foveal choroidal thickness in this study was 334.5µm (±196.7), in comparison to 146µm (±42) as suggested by Delori and Pflibsen (Delori and Pflibsen 1989). Returned values for choroidal light loss, chorio-capillaries thickness and media scatter were all higher than those presented in Delori and Pflibsen (1989).

Based on a single equation (Equation 8.1), Model I proved straightforward to implement. Likewise, the application of Model II was relatively simple, despite the requirement for the simultaneous solution of the four equations (Equation 8.3, Equation 8.4, Equation 8.5 and Equation 8.6).

Of interest to these investigations is the value for V_{RPE}, which returns an estimation of reflections from all retinal layers. It is clear from both model fits that V_{RPE} reflections are higher for the parafoveal than the foveal regions. The results from Model I suggested that the retinal layers are twice as reflective in the parafoveal than foveal location at 1.6% (±0.3SD) and 0.8% (±0.1SD), respectively. It is noteworthy that Knighton et al (1989) have shown retinal reflectance in a macaque monkey to be 1.6% and 0.9%, with and without the RNFL layer respectively. That the difference in parafoveal and foveal reflectance produced in this modelling exercise is almost identical to the known reflectance of the RNFL layer is unlikely to be a coincidence. Despite the higher variation in the results, this difference is corroborated by Model II, with inner retinal reflectance values of 2.6% (±0.8SD) and of 1.3% (±0.4SD) at the parafovea and fovea, respectively.

The results from Model II show higher variation across the participants, for all variables. In particular, the variables describing the thickness of the

haemoglobin layers (V_{cc}, V_{hb} and t_{ch}) showed large inter-participant variation. The larger number of freely varying parameters in Model II is a likely culprit for this increased variability, for example, the additional light loss components in the crystalline lens and choroid (S_{media}, S_{ch} and OD_x). Using the Kubelka-Munk theory of reflectance, these components attempted to account for light scatted both forward and laterally outside the narrow field of view of the densitometer used in the original investigation (Delori and Pflibsen 1989). As the densitometer described in this thesis has a larger field than the region of interest, forward and lateral scattered light are less consequential in comparison to the back scattered light from reflective surfaces. In addition, the Kubelka-Munk theory of reflectance was developed to characterise paint film distribution and is known to break down if the absorbing and scattering media are not uniformly distributed through the media (Kubelka and Munk 1931). For these two reasons, it only provides a description of the complex choroidal absorbance and reflectance properties when illuminated with a spot device. Further, although the additional free parameters will facilitate an excellent fit, the parsimony of the model is compromised.

Both models provide a useful insight into the contribution of the various ocular layers and an excellent description of retinal reflectance. However, in their current format, neither quantifies inner retinal reflectance. This is particularly significant here because the ultimate aim is to quantify visual pigments (which were bleached in this study). Inner retinal reflections (i.e. those occurring before the photoreceptor outer segments) will reduce the contrast between the 'bleached' and dark-adapted retina thereby reducing the measured OD of the visual pigments. In both models, the contributions from the anterior and posterior retinal layers are combined to provide a single retinal reflective surface. Mathematical removal of this layer (V_{RPE}) will include the subtraction of a portion of light which *has* traversed the photoreceptor layer and a proportion which has not. Whilst both models could be adapted to include an additional inner reflective surface, Model II already contains many free parameters and the

introduction of an additional parameter would likely reduce the reliability of any fit. Model I, however, presents the opportunity to add a secondary reflective layer describing inner retinal reflectance whilst retaining a modest number of free parameters in the final model.

8.8. Summary

That the models presented here provide a very good description of bleached ocular reflectance from a narrow field densitometer is not in question. Despite the better fit of Model II to the experimental data, Model I was deemed the most appropriate for these investigations. This was due to both the increased inter-participant variation seen with Model II and the larger number (n = 11) of free parameters used, when compared to Model I (n = 6). Furthermore, isolation of the reflections from an inner retinal surface will require an additional parameter. The next chapter describes the modifications to Model I that were designed to facilitate the isolation of anterior reflections.

Chapter 9 - Development of a Novel Reflection Model

9.1. Introduction

Chapter 8 identified two ocular reflection models relevant to the analysis of data from the Mark II densitometer. Whilst the model proposed by Delori and Pflibsen (1989) provided an excellent fit to the experimental data, it was decided to use the model described by van Norren and Tiemeijer (1986) as it was simpler to implement and utilised fewer free parameters. With only 6 free parameters, this model still provided an excellent description of ocular reflectance, with lower inter-participant variability. The parameters returned plausible values, characterising the contribution of the optical media, macula pigment, melanin, haemoglobin, retinal reflectance and scleral reflectance. Crucially however, the model ignores reflections from the inner retina. This is significant because reflections from the inner retina (i.e. layers anterior to the photoreceptor outer segments) will diminish the measured optical density of the visual pigments.

Furthermore, more accurate descriptions of media absorption, choroidal density and human tissue scattering coefficients now exist (van de Kraats and van Norren 2007; van de Kraats and van Norren 2008; Jacques 2013).

By modifying the model presented by van Norren and Tiemeijer (1986) to include inner retinal reflectivity and by updating the spectral profile of the optical components, based on the latest literature, it may be possible to further improve the model.

9.2. Aims

1. To develop an ocular reflection model capable of isolating inner retinal reflectance.

2. To apply this model to the experimental data and extract information regarding pre-receptoral reflections.

3. To validate the model by comparing both the rod and cone spectra and the topographical maps, returned by the solution of the model, to those in the published literature.

9.3. Description of the 'modified' model

Model I, proposed by van Norren & Tiemeijer (1986) and discussed in Section 8.4.1, forms the basis of this modified ocular reflection model. A schematic describing the modified model is presented in Figure 9.1. The absolute reflectance of each ocular component is the product of the scattering properties of the tissue ($R_\chi(\lambda)$), the optical density of the media anterior to that tissue ($OD_\chi(\lambda)$) and a free fitting variable or scaling parameter (V_χ). During development of this model, the known properties of the different ocular absorbers and reflectors were reviewed and updated. A summary of the published data is provided in Section 9.3.1 and Section 9.3.2.

Equation 9.1 summarises the modified model and Appendix I details the wavelength-dependent parameters. Table 9.1 lists and defines the parameters used in the model,

$$R_{mod}(\lambda) = R_L(\lambda) + R_{R\,IN}(\lambda) + R_{R\,OUT}(\lambda) + R_S(\lambda)$$

(Equation 9.1).

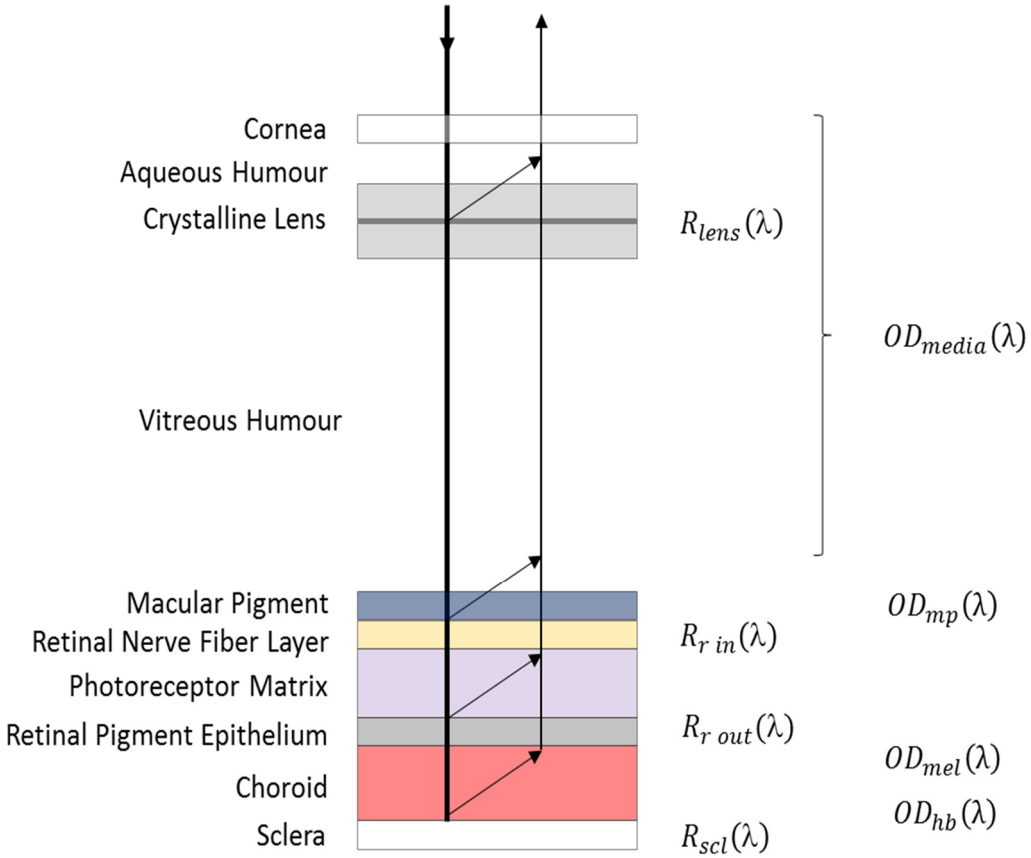

Figure 9.1 A representation of the modified model, designed to characterise ocular reflections based around the contribution of ocular tissues which absorb (denoted OD_{χ}) and reflect (denoted R_{χ}) light – where χ denotes the ocular component. A 'down' arrow represents the incident light, whilst the 'up' arrow represents the imaged light and 'diagonal' arrows represent the contribution from reflective surfaces. The coloured blocks represent the absorbing tissues (named on the left).

Table 9.1 Parameters used in the modified model

Parameter	Definition
$OD_{media}(\lambda)$	Spectral shape defining the light absorbed by the human ocular media. Data obtained from van de Kraats and van Norren (2007).
$OD_{mp}(\lambda)$	Spectral shape defining the light absorbed by human macula pigment. Data obtained from Snodderly et al. (1984).
$OD_{me}(\lambda)$	Spectral shape defining the light absorbed by human melanin. Data obtained from Gabel (1978).
$OD_{hb}(\lambda)$	Spectral shape defining the light absorbed by the haemoglobin present in the choroid (haemoglobin assumed to be 95% oxygenated). Data obtained from van Assendelft (1970).
$R_{lens}(\lambda)$	Spectral shape defining the light reflected from the crystalline lens. Defined by a Rayleigh scattering function (see Chapter 6).
$R_{r\ in}(\lambda)$	Spectral shape defining the light reflected by the inner retinal reflections. Defined by Mie scattering curve (Jacques 2013) as an approximation of the data presented by Knighton (1989).
$V_{r\ out}$*†	Wavelength independent reflections from the outer retinal layers.
$R_{scl}(\lambda)$	Wavelength dependent reflections from the sclera. Defined by
V_{lens}*†	Scaling factor for the crystalline lens.
$V_{r\ in}$*	Scaling factor for the inner retinal reflections.
V_{media}*	Scaling factor for the lens reflection.
V_{mp}§	Scaling factor for macula pigment absorption. defined by Equation 9.4
V_{me}*	Scaling factor for melanin absorption.
V_{hb}*	Scaling factor for the thickness (μm) of the haemoglobin layer within the choroid.
V_{scl}*	Scaling factor for the scleral reflection.
age	The age of the participant, used to define the absorption of light by the ocular media.
R_{mod}	The modelled ocular reflection, as defined by the solution to Equation 9.14
$R_L(\lambda)$	The total amount of light returned from the crystalline lens. Defined in (Equation 9.8
$R_{R\ IN}(\lambda)$	The total amount of light returned from the inner retinal layers. Defined in Equation 9.10
$R_{R\ OUT}(\lambda)$	The total amount of light returned from the outer retinal layers. Defined in (Equation 9.11
$R_S(\lambda)$	The total amount of light returned from the sclera. Defined in Equation 9.13

*variable parameter, † Fixed at foveal value for parafoveal fit § pre-calculated

9.3.1. Ocular absorbers

9.3.1.1. Ocular media

The combined density of the ocular media (cornea, aqueous humour, crystalline lens and vitreous humour) is significant and varies with age (Section 1.5.1). The most authoritative publication on this is perhaps van de Kraats & van Norren (2007). Their model incorporates the optical density of the cornea, aqueous, crystalline lens and vitreous, based on 5 spectral templates: 'Rayleigh losses', 'tryptophan', 'lens young', 'lens old UV' and 'lens old'. Tryptophan is only significant at wavelengths shorter than 300nm and is not relevant to this study. An adjusted model (Figure 9.2), removing the tryptophan component is described by Equation 9.2 (van de Kraats and van Norren 2007). Whilst the model is age-dependent, it is not capable of describing cataract. The participants' age is required to solve Equation 9.2,

$$OD_{media}(\lambda) = d_{RL}(age) \cdot M_{RL}(\lambda) + d_{LY}(age) \cdot M_{LY}(\lambda) + d_{LOUV}(age) \cdot M_{LOUV}(\lambda) + d_{LO}(age) \cdot M_{LO}(\lambda) + d_{neutral}$$

(Equation 9.2).

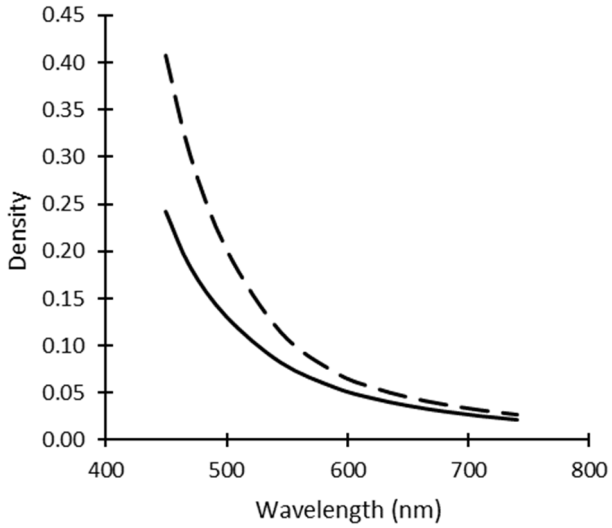

Figure 9.2 Presents the absorption profile of the ocular media for the youngest participant (age 28, solid) and oldest participant (age 52, dashed) imaged in this study, defined by Equation 9.2.

9.3.1.2. Macular pigment

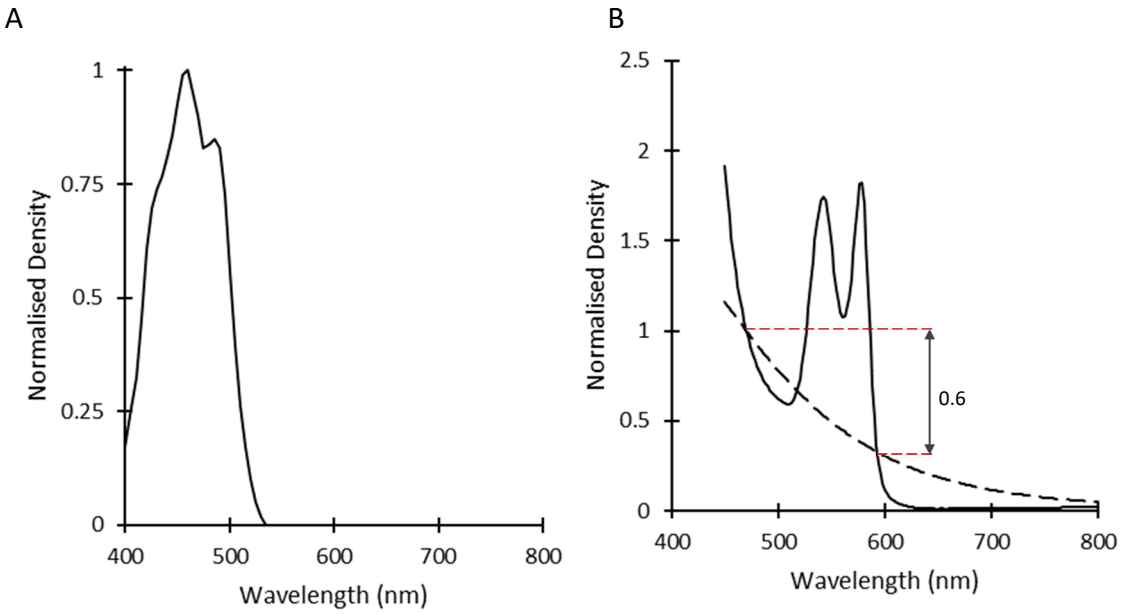

Figure 9.3 A) The absorption spectrum for macula pigment, normalised to peak wavelength (460nm) (Snodderly et al. 1984). B) the absorption spectra of haemoglobin (solid line, (van Assendelft 1970)) and melanin (dashed line (Gabel et al. 1978)). By normalising both components to 470nm, the relative decrease in density of both pigments between 470nm and 590nm is 0.6.

Macula pigment is a short wavelength absorbing layer, present across the central 6° and peaking across the central 2° of the retina (Snodderly et al. 1984; Kilbride et al. 1989). Equation 9.3 can be used to quantify the maximum optical density of macula pigment (Kilbride et al. 1989),

$$MP = \left[log\left(\frac{1}{R_{470}}\right) - 0.6 \cdot log\left(\frac{1}{R_{590}}\right)\right]$$

(Equation 9.3),

where MP is the maximum optical density of macular pigment at peak absorption and R_{470} and R_{590} define the reflectivity of the fovea at the wavelengths 470nm and 590nm, respectively. The wavelengths of 470nm and 590nm were chosen for two reasons. Firstly, 470nm lies near the peak of macula pigment absorption, whereas macular pigment does not absorb light at 590nm (Figure 9.3A). Secondly, melanin and haemoglobin show a relative change in

optical density between these two wavelengths. The value of 0.6 equates to the normalised decrease in melanin and haemoglobin optical density over this spectral range (Figure 9.3B).

For the topographical fitting of the model, described by Equation 9.16, the variable $V_{mp}(x, y)$ was defined by the Gaussian shape described by Equation 9.4, as suggested by Kilbride et al (1989),

$$V_{mp}(x, y) = e^{-\left(\frac{(x-x_{fovea})^2}{2 \cdot w^2} - \frac{(y-y_{fovea})^2}{2 \cdot h^2}\right)} \cdot MP$$

(Equation 9.4),

where $V_{mp}(x, y)$ is the density of macula pigment at any pixel, MP is macular pigment density (as calculated by Equation 9.3), x and y are the pixel locations and w and h represent the FWHM of the width and height of the Gaussian function (in pixels).

9.3.1.3. Melanin

Melanin has a peak absorbance at 335nm and, although decreasing to near-transparency at the far infra-red, it is a strong absorber throughout the visual spectrum (Gabel et al. 1978), as seen in Figure 9.4. Equation 9.5 presents a polynomial function fitted to the data provided by Gabel et al (1978) using a least squares optimisation algorithm (Solver, Excel), allowing interpolation to 2nm (Figure 9.4),

$$OD_{me}(\lambda) = -3.42E^{-8} \cdot \lambda^3 + 7.13E^{-5} \cdot \lambda^2 + 0.05 \cdot \lambda + 12.69$$

(Equation 9.5).

Melanin is present posterior to the retinal layers, in the RPE, choroid and sclera where it acts as a light absorber, reducing intra-ocular scatter (Weiter et al. 1986). There is significant topographical variation; choroidal melanin concentration increases from the posterior pole to the periphery, whilst RPE

melanin concentration decreases (Weiter et al. 1986). Overall, the greatest concentration of melanin is present in the macular region (Weiter et al. 1986). As melanin in the deeper ocular layers is not replaced, a decline in density with age is seen (Weiter et al. 1986). For simplicity, a single layer represents the combined RPE and choroidal melanin absorption. Absorption by scleral melanin is likely to be negligible and thus not included in the model.

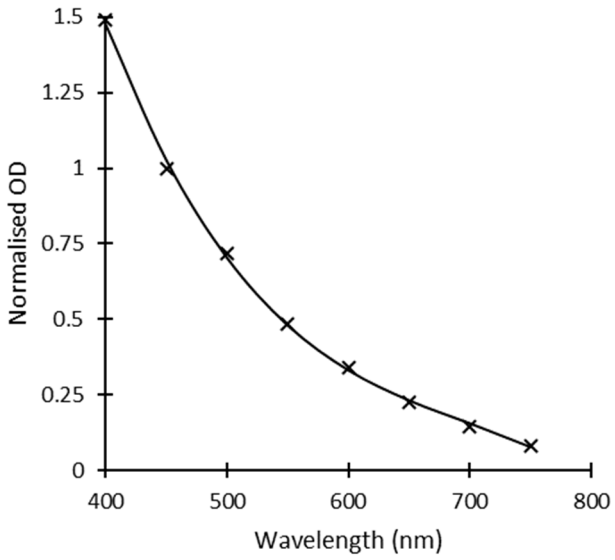

Figure 9.4 Melanin absorption spectrum (solid line), modelled using Equation 9.5 to estimate melanin as published by Gabel (crosses (1978)). Both normalised to 450nm.

9.3.1.4. Haemoglobin

The absorption spectrum of haemoglobin varies between 250nm and 600nm, furthermore, the absorption spectrum differs for oxygenated and deoxygenated blood. Blood in both the inner retinal and choroidal circulations is generally assumed to be 95% oxygenated (van de Kraats et al. 1996).

Regarding the non-uniform distribution of the choroidal vascular system along the incident light path, the solution proposed by van de Kraats and van Norren (2008) to correct for the Beer-Lambert law was adopted in the model and shown in (Equation 9.6,

$$OD_{hb}(\lambda) = -0.01 \cdot log\left[\frac{\left(1 - 10^{OD_{hb_{100}(\lambda)}}\right)}{\left(OD_{hb_{100}}(\lambda) \cdot ln\,10\right)}\right]$$

(Equation 9.6),

where $OD_{hb}(\lambda)$, shown in Figure 9.5, is the density of 95% oxygenated haemoglobin layer with a thickness of 1µm, corrected for the variety of path lengths through the choriocapillaris and vascular lakes within the choroid. $OD_{hb_{100}}(\lambda)$ is density of a 95% oxygenated haemoglobin layer with a thickness of 100µm, taken from van Assendelft (1970).

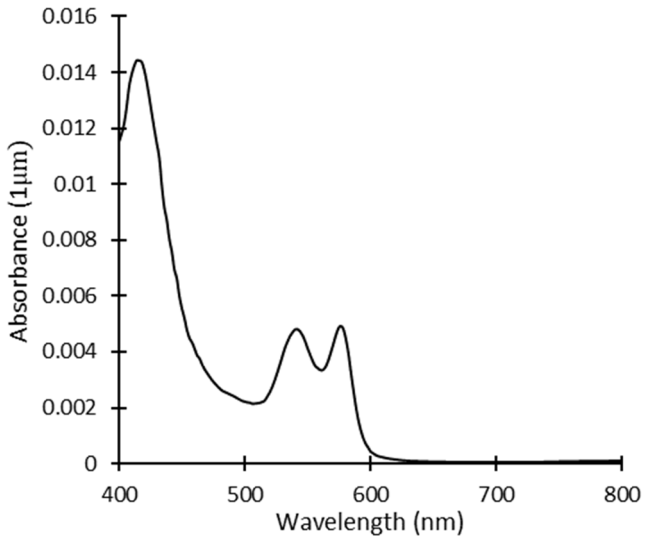

Figure 9.5 The absorbance of 95% oxygenated haemoglobin, calculated for a 'blood wedge' ((Equation 9.6) with a path length of 1µm.

9.3.2. Ocular reflectors

9.3.2.1. Crystalline lens

Whilst reflections from the lens are anticipated to be modest, this layer will provide a considerable proportion of the returned light below 590nm. Acting as a diffuse light source within the crystalline lens, this reflection is thought to be spatially uniform across the image. As discussed in Chapter 6, Rayleigh scattering (

(Equation 9.7) provides a good description of back scattered light from the crystalline lens ($R_{lens}(\lambda)$),

$$R_{lens}(\lambda) = \left(\frac{450}{\lambda}\right)^4$$

(Equation 9.7).

To simplify the handling of reflections from the lens, it was assumed that they originate from a single surface positioned at half depth in the ocular med2a, as shown in Figure 9.1. Hence, the total contribution from the lens ($R_L(\lambda)$) is calculated according to (Equation 9.8,

$$R_L(\lambda) = R_{lens}(\lambda) \cdot 10^{-(OD_{media}(\lambda))} \cdot V_{lens}$$

(Equation 9.8).

9.3.2.2. Inner retina

Knighton et al. (1989) provide spectral reflectivity data for the RNFL (Figure 9.6) and Equation 9.9 provides the Mie scattering function proposed by Jacques (2013),

$$R_{r\,in}(\lambda) = 1.05 \cdot \left\{\left[0.32 \cdot \left(\frac{\lambda}{450}\right)\right]^{-4} + \left[0.68 \cdot \left(\frac{\lambda}{450}\right)\right]^{-1.07}\right\}$$

(Equation 9.9).

It can be seen form Figure 9.6 that this function provides a relatively good description of RNFL reflectance data (Knighton et al. 1989).

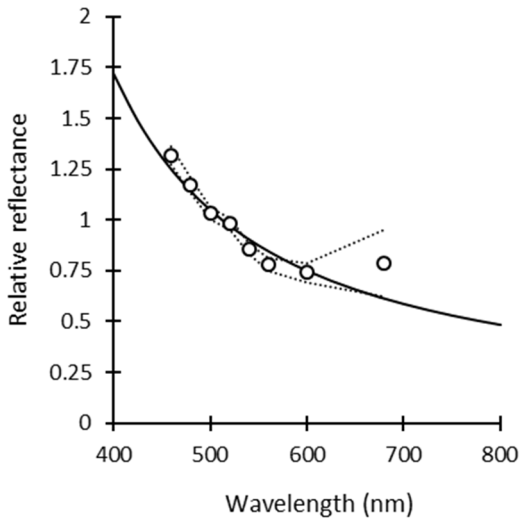

Figure 9.6 The Mie scattering function for brain tissue (solid line, Equation 9.9) provides a good description of the published RNFL reflectance data (open circles, ±1SD) (Knighton et al. 1989).

The reflective surface of the inner retinal component was positioned posterior to the macular pigment layer. Equation 9.10 defines the contribution of the inner retinal layers ($R_{r\,in}(\lambda)$),

$$R_{R\,IN}(\lambda) = R_{r\,in}(\lambda) \cdot 10^{-[2\cdot(OD_{media}(\lambda)+OD_{mp}(\lambda)\cdot V_{mp})]} \cdot V_{r\,in}$$

(Equation 9.10),

where, $R_{r\,in}(\lambda)$ is a Mie scattering function (Jacques 2013), based on the scattering properties of brain tissue and $V_{r\,in}$ is a free scaling variable.

9.3.2.3. Outer retina

In accordance with previous reflection models, reflections from the RPE were assumed to be wavelength-independent (Delori and Pflibsen 1989; van de Kraats et al. 1996; van de Kraats and van Norren 2008). Due to the positioning of the reflective surface at the photoreceptor/RPE junction, the melanin content in the RPE does not impact on the reflectance. (Equation 9.11 defines the contribution from the outer retinal layers ($R_{r\,out}(\lambda)$),

$$R_{R\,OUT}(\lambda) = 10^{-[2\cdot(OD_{media}(\lambda)+OD_{mp}(\lambda)\cdot V_{mp})]} \cdot V_{r\,out}$$

(Equation 9.11).

The positioning of the illumination annulus and imaging beam in the densitometer used in this thesis minimised the Stiles-Crawford effect. Hence, direct reflections from the photoreceptors were assumed to be negligible.

9.3.2.4. Sclera

As the sclera is comprised of large diameter collagen fibres (30-300µm) (Bailey 1987), the reflectance profile is also likely to be dominated by Mie scattering (Jacques 2013). Figure 9.7 shows that the Mie scattering function, described by

, provides a good description for scleral reflectance (Bashkatov et al. 2009),

$$R_{scl}(\lambda) = 0.7 \cdot \left\{\left[0.33 \cdot \left(\frac{\lambda}{400}\right)\right]^{-4} + \left[0.83 \cdot \left(\frac{\lambda}{400}\right)\right]^{0.83}\right\}$$

(Equation 9.12).

The sclera is the most posterior reflective surface in the model. As such, all the absorbing layers described will impact on the contribution from the sclera. Equation 9.13 describes the total scleral contribution to the model,

$$R_S(\lambda) = R_{scl}(\lambda) \cdot 10^{-[2\cdot OD_{media}(\lambda)+(OD_{mp}(\lambda)\cdot V_{mp})+(OD_{hb}(\lambda)\cdot V_{hb})+(OD_{me}(\lambda)\cdot V_{me})]} \cdot V_{scl}$$

(Equation 9.13).

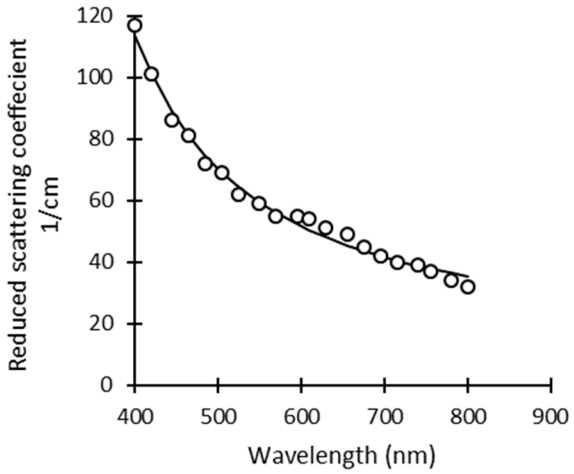

Figure 9.7 The Mie scattering function (solid line,
) fitted to published scleral reflectance data (open circles) (Bashkatov et al. 2009).

9.3.3. The model summarised

In summary, in developing this model it was assumed the eye contains 4 wavelength dependent absorbing filters ($OD_{media}(\lambda)$, OD_{mp}, $OD_{hb}(\lambda)$ and $OD_{me}(\lambda)$), 3 wavelength dependent reflecting surfaces ($R_{lens}(\lambda)$, $R_{r\ in}(\lambda)$ and $R_{scl}(\lambda)$) and a single wavelength independent reflecting surface ($V_{r\ out}(\lambda)$).

Equation 9.1 was expanded to Equation 9.14, where the 6 free variables are V_{lens}, $V_{r\ in}$, $V_{r\ out}$, V_{hb}, V_{me}, V_{scl},

$$
\begin{aligned}
R_{mod}(\lambda) = &\left\{R_{lens}(\lambda)\cdot 10^{-\left(OD_{media}(\lambda)\right)}\cdot V_{lens}\right\} \\
&+\left\{R_{r\ in}(\lambda)\cdot 10^{-\left[2\cdot OD_{media}(\lambda)+\left(OD_{mp}(\lambda)\cdot V_{mp}\right)\right]}\cdot V_{r\ in}\right\} \\
&+\left\{V_{r\ out}\cdot 10^{-\left[2\cdot OD_{media}(\lambda)+\left(OD_{mp}(\lambda)\cdot V_{mp}\right)\right]}\right\} \\
&+\left\{R_{scl}(\lambda)\right. \\
&\left.\cdot 10^{-\left[2\cdot OD_{media}(\lambda)+\left(OD_{mp}(\lambda)\cdot V_{mp}\right)+\left(OD_{hb}(\lambda)\cdot V_{hb}\right)+\left(OD_{me}(\lambda)\cdot V_{me}\right)\right]}\cdot V_{scl}\right\}
\end{aligned}
$$

(Equation 9.14).

The modelling of ocular reflections across the retina required a robust model, with minimal free fitting parameters. By aligning the fitting routine with known retinal anatomy, the number of free parameters could be reduced as follows.

Firstly, it was assumed reflections from the inner retinal surface were negligible in the foveal pit where the inner retina is laterally displaced. Secondly, it was assumed that macular pigment follows the Gaussian distribution described in Equation 9.4 and is negligible in the peripheral retina. Thus, a two-stage fitting process was adopted, with (Equation 9.15 and Equation 9.16 representing ocular reflections from the fovea and parafovea, respectively. Initially, the parameter values for the lens (V_{lens}) and outer retinal reflectance ($V_{r\ out}$) were solved using (Equation 9.15 to fit foveal data, and then input as fixed parameters into Equation 9.16 to provide a model fit for the parafoveal data,

$$
\begin{aligned}
R_{mod}(fovea,\lambda) \\
&= \left\{R_{lens}(\lambda)\cdot 10^{-\left(OD_{media}(\lambda)\right)}\cdot V_{lens}\right\} \\
&+ \left\{V_{r\ out}\cdot 10^{-\left(2\cdot OD_{media}(\lambda)+\left(OD_{mp}(\lambda)\cdot V_{mp}\right)\right)}\right\} \\
&+ \left\{R_{scl}(\lambda)\right. \\
&\cdot 10^{-\left\{2\cdot OD_{media}(\lambda)+\left(OD_{mp}(\lambda)\cdot V_{mp}\right)+\left(OD_{haem}(\lambda)\cdot V_{haem}\right)+\left(OD_{mel}(\lambda)\cdot V_{mel}\right)\right\}} \\
&\left.\cdot V_{scl}\right\}
\end{aligned}
$$

(Equation 9.15),

$$
\begin{aligned}
R_{mod}(x,y,\lambda) &= \left\{R_{lens}(\lambda)\cdot 10^{-\left(OD_{media}(\lambda)\right)}\cdot V_{lens}\right\} \\
&+ \left\{R_{r\ in}(\lambda)\cdot 10^{-\left(2\cdot OD_{media}(\lambda)\right)}\cdot V_{r\ in}\right\} \\
&+ \left\{R_{r\ out}\cdot 10^{-\left(2\cdot OD_{media}(\lambda)\right)}\right\} \\
&+ \left\{R_{sclera}(\lambda)\cdot 10^{-\left\{2\cdot OD_{media}(\lambda)+\left(OD_{haem}(\lambda)\cdot V_{haem}\right)+\left(OD_{mel}(\lambda)\cdot V_{mel}\right)\right\}}\right. \\
&\left.\cdot V_{scl}\right\}
\end{aligned}
$$

(Equation 9.16).

Having defined the modified reflection model, the next step was to fit it to data collected from the densitometer.

9.4. Methods

The participants, hardware, data collection and ocular reflectance calibration used for the investigations in this chapter have been described in Sections 8.5.1 to 8.5.3.

9.4.1. Data analysis

Equation 9.3 (Kilbride et al. 1989) was used to calculate the density of macular pigment (V_{mp}) at the fovea of each participant**.**

9.4.1.1. Model fitting at two discrete retinal locations

A least squares optimisation algorithm (Solver function, Excel) was used to solve (Equation 9.15 against the experimental reflectance from the foveal location, returning values for V_{lens}, $V_{r\ out}$, V_{hb}, V_{me}, V_{scl} at the foveal location only. A secondary fit was used to solve Equation 9.16 using the same algorithm and the foveal values for $V_{r\ out}$ and V_{lens} and provided the values of $V_{r\ in}$, V_{hb}, V_{me}, V_{scl} at the parafoveal location defined in Section 3.5.2 (Chapter 3).

9.4.1.2. Isolation of anterior stray light

Following the solution of Equation 9.16,

was used to calculate the component $R_{ant}(\lambda, x, y)$, which represents the anterior reflections, i.e. the combined contribution of crystalline lens ((Equation 9.8) and inner retinal reflectance (Equation 9.10) to the measured reflectance at any location within the image,

$$R_{ant}(\lambda, x, y) = R_{LENS}(\lambda, x, y) + R_{R\ IN}(\lambda, x, y)$$

(Equation 9.17).

9.4.1.3. Spectral investigation

Having quantified reflections anterior to the photoreceptor outer segments it was possible to quantify the optical density of the visual pigments with greater accuracy, these spectra were subsequently utilised in the topographical investigation (Section 9.4.1.4).

calculates the adjusted optical density ($R_{ant}(x, y, \lambda)$) of the visual pigments at each retinal location using both bleached ($R_b(x, y, \lambda)$) and dark-adapted ($R_d(x, y, \lambda)$) experimental reflectance data together with subtraction of anterior reflections,

$$\Delta OD_{adj}(x, y, \lambda) = log\left[\frac{S_B(x, y, \lambda) - R_{ant}(x, y, \lambda)}{S_{DA}(x, y, \lambda) - R_{ant}(x, y, \lambda)}\right]$$

(Equation 9.18).

9.4.1.4. Topographical investigation

To determine the topographical distribution of rod and cone photoreceptors across the central retina, Equation 9.16 was implemented in MATLAB (2016b, MathWorks Inc, Massachusetts), using the *lsqcurvefit* function and the Trust Region Reflective algorithm, to fit the experimental, bleached, reflection data (x, y) for all 5 participants at all retinal locations. The Trust Region Reflective algorithm is a non-linear optimisation function, capable of handling large-scale bound-constrained minimisation problems (Coleman and Li 1994) and allowed control over the starting points of the algorithm. Appendix K presents all the MATLAB code written for this chapter. The solutions for $V_{r\ out}$ and V_{lens} from (Equation 9.15 were assumed true and constrained to these values for the subsequent fitting routine.

By solving Equation 9.16, the topographical distribution of the inner retinal and scleral reflections, melanin density and choroidal thickness were obtained across the central 30°. Having quantified the anterior reflections on a pixel by pixel basis across the retina, it was possible to use

to quantify the adjusted optical density of the visual pigments at each retinal location.

Equation 4.2 (repeated here, for details see Section 4.5.1, Chapter 4) was solved for all retinal locations, returning the optical density of rhodopsin and cone visual pigments present at each retinal location, immediately following bleach cessation (Kilbride and Keehan 1990),

$$\Delta OD(\lambda, x, y) = OD_r(x, y) \cdot N_r(\lambda) + OD_c(x, y) \cdot N_c(\lambda)$$

(Equation 4.2).

Where $N_r(\lambda)$ and $N_c(\lambda)$ are the normalised rod and cone spectra. The coefficients $OD_r(x, y)$ and $OD_c(x, y)$ define the optical density of the rod and cone pigment present at each retinal location. Equation 4.2 was solved for each retinal location (x, y). As starting points weren't required, the faster *fminsearch* least squares optimisation function in MATLAB (2016b, MathWorks Inc, Massachusetts) was used. This provided the optical density distribution of both rod and cone photopigments across the central 30°. Equation 4.2 was applied to the data twice, for different rod and cone spectra. The initial fitting routine used the known *in vitro* rod and cone spectra in the place of $N_r(\lambda)$ and $N_c(\lambda)$ (Dartnall et al. 1983). The second fitting routine replaced $N_r(\lambda)$ and $N_c(\lambda)$ with the experimental spectra obtained from this data (as presented in Figure 9.11). This is the approach described by Kilbride and Keehan (1990) in their attempt to model visual pigment isolation (Figure 9.25).

To facilitate comparison with previously published photoreceptor density distributions (Curcio et al. 1987; Kilbride and Keehan 1990), a central 1° x 30° horizontal section was extracted for the rod $OD_r(x, y)$ and cone $OD_c(x, y)$ photopigment optical density from each participant.

9.5. Results

9.5.1. Isolation of anterior stray light

Figure 9.8 shows example model fits for foveal ((Equation 9.15) and parafoveal (Equation 9.16) experimental data from participant TM, with Table 9.2 presenting the mean data from all participants. Appendix J presents individual model fits for all participants.

For both retinal locations, the modified model provided a good visual fit for the data, with low RMSE values; 0.0068 (±0.0032) and 0.0026 (±0.0019) for the fovea and parafovea, respectively. V_{hb} was higher at the parafoveal location. The scleral reflectance (V_{scl}) presented an interesting value, with a mean scleral reflectance of 111.63% (±38SD) at the foveal location and a more reasonable 77.99% (±27SD) in the parafoveal location. Appendix J provides the individual model fits for all participants.

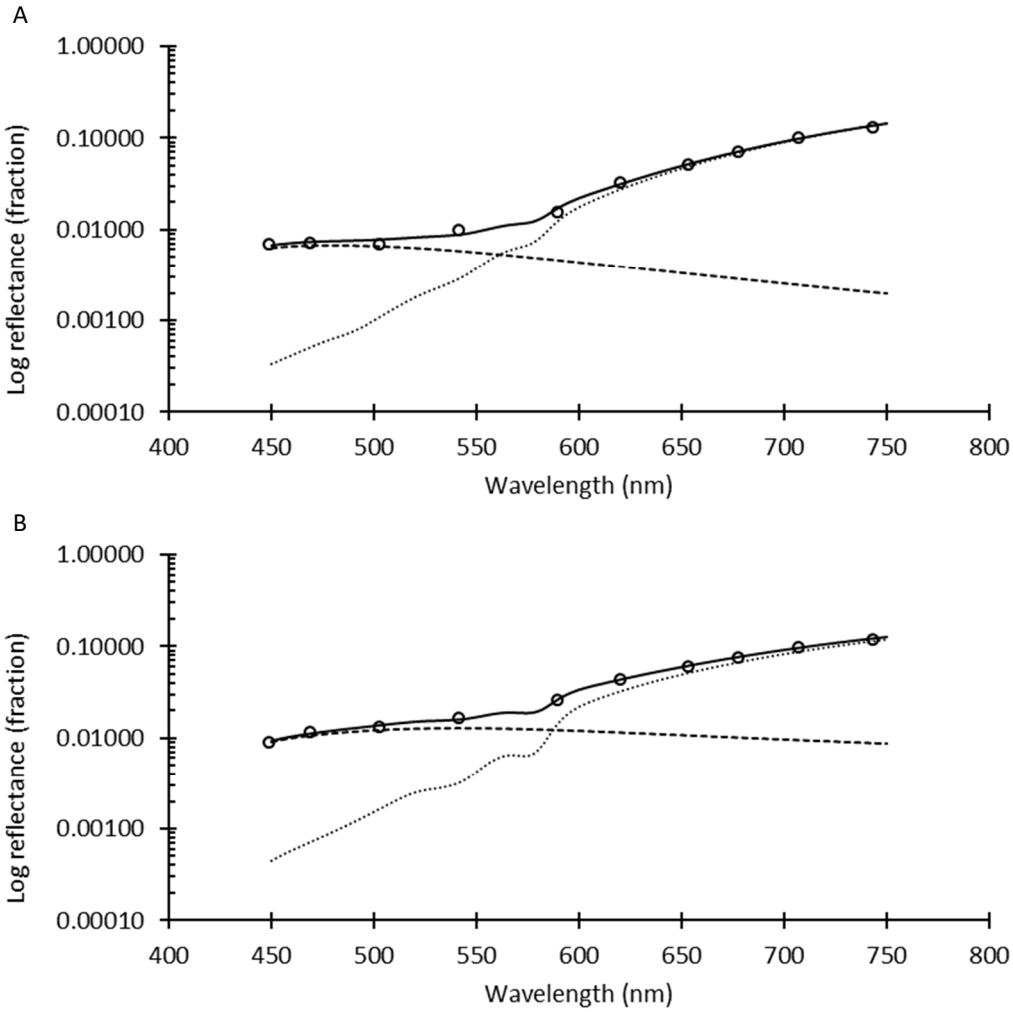

Figure 9.8 Result of the 'modified' model fit for participant TM at two locations. Solid lines represent the model fit, dashed line the contributions from the anterior reflections (lens and inner retina) and the dotted line contributions from the deeper reflections (outer retina and sclera). Spectral data for the model interpolated with 2nm precision.

A) Foveal fit of (Equation 9.15 described by parameter values of: age = 52, V_{lens} = 1.61%, V_{mp} = 0.06, $V_{r\ in}$ = 0%, $V_{r\ out}$ = 0.28%, V_{hb} = 21µm, V_{me} = 2.17 and V_{scl} = 72%. RMSE = 0.0023

B) Parafoveal fit of Equation 9.16 described by parameter values of: age = 52, V_{lens} = 1.61%, V_{mp} = 0.00, $V_{r\ in}$ = 1.62%, $V_{r\ out}$ = 0.28%, V_{hb} = 41µm, V_{me} = 1.64 and V_{scl} = 42% RMSE = 0.0003

Table 9.2 Parameter results for the modified model. Showing group mean and standard deviation.

	Fovea	Parafovea
V_{lens} (%)	0.59 (±0.62)	0.59 (±0.62) †
V_{mp}	0.05 (±0.05) §	0.00 (±0.00) *
$V_{r\ in}$ (%)	0.00 (±0.00) *	1.20 (±0.30)
$V_{r\ out}$ (%)	0.90 (±0.39)	0.90 (±0.39) †
V_{hb} (µm)	140 (±84)	153 (±69)
V_{mel}	2.15 (±0.38)	1.64 (±0.31)
V_{scl} (%)	111.63 (±38.22)	77.99 (±27.20)
RMSE	0.0068 (±0.0032)	0.0026 (±0.0019)

*Fixed at 0.00 for fit, † Fixed at foveal value for fit § pre-calculated

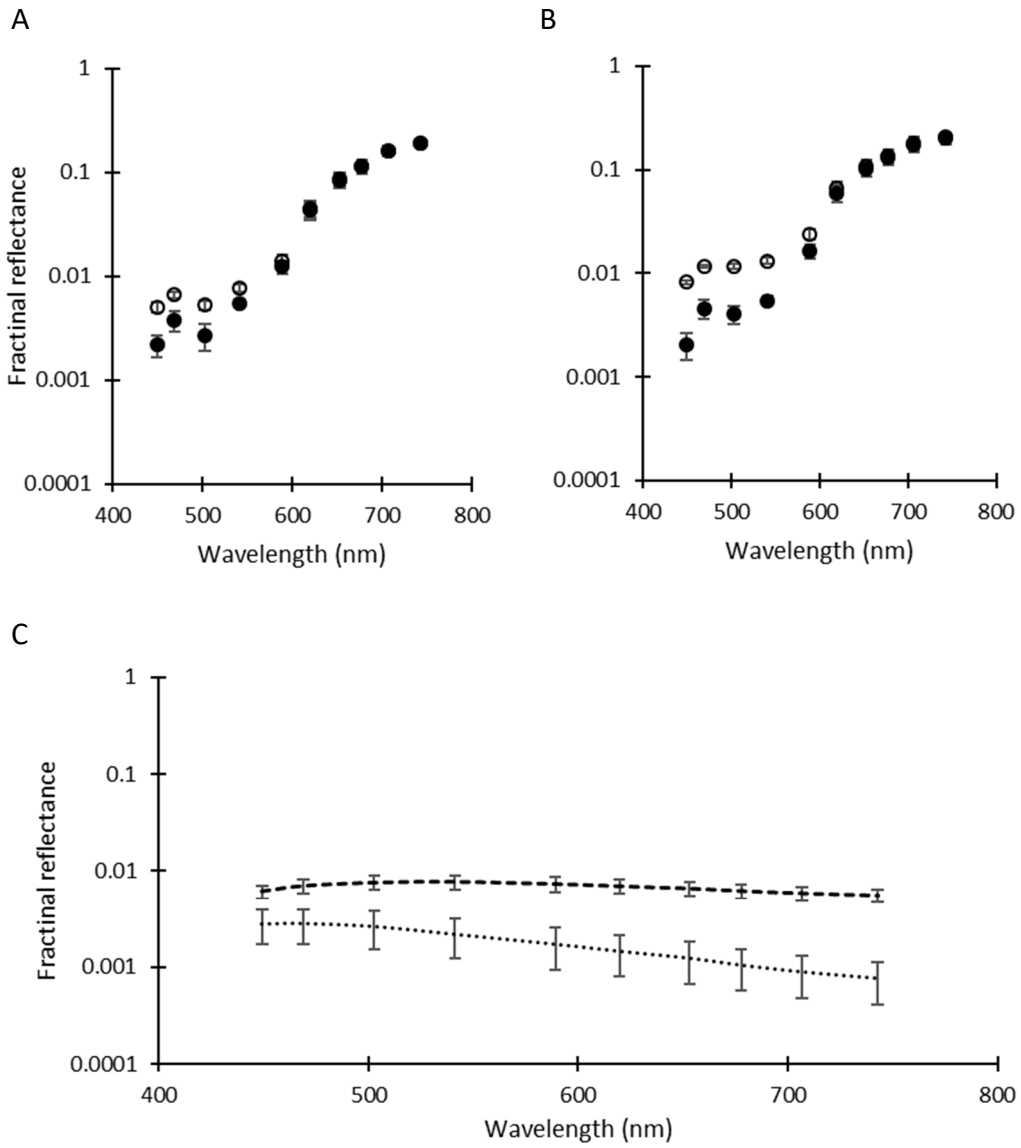

Figure 9.9 Comparing unadjusted reflectance (open circles) to the anterior stray light adjusted reflectance (filled circles) for a bleached retina. A) shows the foveal data B) the parafoveal data and C) the measured anterior stray light at the fovea (dotted) and parafovea (dashed). Data are the mean of 5 participants. Error bars show SEM.

Figure 9.9 shows the adjusted and unadjusted retinal reflectance measured alongside the calculated anterior stray light, for both foveal and parafoveal locations (

). Subtraction of the anterior stray light had a negligible effect above 620nm, but a substantial effect between 450-590nm. The parafoveal data showed a larger reduction in reflectance than the foveal data due to the substantial differences in the inner retinal reflection (Figure 9.9C) at the two locations.

9.5.2. Spectral investigation

Figure 9.10 presents the adjusted and unadjusted foveal and parafoveal absorption spectra. The adjusted foveal ΔOD (Figure 9.10A) peaked at 0.34 at 545nm, an increase from 0.11 at 590nm for the unadjusted data. The adjusted foveal spectrum showed a small short wavelength shift in comparison to the unadjusted spectrum. The change at 450nm showed the largest increase from 0.02 to 0.20. The effect of removing the anterior stray light component from the parafoveal region (Figure 9.10B) had similar effects, with an increase in ΔOD from a peak of 0.10 at 545nm to 0.31 at 500nm. That the peak OD changed from 545nm to 500nm represents a significant short wavelength shift in the spectrum at the parafovea. The large error bars surrounding the 500nm point (Figure 9.10A) are the result of a high value for participant AW and a low value for participant HM.

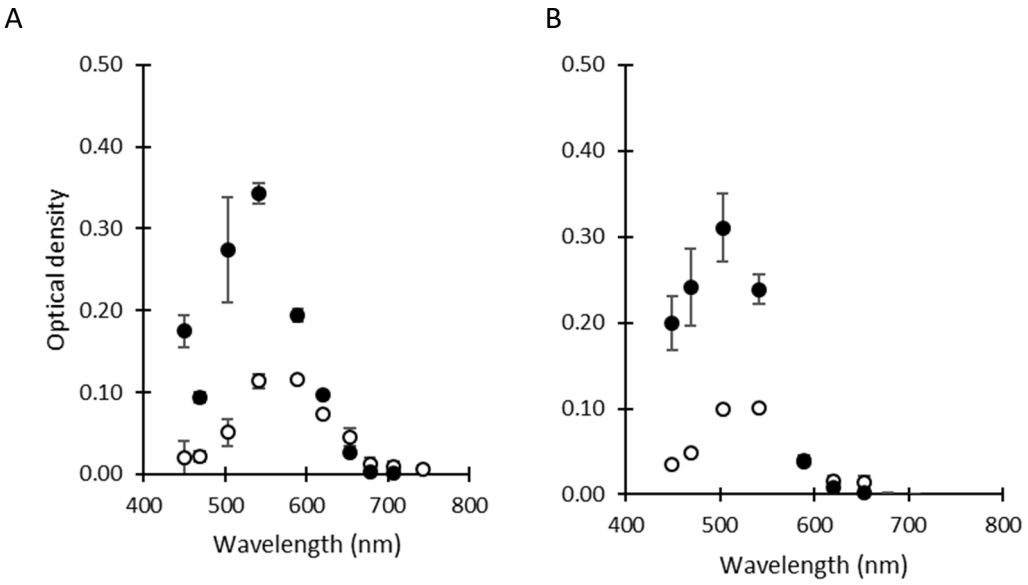

Figure 9.10 The unadjusted (open circles) and adjusted (filled circles) absorption spectra measured at the foveal (A, data are the mean of 4 colour normal participants) and parafoveal (B, data are the mean of all 5 participants) locations. All error bars represent SEM.

Figure 9.11 shows the normalised adjusted absorption spectra together with *in vitro* visual pigment spectra (Dartnall et al. 1983). The spectral shift seen at the parafoveal location (blue circles) shows an improved alignment with the *in vitro*

data for rods (blue dotted line) (Dartnall et al. 1983). The adjusted foveal spectrum (orange circles) is a reasonable match to the *in vitro* M- and L- cone data, lying somewhere in between the two pigment types, albeit closer to the M- cone spectrum.

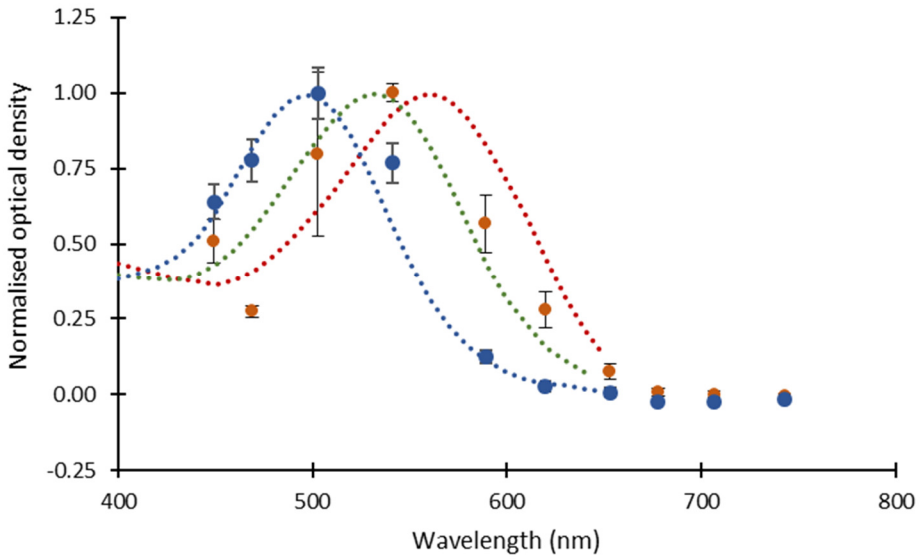

Figure 9.11 displays the adjusted absorption spectra for the group mean for the parafoveal region (blue) and the group mean for the four colour normal participants in the foveal region (orange) with standard error bars. The dotted lines represent the *in vitro* spectra for rhodopsin, M- and L-cones (blue, green, red) (Dartnall et al. 1983).

9.5.3. Topographical investigation

Figure 9.12 to Figure 9.16 display the topographical solution to Equation 9.16, providing maps of inner retinal reflectivity, haemoglobin thickness, melanin density and scleral reflectivity for all participants. As visual aids, the topographical maps provide a simple means of evaluating the data, across all participants. The inner retinal reflectivity maps all show a central dip, with reflections from this layer increasing with eccentricity from the fovea and proximity to the optic nerve head. Reflectivity is approximately 3 times greater surrounding the optic nerve head than at the fovea. Melanin density is relatively uniform in the peripheral locations, with all participants showing a broad central peak. Scleral reflectivity follows a similar pattern to melanin density for all participants, with a uniform peripheral reflectivity and a central peak.

Haemoglobin thickness showed little topographical variation, although in some participants visualisation of a choroidal tigroid like pattern was possible (Figure 9.13). Haemoglobin thickness showed the largest inter-participant variation with a range of ~80µm to ~1200µm.

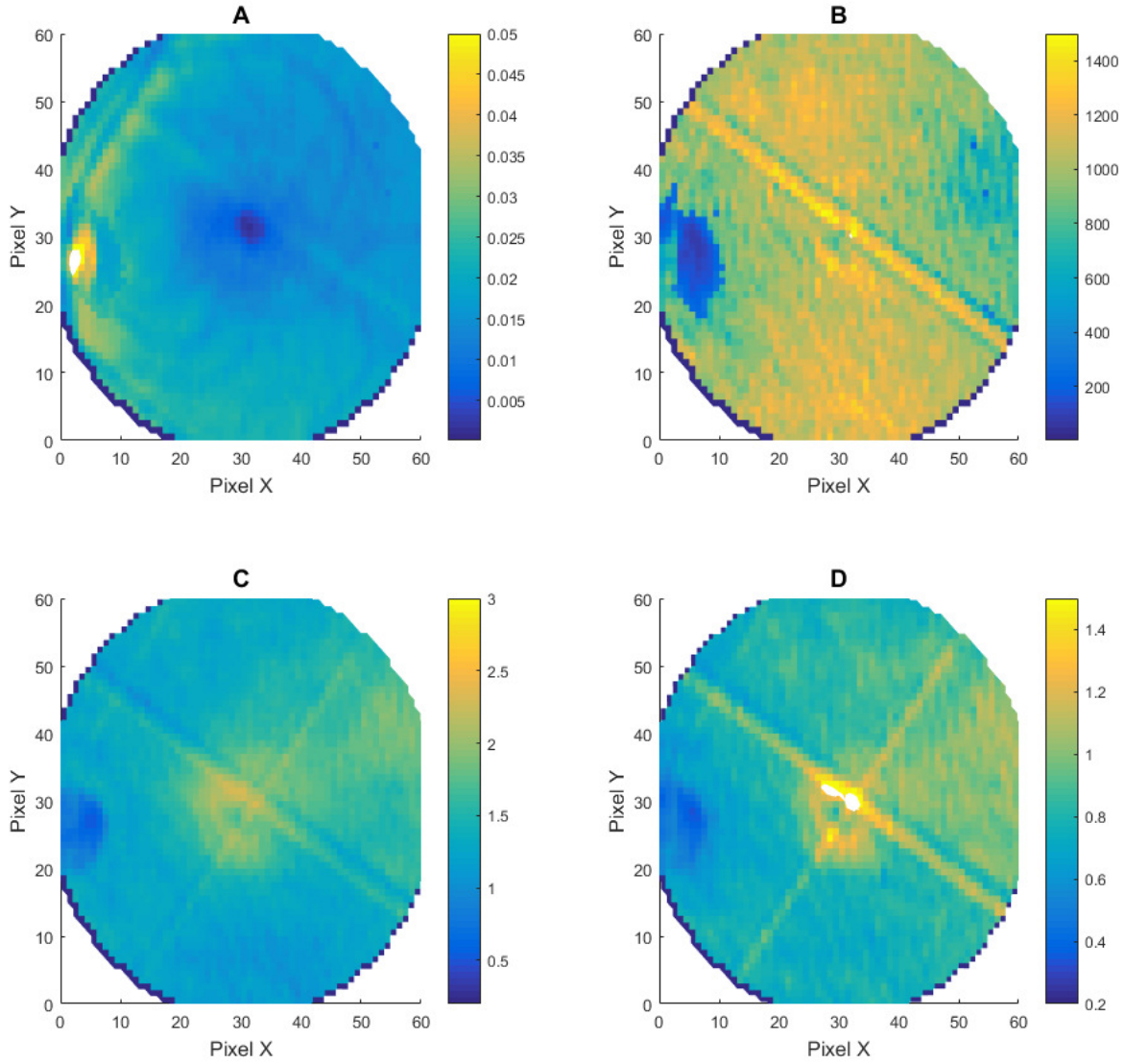

Figure 9.12 Solution to Equation 9.16 for participant CJ. A) Inner retinal fractional reflectance. B) Choroidal thickness (µm), C) Melanin density and D) Scleral fractional reflectance. The obvious cross structure present in all images is the fixation target.

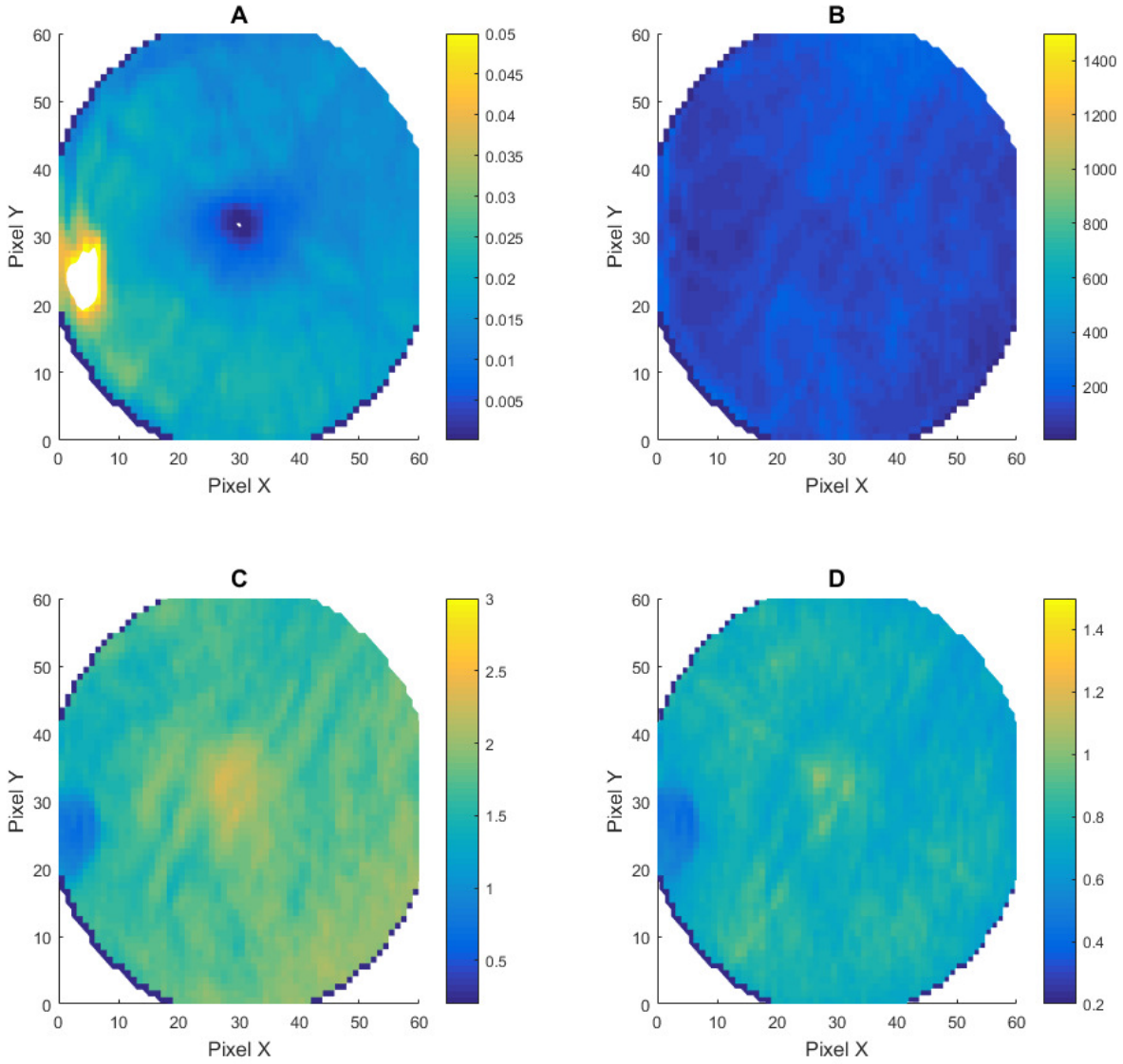

Figure 9.13 Solution to Equation 9.16 for participant HM. A) Inner retinal fractional reflectance, B) Choroidal thickness (µm), C) Melanin density and D) Scleral fractional reflectance. The obvious cross structure present in all images is the fixation target.

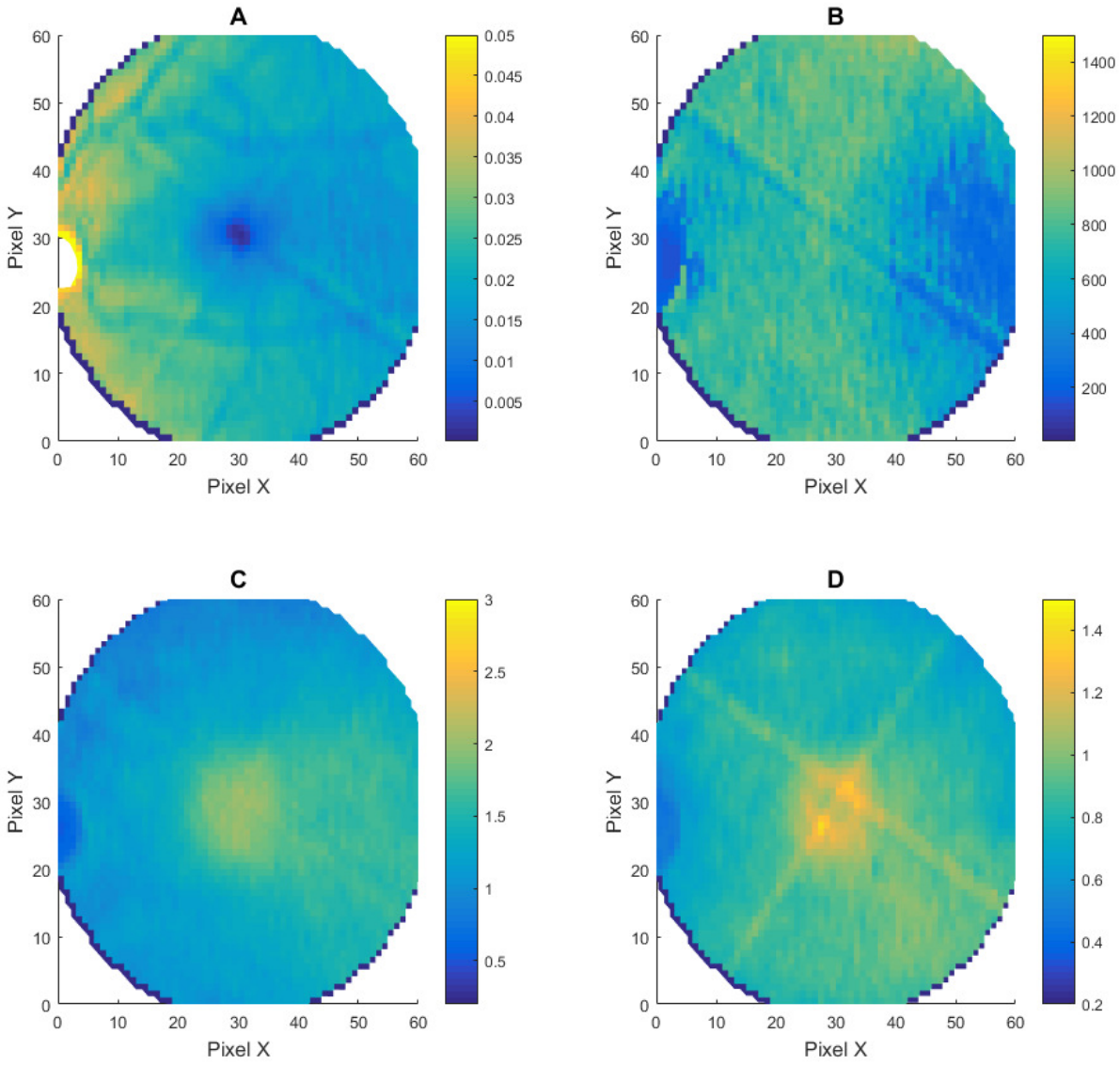

Figure 9.14 Solution to Equation 9.16 for participant JF. A) Inner retinal fractional reflectance, B) Choroidal thickness (µm), C) Melanin density and D) Scleral fractional reflectance. The obvious cross structure present in all images is the fixation target.

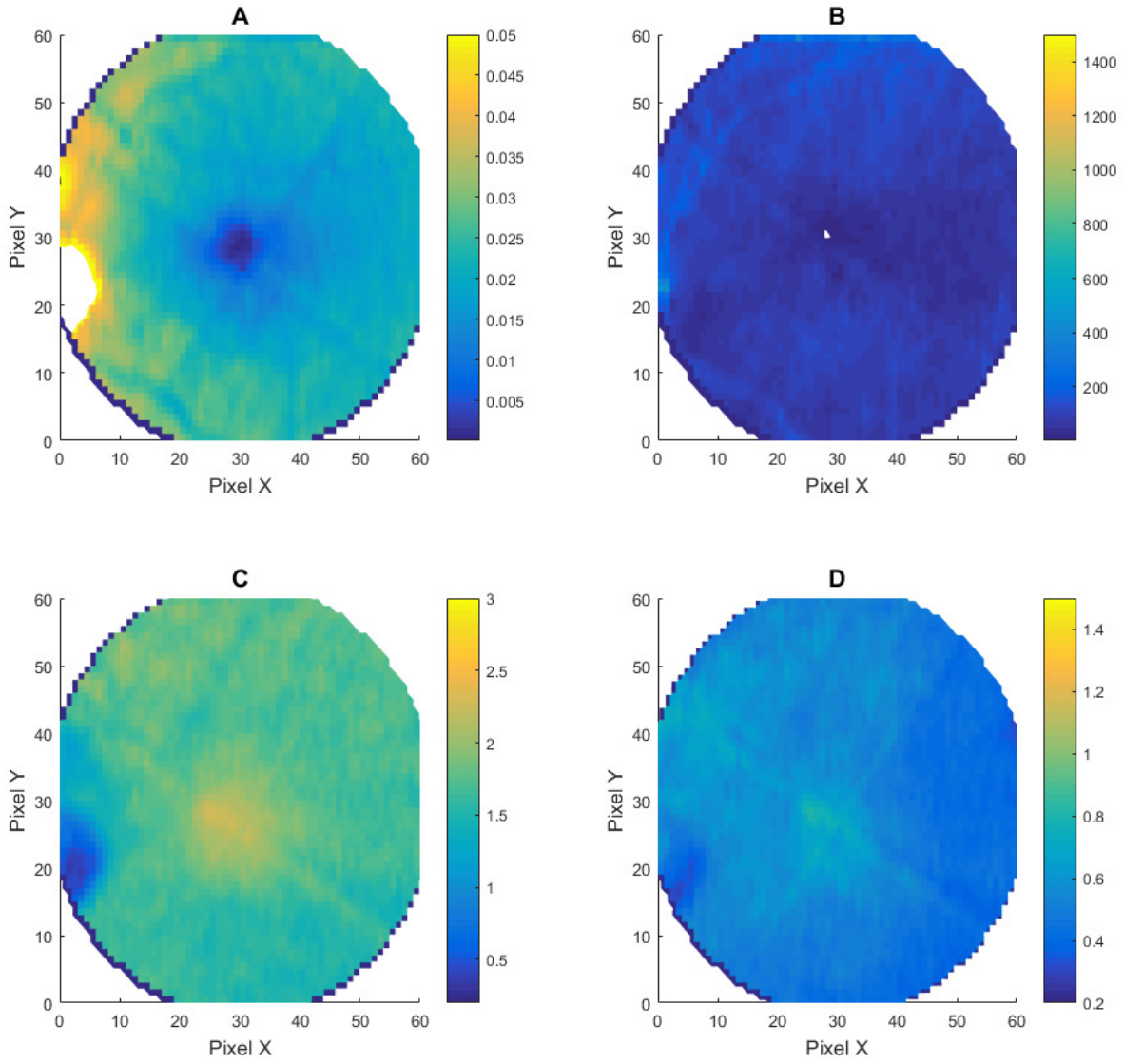

Figure 9.15 Solution to Equation 9.16 for participant TM. A) Inner retinal fractional reflectance, B) Choroidal thickness (µm), C) Melanin density and D) Scleral fractional reflectance. The obvious cross structure present in all images is the fixation target.

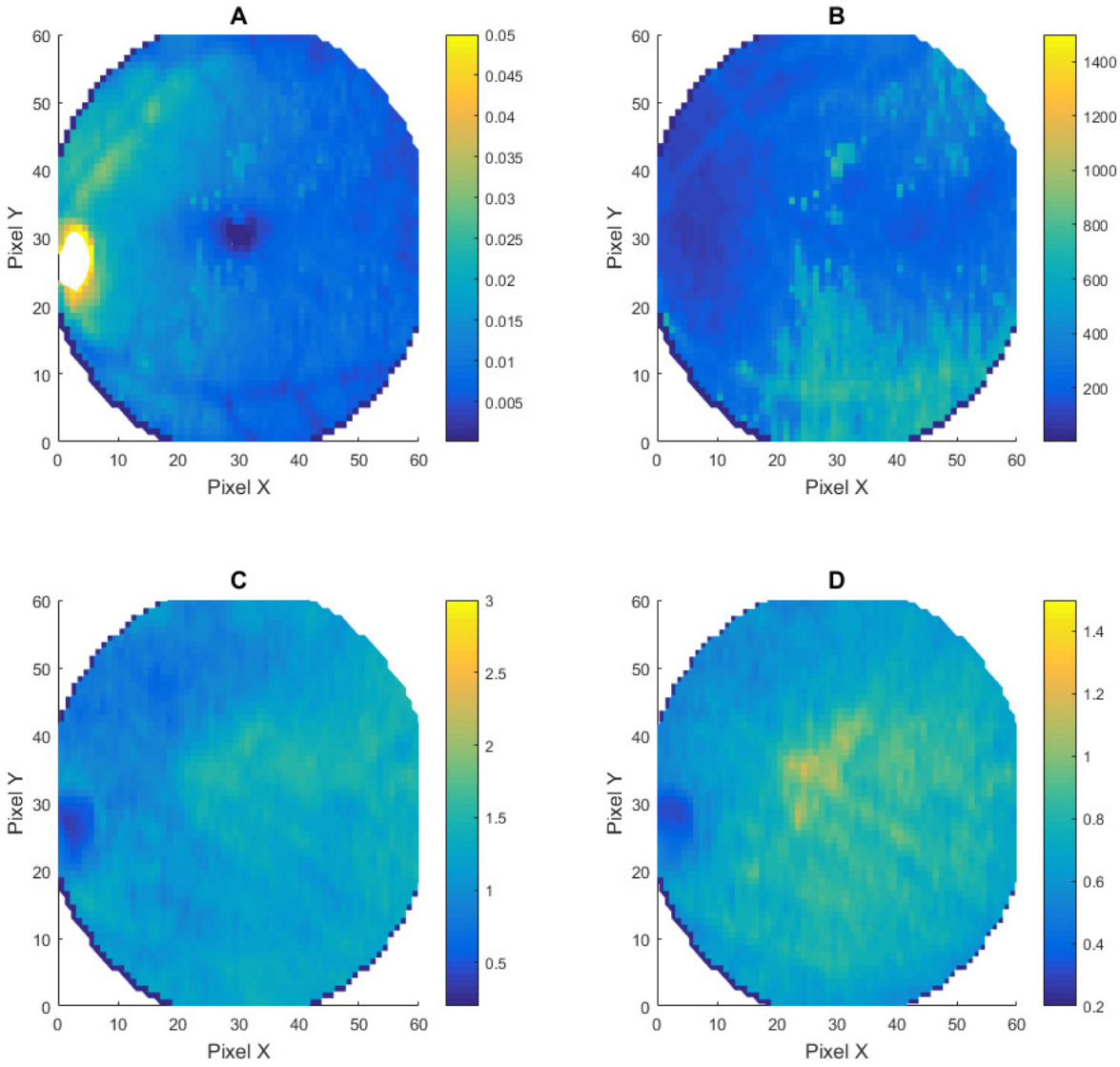

Figure 9.16 Solution to Equation 9.16 for participant AW. A) Inner retinal fractional reflectance, B) Choroidal thickness (µm), C) Melanin density and D) Scleral fractional reflectance. The obvious cross structure present in all images is the fixation target.

A vertical slice was taken through the topographical maps shown in Figure 9.12-Figure 9.16 with the mean data for the group presented in Figure 9.17, with 95% confidence limits. This analysis corroborated the observations made from the visual analysis of the topographical maps. The greater variability of the haemoglobin thickness data than the other parameters is clearly visible.

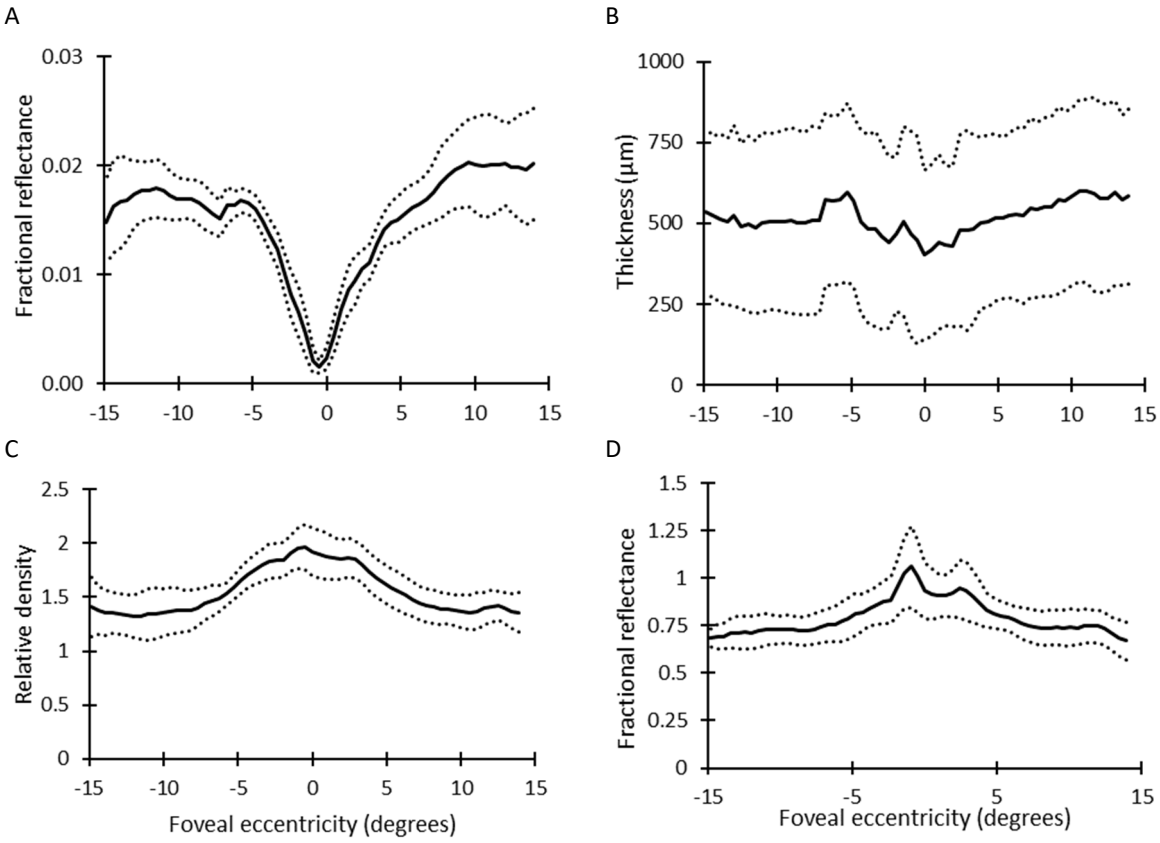

Figure 9.17 showing the central 1° of the topographical solution maps as vertical section through the fovea. Solid lines represent the mean of 5 participants. Interrupted lines denote the 95% confidence intervals. A) shows the inner retinal fractional reflectance, B) Haemoglobin thickness (µm), C) melanin density and D) the scleral fractional reflectance. Left to right across the plots shows superior to inferior retina.

Figure 9.17 highlights the uniformity of all variables toward the peripheral retina. In addition to this, Figure 9.17D shows a distinct double peaked pattern to the central peak of the scleral reflection which is hard to distinguish in Figure 9.12 to Figure 9.16. Re-examining the topographical maps suggests this double peak may be present in only two images (Figure 9.12, Figure 9.14) and to a lesser extent in a third (Figure 9.16).

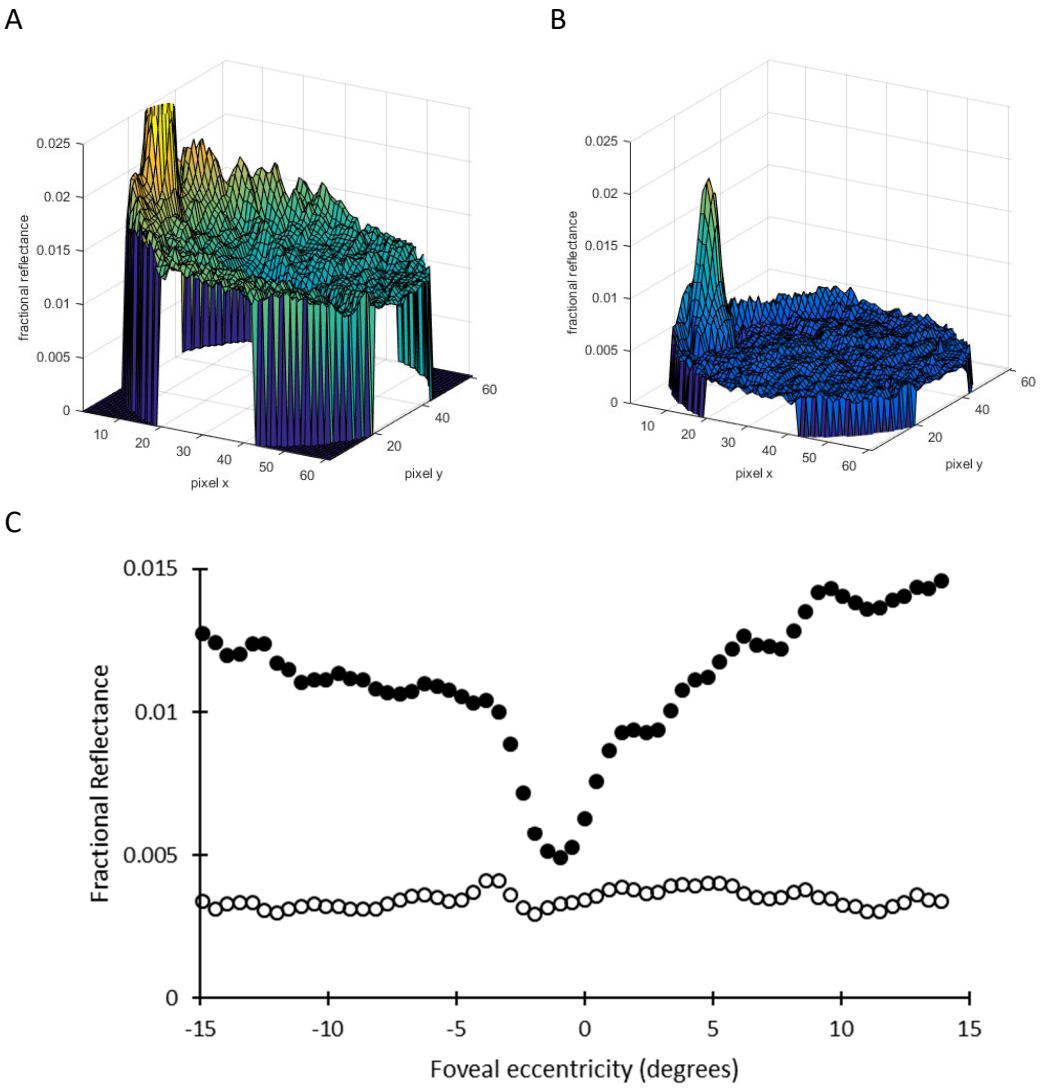

Figure 9.18 showing bleached retinal reflectance measured at 500nm across the central 30° of the retina for a single participant (CJ). A) shows the unadjusted reflectance, B) the reflectance following subtraction of the wavelength specific anterior stray light component and C) shows a 1° vertical section through the fovea for both the unadjusted (filled circles) and adjusted (open circles) reflectance. Left to right across the plot shows nasal to temporal retina.

Figure 9.18 shows the topographical subtraction of the anterior stray light component (i.e. reflections from the crystalline lens (R_{LENS}) and inner retina ($R_{R\ IN}$)) from the unadjusted reflectance, for a single participant at 500nm.

The unadjusted reflectance shows considerable topographical variation in reflectance, with a marked peak at the optic nerve head. Following subtraction of anterior stray light, reflectance is significantly more uniform across the retina, with the ONH providing a clear residual peak (Figure 9.18B). The magnitude of

the anterior stray light contribution is clear in panel C, with an average reduction of 72% (±3.3SD) beyond the central 5°.

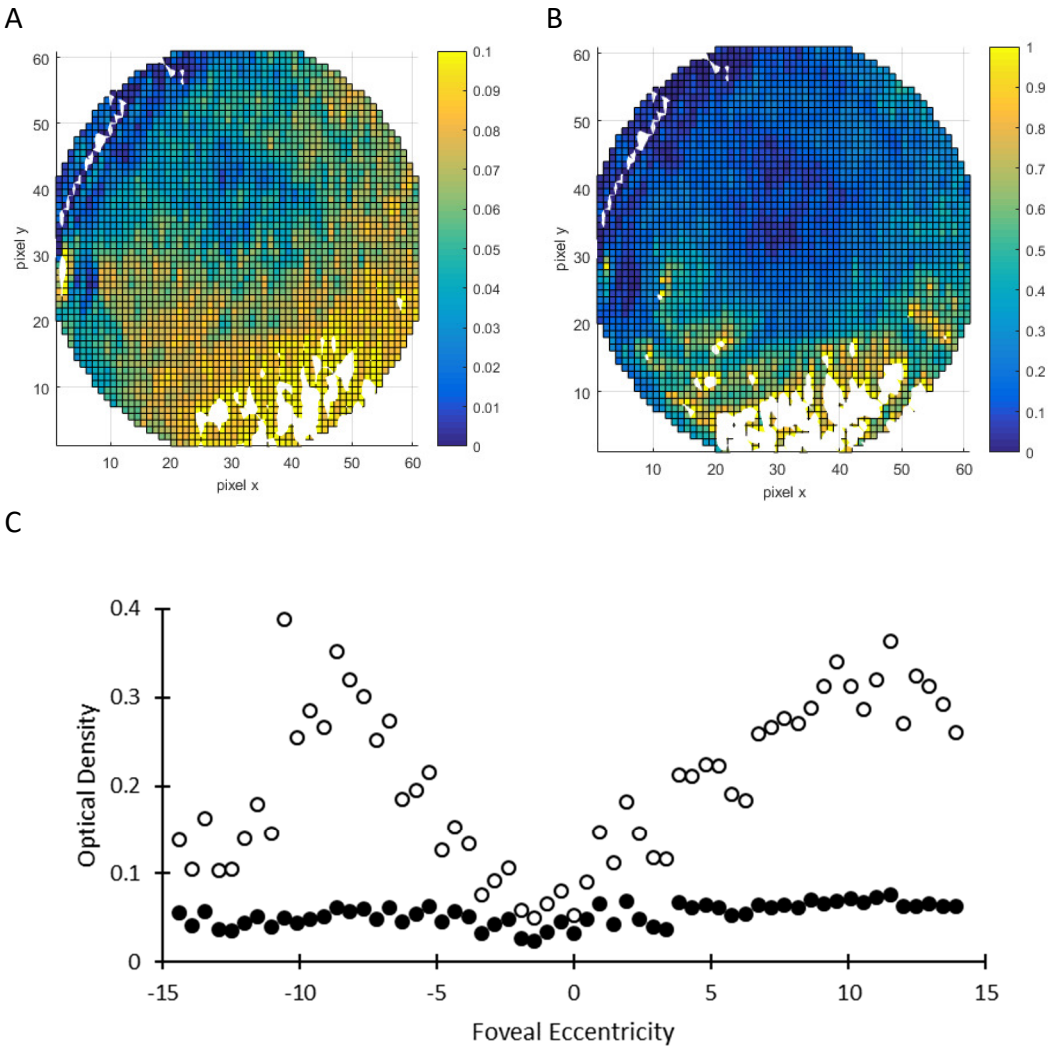

Figure 9.19 showing optical density maps at 500nm across the central 30° of the retina for a single participant (CJ). A) shows the unadjusted optical density, B) the optical density following subtraction of the wavelength specific anterior stray light component. Scaling the Z-axis to peak optical density for each image highlighted the topographical variation in optical density. C) shows a 1° horizontal section through the fovea for both the unadjusted OD (filled circles) and adjusted OD (open circles). Left to right across the plot shows nasal to temporal retina.

Figure 9.19 compares the topographical distribution of unadjusted (Panel A) and adjusted (Panel B) optical density at 500nm (a wavelength likely to elicit peak rod OD). The adjusted OD is higher than the unadjusted OD across the image (note the difference in scale between panels A and B). The unadjusted optical density appears broadly uniform across the image, with only a minimal foveal

decrease (pixel 32,31). In contrast, the adjusted map shows increasing optical density with increasing eccentricity. Panel C highlights this difference, where the adjusted optical density increases from a minimum at the fovea to a peak at around 10° eccentricity. A drop in optical density coincides with the optic nerve head and vascular arcades (-12° to -15°). Both images (panels A and B) show increased optical density in the inferior region, this is more apparent in the adjusted image where the 'background' optical density is more uniform in contrast.

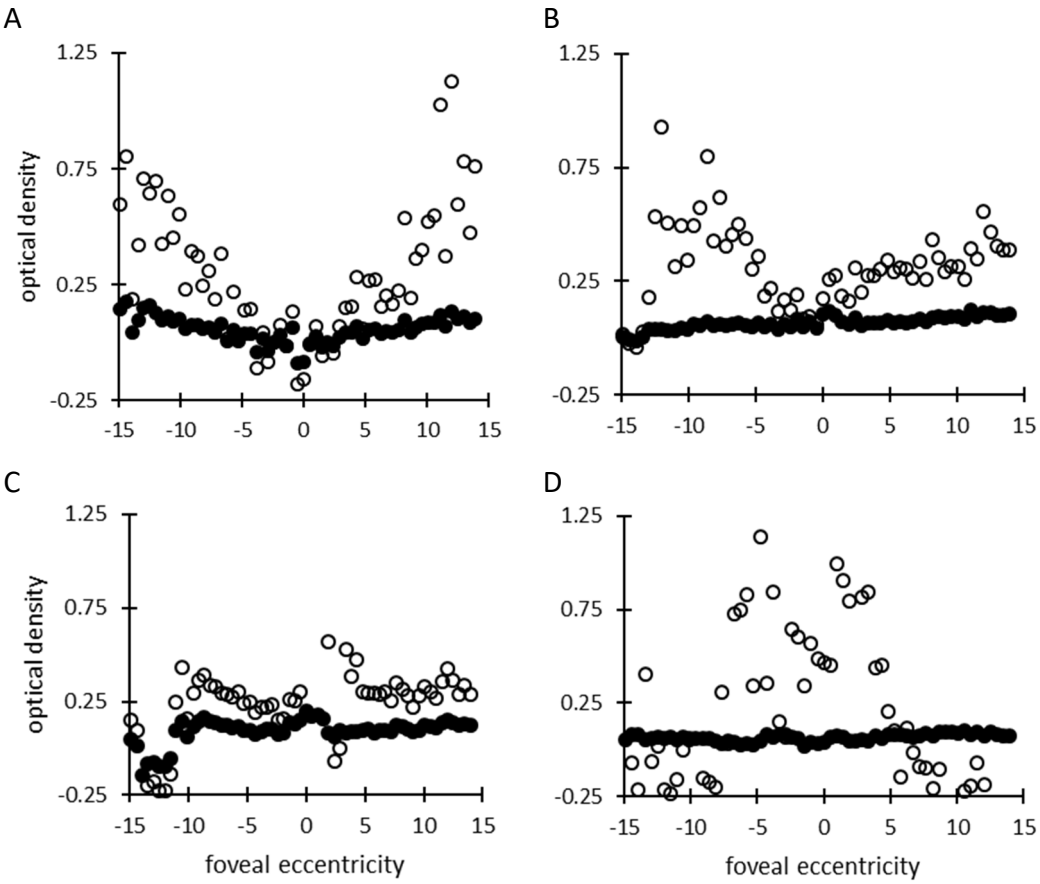

Figure 9.20 showing a 30° x 1° horizontal optical density section through the fovea measured at 500nm for all participants. A) HM, B) JF, C) AW and D) TM. Unadjusted optical density shown in filled circles, adjusted in open circles. Left to right across the plot shows nasal to temporal retina.

Figure 9.20 presents the 500nm horizontal midline data for the remaining four participants. The optical density profiles from two participants (HM, JF) resemble those in Figure 9.19. The OD profile in panel C (AW) shows a small

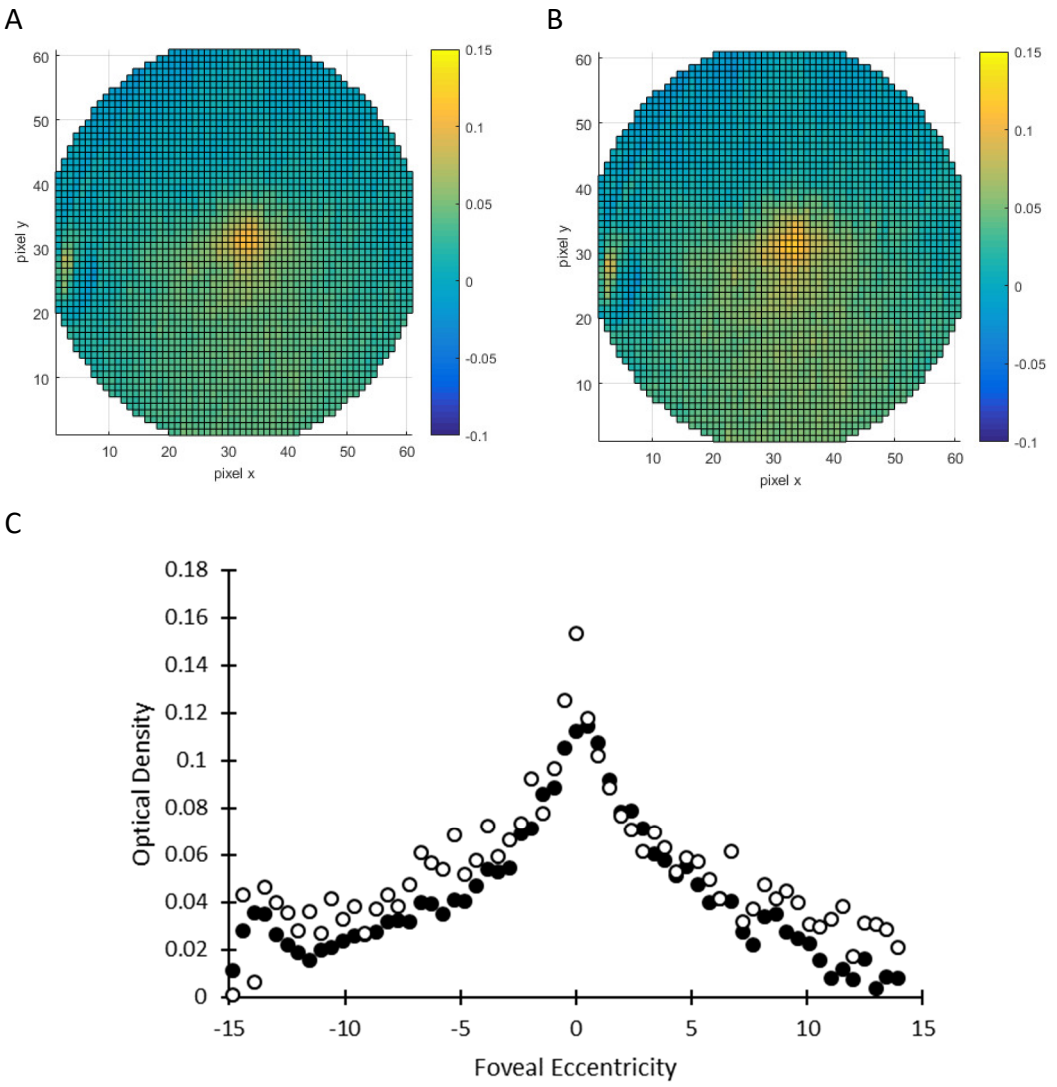

Figure 9.21 showing optical density maps, calculated using the 590nm LED across the central 30° of the retina for a single participant (CJ). A) shows the unadjusted optical density, B) the optical density following subtraction of the wavelength specific anterior stray light component and C) shows a 1° horizontal section through the fovea for both the unadjusted (filled circles) and adjusted (open circles) reflectance. Each image is scaled to peak density to highlight any topographical changes. Left to right across the plot shows nasal to temporal retina.

foveal peak in both adjusted and unadjusted data. The adjusted profile in panel D (TM) has little structure and appears to be mostly noise.

Figure 9.21 replicates Figure 9.19 for the 590nm image (a wavelength at which the separation between rod and cone OD is likely to be maximal). The two optical density maps appear very similar in detail, with a central density peak decreasing in all directions. The horizontal cross section in Panel C corroborates this, with the adjusted optical density showing only a slight increase in optical

density across the retina. A similar pattern may be observed for the remaining participants (see Figure 9.22).

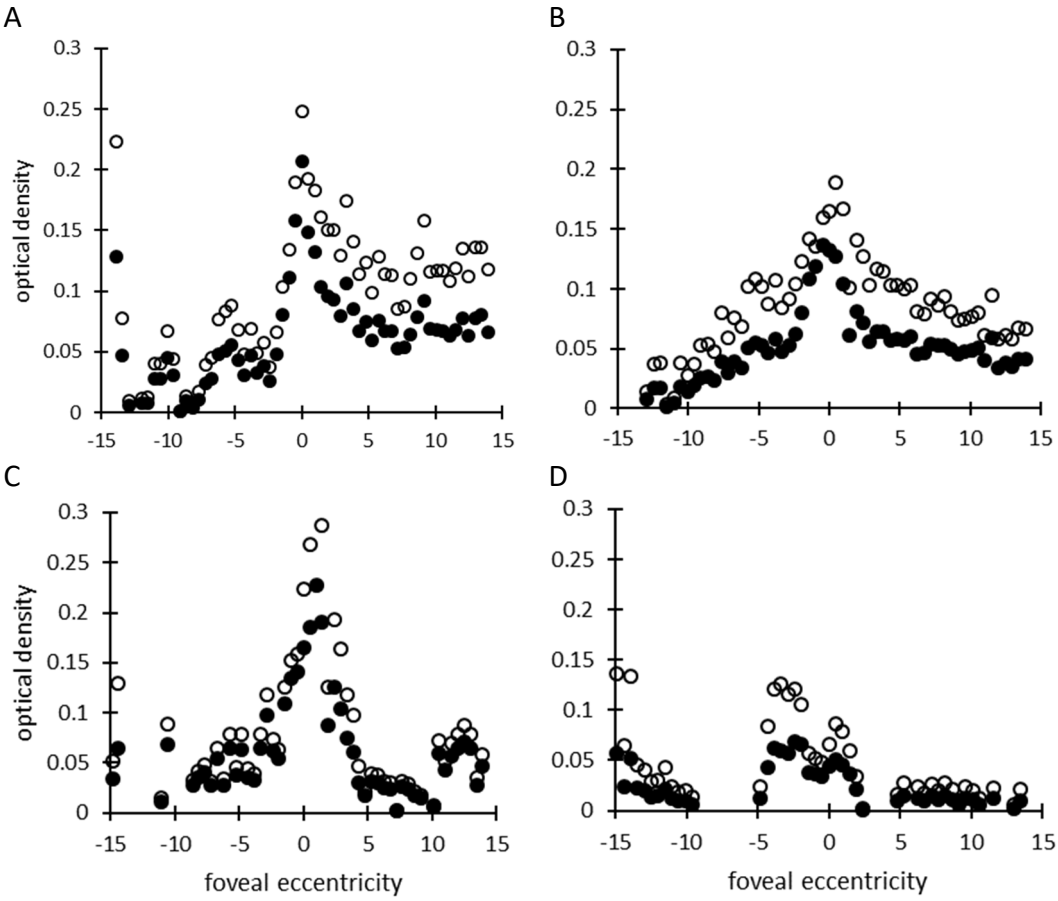

Figure 9.22 showing a 30° x 1° horizontal optical density section through the fovea measured at 590nm for all participants. Unadjusted optical density shown in filled circles, adjusted in open circles. Panels A – C present data from colour normal participants (HM, JF and AW, respectively) and D presents data from a protanope (TM). Left to right across the plot shows nasal to temporal retina.

Having described the topographical variation in OD at two discrete wavelengths (500 nm and 590nm) the following set of results describes the outcome of fitting known visual pigment spectra to the data. The data presented in Figure 9.23 shows the results of fitting the known *in vitro* rod and cone photopigment spectra (Dartnall et al. 1983) to the adjusted optical density maps ($\Delta OD_{adj}(x, y, \lambda)$) to isolate rod and cone visual pigment density, i.e. fitting Equation 4.2. Figure 9.23 presents the distribution across the horizontal midline.

A

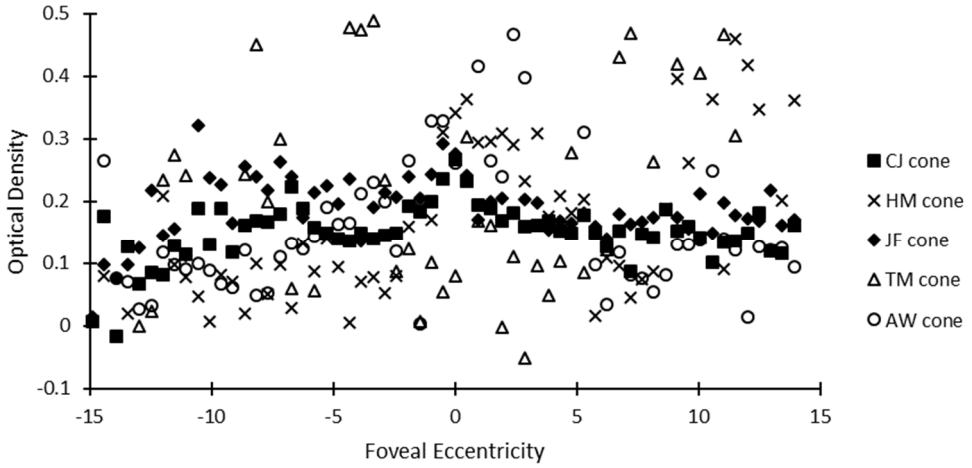

B

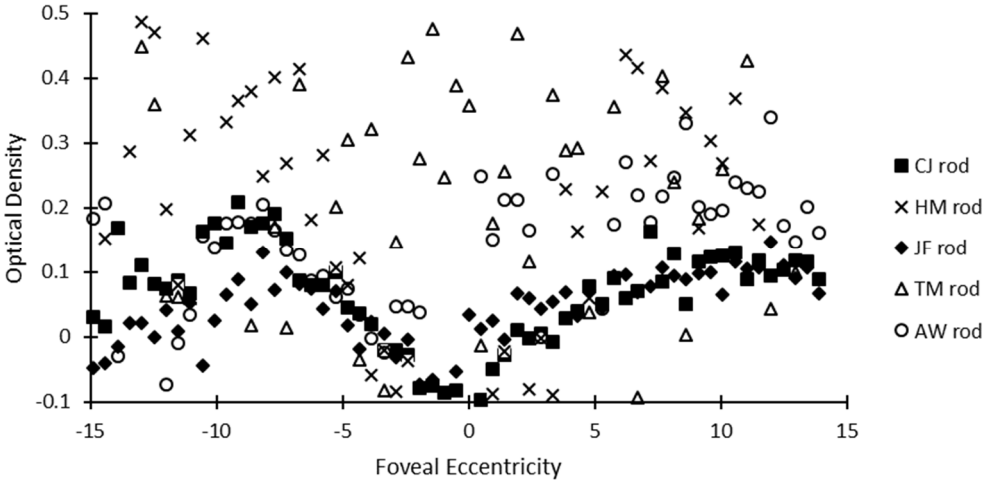

Figure 9.23 The recovered cone (A) and rod (B) optical densities across a horizontal section (30° x 1°) using *in vitro* spectral data in

. In panel A, all participants except TM were fitted, assuming a 50:50 ratio of M- and L- cones, for TM the ratio was assumed to be 100:0. Left to right across the plot shows nasal to temporal retina.

Although there is a general trend towards a peak in cone OD at the fovea and peak in rod OD in the parafovea, the data are rather noisy.

A similar approach is shown in Figure 9.24 but this time the rod and cone spectra used in the fitting routine were those shown in Figure 9.11, i.e. those obtained experimentally rather than from the literature. The results from this approach

are shown in Figure 9.24, which presents the results for the colour normal participants along the horizontal central midline (1^o x 30^o) in panels A and B, together with the mean values in panel C. Mean cone OD peaks at the fovea with an optical density of 0.18 (±0.08SEM) and reduces with eccentricity. Likewise, the modelled values for rod OD are consistent across the datasets. The peak value of 0.5 (±0.14SEM) for rod OD occurs at 12.5^o. Nasally, rod OD increases until either the vascular arcades or the optic nerve head are reached at around -12^o to -15^o, where a significant drop in density occurs.

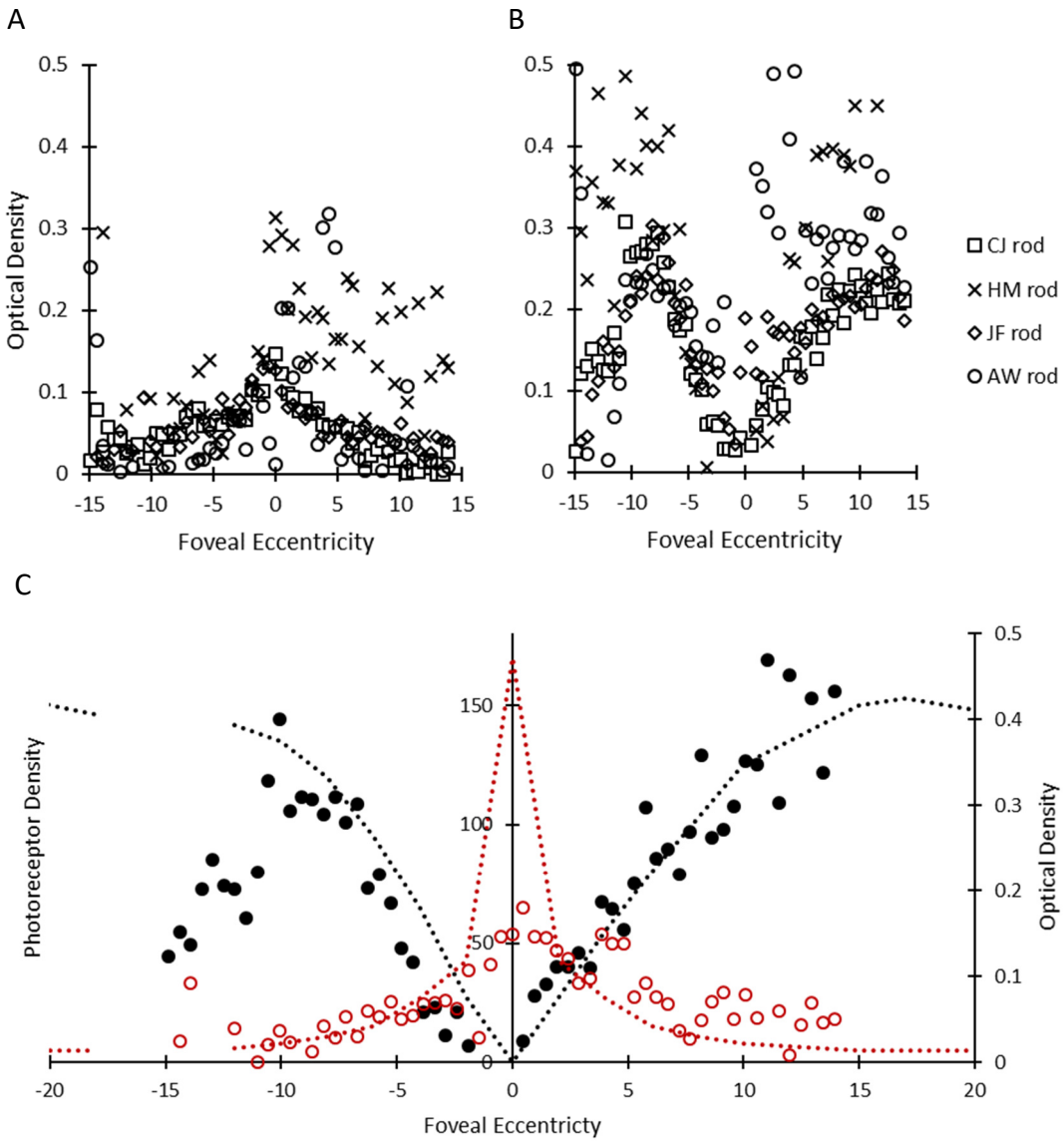

Figure 9.24 The recovered cone (A) and rod (B) optical densities across a horizontal section (30° x 1°) using *in vivo* spectral data (Figure 9.11) in

for colour normal participants only. A) shows the values for cone OD and B) shows the values for rod OD. C) compares the optical density returned for cone OD (open circles) and rod OD (filled circles) against histological data obtained from Curcio (1987) for rods (interrupted black line) and cones (interrupted red line). The break in the histological data represents the location of the ONH. Left to right across the plot shows nasal to temporal retina.

9.6. Discussion

This chapter has described a modified ocular reflection model, based upon that proposed by van Norren and Tiemeijer (1986). The main differences being that the modified model incorporates an anterior retinal reflection and more up to date spectral data for some of the ocular parameters. By applying the model to the experimental data, it was possible to identify pre-receptoral reflections from both the inner retinal layers and the ocular media.

That this model could adequately describe the foveal and parafoveal experimental data was shown in Figure 9.8, and Appendix J. The model provided a fit which was comparable to that achieved with Model I, but with the additional capability of isolating the stray light contributions from both the crystalline lens and inner retinal layers. Furthermore, the returned parameter values for each location (Table 9.2) were physiologically plausible although the estimated OD for macular pigment at the fovea was a little lower than expected.

9.6.1. Isolation of anterior stray light

The modified model described in this chapter incorporated a reflective component from the inner retina. The inclusion of such a component was deemed necessary to recover the OD and spectra of human visual pigments across the central retina. Figure 9.9 demonstrates that the anterior stray light component was wavelength-dependent and, due to the additional contribution from the inner retinal surface, was more prominent for the parafoveal location. That the curves presented in Figure 9.9C vary from the Rayleigh component presented in Chapter 6 highlights the differences between the two approaches. Indeed, when comparing the results to the intraocular stray light presented by Ginis et al (2013), who measured intraocular stray light from the eye as a whole, there are distinct similarities, with both approaches showing a short-wavelength peak at 550nm. However, similarities with the intraocular reflectance presented by Ginis et al (2013) end beyond 600nm where their data are dominated by

choroidal scattering, which is accounted for through the application of this model. Finally, the value for inner retinal reflectance of 1.2% (± 0.30SD, 450nm, Table 9.2) in the parafoveal region, is comparable to that reported by Knighton et al (1989) who showed RNFL reflectance to range from 0.6% to 1.4% at 460nm.

An inspection of Figure 9.12 to Figure 9.16 (Panel A) suggests that the inner retinal component ($R_{R\,IN}$), extracted through this modelling exercise, maps onto the known topographical variation in RNFL thickness. The subtraction of the anterior stray light component not only reduced retinal reflectivity by up to 70% in the peripheral regions, but also increased the uniformity of reflectivity (Figure 9.18). So, it appears that the model can identify the proportion of the reflected camera signal originating from the inner retinal layers. That the topographical distribution of the variable $R_{R\,IN}$ showed low inter participant variance suggests the model is capable of automated application across the varied topographical terrain of the human retina.

9.6.2. Spectral validation

So how well does this model explain the 'red shift' discussed in Chapter 4? Subtraction of the anterior stray light component results in an increase in the calculated optical density of the visual pigments at both foveal and parafoveal locations, with the parafoveal spectra showing a significant reduction in the previously observed red shift (Figure 9.10). The similarity between the adjusted *in vivo* and *in vitro* data suggests this is a valid approach (see Figure 9.11). Indeed, the correction seen here (Figure 9.11) provides a better match to the *in vitro* rhodopsin spectra than the corrected rhodopsin spectra in Chapter 6 (Figure 6.10 A, C).

However, some variation from the *in vitro* data (Dartnall et al. 1983) remains. The adjusted and normalised parafoveal spectrum deviates from the *in vitro* spectrum at 550nm. This wavelength aligns with the peak of cone pigment absorption and may be related to a small proportion of cone visual pigment present at this eccentricity. The foveal spectrum presented in Figure 9.11 is

biased toward the M- cone spectrum. This may be because M- cones dominated the central retina of the participants in this study, or it may represent an over correction of the previously observed 'red shift'.

Consider the distribution of the inner retinal layers. It has been noted previously (Section 1.2.4) that the inner retina is near its thickest in the region surrounding the foveal pit. Further, it is likely that micro-saccades and breaks in fixation, whilst largely accounted for in the image registration routine, have blurred the margins of the foveal pit, introducing stray light from the inner retinal layers. By assuming that reflections from the inner retina were negligible at the fovea, the reflection at the foveal location may have been underestimated, resulting in a slight over-correction of the 'red shift'.

9.6.3. Topographical validation

Whilst the thickness of the haemoglobin layer showed the largest inter-participant variability, the mean values of 140µm (± 84SD) and 153µm (± 69SD) at the foveal and parafoveal locations respectively, compared well with published values for total choroidal thickness. For example, Manjunath et al. (2010) present a mean choroidal thickness of 272µm (± 81SD), assuming approximately 55% of the total thickness is attributable to blood. Melanin content is known to vary across the retina, being of significantly higher density in the fovea than parafovea (Weiter et al. 1986). The results corroborate this, with melanin density increasing by 23% from the parafovea to the fovea. Wieter et al (1984) found a comparable change, with a 29% increase in melanin density across a similar region, albeit from a single participant. Finally, the reflectivity of the sclera, at 112% in the fovea, may seem an unusual value. However, no account was made for scleral melanin content and as a uniform distribution is unlikely, this provides a possible explanation for the variation between foveal and parafoveal reflectance.

At the outset, it was hoped that by correcting for pre-receptoral reflections, it would be possible to use *in vitro* visual pigment spectra to recover the

topographical distribution of the rod and cone photoreceptors. However, the relatively noisy data presented in Figure 9.23 suggests the success of this approach remains limited. The simplest solution, although not the most elegant, was to obtain the spectra from the foveal and parafoveal regions of these participants (see Figure 9.11) and use these to recover visual pigment topography. However, the parafoveal spectra will contain a trace contribution from cones and therefore the resulting maps could never describe the true rod and cone optical density distribution. Despite this, Figure 9.24 suggests that the topographical distribution of cone and rod visual pigment, derived in this way, maps with some accuracy onto the histological distribution of photoreceptors (Curcio et al. 1987).

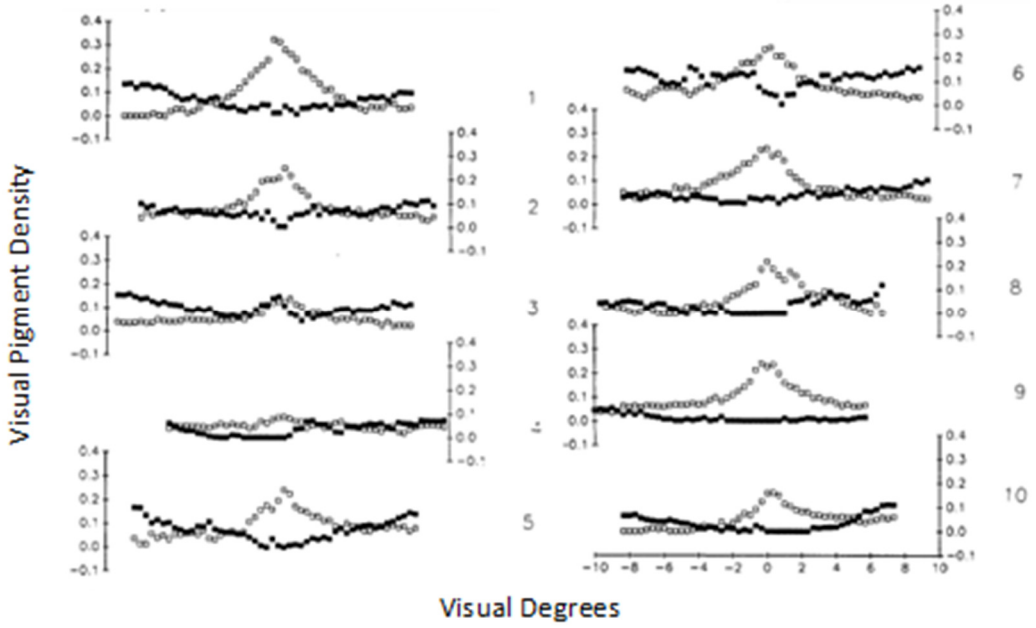

Figure 9.25 Mixed cone visual pigment (open squares) and rhodopsin (filled squares) distributions along the horizontal midline (across 16°) for 10 participants. Adapted from Kilbride and Keehan (1990).

Validation of the visual pigment distribution wouldn't be complete without comparison to the only previous attempt at simultaneously isolating the rod and cone distribution (Kilbride and Keehan 1990), presented in Figure 9.25. Kilbride and Keehan (1990) presented data from 10 participants with a cone distribution similar to that presented in Figure 9.24. However, the rod distribution presented

in Figure 9.25 shows a great deal of inter-participant variance, certainly when compared to that presented in Figure 9.24. Further, there is limited evidence of rhodopsin density increasing with retinal eccentricity seen in Figure 9.25, this variation is displayed in the experimental equivalent (Figure 9.24). It is likely that, by not accounting for reflections from the RNFL, the data presented by Kilbride and Keehan (1990) is an underestimate.

The data presented here aren't without limitations. Firstly, the variable R_{scl} showed an irregular pattern for two participants (see Figure 9.12D, Figure 9.14D). This pattern is reminiscent of the irregularities observed when imaging the model eye (Figure 7.4) and may be related to ongoing uniformity issues within the illumination optics. Perhaps the retinal images modelled in Figure 9.12 and Figure 9.14 were obtained with a slightly different focal plane. It is also worth noting that it was in these participants that the model returned scleral reflectivity values of over 100%.

Finally, the calculated macular pigment optical densities (0.05, ±0.05SD) are low compared to previously reported averages for macular pigment optical density (0.35) (Kilbride et al. 1989). There is the possibility that those taking part in this study had relatively little macular pigment, however it may also reflect an imperfection in the model. Equation 9.3 was taken directly from Kilbride et al (1989) and takes no account for absorption by the ocular media.

9.7. Summary

This chapter has described a modified ocular reflection model that was designed to isolate pre-receptoral stray light. The application of this model was automated in MATLAB and the isolated rod and cone optical density distribution was determined for 5 participants.

In addition to the isolation of the rod and cone optical density distribution, the model derived parameter values for inner retinal reflectance, choroidal

thickness, melanin density and scleral reflectance, highlighting the potential of multispectral imaging and this type of approach. Comparison of these parameters to the values and distributions expected from the literature helped to validate this approach. In particular, the distribution of the inner retinal reflections appears to be particularly appropriate.

The removal of the anterior stray light component was a partial success. It facilitated the close alignment of the *in vivo* and *in vitro* absorption spectra. Likewise, the experimental *in vivo* topographical distribution of both visual pigments was a good match with histology (Figure 9.25).

However, isolation of topographical rod and cone density distribution relied not upon the published *in vitro* absorption spectra as hoped, but on the experimental *in vivo* absorption spectra, adjusted for the stray light contribution. The inability to isolate the contributions of the rod and cone visual pigments using the *in vitro* visual pigment spectra alone was a disappointment. A pragmatic solution was to use the averaged spectra from 5 participants. However, this approach is also limited because of the large inter-participant range in the ratio of M:L cones in colour normal individuals (Roorda and Williams 1999).

The modest mismatch between the reported results and published data may stem from the fact that the modified model presented here has not been designed to provide a comprehensive model of retinal reflectance. Rather, the modified model was a pragmatic approach to modelling retinal reflectance designed to quantify anterior retinal reflections whilst keeping the number of free parameters to a minimum. An alternative outlook could link these deviations to inadequacies in the device alignment. These two factors are entwined to such an extent that it is difficult to isolate one hypothesis from the other.

Chapter 10 - Discussion and Future Work

10.1. Discussion

The work presented in this thesis describes the evaluation of a unique multispectral retinal imaging densitometer. This device was developed to facilitate understanding of the difficulties presented by imaging densitometry. The intention was to inform the design of a clinical device, capable of providing clinicians with a means of investigating the isolated optical density and regeneration rates of the rod, M- and L- cone visual pigments, across the central retina.

A systematic review of the densitometry literature highlighted not only the potential of retinal densitometry as a clinical tool, but also some of the technological difficulties that have limited the techniques development and clinical utility. Densitometry devices have long struggled to overcome the issues associated with ocular stray light, with imaging-based devices most strongly impacted. This is evidenced in the literature by a range of peak optical density measurements and a characteristic spectral shift toward longer wavelengths. Thus, this densitometer was to be evaluated through the characterisation of the measured *in vivo* absorption spectra, regeneration rates, peak optical density and topographical distribution of the visual pigments. Through the course of the preliminary studies, and the comparison of findings to the published literature, it became apparent that stray light and ocular reflectance also required characterisation.

The pilot investigations, described in Chapter 4, sought to explore both the spectral and temporal capabilities of this device. Specific aims were to measure rod and cone visual pigment absorption spectra and peak optical density as well as assess visual pigment regeneration kinetics. A comparison of findings to published *in vivo* and *in vitro* data was carried out in order to validate the results. The device was shown to be capable of measuring visual pigment regeneration. The rate-limited MLP model of regeneration proved a good fit for the visual pigment regeneration rates, which were well corroborated by the published literature. However, the absorption spectra of the visual pigments showed a distinct shift toward the longer wavelengths when compared to published data, leading to speculation over the probable cause. The pilot investigations also raised some pertinent questions regarding the bleaching potential of the light source, possible contamination by the transient molecule metarhodopsin III and the presence of an intrinsic retinal signal affecting the near infrared part of the spectra.

The investigations described in Chapter 5 were aimed at addressing these questions. It was shown that no intrinsic retinal signals were measurable in the near infrared (740nm) part of the spectrum. However, the classic value of the half-bleach constant (4.44 log scotopic trolands), used to define the intensity of light required to bleach 50% of rhodopsin (I_{Rh}) following exposure to an equilibrium bleaching source, was shown to provide a poor description of the bleaching kinetics. A re-evaluation of the effect of retinal illuminance upon the fraction of pigment present suggested that a value of 4.62 log scotopic trolands provides a more appropriate description of rhodopsin bleaching. Indeed, the increase in the half bleach constant in equilibrium conditions seen in Chapter 5 is consistent with the increase in the half-bleach constant for a flash bleach, as suggested by Morgan and Pugh (2013). This result suggests a higher intensity light source is required to bleach an equivalent amount of rhodopsin than had previously been thought. However, at the relatively high intensity retinal illuminance (5.4 log photopic trolands and 6.4 log scotopic trolands) used during

these experiments, this difference in I_{Rh} has a negligible effect on the calculated fraction of rhodopsin bleached (~98%). Consequently, the low optical density measured using this device is unlikely to be explained by insufficient bleaching. It is also shown that, under the conditions implemented here, metarhodopsin III is likely to have a minimal effect upon the measured visual pigment spectrum.

The cause of the red shift evident in the pilot study data was addressed in Chapter 6, which set out to test the hypothesis that a measurable back scatter correction could be used to align the experimental *in vivo* rod and cone spectra with the established *in vitro* functions. In this chapter it was demonstrated that a considerable amount of stray light was polluting the image (e.g. see Figure 6.2, Chapter 6). The optical media were a significant source of this stray light, accounting for 50-60% of the signal at 500nm. The spectral profile of this stray light was reminiscent of Rayleigh scattering. By removing this component in the optical density calculations, an increase in measured optical density and a partial correction of the red shift was achieved. However, the correction of the rod spectrum, applied to the parafoveal data, was less accurate than that of the cone spectrum. The relative difference for the cone pigment spectrum in contrast to the rod pigment spectrum was indicative of an additional source of stray light, predominately in the peripheral retina. This led to the hypothesis that reflections from the inner retinal layers present in the periphery provided an additional source of anterior stray light and an alternative approach would be to fully characterise the contributions of all reflective surfaces. It was further hypothesised that an ocular reflection model could provide a more complete description of anterior stray light. However, this would require a method of calibrating the absolute reflectance of the image.

To facilitate absolute reflectance measurements a model eye was constructed. Chapter 7 described the design, construction and performance of the 'Cardiff Model Eye'. During this work, it was apparent that either the illumination or imaging optics were non-uniform. The model eye was shown capable of correcting for this non-uniformity and returning an accurate value of ocular

reflectance across the image. Given the high anatomical fidelity of this model eye, its applications are not limited to the calibration of ocular reflections discussed here. The most obvious applications are for calibrations within retinal imaging, such as magnification, axial length and retinal curvature measurements on OCT devices and fundus cameras. Calibration possibilities also extend to the measurement of corneal and lenticular curvature for keratometry on devices such as the Pentacam (OCULUS Optikgeräte GmbH, Wetzlar). Finally, there is potential for use as a demonstration or teaching aid for a range of primary eye care techniques including retinoscopy, slit lamp biomicroscopy and all forms of fundoscopy.

The ability to measure the absolute reflectance of the images enabled modelling of the ocular reflection profile, the ultimate aim being the subtraction of anterior stray light from the images. Chapter 8 assessed the performance of published ocular reflection models. Two published models (van Norren and Tiemeijer 1986; Delori and Pflibsen 1989) were highlighted because they were capable of characterising ocular reflections across the image. However, whilst the application of these models provided useful insight, neither was capable of isolating anterior stray light. The simpler model (van Norren and Tiemeijer 1986) provided a good description of the ocular reflectance profile, but lacked an accurate description of anterior retinal reflections. The more complex model (Delori and Pflibsen 1989) contained 11 free parameters, that contributed to a relatively unstable fitting process and was deemed too unwieldly for automated analysis across the retinal image. Hence, the decision was made to develop a novel reflection model to isolate inner and outer retinal reflections.

Chapter 9 describes an updated ocular reflection model and its subsequent application to experimental data in order to obtain rod and cone spectra and topographical maps of photopigment density. The aim was to validate the model by comparing the experimental data, returned by the solution of the model, to those in the published literature. The model was shown capable of characterising inner retinal reflectance appropriately and facilitated the

extraction of physiologically plausible absorption spectra and topographical pigment density distributions. Further, the corrected absorption spectrum of both rod and cone visual pigments showed minimal red shift and was comparable to those published by Dartnall et al (1983). It is worth noting that although the comparison against *in vitro* visual pigment spectra was performed against those published by Dartnall et al (1983), alternative *in vitro* visual pigment spectra have been presented by Stockman and Sharpe (2000) and Kraft (1993). The variation in peak wavelength between the published *in vitro* visual pigment spectra is minimal, however those presented by Stockman and Sharpe (2000) present a narrower absorption profile. When regarding the work presented here, these variations are likely to be inconsequential. Despite the current limitations, it seems that following this approach will reward the researcher with an accurate method of isolating visual pigments, facilitating the investigation of optical density distribution and regeneration rates across the retina. However, inter-participant variability was high, with some datasets adversely affected by noise. Evaluation of the modelling results suggested inconsistent alignment of the device was an issue.

10.2. Key findings

The overarching objective of the work described in this thesis was to understand some of the challenges associated with imaging densitometry. Towards this goal, many pertinent avenues were explored, and conclusions drawn. Some of these conclusions suggest the need for further research. Outlined below are the key findings of this thesis.

1. A novel ocular reflection model was developed, capable of characterising the contribution of key ocular tissues to the total ocular reflectance. The topographical application of this model across the retina highlights the potential of reflectance modelling. This is demonstrated in Chapter 9 where the first simultaneous acquisition of topographical maps

describing inner retinal thickness, melanin distribution, choroidal thickness and scleral reflectance are shown.

2. The work culminating in Chapter 9 enabled the production of topographical visual pigment density maps. When compared to the data of Kilbride and Keehan (1990), the experimental rod and cone density distribution along the horizontal midline (Figure 9.25, Chapter 9) shows less inter-participant variability. This further demonstrates the capability of the ocular reflection model.

3. The development of the ocular reflection model widens the capability of the device from a retinal densitometer to a multi-spectral reflectometry device. The application of the reflection model facilitates the simultaneous characterisation of retinal reflection data across the 3600 discreet retinal locations, with a resolution of 0.48^{o}x0.48^{o}. Further development of this model may facilitate the investigation of diseases affecting the nerve fibre layer (such as glaucoma), changes in melanin and macula pigment density and choroidal haemoglobin content.

4. Investigation of the half bleach constant I_{Rh}, showed the classical value of 4.44 log scotopic trolands to over-estimate the bleaching potential of a light source under equilibrium conditions. The value of 4.62 log scotopic trolands not only provides a better description, but corroborates recent investigations into I_{Rh} following exposure to a flash bleach.

5. The Cardiff Model Eye, developed for this thesis produced an anatomically accurate model. This model should prove capable of calibrating a host of retinal imaging and ocular diagnostic devices. Crucially, the model eye is simple to produce and maintain.

10.3. Future work

The multispectral imaging device described in this thesis was developed as a prototype, a 'stepping stone' to a clinically viable instrument. The work described here has raised many questions and helped identify potential hardware improvements. The following is not exhaustive, but outlines the key challenges and future work following on from this thesis.

10.3.1. Hardware Updates

As an opportunity to better understand the complexities of densitometry, the modified fundus camera described in this thesis provided a crucial insight for the construction of a purpose-built device. Whilst the intricacies and feasibility of the revised design are beyond the scope of this thesis, desirable improvements to the hardware are listed below.

An obvious update must be the characterisation of the uniformity of the illumination, imaging and bleaching optics, as identified through the application of the model eye (Chapter 7). In a conventional imaging device, such as a retinal imaging camera, uniformity is not crucial. However, for accurate objective reflectometry purposes, knowledge of the illumination and imaging optics is crucial. As such, a simple method of calibration should be present. The model eye described in Chapter 7 demonstrates the power of purpose-built calibration tools, essential both for the maintenance of commercial devices and ensuring the accuracy of any research undertaken.

A recurring theme in this thesis has been the confounding issue of intraocular stray light. It is unlikely that any conventional imaging device can overcome this issue completely. However, efforts can be made to reduce the impact of stray light upon the measurement procedure. Ensuring adequate separation of the imaging and illumination pathways within the crystalline lens (Figure 6.1, Chapter 6) will play a key role in minimising the contribution from the ocular

media. This optimisation will not be a simple task as reduction of the imaging aperture has a direct impact on the measured signal, limiting the signal to noise ratio. Likewise, the size of the illumination aperture is constrained by the size of a dilated pupil. Chapter 6 described an investigation using a series of masks to characterise ocular media scatter. Whilst this experiment showed promise, it was limited by the availability of suitable apertures and a slight focussing issue. Inclusion of masks to quantify stray light from the ocular media may facilitate the subtraction of this component. An alternative solution to the stray light issue lies with the application of scanning laser imaging techniques. However, due to current limitations with technology, the number of laser wavelengths that can be incorporated restricts the spectral resolution of such devices. These issues are likely to be further confounded by increased stray light related to the aging eye and ocular pathology (principally, but not limited to, cataracts).

Finally, from a usability perspective, the current device requires a high degree of experimenter expertise to set up and align the system. Likewise, a high degree of observer cooperation is essential. In fact, if densitometry were to become a viable clinical technique, perhaps the key to success lies here. In the current format, the device is dependent upon a lengthy and subjective alignment procedure (Section 3.5, Chapter 3). An objective alignment procedure would simplify the routine for participant and observer alike. Better still would be real time tracking of small, subconscious eye movements and subtle changes in head position. If this challenging task could be completed with accuracy, the benefits would be significant and may impact across a range of clinical imaging techniques. For densitometry, the benefits are clear; the bite bar would be redundant, participants would no longer require rigorous training in the use of the device and alignment would remain stable throughout the recording.

10.3.2. Investigations

With the hardware improvements described above, the currently laborious data collection process would be eased. Thus, it should be possible to obtain

densitometric measurements across a wider range of participants. Further, the investigations discussed in this thesis have opened several further avenues of investigation. Some of these will be discussed below.

Large scale studies and data collection simply were not possible with the current device. It is anticipated that following the removal of the bite bar, accurate eye tracking and an objective alignment procedure, data collection from a wider range of participants will be possible. This will allow a repeatability study to be undertaken and will facilitate the establishment of a normative database for visual pigment distribution, regeneration rates and model outputs (e.g. inner retinal reflectance, outer retinal reflectance, melanin density). This normative database would provide the means to assess differences between participants with and without early AMD.

The ocular reflection model described in Chapter 9 shows promise and has the potential to become a fundamental part of reflectometry measurements. One unusual aspect of the result presented in Chapter 9 was the unusually low macular pigment density of 0.05. This was thought to be related to light scattering from the ocular media and could be addressed prior to any hardware updates through the inclusion of a media scattering component to Equation 9.3. More crucial is the small participant group size. Analysis of a larger database of accurately recorded and calibrated reflection images will facilitate refinements to the parameters used and further validate the model.

For a robust clinical investigation of dark adaptation, a thorough understanding of pigment bleaching kinetics is required. The bleaching of visual pigment is defined both by the sensitivity of the opsin to light and the rate of its regeneration. As such, the classical first order bleaching equations (Equation 5.1, Chapter 5) may be considered as outdated. To truly understand photopigment bleaching constants, consideration should be given to the rate of regeneration, as in equation A12 (Lamb and Pugh 2004). As the purpose of Chapter 5 was to investigate the bleaching potential of the light source, the investigation of a

single pigment (in this case rhodopsin) was deemed adequate. When regarding that the first order equations used to obtain I_{Rh} in the classical literature are out of date, it would be prudent to explore the intensity required to bleach 50% of both rhodopsin and iodopsin, using a rate limited bleaching equation.

Much of this thesis was devoted to the measurement of the anterior stray light contribution contained in the ocular images. This was for the sole purpose of extracting the precise contribution of the various visual pigments present at any retinal location, facilitating the measurement of regeneration rates of isolated visual pigments. Whilst the investigations and modelling procedures described here show promise, consideration should also be given to alternative methods. The simplest is to obtain the *in vivo* visual pigment absorption spectra of the rods and cones on an individual basis (as described in Section 4.4, Chapter 4) and use these in the final visual pigment modelling described by Equation 9.19 (Chapter 9), thus overcoming the unknown ratio of M:L cones. However, as has been previously shown (Kilbride and Keehan 1990) this method was of limited success across the parafoveal region, likely due to increased reflections from the inner retinal layers. Still, it should prove possible to obtain accurate regeneration information (as shown in Section 4.5, Chapter 4). An alternative approach is to exploit the differing regeneration rates of the two visual pigments. Principle component analysis has long been used to study the interaction of components with various time courses of decay (Anderson 1963; Cochran and Horne 1977; Halaka et al. 1985; Jolliffe and Cadima 2016). The potential benefits of this analysis technique have been highlighted in a recent review by Jolliffe and Cadima (2016), namely as a method of reducing the dimensionality of large datasets. In the case of photopigment regeneration the multiple absorbers with the same time course of decay (i.e. the various cone visual pigments) are named as a single component. Thus, the contribution of rod and cone visual pigments may be isolated through regeneration kinetics alone, bypassing the requirement to know either the exact M:L cone ratio or their absorption spectra. That principle component analysis has yet to be applied to the intricacies of visual

pigment kinetics may be related to the requirement for relatively low noise data. However, it remains an area of research which may open great possibilities, and potentially of considerable power if paired with a scanning laser system.

10.4. Conclusion

The work discussed in this thesis has evaluated the temporal, spectral and spatial characteristics of a novel multispectral retinal imaging densitometer. Whilst at the outset it was hoped to present the first description of isolated pigment regeneration rates across the retina, several limiting factors were identified during the work that prevented the full realisation of this.

The data were clouded by anterior stray light, resulting in the dilution of the measured signal and a spectral shift to the longer wavelengths, thwarting isolation of the individual visual pigments on a spectral basis. These issues were partly overcome, and it was possible to obtain topographical maps of rod and cone pigment optical density, as shown in Chapter 9. A further outcome of the ocular reflection modelling was the production of topographical maps of the retinal nerve fibre layer thickness, a key biomarker for monitoring the progression of glaucoma. Both results bode well for the clinical development of densitometry.

Alignment of the device had a less direct impact on the data, but made data collection problematic. Alignment of the device was believed to have been solved during the initial testing period following a rigorous alignment procedure, the use of a bite bar, excellent participants and image registration. It was not until the avenues of stray light and ocular reflection modelling had been followed that alignment issues again became apparent, with the results of the reflection modelling highlighting the susceptibility of the device to un-noticeable differences in alignment. Improvement of alignment is critical for the success of the technique.

Through the investigations presented here, it was possible to further the understanding of the challenges associated with imaging densitometry and further the knowledge of the technique. This research has shown that imaging densitometry can be used to map visual pigment optical density across the central retina and that with further development, the technique is likely to become a useful tool in the diagnosis and monitoring of outer retinal disease.

Appendix

Appendix A. Literature review papers table

	Reference	Purpose & Device	Participants	λ Used	Methods	Results	Conclusion	Comments
				Rushton's early densitometry work				
1	(Rushton and Campbell 1954)	Development of reflection densitometry for humans	Any participants other than Rushton not stated.	Alternating 'Blue-Green' measuring and 'orange' reference beam.	Purple wedge, mimicking the rhodopsin absorption spectrum, was inserted into the measuring beam.	The device was shown to measure rhodopsin.	Very likely that it is rhodopsin being measured.	First *in vivo* measurement of rhodopsin in humans. What was the spectrum of the 'purple' wedge? Was it taken from the *in vitro* rhodopsin spectrum? Likely obtained from Crescitelli and Dartnall, (Crescitelli and Dartnall 1953)

2	(Campbell and Rushton 1955)	Measuring human scotopic pigment *in vivo.* 'Rhodopsinometer' (spot device).	Any participants other than Rushton not stated.	Alternating 'Blue-Green' measuring and 'orange' reference beam.	Several methods used, none fully explained. Device was dependent upon wedge setting. Time course of bleaching measured, used the measuring beam at 50,000trolands. Time course of dark adaptation was measured. OD was measured across the horizontal midline.	Results were all normalised with actual OD not provided. Normalised rhodopsin density across horizontal midline related well to Osterberg, except between fovea and disk. Tau (τ) = 458 seconds.	Results compared well to Osterberg and their own previous (unpublished) studies. 10^0 nasal gives half OD.	Dark adaptation measurement limited by objectivity and speed of wedge measurement. Unknown wavelengths of the green/orange lights. Contamination by cones/photo intermediaries? NFL scatter cause of reduced OD at 10^o and poor relation to Osterberg between ONH and fovea. How many participants in experiment?
3	(Rushton 1956a)	Difference spectrum and photosensitivity of rhodopsin in the living human eye.	'mostly young male adults' How many?	460nm 480nm 505nm 530nm 550nm 575nm	Dilated. 15min dark adaptation.	Results mimic Crescitelli and Dartnall, (Crescitelli and Dartnall 1953) *in vitro* data, but with a	Photoproducts may affect data, by absorbing in blue and green. Different to *in vitro* studies.	First mention of contamination by photoproducts.

		‘Stiles – Double monochromator’ (spot device)		‘Orange’ reference beam	6 wavelength readings were taken in 1 min. repeated immediately. 700,000 td bleach light was presented for 5-10mins. Above readings repeated twice, with an occasional 10sec ‘re-bleach’. Repeated above with 1min bleaches.	consistent shift to longer wavelengths. Longer duration bleaches gave results closer to Dartnall.	Rhodopsin photoproduct was orange and decayed within minutes. Data from long bleaches have less photoproduct contamination than those with shorter bleaches.	Comparison of *in vivo* to *in vitro* spectrum. Noticed ‘red shift’, unknown cause. Black tape on nose reduced scatter on temporal retina. Suggesting poor device optics.
4	(Rushton 1956b)	Theory (continuation of previous paper) ‘Stiles – Double monochromator’ (spot device).	As above	As above but with ‘Red’ reference beam	Theory paper, discusses inaccuracies and limitations with the current technique.		Given all the inaccuracies an OD 0.15 appears to be accurate	First discussion of intraocular light scatter and possible implications for densitometry.
5	(Rushton 1961a)	Investigation into rhodopsin kinetics	unknown	Measuring beam 516nm.	Dilated 3^0 measurement area, 12^0 from fovea.	Rods were shown to take over from cones at 92% regeneration.	Suggested there is a linear relationship between visual threshold and	How bright was the bleach? Explanation of how wedge densitometry works.

		Spot device, new design. Uses neutral density filter over 'purple' filter. Similar to 1955 rhodopsinometer.		Reference beam 'deep red'.	30sec 20^0 bleach 3 intensities used: 100%, 35% & 25%. Measurements were taken at intervals, participants could leave machine between them. The break between intervals increased as regeneration rates slowed. Dark adaptation also measured.	Independent from bleach intensity Tau (τ) = 302 seconds. Constant for all bleach intensities.	rhodopsin regeneration Final 8% of rhodopsin recovery proved very noisy.	
6	(Rushton 1961b)	Rhodopsin measurement with deficient cone vision Spot – 1961 design	One rod monochromat (no cone pigment)	Measuring beam 516nm. Reference beam 'deep red'.	Dilated 3^0 measurement area, 12^0 from fovea. 30sec 20^0 bleach 10^6 td. Measurements were taken at intervals, participant could leave machine	Rod optical density and regeneration was normal. A linear relationship between rhodopsin regeneration and threshold was found.	Corroborates the conclusions of previous paper. Results from a rod monochromat represent the isolated rod data.	Recognised the presence of cones in the periphery as an issue. A reasonable, but not very practical solution.

					between them. The break between intervals increased as regeneration rates slowed. Repeated in fovea. Dark adaptation was also measured.			
7	(Rushton 1963a)	Is it possible to measure the foveal visual pigment in a protanope? Modified from the device used in Rushton / 1956a	Unclear. 1 Protanope?	492, 516, 527, 552, 576, 590 and 615nm measuring beams. 700nm reference beam.	Dilated. Dark adapted reflectivity was recorded. Bleaching began whilst measurements continued. When regeneration and bleaching were equal the bleach intensity was increased. After 'total' bleaching, a regeneration recording began.	7 min regeneration. 3-4x shorter than for rhodopsin. Peak MWS sensitivity at 540nm. Absorption spectrum stable regardless of bleaching light wavelength.	Protanopes have only one detectable cone pigment (chlorolabe) in the fovea.	Names MWS cone visual pigment chlorolabe
8	(Rushton 1963c)	Is it possible to measure the foveal visual	One protanope	545nm, 580m, and 660nm.	As above, but mixed 545nm with 660nm and compared	Raw OD of 0.13	Chlorolabe OD of 0.35 is twice rhodopsin OD.	Substantial increase in OD after taking scatter into account. However, the

		pigment in a protanope? 1961 device.			this with 580nm. Theory in paper.	After making some assumptions for scatter, OD was 0.35?	Chlorolabe is present in small quantity but high density. ~10% of stray light arises from the pre-retinal region. Most stray light is due to the foveal reflex and light passing between cones.	assumption that scatter is related to light guide and inter-photoreceptor matrix only may not be complete. What about crystalline lens and other pre-retinal reflective surfaces.
9	(Rushton 1963b)	Investigation of the foveal visual pigment chlorolabe kinetics. 1961 device	One protanope	535nm 700nm	Identical to 1963a, but with recordings of steadily increasing bleach intensity. Repeated for both short duration (10 sec) and 'equilibrium' bleach.	Half bleach constant for chlorolabe was 4.1 log phot (?) td for equilibrium conditions and ~5 log phot td following a flash bleach. Tau (τ) = 125 seconds (range 120-140)	Higher intensity bleach required for shorter duration bleaches. Chlorolabe regeneration can be related to cone visual threshold. Some discussion on light guide effects. Suggests that the	Not sure how equilibrium is defined. But at around 3td, equilibrium will take many tens of minutes to achieve. These 3 papers on chlorolabe set the ground work for subsequent cone pigment investigations.

							higher chlorolabe density measured is due to this effect (i.e. less 'stray' light).	
10	(Rushton and Henry 1968)	Regeneration and bleaching in man. Florida device.	unknown	560nm	Cone regeneration was measured following two separate bleaching conditions (1 sec and 2 minutes).	Cone regeneration was twice as fast after a 1sec bleach in comparison to the 'equivalent' 2 minute bleach	The regeneration rate depends upon the amount of 11- cis retinal immediately available, and during a prolonged bleach this is largely exhausted	Corroborated by Alpern (Alpern 1971).

Ripps and Weale early densitometry work

11	(Weale 1959)	Comparison of the absorption spectrum from a colour normal and a cone monochromat. Ripps/Weale spot device (see Figure 2.3).	Unknown, at least one cone monochromat	26 wavelengths covering the range of 405-680n for measurement. Reference beam taken from fellow eye.	Dilated, dental bar. 12 minute dark adaptation Bleaching, (7 log phot td / 30 seconds? unclear). Absorption spectrum was obtained from all wavelengths.	The absorption spectrum was dependent upon wavelength of bleaching source.	Suggests at least 2 visual pigments are present in the fovea.	Significant increase in the spectral resolution of the device in comparison to the Rushton device. Measurement no longer subjective.

					Experiment repeated with different wavelength bleaches.			
12	(Ripps and Weale 1963)	Effect of the bleaching source wavelength upon foveal visual pigment. Ripps/Weale spot device (see Figure 2.3).	Two colour normal participants	26 wavelengths covering the range of 405-680n for measurement. Bleaching lights, 431, 469, 488, 516, 547, 575 & 680nm. Reference beam taken from fellow eye.	Dilated, dental bar. 12 minute dark adaptation Bleaching, (7 log phot td / 30 seconds? unclear). Regeneration was measuring using all wavelengths Experiment repeated with different wavelength bleaches.	Absorption spectrum was dependent upon the bleaching wavelength alone, with the exception of low intensity red bleaches. Density measured was dependent upon bleaching wavelength and intensity.	Different photosensitivity's to red of the two foveal pigments. The measured spectra are well corroborated by the subjective foveal sensitivity curve.	Mixed cone pigments.
13	(Ripps and Weale 1964)	Measuring the directional sensitivity of reflections from	Likely two colour normal participants?	26 wavelengths covering the range of 405-680nm.	A prism was used to achieve the desired shift in location of the incident beam within the pupil,	Lower OD measured with offset pupil position. Most noticeable across 520nm-590nm.	Less light is absorbed by an offset pupil position, corroborates waveguide	Noted the crystalline lens as a significant absorber. Could higher stray light in the oblique pupil position

		the human fovea Ripps/Weale spot device (see Figure 2.3).		‘blue’ and ‘orange’ bleach. Reference beam taken from fellow eye.	allowing non-direction light to be investigated.		effect/Styles-Crawford theory. Higher absorption by the crystalline in the oblique pupil position could also explain the lower OD measured at this location	also explain the lower OD measured at this location.
14	(Ripps and Weale 1965)	Analysis of human foveal densitometry. Ripps/Weale spot device (see Figure 2.3).	Theory paper		Discussion of the optics of light within photoreceptors.		Some light passes through the spaces in the interphotoreceptor matrix, therefore does not contribute to the optical density measurement, resulting in an underestimation.	No mention of reflection or absorption layers. Applicable to rods as well as cones?
15	(Carr and Ripps 1967)	Investigation of how rhodopsin kinetics are affected in Oguchi’s disease.	Single participant with Oguchi’s disease. (18, F)	See Ripps and Weale, 1963.	White light bleach. 6.02 log td, 30 sec. Absorption spectrum measured using all wavelengths and	30 minutes to regenerate to 95%. 60 minutes to 100% (faster than subjective dark adaptation).	Regeneration and visual threshold proceed independently in Oguchi’s. It is likely that the cause of	First use of densitometry to investigate pathology. A single participant.

		Ripps/Weale spot device (see Figure 2.3).			regeneration measured using 500nm only. 4 hour dark adaptation period.	Spectrum peak at 500nm.	slowed return to visual threshold lies in NFL, not rhodopsin regeneration.	
16	(Villermet and Weale 1966)	Investigating the application of 'clearing' bleaches. (i.e. a brief intense bleach, designed to clear the previous light history prior to dark adaptation). Ripps/Weale spot device (see Figure 2.3).	2 participants	Blue wavelength 400(?)-510nm up to 5.9logTD, green 490-550nm up to 6.3logTD. Measuring light – 450, 520, 560 and 580nm	12min DA. Dark adapted reflection spectrum recorded. 30s bleach of green or blue light. Bleached reflection spectrum recorded.	No OD or regeneration time was presented. OD appears to be 0.2 If a clearing bleach of over 7.7log td is used photolysability is reduced by a factor of 4-5, a second bleach can reduce it further.	Mechanism for protection of visual pathway? The reduction in photolysability is spectrally different. Peak difference at 540-560nm. Effect can last over 25mins. Photopigment regeneration doesn't seem to be affected.	What is field size and where is it centred. What wavelength is the bleaching light? Our bleach is 5.5log td (phot) at 60%. If we go higher, we may have to counter this in.
17	(Ripps and Weale 1969a)	Determination of Rhodopsin	3 participants	400-680nm at 10nm intervals	2^0 measurements were recorded, 18^0 temporal on the horizontal meridian.	OD peaked at 510-512nm with 0.17 and 0.19 for a 30sec	Absorption spectrum displaced to longer wavelengths. Caused	Orange photoproduct = meta III.

		bleaching with white light. Comparison of flash and continuous bleaching. Ripps/Weale spot device (see Figure 2.3).			Dilated. Bleach light was calibrated both objectively and subjectively. Bleached with 1ms intense flash and 30sec equivalent brightness flash.	bleach and 516-518nm for a 1ms bleach. Half bleach constant for flash bleaches = 5.62 log td.	by an 'orange photoproduct'. Less photoproduct present after longer duration bleaching.	Scotopic or photopic trolands? Corroborates Rushton (Rushton 1956b)
18	(Ripps and Weale 1969b)	Investigation into presence of metarhodopsin III. Ripps/Weale spot device (see Figure 2.3).	3 participants	Assumed the same data set as above.	Assumed the same data set as above. Modelling	The difference spectra at varying timepoints following a bleach varies. Data modelled to isolate rhodopsin and metarhodopsin III spectrum. Meta II peaks at ~460nm, rhodopsin at ~510nm.	Suggests two light absorbing pigments, with differing time course of decay. Metarhodopsin will be present in minimal concentrations following prolonged bleaching protocols.	Rhodopsin spectrum still shows red shift in comparison to *in vitro* data. Supports previous paper well. Meta III appears to peak at 1min after exposure to bleach, and decays relatively rapidly.

Florida device								
19	(Rushton et al. 1969)	Comparison of dark adaptation and densitometry with regard to regeneration after flash and equilibrium bleaching Florida device.	1 participant	581nm	5 second 'full bleach' 2 minutes '95% bleach'	Regeneration is faster after a brief bleach than an equilibrium bleach. Visual threshold is independent to the rate of regeneration, rather it is dependent on the proportion of rhodopsin present.	Confirms Rushton and Henry (Rushton and Henry 1968).	What were the bleaching intensities and wavelengths! i.e. how were the bleach proportions calculated?
20	(Hood and Rushton 1971)	Description and evaluation of a new densitometer Florida 1971 version.	No subjects	560nm	Dilated. Describes calibration with model eye, real eye and measuring light bleaching amounts.	None Theory paper.		Better accuracy using one wavelength? Record bleach from measuring beams – do individually for each wavelength, have to repeat for separate wavelengths.

								Fixation cross hairs for fovea, nothing for periphery
21	(King-Smith 1973a)	Optical density of Erythrolabe. Florida densitometer	5 participants. 2x deuteranopes, 2x deuteranomalous 1x colour normal	560nm and 620nm	Given in King-Smith (King-Smith 1973b)	OD ranges from 0.2-0.43. Mean 0.42.	Differences in peak optical density readings related to stray light	Assumes intra-ocular stray light to be wavelength independent. See Ginis et al (Ginis et al. 2013), this is unlikely.
22	(King-Smith 1973b)	Optical density of Erythrolabe. Florida densitometer	5 participants. 2x deuteranopes, 2x deuteranomalous 1x colour normal	560nm and 620nm measuring beams. 540nm bleaching beam.	3^0 illumination and 2^0 recording. Dark adapted measurements recorded with red and green light. Green bleach (2mins) Bleached measurements recorded using alternating red and green. White bleach (99%, 2 mins)	As above	As above	These two papers should be read in conjunction with each other

					Bleached measurements recorded using alternating red and green.			
23	(Alpern 1971)	*In vivo* Rhodopsin kinetics. Modified Florida densitometer.	Bleaching kinetics, 1 participant. Time constant 4 participants and many repeats (64 across the 4 λ's)	495nm 525nm 555nm 565nm	18^0 temporal. 5^0 measuring field. 10^0 bleaching field. 30 minute dark adaptation Dark adapted recordings were taken for 6mins. A bright flash and equivalent bleaching 'steady light' presented. Measurements. Increase flash intensity and repeat above. Final 3min bleach (6.2logTD).	Time constant of regeneration =386sec (±10 8 sec). Half bleach constant from an equilibrium bleach = 4.44 log scotopic trolands	Time constant agrees with Rushton (Rushton 1961a), but not Ripps and Weale (Ripps and Weale 1969a). Ripps used a brief flash. Regeneration kinetics largely independent to wavelength.	Rhodopsin absorption shift to 465nm. Recorded amount of bleach from measuring light. Small data set. Does bleach duration effect regeneration. First mention of 'scotopic trolands'. What have previous papers used?

24	(Hollins and Alpern 1973)	Measure rhodopsin OD/ photosensitivity . Prove this machine + methods measure rhodopsin Florida Densitometer	Unknown	570nm	Measurement of 5^0 at 18^0 temporal. Several different experiments described. Measured optical density and regeneration.	Greater variance of OD at longer λ's. Regeneration of rhodopsin = 374 ± 13sec. OD = 0.35	Methods accurate. Higher OD in periphery due to less stray light.	Blue light scatter doesn't need to be accounted for. 560nm or 570nm?
25	(Alpern and Pugh Jr. 1974)	Rhodopsin flash kinetics. Florida Densitometer (1971)	1 healthy participant	555nm	Dilated. Illumination 15.2^0, centred 18^0 temporal. Bleach of varying brightness presented in either 600µsec flash or equivalent 30sec. Pigment at end of bleach measured.	600µsec flash was not capable of bleaching more than 60%, even at 8logTD	Saturation of bleaching curve at 75-80% bleach, not previously noted as bleach intensities not bright enough (Ripps and Weale 1969a; Alpern 1971). Forward and back reaction of metarhodopsin I to	Experiment set up similar to 'mode 2'

					Regeneration time measured. Second experiment involved flash, measure, flash, measure etc.		metarhodopsin II is approximately equal.	
26	(Perlman and Auerbach 1981)	Visual sensitivity & rhodopsin OD in RP and normal. Florida Densitometer	11 participants with RP. Age 16-40. 9 normal subjects.	540nm. Bleach (500nm?).	Bleach 8^0 Measure 4^0 Dilated. DA 40mins. Reflectance measured. 60sec bleach, 7log troland. Reflectance measured. Occasionally the bleach was increased for more measurements.	Large range of variance in OD (between normal participants and RP participants). Highest OD at 18^0 (0.35). At 6^0 OD is 50%. Rod OD lower with RP, at all locations. However, rod OD did not correspond to sensitivity.	Appears to be two groups with varying ratios of OD loss: sensitivity loss. Autosomal recessive RP characterised by log-linear dependency of threshold on rhodopsin loss. Whereas dominant RP shows a direct relationship between the two. Does stray light affect the above relationships?	Estimate stray light at 15% - higher than previously thought. Assumed that the fraction of stray light used to calculate rhodopsin was dependent (negligibly) on retinal eccentricity. Not clear where retinal loci are, appears to be 6, 10, 18 and 25^0? Temporal? Isolates stray light as a problem. This would have been a painstaking investigation using a spot densitometer.

					A 2nd retinal locus was investigated. Above was repeated on normal.			
27	(Fulton and Hansen 1987)	Relationship of rhodopsin to scotopic sensitivity in chloridaemia. Modified Florida Densitometer	2 participants with chloridaemia age 12 and 29 21 controls age 21-29.	560nm	Standard bleach 15^0 at 6.2 log (scot) and, measure 2^0 at pre-determined locations. In abnormal subjects, retinal locations were specific to areas in retinotopic map that gave poor field results and those that gave normal. 5^0 measuring light 5 repeats averaged together (mean) per person.	Highest OD (mean of 0.16) found at 18^0 temporal (in normal participants).	Low scotopic sensitivity is not proportional to rhodopsin loss. Large areas of sclera could cause an over-estimation of rhodopsin – the authors feel the difference isn't big enough.	vertical axis (only paper). Repeated or substantial bleach = lower OD (rhodopsin). Rhodopsin peaks on Horizontal mid line
28	(Fulton and Hansen 1988)	Cone pigment density and sensitivity with	3 participants with Ushers' syndrome and	560nm measuring beam	2 min Bleach with 10^6trolands.	Normal log TC is straight line. Ushers participant results	Due to increased separation of PR's from RPE. Normal	Stray light estimated 10-20%

		Ushers syndrome Modified Florida Densitometer	possibly related fundus dystrophy. Compromised scotopic sensitivity. 4 controls.	685nm reference beam Later measured regeneration with 520 and 600nm to check effect of photoproducts.	10sec bleach bleaching 95% of photopigments.	show slower second phase of recovery. OD was similar. 0.105 for normal participants and 0.101 for Ushers participants. After a short bleach, recovery is faster than for normal participants 520nm data similar to 560nm data. 600nm data similar to normal participants	participants OD range corresponds to Utrecht, although average is lower. Results from participants is similar to other x-linked retinal dystrophies – could become a useful clinical tool for young participants with suspect retinas. 600nm closer to normal suggests role of short wavelength photo-intermediaries	Wedge settings slow (up to 60sec to take) Prone to poor fixation. Why does regeneration change for 520/560 and 600nm?
29	(Baker et al. 1989)	Describe modifications to a current densitometer which can measure cone regeneration	1 participant	12 λ's with 10nm half bandwidths.	8ms exposures. Photon counting. Undilated.	Found an exponential curve for regeneration. OD not measured	This device can measure at dimmer levels. 'Accurate' comparison between pigment and dark adaptation.	What λ's were used? What is the size and area assessed? Scatter?

		Developed from Florida densitometer / Spectral						Showed variance with pupil size – not controlled.
30	(Baker et al. 1991)	Assessing stray light in densitometry Bakers 1989 'Florida' Densitometer. Additional fibre optic bundle inserted into photocathode.	3 participants – all with significantly different regeneration curves and OD. (previous experiments) 2 participants repeated 3x and 1 participant repeated 8x.	589nm 1.4^0 measuring beam. Location not mentioned, assume at fovea.	Dark-adapted for 30mins. Bleached for 1min with 5^0, 5.8log troland light. Recovery recorded over 13mins. 0, 50, 100, or 200 photons a sec were added to the photocathode. Computer simulation added 3, 10, 30, 400, 800/s to the results.	OD's varied from 0.13 – 0.2. Increased stray light = reduced OD = reduced individual variance. Regeneration not affected by stray light. OD underestimated by (average) 0.15 log units in this machine.	Currently OD's can only be used for experimental comparison with own techniques. Regeneration curves appear to be equal across the board. Higher OD's have higher under estimation	Still no spectral characteristics. Only at 589nm where cone reflectance is quite high and stray light relatively low. Retinal location?
31	(Baker et al. 1991)	Dark adaptation, photopigment regeneration and age	58 participants for dark adaptation.	Measuring beams 589nm and near IR. Alternating.	15mins dark adaptation period. 1 min baseline measurement, 1 min 5^0 log	Slowing of regeneration curve with age (~12.6 sec/decade).	Pigment regeneration rate contributes to dark adaptation. Sensitivity and OD decrease with age.	Foveal cone dark adaptation and age not been investigated before. OD not recorded?

		Bakers 1989 'Florida' Densitometer. The intensity of the measuring beam can be adjusted by participant	60 participants for pigment regeneration 31 participants both. All healthy eyes. Aged 10-78. Longitudinal data for one participant, previous data overlaid.		5.8 td bleach light, 13 min recovery recording. Data averaged every 10s for 1st 4mins then every 60secs for the remainder. Same procedure for DA and pigment regeneration. No Dilation	Greater variance with age? Although lots of variance throughout age-range. Pigment regen and DA follow same trend with significant correlation. Longitudinal data follows same trend. ~96 sec TC at age 40	The increased variability with age suggests the sudden change often seen with age, with pigment recovery rate decreasing slowly before 50 and quickly after 50.	
32	(Sieving et al. 1995)	Testing rhodopsin levels in participants with reduced night vision and RP in family. Modified 'Florida' machine	1 participant 38 year old proband. 4 normal participants?	530nm and 590nm measuring beams. 880nm reference beam – used separately.	7^0 measuring field and 9.1^0 bleaching field. Bleached with either white light or monochromatic (choice of ten 10nm wavelengths) Measurements taken 17.8^0 temporal.	Regeneration time constant of 288sec. With 590nm normal OD range 0.24-0.49. With 530nm normal OD range 0.16 ±0.04.	Difference in OD between 530 and 590nm is due to metarhodopsin I II & III. Discussion largely irrelevant to densitometry.	590nm used to minimise distortion from metarhodopsin I II & III? Proband: a person serving as the starting point for the genetic study of a family

		Spatial.			2secs intervals between recordings.			

Utrecht device

33	(van Norren and van de Kraats 1981)	Describing a new densitometer, the Utrecht I. (A spot device).	1 participant	16 wavelengths, evenly distributed across the visible spectrum. Reference 711nm.	theory and description of the device only. Description of device, a modified camera. Capable of spectral and temporal resolution due to the filter wheel and computer processing of the data. Imaging optics were modified to reduce intra ocular stray light		Useful for measurement of fast cone kinetics. Minimised stray light, although still present.	Spot densitometer. Use a bite bar, nose piece and temple pads to ensure head alignment.
34	(Smith et al. 1983)	Human cone pigment kinetics. Utrecht I device	2 normal participants 5 deuteranopes 1 protanope Age range 20-40	Measuring 554nm, 535nm or 605nm. Reference 711nm.	3.8^0 bleach and 1.8^0 measuring fields. Dilated. Central location. 2min Bleach at 10^6TD.	OD ~0.3 (min 0.26/ max 0.36 ~3% bleach from measuring lights. ~99% bleach from bleach light.	Utrecht machine sensitive and accurate. Deemed stray light not to be a problem. Data agrees with previous studies.	Show an OD range from 0.25-0.39 with the same input into various equations. Lots of scatter info/equations. Assumed 6% stray light

					Regeneration measured for 7mins. Photolysis measured with either a 'step up' or step down (see paper). Repeated within one hour. Finally bleach of either 2 min or 10sec followed by 6min regeneration measurements. Cycled 2min/10sec bleach's with 6min recoveries on 4 repeats in a row	70sec TC for 10sec bleach and 140 sec for 2min bleach.	Rate of recovery not constant but accelerates with time – not significant enough to rule out linear models.	
35	(Keunen et al. 1987)	Density of foveal cone pigments with age. Utrecht I device	55 healthy participants (used 75 eyes). On 34 data sets (29 participants) proved accurate enough to use.	Reference beam 711nm Measuring beam 554nm. Bleach cut off below 530nm by filter.	3.8^0 illuminated. 2.5^0 recording diameter. Dilated. Bleach 2min 6logTD.	54% of data sets didn't meet requirements – mean age of discarded participants – 64. Regeneration reduced with age.	Changes in OD – PR changes or increased scatter? Densitometry does not differentiate between factors.	Plenty of disagreement whether densitometry can pick up changes with age. Elderly struggled to fixate, had denture problems on bite bar etc. (discarded these sets).

			Resulting age range 39-79. 1 deuteranope.		Measured at 30s intervals for 6-10mins after bleach cessation. Re-bleach. Data discarded if the two bleach values weren't within 0.05OD.	OD only significant different 60+	Favour reduction in cones as cause of changes. Significant difference with Kilbride – likely due to the illumination field size.	Micro-spectrometry of foveal cone density/age?
36	(Coolen and van Norren 1988)	Cone photopigment kinetics, with respect to Rushton-Henry model Utrecht I device	2 participants Normal CV	554nm	Measured 2.5^0, 3.5^0 illuminated. Dilated Repeated flash bleaches.	Bleach history slows regeneration.	A small store of 11-cis- retinal is utilized following a flash bleach. This store is exhausted with exposure to successive bleaches.	Attempts to explain the differences in regeneration kinetics following exposure to flash and equilibrium bleaching as well as the effect of 'clearing' bleaches. Of relevance for flash bleaching experiments.
37	(Keunen et al. 1989)	Densitometry in acute posterior multifocal placoid pigment epitheliopathy (APMPEE)	6 participants with APMPPE and 23+10 age matched Controls	Measuring beam 554nm Reference beam 711nm	Dilated. 2min Bleach 10^6 TD. Measurements at fovea and 5^0 temporal to fovea.	Normal results: Foveal OD = 0.32 Tau (τ) = 99sec Parafoveal OD =0.05 Tau (τ) = 115 sec.	Allows objective monitoring of participant recovery.	Inconclusive Parafoveal fixation. Densitometry proved useful for the monitoring and

		Utrecht I device			Re-bleach. Serial tests, repeated during course of pathology.	Most APMPPE participants showed reduced OD and increased regeneration. Both improved with progression. Only participant 3 showed normal OD after 12 months. 4 participants showed normal TC's after 12months.	Steroidal treatment ineffective for APMPEE. Parafoveal results inconclusive – suggests difficulty in fixation and measuring regeneration in that region. Possibly hints at Rod involvement too.	assessment of slowed regeneration kinetics.
38	(van Norren and van de Kraats 1989b)	Attempt to design a small user friendly densitometer. The Utrecht II device (a spot device)	17 participants Age 20-45	16 λ's spread across visible spectrum. 419nm and 730nm used as reference.	Can choose from 2.3^0, 3^0, 4.5^0 and 6.9^0 input beams. Recording beam via adjustable diaphragm and set to 25% less than input beam. Foveal alignment / 16^0 horizontal. Field size 2.4^0 / $5.4^{0.}$	Foveal OD between 0.35/0.49 Rod OD max 0.16 Time constant of recovery at fovea = 100sec and 300sec at 16^0 alignment.	Decreased entrance pupil (1.2mm) increased OD by 0.12	Acknowledgement of the limitations of previous densitometers. Blue light used to aid fixation during dark adaptation following bleach. Decreased pupil size aided with stray light.

					Bleach 2mins / 3mins. Light off (DA) 8-15mins (depending on age / health etc) / 32mins Bleach on 2-3mins / 3mins Recording throughout.			
39	(Liem et al. 1991)	Rod photopigment changes with age / comparison to histological studies. Utrecht II device	44 participants age range 12-78, healthy. >40's pseudophakic and clear lens participants compared.	15 λ's from 380-670nm.	16^0 temporal to fovea 4.5^0 Bleached for 3mins Dark adapted during measurement. After 7-10mins Participant allowed to lean back (remaining in dark). Resume position carryon on measuring. 7-10mins later bleach for 3 minutes. The whole procedure takes 40mins	OD higher for >40's (~0.21) than for <40's (~0.18). No gender differences. No statistical difference between IOL and clear lens. Time constant increases by 28secs/decade ±8secs.	Raised OD's due to thicker and longer ROS's.	Why carry on recording during break? 40mins long time. What effect does the break have?

40	(Bruggen et al. 1992)	Foveal cone photopigments in myotonic dystrophy (MyD). Utrecht II device	12 participants with +ve family history of MyD 8male / 4 female. Age 12-39 Some show minor lens opacities. 12 age matched normal participants.	Measuring beam - 554nm (assume 711nm reference beam)	2.8^0 illumination field. 2 min bleach 5.6logTD. Regeneration measured. 2min re-bleach.	Mean MyD OD 0.29. Mean normal OD 0.38. TC of 66s for MyD participants and 69s for normal participants	Densitometry shows subclinical change in early MyD – possibly due to increased stray light?	Assume in fovea region. Also appear to have done some peripheral measurements – not in methods.
41	(Berendschot et al. 1996a)	Investigating the tapetum like reflex with reflectometry. (female, carriers of RP) Utrecht II device & Homemade SLO device	3 carriers of RP age 25, 22 and 46. Participants 3 (46) couldn't finish tests. 10 normal participants.	13 wavelengths on Utrecht machine SLO uses 514nm only	Illumination field 1.9^0 and recording field 1.6^0 for fovea and 2.8^0 – 2.4^0 for periphery. Measurements taken at fovea, 4, 8 and 16^0 temporal.	Raised foveal reflectance in carriers below 550nm – normal above 550nm. Raised temporal reflectance (8^0) below 600nm – normal above.	Assume PR OS most likely source of tapetal reflex – due to the changes in reflectance below 600nm and the stability above 600nm. Blood is a steady absorber of light above 600nm, so	Eastman 6080 is spectrally flat. 16^0 temporal shows same 'kick' up in OD at very lowest wavelengths as our preliminary data – why? Not found at other locations.

					Measured bleached and DA. Time regen not recorded. 10 foveal Normal measurements. 4 temporal (4^0+16^0) normal measurements. Spatial measurements taken with SLO – central 23x18 of retina.	8^0 max OD at 520nm. Density images from SLO show foveal peak.	the cause of the reflections must be anterior. Have suggested OS discs over other anatomical features.	Used both Spatial and Spectral machines in this paper Was the SLO device that described in (van Norren and van de Kraats 1989a), not clear. Discussion of blood as crucial absorption layer. Highlights potential difficulty of technique for participants with pathology
42	(Berendschot et al. 1996b)	Foveal cone mosaic and visual pigment density in dichromats Utrecht II device	27 participants 10 colour normal participants, 10 protanopes and 7 deuteranopes	16 λ's spread across visible spectrum. 419nm and 730nm used as reference.	Bleach field 1.9^0 and measuring field 1.6^0. Measured centrally and at 2.5mm from pupil centre.	Absorption curves differ between trichromats and dichromats. OD higher for normal participants (0.44) than for protanopes (0.31) and deuteranopes (0.35).	Empty space model rejected, replacement model favoured. Limited dichromat data available in literature – all very variable.	Colour defectives have less MP than colour normal participants.

						OD peak at 552nm for normal participants, 535nm for protanopes & 558nm for deuteranopes.	A lower visual pigment density is accompanied by a lower MP density.	
Scanning laser ophthalmoscope devices								
43	(van Norren and van de Kraats 1989a)	Description of a purpose built SLO densitometry device Utrecht SLO device.	1 participant	514nm measuring. 633nm bleaching (selective cone bleach)	Beam area 0.9^0, area scanned 23^0 H and 18.5^0 V centred between fovea and ON. 3x2 binning. Dilated. 4 DA images taken. Bleach 2 min. 4 Bleached images taken.	Highest OD at fovea, lowest at ON. At fovea OD = 0.35-0.45	OD extremes due to bleaching light of 633nm (bleaches 90% of cone pigment and 25% rod pigment). Results repeatable (with experienced user) & comparable to Utrecht model	Small exit pupil resulted in worse retinal resolution. No regen curve, only OD – although of little consequence when binning is included. Images were not re-aligned. Less stray light than previous models. Limited opportunities for spectral analysis.
44	(Elsner et al. 1992)	Reflectometry in retinal tears	4 participants with resolved	594mm	Dilate	Peak normal foveal OD 0.2-0.45.	The technique used in this paper minimizes	Good section on Theory.

		and detachments Research SLO densitometry device.	posterior pole retinal detachments. VA in ¾ returned to normal levels. Normal controls.		15min dark adaptation period Aligned with 830nm light. Steady bleach 2mins with 5.2logTD. At initial exposure 4 consecutive images are recorded, at 1min intervals. Images were averaged together.		problems specific to retinal densitometry. Cone OD from densitometry and psychophysics complement each other. Simple test – could be of clinical use.	Thorough and decisive 830nm aligning light shouldn't bleach pigments, but how does this affect the focus?
45	(Elsner et al. 1993a)	Mapping cone photopigment OD by densitometry and colour matching. Research SLO densitometry device, (Elsner et al. 1992)	7 participants, 21-55years old, Normal CV used for both techniques. 9 extra participants for colour matching only.	Reference beam, 830nm. Bleach beam, 594nm.	Dilation 15min dark adaptation period Alignment with 830nm 23^0 bleach at 5.2logTD 4 measurements taken at initial exposure, then with 1min intervals till	Central OD dip due to foveal reflex in young participant (artefact). Highest OD recorded about 0.3. Appears to decrease with age. Noise increases with eccentricity. Follows shape of psychophysics, lower magnitude.	Comparable results from colour matching and densitometry at fovea. Colour matching always higher. Difference at 4^0 due to decreased cone coverage.	Great summary of densitometry theory Suggests large individual variance between cone lengths. Achieved foveal cone pigment mapping through selective bleaching.

						OD at half peak by 2^0 eccentricity. By 4^0 many participants had no signal with densitometry.	Large individual variance with Cone orientation, extinction spectra and optical density affect both techniques. Can't prove aging affects peripheral OD (need more participants)	
46	(van Meel et al. 1993)	Investigating multiple evanescent white dot syndrome with SLO densitometry. Utrecht SLO device. Utrecht II spot device.	One participant with multiple evanescent white dot syndrome. (male, 28)	SLO 514nm images. Utrecht II - 16 λ's spread across visible spectrum.	Central 20^o images were recorded with the SLO densitometer. Rod and cone density was measured using the Utrecht II at central and 16^o temporal locations.	Density maps revealed localised regions where visual pigment was absent in acute disease stage. These regions remained faintly visible in the resolved disease stages. Foveal cone OD normal.	multiple evanescent white dot syndrome presents due to a metabolic disturbance at the level of the RPE-photoreceptor junction.	Area of pigment loss visible with the image shows that either SLO is less effected by stray light, or that the spot reading at 16^o missed one of these localised lesions.

						Rod OD was reduced and showed an extended time course of regeneration. This returned to normal with resolution		
47	(DeLint et al. 1996)	Foveal Cone function in participants with VA loss. Utrecht SLO device.	14 participants with unknown central VA loss. 15 normal participants.	514nm measuring. 633nm bleaching (selective cone bleach)	Central 22^0 x 18^0 – 256x256 pixels. Macula (8^0x6^0) and Fovea (2^0x2^0) analysed further.	Mean 'normal' OD = 0.28-45. 3 participants with reduced OD. (0.05, 0.20, 0.20) although the 3rd participants had normal OD at 3^0 and beyond.	Cone dysfunction Responsible for <VA in 3 participants. Likely: Loss of Cone PR's or PR disorientation. Densitometry may be useful with early PR dystrophies.	Small measuring beam on SL0 (0.43^0) reduces stray light and increased OD. Densitometry being used to investigate pathology with increasing regularity. Produced foveal visual pigment maps.
48	(Marcos et al. 1996)	Investigation of foveal cone spacing. Rodenstock SLO	3 participants	488, 514 and 594	~central 30^o imaged.	Cone visual pigment density decreased away from foveal peak in line with cone photoreceptor density	Photoreceptors and visual pigment are proportional to each other.	Densitometry performed using a commercial device, albeit with modifications.

49	(Elsner et al. 1998)	Foveal cone pigment distribution with MP distribution. Research SLO densitometry device, (Elsner et al. 1992)	11 healthy participants Age 31-59	488, 514, (MP) 594 (visual Pigments) and 830-860nm (sub retinal) measuring lights.	Dilated. 15min dark adaptation period Large field size (28.6^0x23^0) Bleach with 5.4logTD Recording regeneration immediately and 1,2,3+4mins after bleach.	Beyond 6^0 cone OD too low to measure accurately. 3 groups depending upon cones and MP distribution. Retinal defects correspond to photopigment defects.	Largely irrelevant to our studies. But does interphotoreceptor space increase with age (i.e. increase scatter) Discusses vague foveal cone alterations with age – nothing quantifiable.	No OD's or TC's given. Only fundus maps.
50	(Tornow et al. 1999)	2 methods of assessing photopigment density with retinal degeneration (including SLO densitometry)	2 participants with Cone dystrophy and RP. 6 control participants.	IR – 780nm 514nm for bleach and measuring laser. Aligned using IR	30min dark adaptation period. Dark adapted data recorded. Bleach 4mins. Field size 34^0x24^0.	Normal: Max OD 0.35 at fovea. Min OD 0.05 (at -3^0). Mean OD for central 2^0x2^0 is 0.30. RP: Central OD = 0.16 no density found beyond central 5^0. Cone Dystrophy: Central OD <0.05.	Discusses physiological differences between the 3 participants types. One unusual finding of rods in fovea of cone dystrophy participants? Not discussed	Noise increases with nasal eccentricity. Doesn't explain increase in OD with temporal eccentricity. Or the drop in M cones at fovea?

		Modified Rodenstock SLO device			Also focused on central 2^0x2^0. Use variable averaging of pixels.	Peaks at 13^0 temporal with 0.23 and 10^0 nasal with 0.15.	SLO works well to define areas of damage, could be used to assess treatments? Difficult to get spectrum data – limited by λ's.	
51	(Hofer et al. 2005)	Examine foveal cone mosaic Rochester AOSLO device	8 participants all normal CV. 7 male 1 female (known protan carrier)	560nm	Doesn't describe densitometry methods.	Large range - L:M ratio 1.1:1 to 16.5:1 (52.7–94.3% L) for the normal participants and (0.37:1; 27% L), for the carrier.	irrelevant	Poor description of densitometry methods. Used as a means of confirming other techniques.
52	(Theelen et al. 2008)	Modified Heidelberg SLO device	1 normal participant, 3 runs. Repeated tests on participants with macula dystrophies – stargardts/ cone/rod	Reference 787nm Bleach & measuring 488nm.	Central 30^0 bleached. Central 25^0 measured. Dilated. 20min dark adaptation period. 60 second bleach	OD at 488nm 0.11. Lower OD at fovea.	Stargardts showed areas of increased (?) FAF and normal FAF (damaged and un damaged). Reduced OD due to high angle of incidence of lasers (at peripheral locations).	OD much lower than compared to other SLO densitometers. – likely attributable to the wavelengths investigated.

			dystrophy/ chloridaemia		Repeated central and at 15^0 temporal.		Lower OD at fovea due to MP and 488nm. Would use 532nm in future experiments.	
53	(Sekiryu et al. 2009)	Evaluation of Autofluorescence Densitometer Auto Fluorescence densitometry/ SLO	20 control participants (16 male & 4 female) Age 26-73. 14 diseased eyes. 3 Macula hole 4 BRAO 3 BRVO 4 CSC	488nm	Dilated.30^0 imaging field. 30min dark adaptation period 40sec recording period. External fixation. Sessions repeated after 1 month on all participants.	OD concentric in all normal participants (as is rod dominated). OD affected/reduced, usually to nil in all diseased participants.	Technique contains problems with bleaching.	Hindered by macular pigment and thickness of sensory retina. Vague description of methods and device used. What was the bleach?
54	(Ojima et al. 2011)	Investigating central serous chorioretinopathy, in particular macula serous RD (SRD)	16 participants 14 male 2 female Age range 31-71.	488nm	Discussed in a previous paper. Dilated (tropicamide & phenylephrine).	OD change concentric pattern in 10 controls. No total OD given – highest marked as 100%.	Photopigment density reduced in region affected. Remained low after VA returned to normal. Is this related to participants whose VA improves	Single wavelength only. Vague description of device, methods and results.

		Auto Fluorescence densitometry/ SLO	All had SRD >3DD at fovea in acute phase. 10 controls. (31-55)		30min dark adaptation period. 40Sec recording time. 30^0 recording area. 6x6mm square centred on fovea, divided into 9x9 grid. Intensity given grey scale value. OCT used to mark CRD boundary	All SRD showed a drop in OD to 0% which regains after resolution.	back to normal, still c/o problems?	
55	(Morgan and Pugh 2013)	SLO measurement of fundus (rhodopsin) reflectance and autofluorescence. SLO Optos200C and own design	12 participant – age 19-63. 3 male and 9 female	532nm and 633nm.	Undilated. 4.8^0 of retina bleached centred 16^0 temporal – although SLO machine measures 61^0 x 61^0. 30min dark adaptation period	Used van De Kraats model of foveal fundus reflectance. Rate limited recovery of 7.3% and 9% for 2 subjects. Mean OD (RDR) 0.32 +/-0.04.	Rhodopsin reflectance can be measured with a clinically available SLO. Results consistent with previous experiments.	Bleach and measuring systems different. Limited by only two wavelengths, but can have a large field of view – this machine doesn't. Comparing signal from bleached area to annulus

		ganzfeld bleach bowl.			3SLO scans – 1min intervals. 8sec bleach 7.7 log scot TD. Repositioned on the SLO for measurement – 10sec delay. 3 separate methods: bleach VS intensity (one single scan post bleach; bleach intensity varies), bleach/recovery (scans at 5min intervals for 25mins), autofluorescence imaging (same as above, but with 532nm only).	Autofluorescence reduces at same/similar rate to rhodopsin. Flash half bleach constant re-addressed and shown to be 0.3 log scot td higher than previously thought.	Does autofluorescence increase with bleaching? As a by-product? Autofluorescence is increased with some retinal diseases; however, is this just because rhodopsin levels are reduced/regeneration slowed so it becomes more visible? Densitometry is the only way to determine between less rhodopsin and more autofluorescence.	around this area improved inter participant repeatability! Good at measuring rods, however the wavelengths make measuring cone PR problematic. Half bleach constant different to original papers.
56	(Sabesan et al. 2015)	Characterise the optical properties of	4 colour normal 1 protanope	Measuring beams - 543nm and 842nm.	Selective bleaching of different cone types to	M- cone OD = 0.34 (mean)	Improvements seen in AOSLO over AO fundus image related	Adaptive optics utilised in human densitometry to

		and spectral types of the human cone photoreceptor matrix using bleaching kinetics Rochester AOSLO device		Bleaching beams 470nm, 543nm and 680nm.	separate contribution from each photoreceptor type. Central 1.2^{o} of retina imaged. (fovea only)	L- cone OD = 0.32 (mean) Improved classification of photoreceptor matrix using (AOSLO) densitometry over (AO) fundus images	to improved image resolution and additional the use of bleaching kinetics. Inner retinal light scatter contaminated (attenuated) OD results.	isolate photoreceptor types. Retinal imaging densitometry on a micro scale.

Wide-field imaging based devices

57	(Kilbride et al. 1983)	Investigation of cone pigment density in spatially resolved regions of the retina. A modified Zeiss fundus camera.	Six participants	14 measuring beams spread between 460nm to 700nm. Bleach 605nm.	15 minute dark adaptation period. Dark adapted reflectance measured (3 cycles). 97% cone pigment bleach. Bleached reflectance measured (3 cycles).	Pigment density maps produced over the central 6^{o}s. Central 2^{o} OD range 0.24 – 0.28. 2^{o}-4^{o} OD range 0.013 – 0.18 4^{o}-6^{o} OD range 0.08 – 0.11	Use of a bright red light allows selective bleaching of foveal cone pigments, with minimal effect upon rhodopsin and S-cones (as evidenced by the similarity between the normalised absorption spectra	First topographical maps of pigment density produced. Simultaneous bleaching and assessment of rod and cone density not possible with this bleaching method. Small imaging field (6^{o}

					Images analysed as central 2^o 2^o-4^o annulus and a 4^o-6^o annulus.	Peak of absorption spectrum at ~560nm. Little change with eccentricity. Horizontal 'cone' OD shows a clear peak and decrease to almost nil by 3^o, similar to Osterberg (Osterberg 1935).	from the difference locations).	
58	(Faulkner and Kemp 1984)	Assessment of Rhodopsin and of a TV imaging reflectometry TV Based imaging reflectometer Spatial information with repeated	2 participants One normal One RP	470, 500, 560, 598, 670nm	25^0 area of retina measured, centred 30^0 temporal to fovea. 95% bleach. Measurements taken at 2, 4,8,16 and 25mins after bleach. Re-bleached for final (25min) recording	4 min half regeneration time. Peak at 500nm, but affected by blue photoproducts (authors suspect – MRIII) 560nm OD = 0.06 RP shows up clearly.	Results are from rhodopsin. Compare well with Ripps et al 1978. 560 and 600nm repeatedly higher than expected – stray light? Cones? Difference between normal and RP due to OS length or density.	OD at 500 unknown appears to be 60% more than at 560 ~ 1.4? Stray light affects image quality. How well will each image be aligned after each 'break' from bite bar.

		measurements over time.					TV based systems better for spatial resolution, worse for sensitivity	
59	(Kilbride et al. 1986)	Effect of age upon foveal cone pigment OD TV based imaging reflectometer	19 healthy subjects with no ocular media and good VA. Age 22-70 8 Female, 11 Male.	460-700nm at 20nm intervals (14 λ's)	15 minute dark adaptation period. Dark adapted reflectance measured (3 cycles). 97% cone pigment bleach. Bleached reflectance measured (3 cycles). Central 2^{o} imaged.	Decrease in cone OD with age. Spectral peak at 560nm. Average spectral peak for <40's = 0.24 and for >40's = 0.16. Range from 0.08 – 0.28	Results differ from (van Meel et al. 1993). Stray light un-accounted for. Similar results to anatomical and psychophysical studies. Effect of stray light found to be significantly insignificant with age. Reduction in cone numbers rather than structure.	Is it similar to psychophysical studies? – Peak at 560nm?

60	(Kilbride et al. 1986)	Foveal cone pigment OD in RP TV based imaging reflectometer	14 participants with RP. 8 participants with dominant inheritance., 2 with recessive inheritance and 4 with Ushers syndrome.	460-700nm at 20nm intervals (14 λ's)	15 minute dark adaptation period. Dark adapted reflectance measured (3 cycles). 97% cone pigment bleach. Bleached reflectance measured (3 cycles).	Dominantly inherited RP showed normal or only slightly reduced cone pigment density. Recessively inherited RP significantly reduced cone pigment density	RP patients have differing patterns of degeneration depending upon their genetic condition. Not possible without a spatial device.	Only investigated central retina, despite using an imaging device Don't present maps of RP degeneration. Reveals the ability of spatial densitometry to monitor/diagnose outer retinal pathology.
61	(Kemp et al. 1988)	Effect of vitamin A on rhodopsin function with chrons and primary biliary cirrhosis. The TV-based broad-field imaging fundus reflectometer Faulkner and Kemp / 1984 imaging device	3 participants suffering from night blindness 2 with primary biliary cirrhosis. 1 with chrons. Controls used. Unknown quantity.	470, 500, 560, 598, 670nm	Dark adaptometry performed 2hours prior to reflectometry. 25^0 measuring beam. 5^0x5^0 binning. 45 sec bleach. Reflectometry measurements taken over 'a time similar to DA results'. 2^{nd} bleach for 2^{nd} set of light adapted results. Serum vitamin A levels recorded.	Low vitamin A levels showed slower regeneration constants and lower OD. When serum vitamin A normal results were within normal range	Vitamin A levels determine rate of rhodopsin regeneration, although unless severely depleted final OD is within normal range, but regeneration constant is reduced. Eventually cone regeneration will be affected.	What's the benefit of 2^{nd} set of light adapted results? Few reflectometry results for participant 3 with abnormal vitamin A levels. Reflectometric results compared well to DA results. What affect will vitamin A levels have upon our studies?

62	(Sandberg et al. 1999)	Cone pigment regeneration in RP patients. Video imaging fundus reflectometer	13 participants with RP. 7male, 6female. Age 39.7 ±3.1 11 normal.	560nm measuring beam. 540nm bleach.	15^0 measuring field. 8^0 bleach field 6.4 log TD. 15min DA Record. 2min bleach. Record for 15mins (with increasing brightness – up to 5.1 log TD). 10min break and repeat. Central 2^0 used.	TC's 172 s with RP / 118s in normal participants. Mean OD of 0.19 - range from 0.05-0.24	Reduced TC correlates with reduced VA recovery after bleach. Even stronger for certain mutations. Is delay in VA recovery or pigment regeneration a better assessment of PR cell death?	Why use such a large field if only assessing central 2^0? Test beam passes through edge of pupil (too large) = reduced OD. PR cell death isn't the only cause of reduced TC (maybe in RP).
63	(Prieto et al. 2005)	Single light pass absorption of photopigments by means of lipofuscin fluorescence Burns imaging reflectometer. (described in 1995)	3 normal subjects age 30-36. 1 participant is deuteranomalous	543nm. 592nm bleach. Seem to have used more, but not defined. (See Burns 1995?)	18µm pinhole, conjugate with participant pupil. Location within pupil controlled. Measurement from 2^0 around stimulus. 8^0 bleach. Recorded DA pigments, DA fluorescence, bleached pigments, bleached fluorescence. DA for 30mins. Bleach was left on between recordings to retain constant bleach state.	Fluorescence is sensitive to bleaching. (is higher after bleach). Fluorescence provides noisy but essentially flat OD. Pigment OD peaks at the optical centre (OSC).	'Proves' light must pass through cones on both directions. Light reflected from deeper layers shows no direction. Light that escapes OS is not re-coupled with directional light from OS. Fluorescence allows investigation of signal light passes.	High signal:noise ratio with lipofuscin? Varying amounts of lipofuscin between individuals. Made up of hypothesis and theories. Some useful equations.

					3 repeats, each ~1 month apart.			
64	(Bone et al. 2007)	Distributions of macular pigment, visual pigment and melanin. With regard to AMD. Self-made Topcon non – mydriatic. DXC970MD video camera. (based on Florida machine)	22 participants age 18-24	460nm (B) 528nm (G) 610nm (R) 670nm (reference) Half band width 20nm	Measurements from central 15^0. 1.5^0 4000 td light alternating between 540nm & 460nm. Not dilated. Compared to HFP. Repeated 6-8 times OD measured as difference between DA and Bleached (3mins at 5.5 log troland) photopigments.	Cone OD – 0.46 DA and 0.16 Bleached Rod OD – 0.29 DA and 0.09 Bleached.	Quick MP measurement. Cheap and well repeatable machine.	Omitted Scatter from model Well written and useful background, but mainly covers MP and only briefly touches visual pigments. Good eccentricity data.

Other devices

65	(Horio et al. 1999)	Kinetics of cone photopigment in (non-pathogenic) myopia	45 participants. 22 males, 23 females.	562nm measuring beam. 803nm reference beam.	Central 3^0 of fovea bleached and central 1^0 measured. Rx corrected over -4.00 with contact lens.	Mean DD of 0.37 ±0.10 No correlation with DD and Rx	Myopia itself does not appear to damage the photoreceptor layer and arrangement and	Few other investigations to back up the myopia TC correlation, but does back up with ERG, EOG and photo stress.

		See Saito for full description Fundus camera modified. Time data only.	Rx range from +2.00DS >-14.50DS. Age range 18-47. All eyes healthy.		Dilated 5min 6log (phot) td bleach Record continuously for 7mins.	TC increased as Rx increased. Mean TC not stated.	proportion of PR's remain constant despite axial length. Myopia may cause a functional disorder of RPE which is displayed as a decreased TC.	No precise details of actual machine used. (Saito is in Japanese)
66	(Okamoto et al. 2004)	Foveal pathophysiology of Vogt-Koyanagi-Harada. Specifically cone regeneration Foveal cone densitometry (FCD). Device described by Horio et al	3 participants (6 eyes) with Vogt-Koyanagi-Harada. VA 0.1 or better	Measuring beam 562nm Reference beam 803nm	Bleached central 3^0, measured central 1^0. Bleached for 5mins, recorded for 7mins. FCD as above was done at random monthly intervals.	Photopigment kinetics begin to improve after 15months Improvements in 3/6 Final OD 0.21, 0.41, 0.29 Mean tau (τ) = 149 seconds	Poor pigment regeneration (up to 15months) due to inflammation.	Can't be sure if pigment kinetics returned to normal sooner due to spacing of tests. OD and Tau for participants with Vogt-Koyanagi Harada disease. No precise details of actual machine used. (Saito is in Japanese)

Appendix B. List of parameters in main thesis

Parameters used within thesis, in order of appearance. Followed by the parameters used to define the ocular reflection models.

C	Bias level of the EMCCD
X	Background light levels within the instrument
E	Quantum efficiency of the EMCCD
$S_0(\lambda, x, y)$	Black 'reference' signal at any pixel and wavelength.
$S_{DA}(\lambda, x, y, t)$	The dark-adapted camera signal at any wavelength, retinal location and time point.
$S_B(\lambda, x, y, t)$	The dark-adapted retinal reflectance, at any wavelength, retinal location and time point.
$R_{DA}(\lambda, x, y, t)$	The contribution of the dark adapted retinal reflectance to the final camera signal at any wavelength, retinal location and time point.
$R_B(\lambda, x, y, t)$	The contribution of the bleached retinal reflectance to the final camera signal at any wavelength, retinal location and time point.
N	Noise
S	Signal
$\Delta OD(\lambda, t)$	Double pass optical density calculated using equation 4.1, for any wavelength and timepoint,
D_r	Density of rod pigment present, calculated from the solution to Equation 4.2
$N_r(\lambda)$	Isolated, experimental rod absorption spectrum
D_c	Density of cone pigment present, calculated from the solution to Equation 4.2
$N_c(\lambda)$	Isolated, experimental cone absorption spectrum
K_m	Michaelis constant
W	Lambert-W function
r	initial rate of regeneration after a total bleach
σ	asymptotic density of the pigment
t	Time (seconds)
τ	Time taken for the visual pigment to return to $1 - {}^{1}/_{e}$ (i.e. approximately 63.3%) of it maximum value.
$\Delta DD(\lambda)$	Density difference (double pass), calculated using Equation 5.3
$S_o(\lambda)$	Camera signal immediately after bleach cessation (for all wavelengths)
$S_t(\lambda)$	Camera signal at any given time following bleach cessation (for all wavelengths)
p	Proportion of visual pigment present after exposure to a light source of known intensity (I) and duration (t_B). Calculated using Equation 5.1.
P_{eq}	Proportion of visual pigment present after exposure to an equilibrium bleach. Calculated using Equation 5.2.
t	The proportion of visual pigment present at a given time (t) after cessation of the bleaching source. Calculated using Equation 5.3.
I	Intensity, in scotopic trolands, of the bleaching source.
I_{Rh}	Intensity, in scotopic trolands, required to bleach 50% of the rhodopsin present in a fully dark adapted, healthy retina.
t_B	Duration of the bleach, in seconds.
τ_{Rh}	Time taken for rhodopsin to return to $1 - {}^{1}/_{e}$ (i.e. approximately 63.3%) of it maximum value.
$SL(\lambda)$	wavelength dependent 'scatter', calculated using Equation 6.2.
$50^o(\lambda)$	Stray light measured in the foveal region from a 50° field of illumination, for all wavelengths.

$0^o(\lambda)$	Stray light in the foveal region, estimated for a 0° field of illumination using linear regression, for all wavelengths.
$\Delta OD_{adj}(\lambda)$	Double pass optical density, for any wavelength and timepoint. Adjusted for a stray light component as in Equation 6.3 and Equation 9.18.
$\Delta ODmax$	The theoretical optical density present after a 100% visual pigment bleach.
$GS(\lambda, x, y)$	Camera signal measured from the grey calibration surface, for all wavelengths and pixel locations.
$WS(\lambda, x, y)$	Camera signal measured from the white calibration surface (BaSO4), for all wavelengths and pixel locations.
$GR(\lambda, x, y)$	Reflectance of the grey surface, calculated using Equation 7.1.
$S_{ME}(\lambda, x, y)$	Camera signal measured from the model eye measuring surface, for all wavelengths and pixel locations.
$S_{ME}100(\lambda, x, y)$	Camera signal measured from the model eye measuring surface scaled up to a surface of 100% reflectance using Equation 7.3, for all wavelengths and pixel locations.
$OR(\lambda, x, y)$	Ocular reflectance calculated using Equation 7.4, for all wavelengths and pixel locations.
$R_{ant}(\lambda, x, y)$	Pre-receptoral stray light, obtained from the solution to

Parameters used to define Model I

$OD_{media}(\lambda)$	Spectral shape defining the light absorbed by the human ocular media. Data obtained from Vos and van Norren (1974).
$OD_{mp}(\lambda)$	Spectral shape defining the light absorbed by human macula pigment. Data obtained from Snodderly et al. (1984).
$OD_{me}(\lambda)$	Spectral shape defining the light absorbed by human melanin. Data obtained from Gabel (1978).
$OD_{hb}(\lambda)$	Spectral shape defining the light absorbed by the haemoglobin present in the choroid (haemoglobin assumed to be 95% oxygenated). Data obtained from van Assendelft (1970).
R_{RPE}	Wavelength independent reflections from a surface positioned behind the photoreceptors.
R_{scl}	Wavelength independent reflections from a surface positioned behind the choroid.
V_{media}	A scaling factor, defining the amount of light absorbed by the human ocular media.
V_{mp}	A scaling factor, defining the amount of light absorbed by macula pigment.
V_{me}	A scaling factor, defining the amount of light absorbed by melanin.
V_{hb}	A scaling factor, defining the thickness (µm) of the haemoglobin layer present within the choroid.

Additional parameters used to define Model II

OD_x	Describing spectrally neutral light loss within the choroid of unknown origin.
S_{media}	Forward scattered light loss from the optical media.
$OD_{RPE}(\lambda)$	Spectral shape defining the light absorbed by human melanin. Data obtained from Gabel (1978).
S_{ch}	Forward scattered light loss from within the choroid.
$R_{scl}(\lambda)$	Wavelength dependent scleral reflectance, defined by Equation 8.2.
t_{ch}	Thickness of the choroid (µm), none haemoglobin portion.
V_{cc}	Thickness of the choriocapillaris (µm).

$R_{ch}(\lambda)$	Wavelength dependent reflectance from the choroid, defined by the simultaneous solution to Equations 8.4 – 8.6.

Parameters used to define the modified model

$OD_{media}(\lambda)$	Spectral shape defining the light absorbed by the human ocular media. Data obtained from van de Kraats and van Norren (2007).
$OD_{mp}(\lambda)$	Spectral shape defining the light absorbed by human macula pigment. Data obtained from Snodderly et al. (1984).
$OD_{me}(\lambda)$	Spectral shape defining the light absorbed by human melanin. Data obtained from Gabel (1978).
$OD_{hb}(\lambda)$	Spectral shape defining the light absorbed by the haemoglobin present in the choroid (haemoglobin assumed to be 95% oxygenated). Data obtained from van Assendelft (1970).
$R_{lens}(\lambda)$	Spectral shape defining the light reflected from the crystalline lens. Defined by a Rayleigh scattering function (see Chapter 6).
$R_{r\ in}(\lambda)$	Spectral shape defining the light reflected by the inner retinal reflections. Defined by Mie scattering curve (Jacques 2013) as an approximation of the data presented by Knighton (1989).
$V_{r\ out}$*†	Wavelength independent reflections from the outer retinal layers.
$R_{scl}(\lambda)$	Wavelength dependent reflections from the sclera. Defined by
V_{lens}*†	Scaling factor for the crystalline lens.
$V_{r\ in}$*	Scaling factor for the inner retinal reflections.
V_{media}*	Scaling factor for the lens reflection.
V_{mp}§	Scaling factor for macula pigment absorption. defined by Equation 9.4
V_{me}*	Scaling factor for melanin absorption.
V_{hb}*	Scaling factor for the thickness (µm) of the haemoglobin layer within the choroid.
V_{scl}*	Scaling factor for the scleral reflection.
age	The age of the participant, used to define the absorption of light by the ocular media.
R_{mod}	The modelled ocular reflection, as defined by the solution to Equation 9.14
$R_L(\lambda)$	The total amount of light returned from the crystalline lens. Defined in (Equation 9.8
$R_{R\ IN}(\lambda)$	The total amount of light returned from the inner retinal layers. Defined in Equation 9.10
$R_{R\ OUT}(\lambda)$	The total amount of light returned from the outer retinal layers. Defined in (Equation 9.11
$R_S(\lambda)$	The total amount of light returned from the sclera. Defined in Equation 9.13

*variable parameter, † Fixed at foveal value for parafoveal fit § pre-calculated

Appendix C. Spectral output from the Mark II LEDs

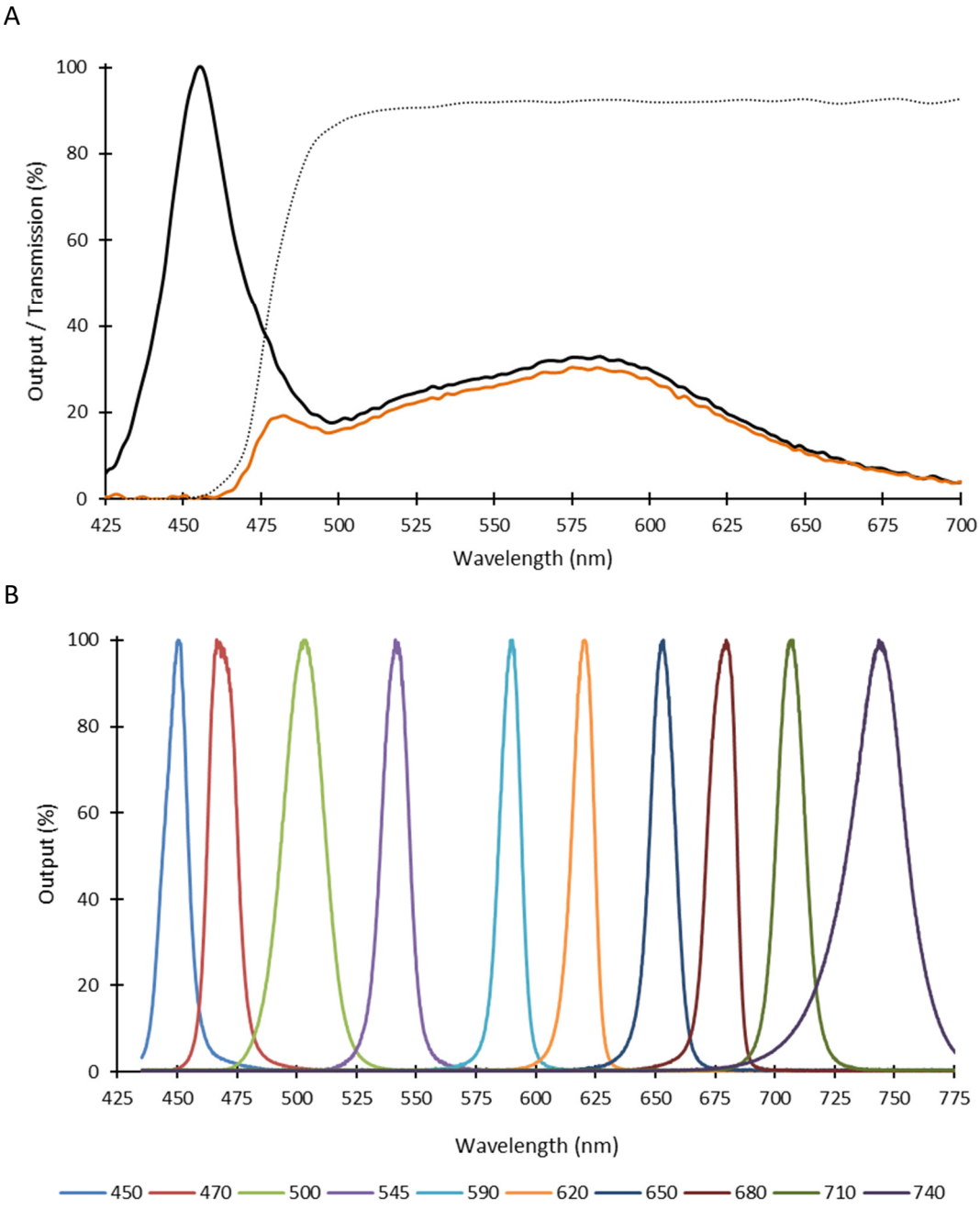

Figure C.1. Spectral output of the LEDs, measured using the Jeti Specbos 1201 (JETI Technische Instrumente GmbH, Jena) and normalised to peak wavelength. A) Presents the spectral output of the white light LED, together with the transmission of the Schott Glass filter and subsequent spectral output, as used in Chapter 5. B) Presents the output of the imaging LEDs, see Table 3.1 for peak output.

Appendix D. Calibration of a Maxwellian view system

The retinal illuminance provided by both the measuring and bleaching source was calibrated for each LED intensity used. All calibrations were carried out using an ILT1700 research radiometer (International Light Technologies Incorporated, USA; calibration certificate no. 607057219, date 06.07.2016), corrected to the C.I.E. human eye response with filter Y29295 (International Light Technologies Incorporated, USA). The calibration procedures were based on those described by Westheimer (1966) for a Maxwellian view optical system.

Equation D.1 provides a method of calculating the retinal illuminance (E, in photopic trolands) using knowledge of the luminance of the light source (B, in millilamberts), the distance between the light source and the reflective surface (x) and the reflectance of the surface (ř),

$$E = 10^7 \cdot B \cdot \frac{x^2}{\check{r}}$$

(Equation D.1).

Methods

Figure D.1 indicates the set up for the high intensity white light source (i.e. the bleach).

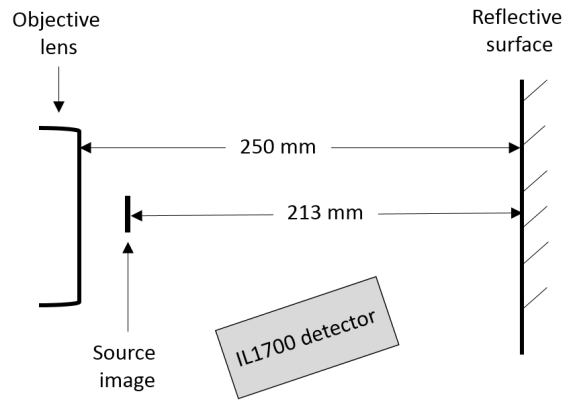

Figure D.1. Experimental set up to measure retinal illuminance (in photopic trolands). The IL1700 meter with lens and photopic filter are pointed at the reflective surface to get a reading in candelas m^2.

Plan white paper was used as the reflective surface. The reflectance of the paper was calibrated against the known reflectance of 3 Munsell chips of known reflectivity (90.0%, 84.2% and 78.7%), returning a value of 77.9% reflectivity.

To calibrate the dim illumination beam sources the luminance values produced were below the operating range of the detector. To more precisely work out what the luminance would be at one point in the illuminated field we can remove the lens (keeping the photopic filter in place) and alter the set up as per Figure D.2.

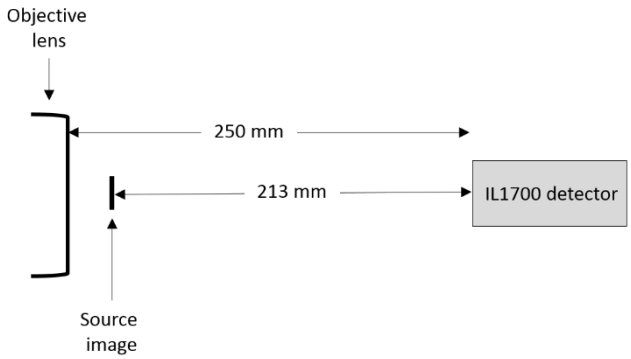

Figure D.2. Modified experimental set up to measure retinal illuminance. The IL1700 meter, with lens now removed but photopic filter still in place, was positioned so that the detector is in the plane once occupied by the reflective surface. The reading from the meter is no longer candelas m^2, but in volts, which was subsequently converted back to candelas m^2.

Conversion to retinal illuminance

The conversion factor between the two methods was obtained through measuring the luminance of the white light LED source using both methods. This give a conversion factor of 0.00461, as described by Equation D.2,

$$Conversion\ Factor = \left(\frac{\text{L'}}{\text{Ÿ}}\right)\Big/_{\text{þ}} = 0.00461$$

(Equation D.2),

where the Ľ is the luminance (candelas m^2) as measured using the method described in Figure D.1, the voltage (þ) as measured using the methods described in Figure D.2.

Westheimer's original 1966 equation uses the non-SI unit, the millilambert. As 1 millilambert is equivalent to $\frac{\pi}{10}$ candela m^2, to convert the returned value to millilamberts Equation D.2 was updated to Equation D.3,

$$Conversion\ Factor = (0.00461) \cdot \left(\frac{\pi}{10}\right) = 0.00145$$

(Equation D.3).

This allows

to be updated, to allow for a direct measurement of luminance in voltage, rather than millilamberts. Thus, the retinal illuminance (E, in photopic trolands) could be calculated for any luminance (Ƥ, in volts) using Equation D.4,

$$E = 10^7 \cdot [0.00145 \cdot \text{Ƥ}] \cdot 0.77^2$$

(Equation D.4).

Finally, for the calculation of scotopic trolands (Ë),

was used,

$$\ddot{\mathrm{E}} = \{10^7 \cdot [0.00145 \cdot \mathrm{P}] \cdot 0.77^2\} \cdot \varphi(\lambda)$$

(Equation D.5),

where $\varphi(\lambda)$ was the wavelength dependent photopic troland to scotopic troland conversion factor, as defined by Wyzecki and Styles (2000). Table D.1 provides the values used for $\varphi(\lambda)$.

Table D.1. Showing values used for the photopic to scotopic conversion factor $\varphi(\lambda)$

Wavelength	$\varphi(\lambda)$
449	29.800
469	18.490
503	7.570
541	1.450
589	0.215
620	0.048
653	0.016
678	0.011
707	0.000
743	0.000
Bleaching source	11.45
Filtered Bleaching source	2.587

Appendix E. Meta data configuration file

Each imaging procedure generated an excel readable .CSV configuration file containing the recording protocol used. This config file was accessed by IDL to deinterleave the dataset into the correct wavelength stacks, remove the images acquired during the bleach and perform the image registration routine. Further information includes the LED intensity used, the date, time and duration of the imaging procedure. An example is provided in Table E.1.

Table E.1 – An example configuration file, generated during the bleaching and subsequent imaging of participant HM for the investigations discussed in Chapters 8 and 9.

PARAM_ID	VALUE	TYPE	COMMENT
Date	19/09/2016	STRING	Date of data set acquisition
Time	19:15	STRING	Time data set acquisition began
DATANAME	C:\AMD\Data\HM 190916 bleach reflectance\HM 190916 bleach reflectance	STRING	Data Set Path\Name.
NFRAMES	4800	U16	Total Number of Frames in Acquisition. (including those acquired during bleach)
NSOURCES	10	U16	Number of L.I. Sources in Acquisition (not including bleaching source).
NBLEACH	300	U16	Number of bleaching Frames.
NCYCLE	450	U16	Number of cycles (through all selected sources).
XPIX	1000	U16	Number of pixels in x-axis (to be binned).
YPIX	1000	U16	Number of pixels in y-axis (to be binned).
XBIN	8	U16	Binning factor in x-axis.
YBIN	8	U16	Binning factor in y-axis.
XMEGPIX	125	U16	Number of resultant binned megapixels in x-axis.
YMEGPIX	125	U16	Number of resultant binned megapixels in y-axis.
LED.I0	63.8	DOUBLE	Intensity (%) of LED Source 0
LED.I1	30.4	DOUBLE	Intensity (%) of LED Source 1
LED.I2	17.76	DOUBLE	Intensity (%) of LED Source 2
LED.I3	98.36	DOUBLE	Intensity (%) of LED Source 3
LED.I4	81.31	DOUBLE	Intensity (%) of LED Source 4
LED.I5	22.47	DOUBLE	Intensity (%) of LED Source 5

LED.I6	63.2	DOUBLE	Intensity (%) of LED Source 6
LED.I7	34.5	DOUBLE	Intensity (%) of LED Source 7
LED.I8	47.25	DOUBLE	Intensity (%) of LED Source 8
LED.I9	24.56	DOUBLE	Intensity (%) of LED Source 9
LED.I10	0	DOUBLE	Intensity (%) of LED Source 10
LED.I11	0	DOUBLE	Intensity (%) of LED Source 11
LED.I12	100	DOUBLE	Intensity (%) of LED Source 12
LED.I13	0	DOUBLE	Intensity (%) of LED Source 13
LED.I14	0	DOUBLE	Intensity (%) of LED Source 14
LED.I15	0	DOUBLE	Intensity (%) of LED Source 15
EXPTIME	0.2	SINGLE	Frame Exposure Time (s).
PERIODTIME	0.2009	SINGLE	Frame Period Time (s) = Exposure Time + Frame Transfer Time
FPS	4.9776	SINGLE	Frames Per Second (Hz).
FIXTIME	0.2009	SINGLE	Time on each fixation target location (s).
BLEACHTIME	60.27	SINGLE	Time on the bleaching source (s).
ACQTIME	964.32	SINGLE	Total Acquisition Time (s)

Appendix F. Schematics of the Cardiff Model Eye

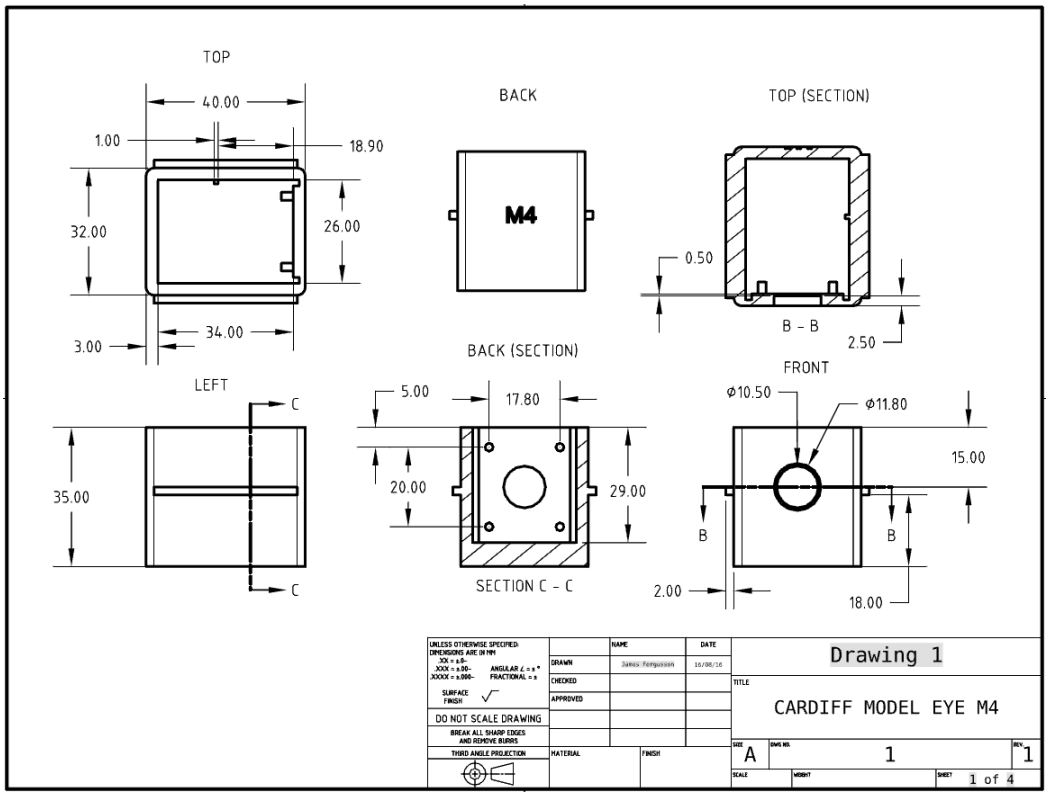

Figure F.1Schematic of the Cardiff Model Eye. Showing detail of the main body. Created in Onshape (Cambridge) by James Fergusson, Cardiff University

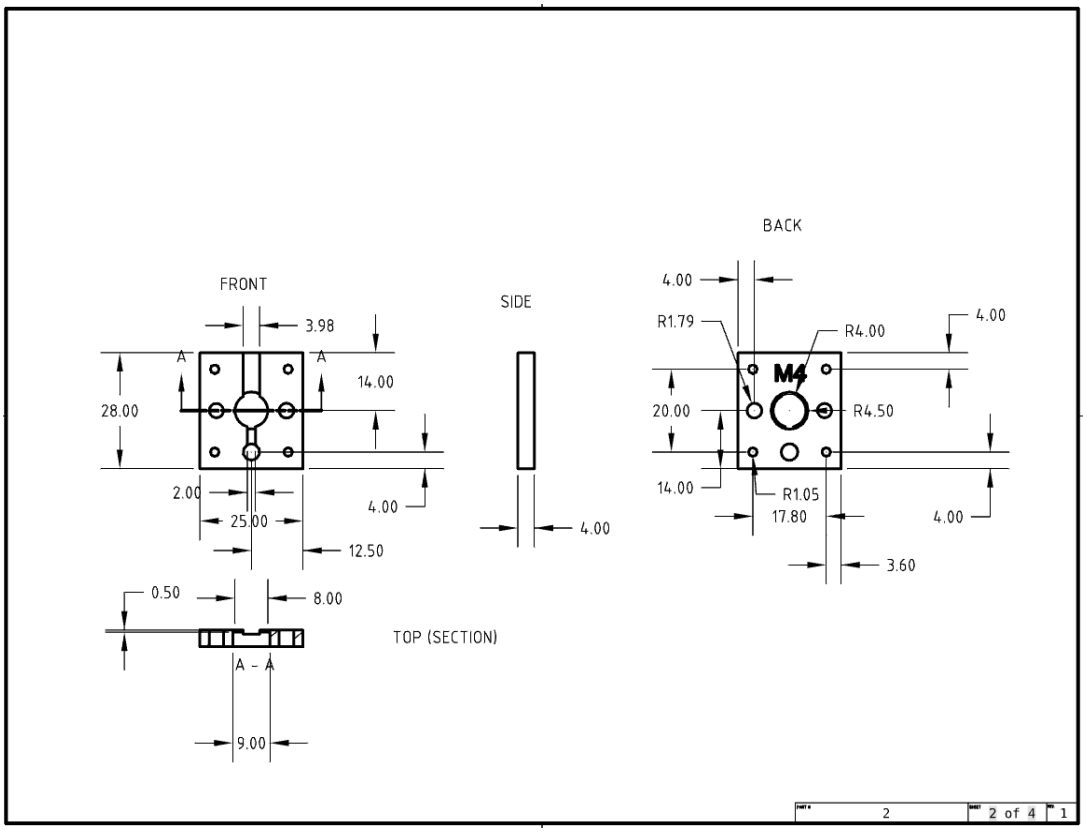

Figure F.2 Schematic of the Cardiff Model Eye. Showing detail of the iris and crystalline lens mount. Created in Onshape (Cambridge) by James Fergusson, Cardiff University

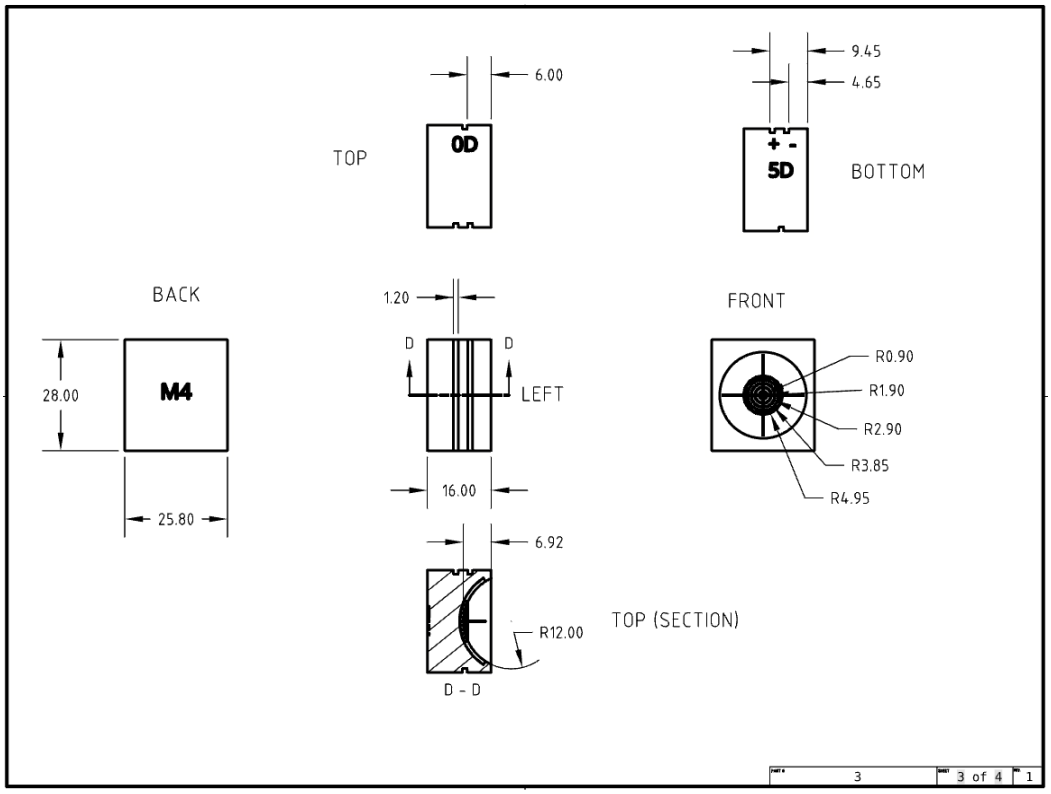

Figure F.3 Schematic of the Cardiff Model Eye. Showing detail of the retina (with alignment graticule). Created in Onshape (Cambridge) by James Fergusson, Cardiff University

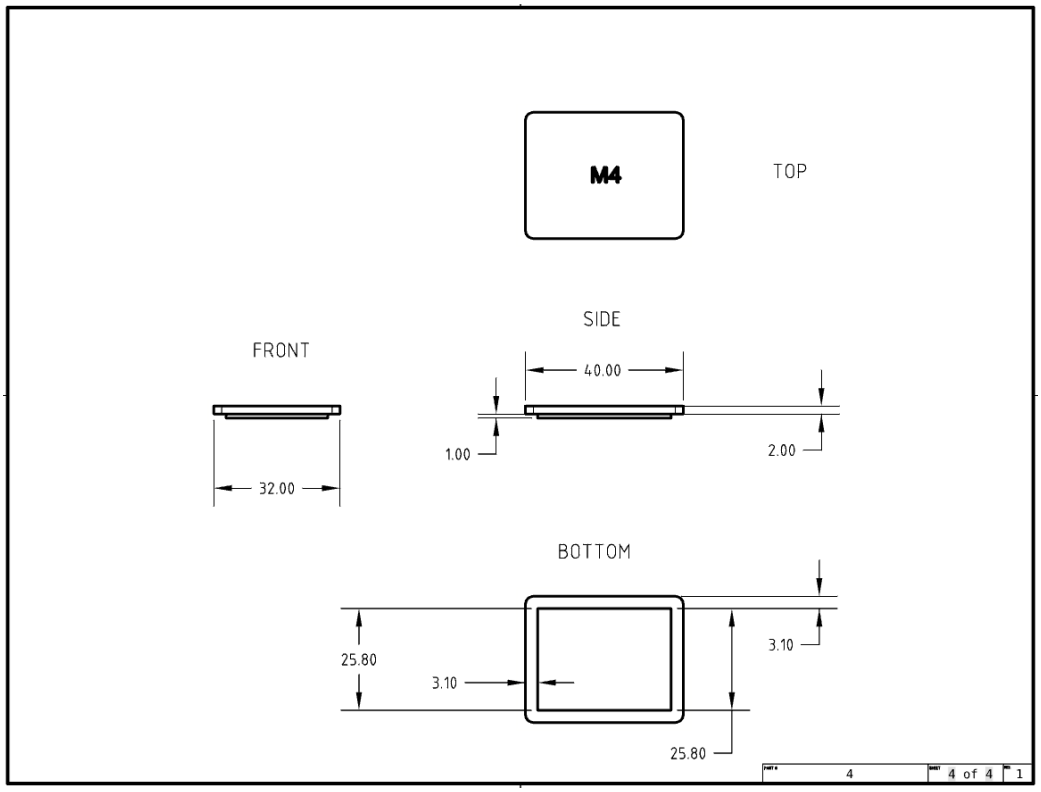

Figure F.4 Schematic of the Cardiff Model Eye. Showing detail of the cover. Created in Onshape (Cambridge) by James Fergusson, Cardiff University

Appendix G. Calibration of absolute retinal reflectance

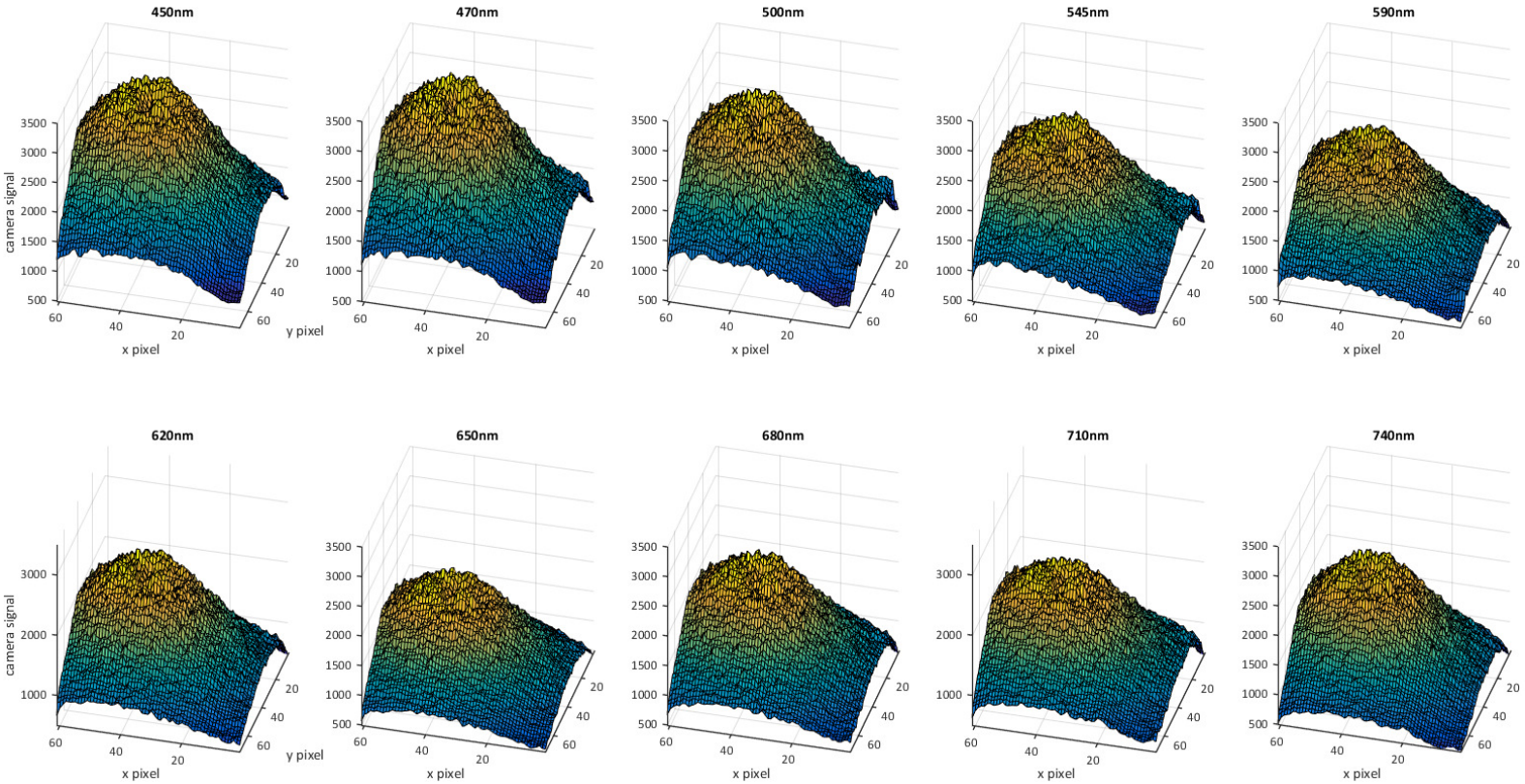

Figure G.1 Unadjusted camera signal obtained from model eye imaging surface, for all wavelengths. Central 30 degrees.

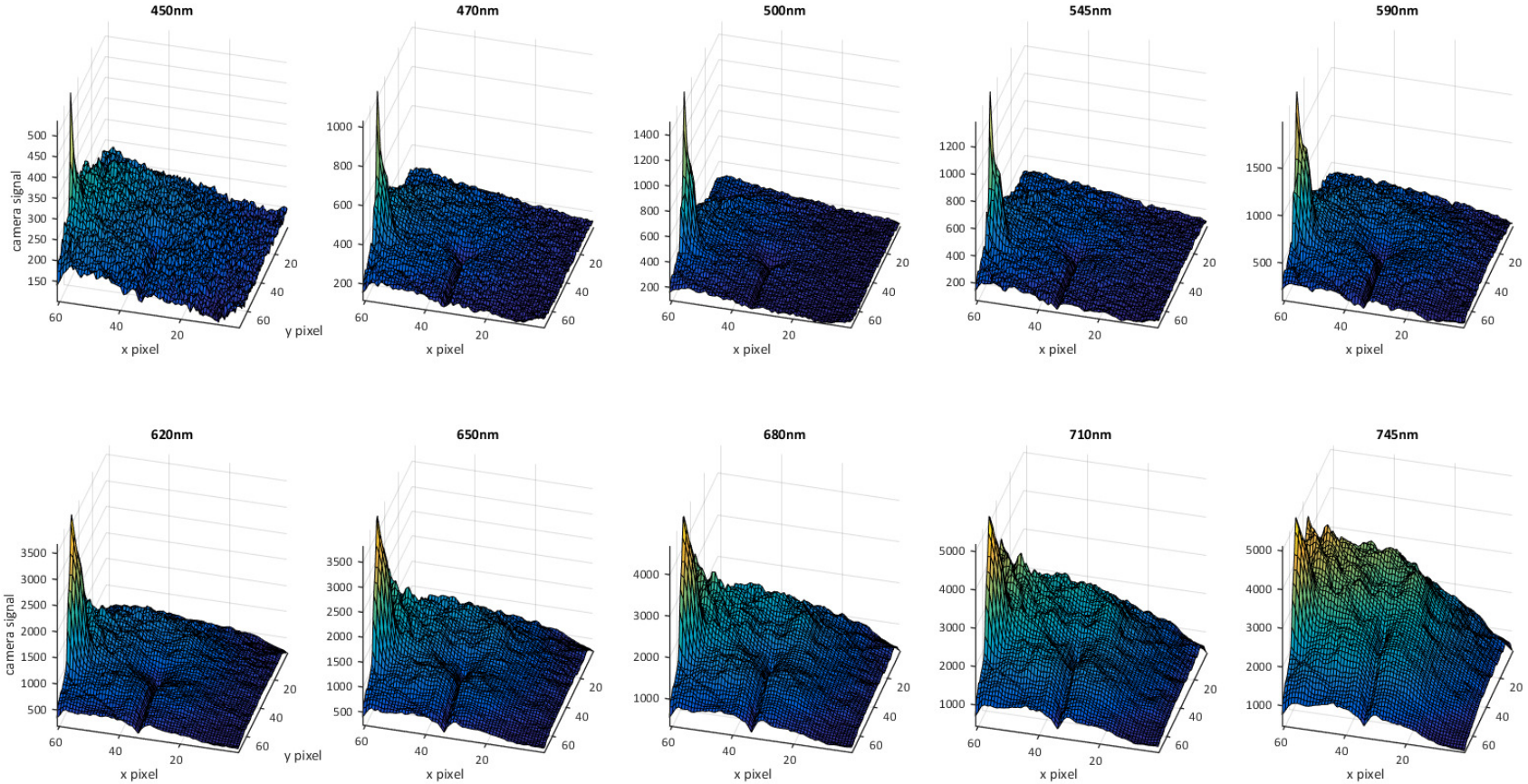

Figure G.2 Unadjusted camera signal obtained from a dark-adapted retina, for all wavelengths. Central 30 degrees only. Note the increase in Z axis with wavelength.

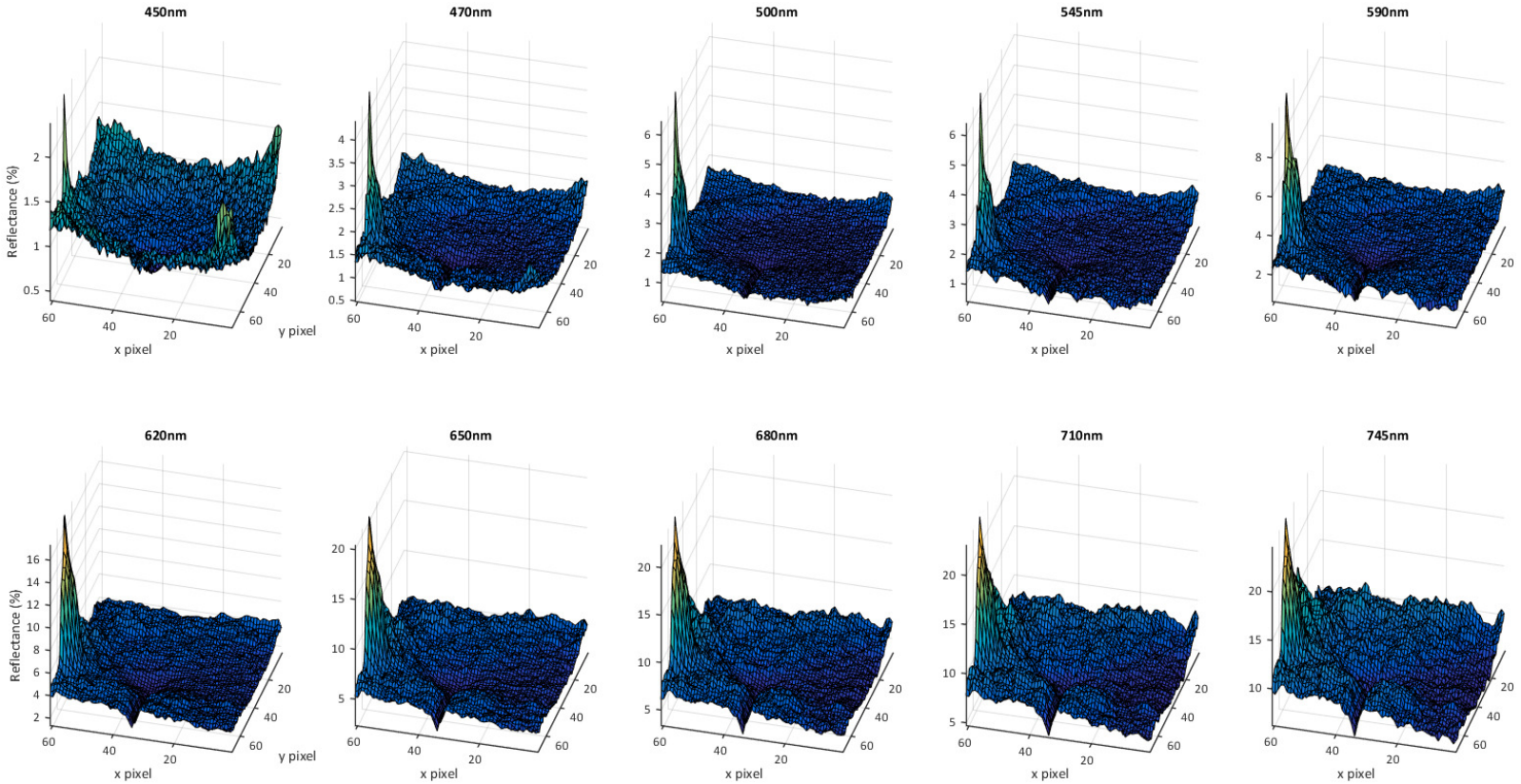

Figure G.3 Dark adapted ocular reflectance for all wavelengths, central 30 degrees. Calculated using Equation 7.4 and the data presented in Figure G.1 and Figure G.2. Improved spatial fidelity over Figure G.2 is due to correction for the imperfect illumination optics, evidenced by greater clarity of blood vessels and nerve fibre layer striations. Note the increase in Z axis with wavelength.

Appendix H. Individual participant fits for Models I and II

Model I (van Norren & Tiemeijer (1986))

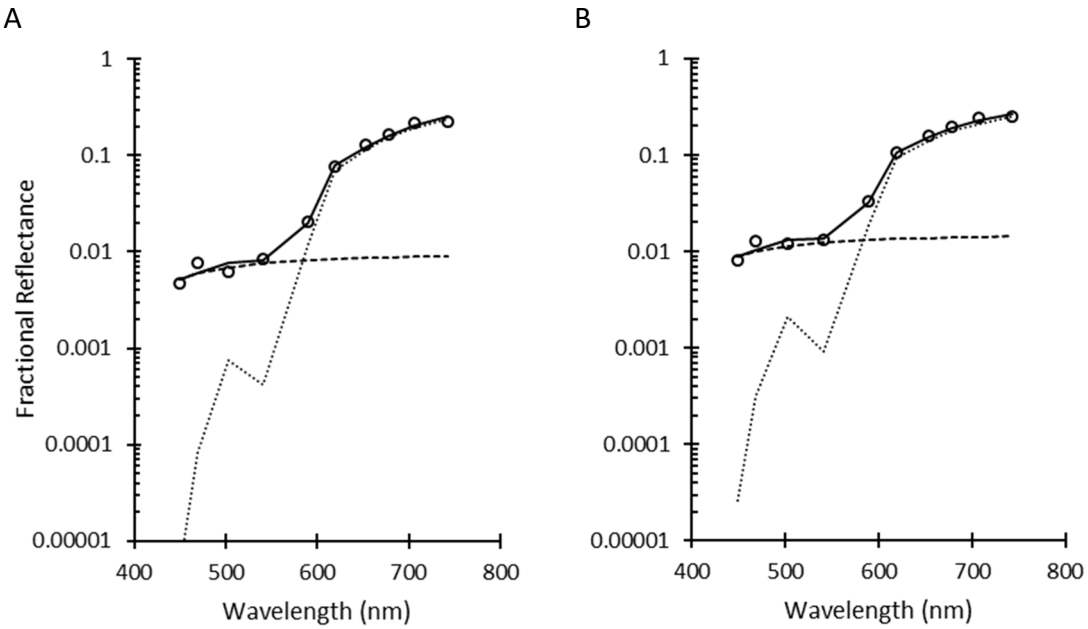

Figure H.1 The results of the model fit for participant AW at the two retinal locations investigated. Solid lines represent the model fit, dotted line the contributions from the RPE reflection and the dashed line contributions from the scleral reflection.

A) Foveal fit described by parameter values of V_{media} = 0.13, V_{mp} = 0.00, V_{me} = 1.42, V_{hb} = 163µm, R_{RPE} = 0.9% and R_{scl} = 48.3%. RMSE = 0.0075.

B) Parafoveal fit described by parameter values of V_{media} = 0.11, V_{mp} = 0.00, V_{me} = 1.23, V_{hb} = 156.0µm, R_{RPE} = 1.5% and R_{scl} = 43.6%. RMSE = 0.0042.

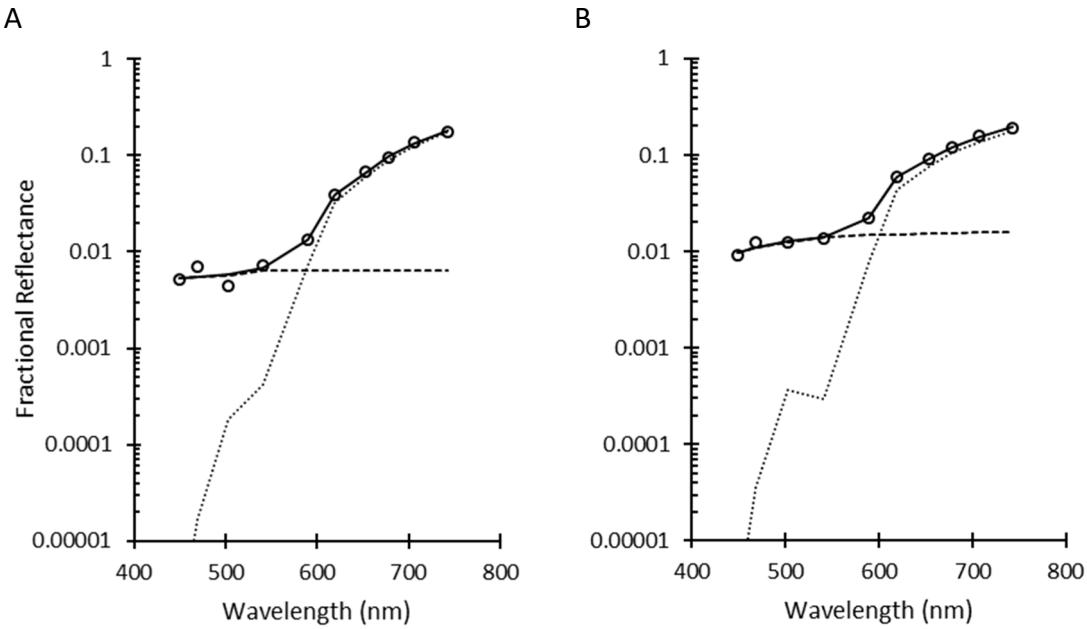

Figure H.2 The results of the model fit for participant HM at the two retinal locations investigated. Solid lines represent the model fit, dotted line the contributions from the RPE reflection and the dashed line contributions from the scleral reflection.

A) Foveal fit described by parameter values of V_{media} = 0.00, V_{mp} = 0.04, V_{me} = 2.14, V_{hb} = 102.0µm, R_{RPE} = 0.6% and R_{scl} = 43.9%. RMSE = 0.009.

B) Parafoveal fit described by parameter values of V_{media} = 0.12, V_{mp} = 0.00, V_{me} = 1.62, V_{hb} = 149.7 µm, R_{RPE} = 1.7% and R_{scl} = 38.6%. RMSE = 0.001.

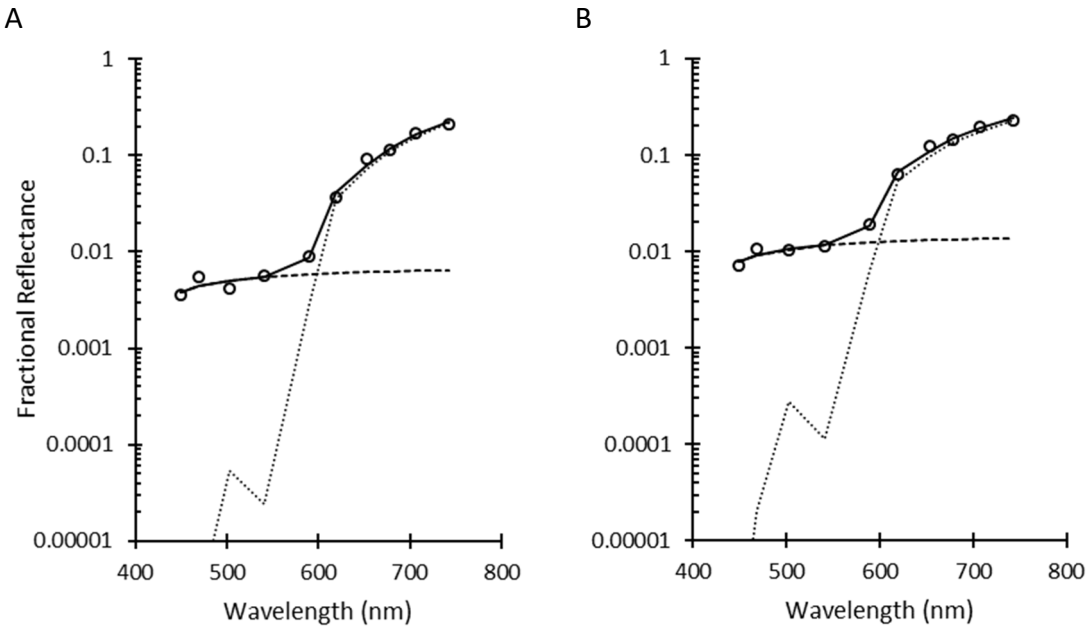

Figure H.3 The results of the model fit for participant JF at the two retinal locations investigated. Solid lines represent the model fit, dotted line the contributions from the RPE reflection and the dashed line contributions from the scleral reflection.

A) Foveal fit described by parameter values of V_{media} = 0.12, V_{mp} = 0.00, V_{me} = 2.12, V_{hb} = 231.9µm, R_{RPE} = 0.7% and R_{scl} = 59.2%. RMSE = 0.0089.

B) Parafoveal fit described by parameter values of V_{media} = 0.13, V_{mp} = 0.00, V_{me} = 1.62, V_{hb} = 203.0µm, R_{RPE} = 1.4% and R_{scl} = 49.8. RMSE = 0.0033.

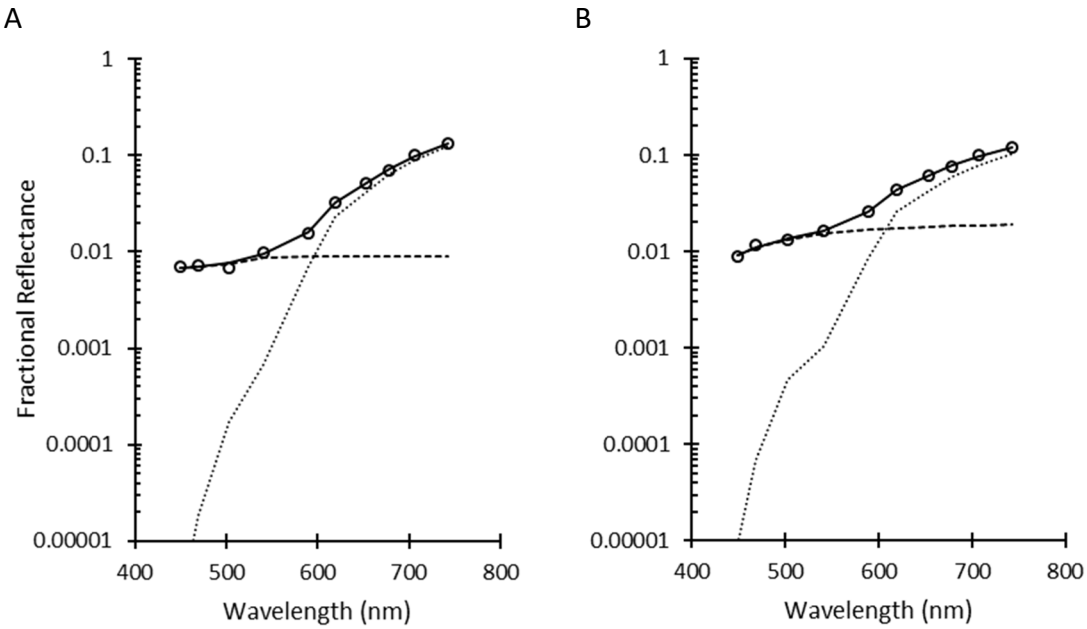

Figure H.4 The results of the model fit for participant TM at the two retinal locations investigated. Solid lines represent the model fit, dotted line the contributions from the RPE reflection and the dashed line contributions from the scleral reflection.

A) Foveal fit described by parameter values of V_{media} = 0.00, V_{mp} = 0.06, V_{me} = 2.15, V_{hb} = 65.17µm, R_{RPE} = 0.9% and R_{scl} = 31.3%. RMSE = 0.0012

B) Parafoveal fit described by parameter values of V_{media} = 0.16, V_{mp} = 0.00, V_{me} = 1.84, V_{hb} = 68.9µm, R_{RPE} = 2.0% and R_{scl} = 21.8%. RMSE = 0.0003

Model II (Delori & Pflibsen (1989))

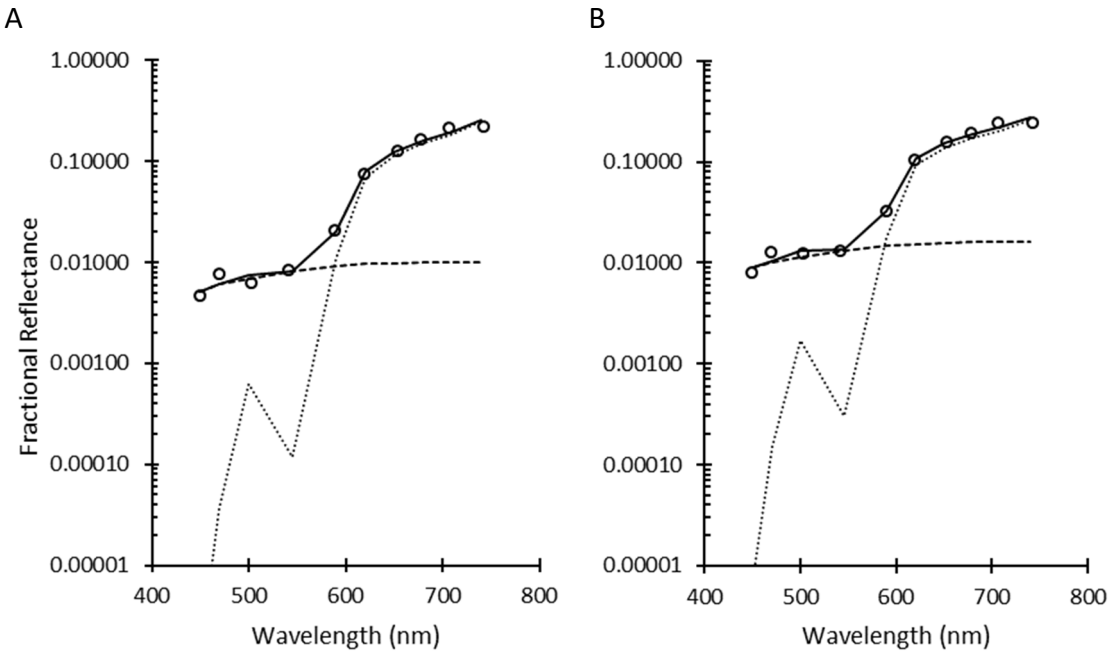

Figure H.5 example results of the free model fit for participant AW at two locations, all parameters allowed to vary. Solid lines represent the model fit, dashed line the contributions from the RPE reflection and the interrupted line contributions from the scleral reflection.

A) Foveal fit described by parameter values of V_{media} = 0.068, V_{mp} = 0.098, V_{me} = 3.35, V_{hb} = 523.8µm, V_{RPE} = 2.45, V_{cc} = 67.0µm, OD_x = 1.2, R_{RPE} = 1.0%, S_{ch} = 0.88, S_{media} = 0.06 and t_{ch} = 64.7µm. RMSE = 0.0029.

B) Parafoveal fit described by parameter values of V_{media} = 0.13, V_{mp} = 0.00, V_{me} = 3.62, V_{hb} = 435.3µm, V_{RPE} = 0.96, V_{cc} = 67µm, OD_x = 1.74, R_{RPE} = 2.33%, S_{ch} = 0.57, S_{media} = 0.08 and t_{ch} = 41.9µm. RMSE = 0.0035.

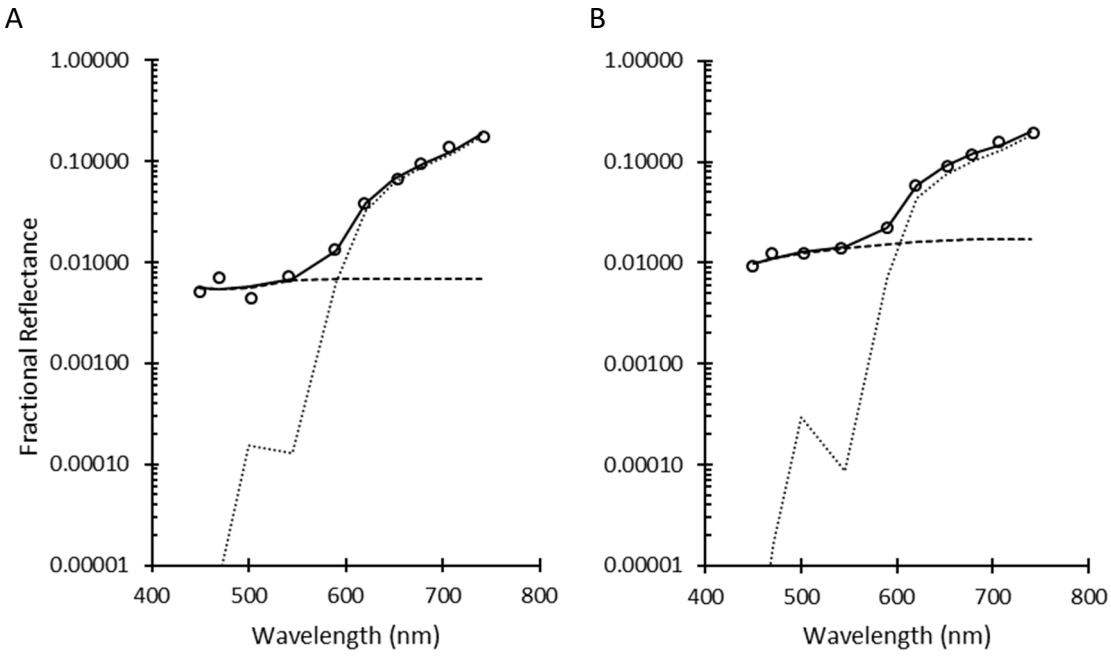

Figure H.6 example results of the free model fit for participant HM at two locations, all parameters allowed to vary. Solid lines represent the model fit, dashed line the contributions from the RPE reflection and the interrupted line contributions from the scleral reflection.

A) Foveal fit described by parameter values of V_{media} = 0.00, V_{mp} = 0.07, V_{me} = 0.00, V_{hb} = 496.2µm, V_{RPE} = 2.89, V_{cc} = 0.00µm, OD_x = 0.00, R_{RPE} = 1.46%, S_{ch} = 0.04, S_{media} = 0.18 and t_{ch} = 349.2µm. RMSE = 0.0081.

B) Parafoveal fit described by parameter values of V_{media} = 0.12, V_{mp} = 0.00, V_{me} = 0.20, V_{hb} = 638.2µm, V_{RPE} = 1.70, V_{cc} = 51.0µm, OD_x = 2.25, R_{RPE} = 2.23%, S_{ch} = 0.04, S_{media} = 0.06 and t_{ch} = 369.1µm. RMSE = 0.0011.

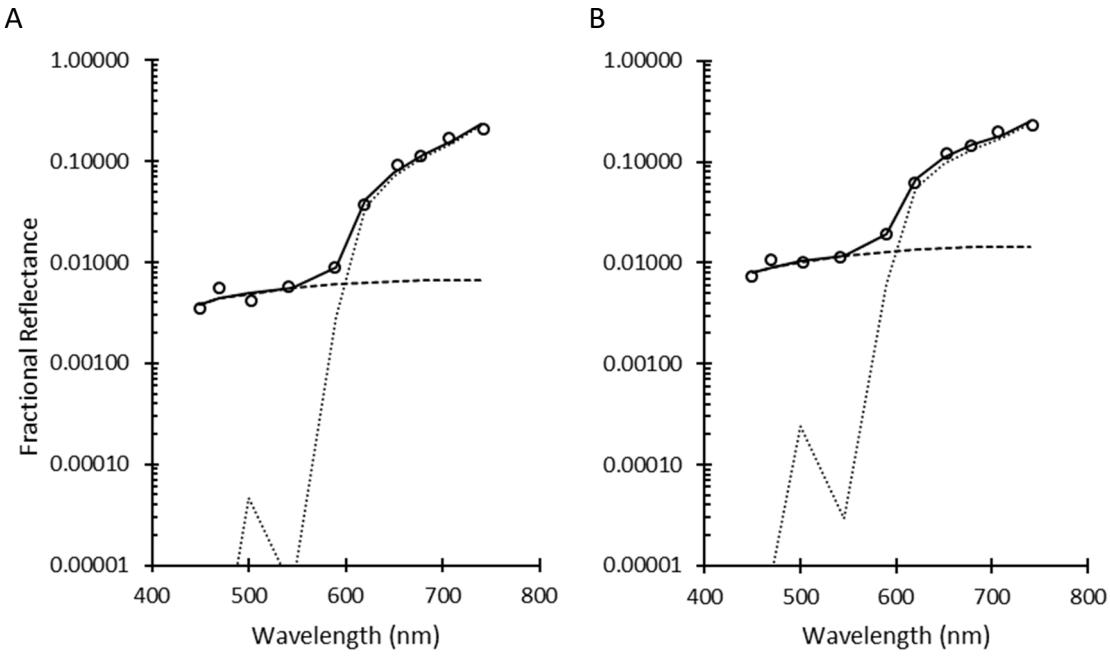

Figure H.7 example results of the free model fit for participant JF at two locations, all parameters allowed to vary. Solid lines represent the model fit, dashed line the contributions from the RPE reflection and the interrupted line contributions from the scleral reflection.

A) Foveal fit described by parameter values of V_{media} = 0.12, V_{mp} = 0.00, V_{me} = 0.21, V_{hb} = 119.4µm, V_{RPE} = 2.39, V_{cc} = 109.0µm, OD_x = 3.17, R_{RPE} = 1.03%, S_{ch} = 0.87, S_{media} = 0.09 and t_{ch} = 269.1µm. RMSE = 0.0083.

B) Parafoveal fit described by parameter values of V_{media} = 0.13, V_{mp} = 0.00, V_{me} = 0.21, V_{hb} = 123.8µm, V_{RPE} = 1.79, V_{cc} = 97.8µm, OD_x = 4.02, R_{RPE} = 2.20%, S_{ch} = 0.62, S_{media} = 0.09 and t_{ch} = 191.9µm. RMSE = 0.0032.

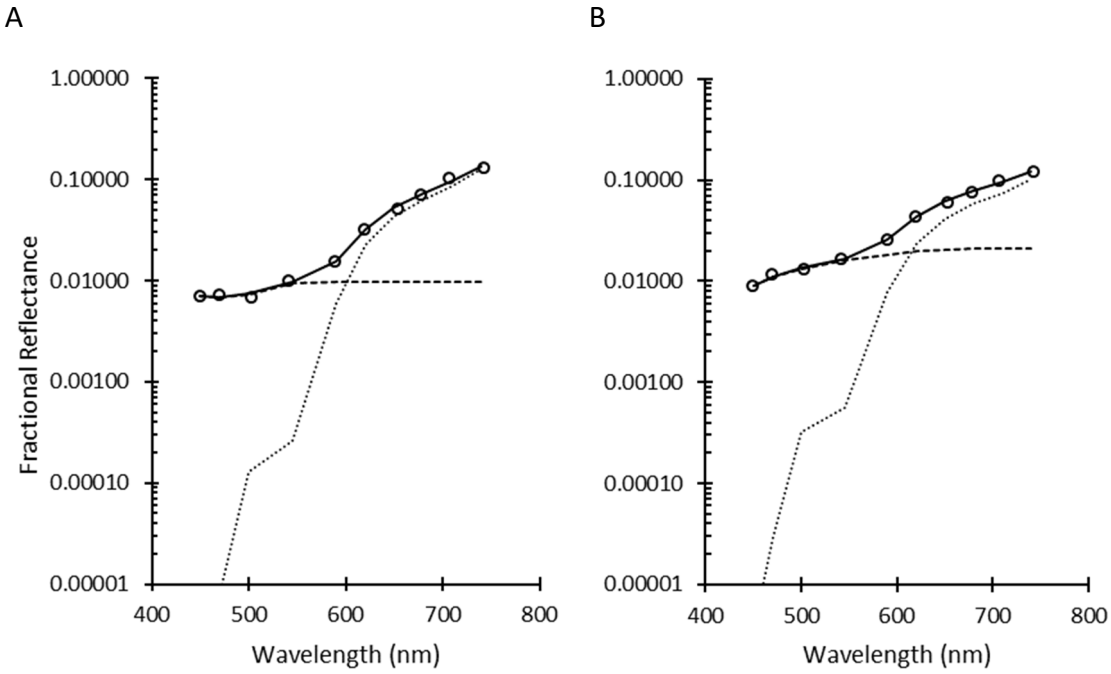

Figure H.8 example results of the free model fit for participant TM at two locations, all parameters allowed to vary. Solid lines represent the model fit, dashed line the contributions from the RPE reflection and the interrupted line contributions from the scleral reflection.

A) Foveal fit described by parameter values of V_{media} = 0.00, V_{mp} = 0.15, V_{me} = 0.20, V_{hb} = 130.1µm, V_{RPE} = 2.30, V_{cc} = 28.5µm, OD_x = 4.27, R_{RPE} = 1.99%, S_{ch} = 0.45, S_{media} = 0.16 and t_{ch} = 138.6µm. RMSE = 0.0007.

B) Parafoveal fit described by parameter values of V_{media} = 0.18, V_{mp} = 0.00, V_{me} = 0.20, V_{hb} = 69.6µm, V_{RPE} = 1.74, V_{cc} = 25.6µm, OD_x = 5.77, R_{RPE} = 4.15%, S_{ch} = 0.27, S_{media} = 0.15 and t_{ch} = 102.4µm. RMSE = 0.0004.

Appendix I. Spectral data used in the 'modified' model

Table I.1 Spectral data used in the 'modified' model

Wavelength (nm)	$R_{lens}(\lambda)$	$R_{r\,in}(\lambda)$	$OD_{mp}(\lambda)$	$OD_{hb}(\lambda)$ (µm)	$OD_{me}(\lambda)$	$R_{scl}(\lambda)$	$OD_{media}(\lambda)$
449	1.01	1.05	0.92	0.00576	1.01	0.94	0.28
469	0.85	0.97	0.91	0.00330	0.86	0.86	0.21
503	0.64	0.85	0.50	0.00218	0.66	0.77	0.14
541	0.48	0.75	0.00	0.00479	0.50	0.67	0.09
589	0.34	0.65	0.00	0.00193	0.37	0.60	0.06
620	0.28	0.60	0.00	0.00014	0.30	0.56	0.05
653	0.23	0.55	0.00	0.00006	0.25	0.52	0.04
678	0.19	0.53	0.00	0.00005	0.22	0.49	0.03
707	0.16	0.49	0.00	0.00004	0.19	0.47	0.03
743	0.13	0.46	0.00	0.00006	0.16	0.45	0.02

$R_{lens}(\lambda)$ represented by Rayleigh scattering (Chapter 6), normalised to 450m. $R_{r\,in}(\lambda)$ represented by Mie scattering (Jacques 2013), normalised to 450nm. $OD_{mp}(\lambda)$ has been obtained from Snodderly et al (1984), $OD_{hb}(\lambda)$ represents 1µm of 95% oxygenated haemoglobin, obtained from van Assendelft (1970). $OD_{me}(\lambda)$ has been obtained from Gabel et al (1978). $R_{scl}(\lambda)$ is represented by Mie scattering, normalised to 50% at 675nm (Chapter 9). $OD_{media}(\lambda)$ has been obtained from van de kraats (2007) and given here for an age of 30.

Appendix J. Individual participant fits for the 'modified' model

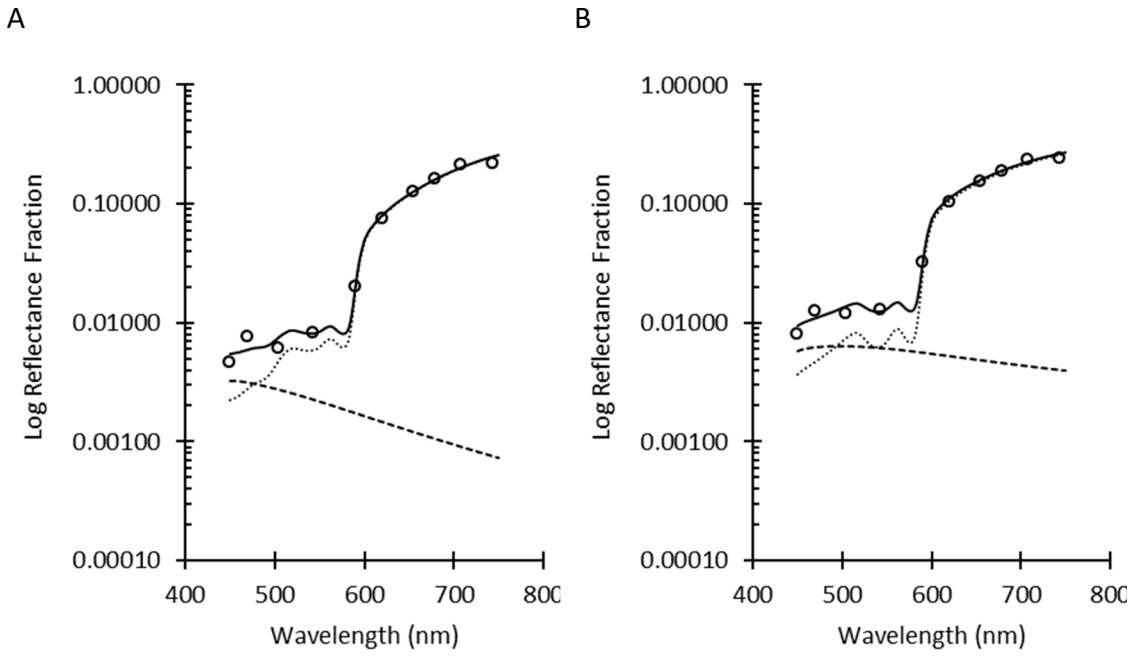

Figure J.1 result of the 'modified' model fit for participant AW at two locations. Solid lines represent the model fit, dashed line the contributions from the anterior reflections (lens and inner retina) and the dotted line contributions from the deeper reflections (outer retina and sclera).

A) Foveal fit of Equation 9.15 described by parameter values of: age = 32, V_{lens} = 0.6%, V_{mp} = 0.11, $V_{r\ in}$ = 0.00%, $V_{r\ out}$ = 1.8%, V_{hb} = 183.3µm, V_{me} = 1.49 and V_{scl} = 82%. RMSE = 0.0074

B) Parafoveal fit of Equation 9.16 described by parameter values of: age = 32, V_{lens} = 0.6%, V_{mp} = 0.00, $V_{r\ in}$ = 0.8%, $V_{r\ out}$ = 1.8%, V_{hb} = 178.0µm, V_{me} = 1.10 and V_{scl} = 65% RMSE = 0.0040

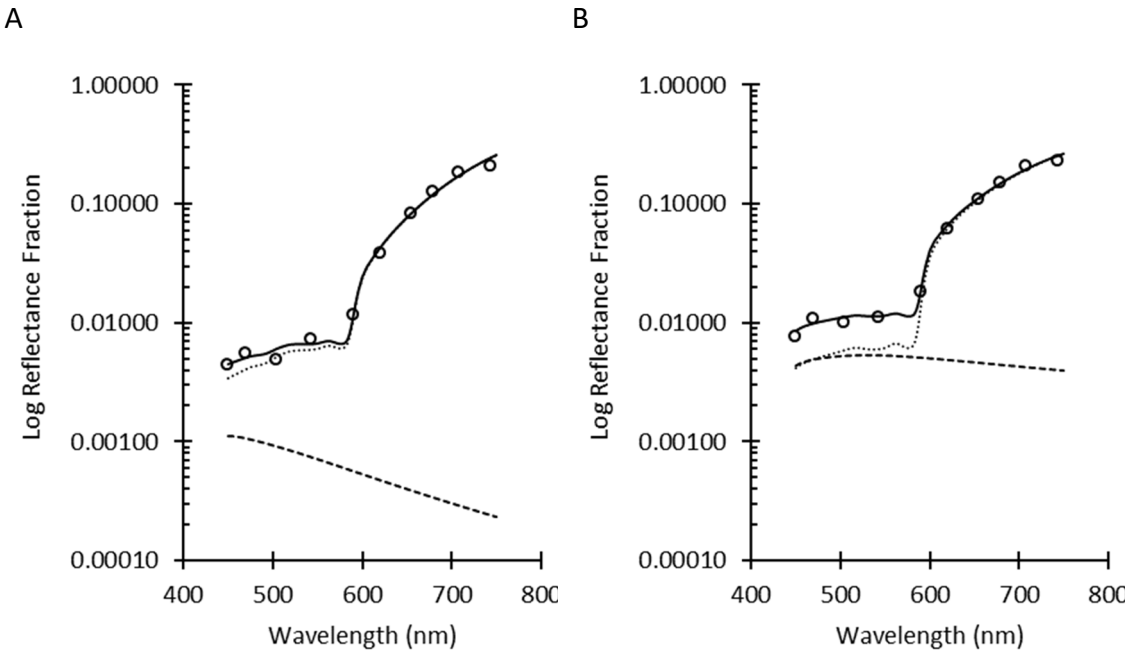

Figure J.2 result of the 'modified' model fit for participant CJ at two locations. Solid lines represent the model fit, dashed line the contributions from the anterior reflections (lens and inner retina) and the dotted line contributions from the deeper reflections (outer retina and sclera).

A) Foveal fit of Equation 9.15 described by parameter values of: age = 28, V_{lens} = 0.2%, V_{mp} = 0.05, $V_{r\ in}$ = 0.00%, $V_{r\ out}$ = 1.2%, V_{hb} = 174.1µm, V_{me} = 2.47 and V_{scl} = 161%. RMSE = 0.0050

B) Parafoveal fit of Equation 9.16 described by parameter values of: age = 28, V_{lens} = 0.2%, V_{mp} = 0.00, $V_{r\ in}$ = 0.9%, $V_{r\ out}$ = 1.2%, V_{hb} = 200.1µm, V_{me} = 1.89 and V_{scl} = 111% RMSE = 0.0023

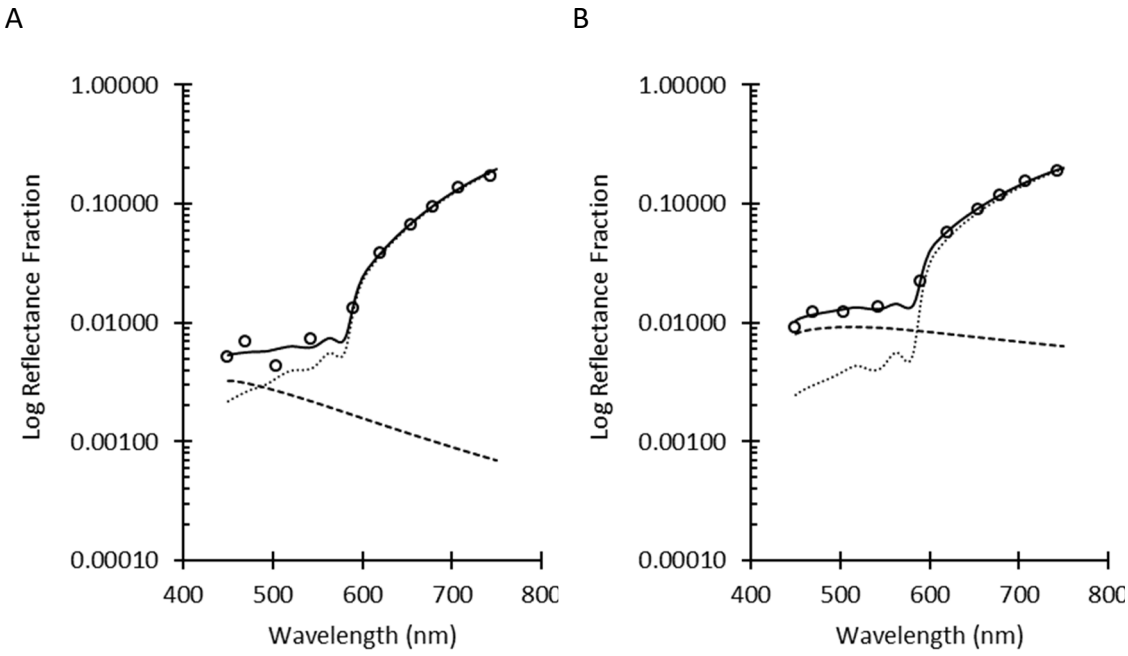

Figure J.3 result of the 'modified' model fit for participant HM at two locations. Solid lines represent the model fit, dashed line the contributions from the anterior reflections (lens and inner retina) and the dotted line contributions from the deeper reflections (outer retina and sclera).

A) Foveal fit of Equation 9.15 described by parameter values of: age = 29, V_{lens} = 0.6%, V_{mp} = 0.03, $V_{r\ in}$ = 0.00%, $V_{r\ out}$ = 0.74%, V_{hb} = 90.7µm, V_{me} = 2.26 and V_{scl} = 102%. RMSE = 0.0098

B) Parafoveal fit of Equation 9.16 described by parameter values of: age = 29, V_{lens} = 0.6%, V_{mp} = 0.00, $V_{r\ in}$ = 1.4%, $V_{r\ out}$ = 0.74%, V_{hb} = 131.3µm, V_{me} = 1.75 and V_{scl} = 75% RMSE = 0.0015

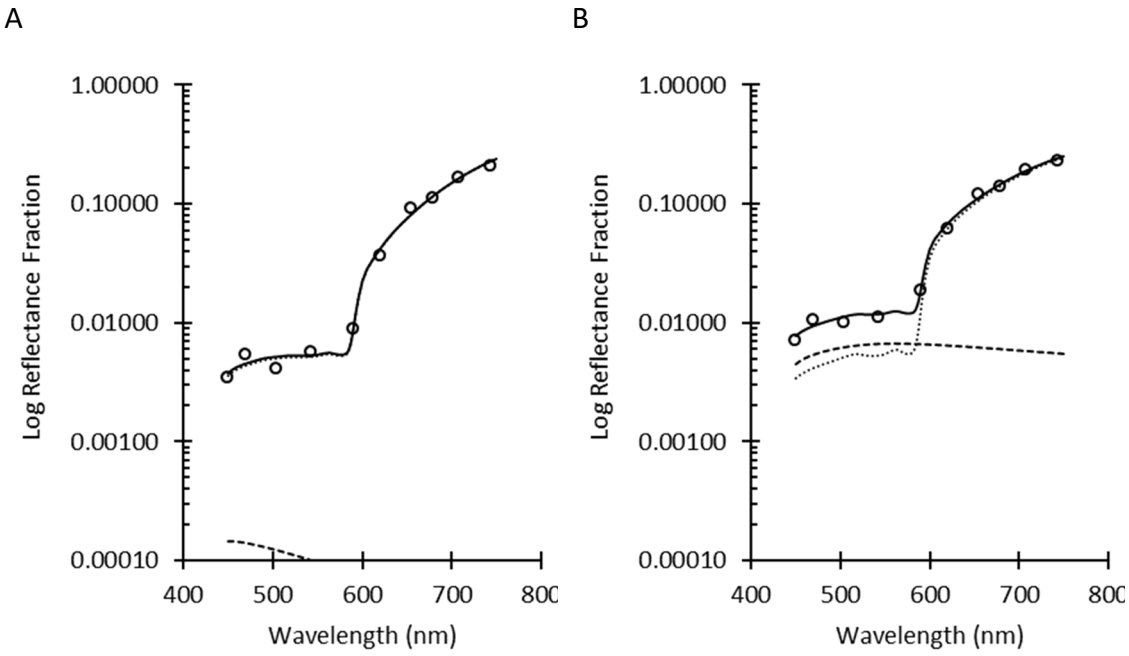

Figure J.4 result of the 'modified' model fit for participant JF at two locations. Solid lines represent the model fit, dashed line the contributions from the anterior reflections (lens and inner retina) and the dotted line contributions from the deeper reflections (outer retina and sclera).

A) Foveal fit of Equation 9.15 described by parameter values of: age = 32, V_{lens} = 0.0%, V_{mp} = 0.00, $V_{r\ in}$ = 0.00%, $V_{r\ out}$ = 1.1%, V_{hb} = 231.1µm, V_{me} = 2.34 and V_{scl} = 141%. RMSE = 0.0096.

B) Parafoveal fit of Equation 9.16 described by parameter values of: age = 32, V_{lens} = 0.0%, V_{mp} = 0.00, $V_{r\ in}$ = 1.3%, $V_{r\ out}$ = 1.1%, V_{hb} = 215.0µm, V_{me} = 1.77 and V_{scl} = 97%. RMSE = 0.0050.

Appendix K. MATLAB code

Main Code: Topographical modelling

```
% Written by CJ 04/09/16 this program models the retinal reflections
% present in the mark II dataset. It does this according to a routine
% defined by TM in Aug 2016.

%Edit Jan 2017

%This require accurate retinal reflection data to work correctly. The
model
%eye data is used to convert camera signal to retinal reflection after
%the CCD bias and blinks have been removed, but BEFORE image
registration.
%(this process occurs in IDL).

% The free fit is run topographically with Lens, Macular Pigment and
Outer % retinal reflectance parameters fixed to the values obtained
for each
% participant in the fovea. (manual input) The anterior reflections
are
% returned at each x, y pixel location. This should provide a
% physiologically plausible map of the RNFL and melanin density.

% finally, the sum of the anterior reflections is subtracted from the
raw
% reflection data and the true OD calculated.

close all; clc; clear

%define the wavelengths used in the mark II densitometer.
wavelengths = [450,470,500,545,590,620,650,680,710,740];

% loads the images, the first argument defines whether the bleached
images
```

```
% are loaded, the second argument defines whether the dark-adapted
images

% are loaded ('yes' or 'no').

[bleach, ~] = load_images('yes','no');


% finds the lowest pixel in the image, this is the 450nm fovea (due to
the % absorbing macular pigment)

[fovea_x, fovea_y, min_val] = foveal_location(bleach(1,:,:));


% performs a circular crop, centred on the fovea, 30 pixel radius (~15

% degrees radius;

[bleach] = circular_crop(bleach, 'no', fovea_y, fovea_x);

% crops image to the central 30 degrees (60 pixels)

bleach = bleach(:,fovea_y-30:fovea_y+30,fovea_x-30:fovea_x+30);


% run the model

[topography_maps, anterior_stray_light_stack, constants,
media_density] = Chapter_8_reflection_model_May2017(bleach);


%load and calculate the Dark data

[~, dark] = load_images('no','yes');


% performs a circular crop, centered on the fovea, 30 pixel radius
(~15

% degrees radius)

[dark] = circular_crop(dark, 'no', fovea_y, fovea_x);


% crops image to the central 30 degrees (60 pixels)

dark = dark(:,fovea_y-30:fovea_y+30,fovea_x-30:fovea_x+30);


% subtract the stray light reflectance contribution from the bleach
data

true_bleach = bleach - anterior_stray_light_stack;


% subtract anterior stray light from dark images

true_dark = dark - anterior_stray_light_stack;


% calculate the 'true' OD maps
```

```
true_OD = real(log10(true_bleach./true_dark));

% select either the experimental spectra for rod and 'mixed' cone, or
the dartnall data by commenting/uncommenting the relevant lines.

% m_cone = [0.429 0.555 0.823 0.955 0.427 0.155 0 0 0 0]; % dartnall

% l_cone = [0.363 0.41 0.594 0.9505 0.822 0.449 0.127 0 0 0]; %
dartnall

% mixed_cone (m_cone+l_cone)/2; % dartnall

rod = [0.605 0.83 0.995 0.5075 0.11 0.037 0 0 0 0]; %experimental
spectra

mixed_cone = [0.640 0.777 1.00 0.768 0.125 0.0271 0.007 -0.022 -0.025
-0.017]; %experimental spectra


% run the photopigment isolation model

[rod_photoreceptors, cone_photoreceptors] =
Image_fit_2_spectra_to_model_aveOD(true_OD,rod,mixed_cone);
```

Function: Load images

```
function [bleach_stack, dark_stack] =
load_images(load_bleach,load_dark)


% loads the images, the first argument defines whether the bleached
images

% are loaded, the second argument defines whether the dark adapted
images

% are loaded (ans 'yes' or 'no'). Further options are then available
to

% select the correct folder, filename and if the images are averaged
or

% not. Can load either the full times sequence or the averaged images
for

% the dark adapted series (only)


%Load retinal reflectance images, created by IDL.

image_location = uigetdir('F:\PhD\Thesis\Chapter 8 - Ocular reflection
model\retinal reflectance images\');

if strcmp(load_bleach, 'yes');

    % loads a dialog box where the user can define the filename of the

    % images to be loaded.

    [image_identifier] = load_image_dialog_box('bleach');
```

```
    %The full time series for the bleached image is loaded.
    for LEDs = 1:10
        LEDs;
        image_name = ([num2str(LEDs-1),image_identifier,'.tif']); %
sort the filename
        image_dir = strcat(image_location, '\', image_name); % sort
the filename
        data(:,:,:) = double(imread(image_dir)); % load the images
        bleach = data(1:15,:,:); % Crop the time series to the first
30 seconds.
        [bleach] = remove_blinks_image(bleach); % remove blinks.
        bleach = imrotate(bleach,180,'bilinear'); % rotate to correct
orientation.
        bleach_stack(LEDs,:,:) = bleach; % save the average images
into an LED indexed stack

        clear data % reset the 'data'

    end
    disp('bleached time sequence loaded') % remind user which images
loaded
else
    bleach_stack = zeros; %empty output to keep arguments happy
    disp ('bleached images not loaded') % remind user which images
loaded

end

if strcmp(load_dark, 'yes');
    % loads a dialog box
    [choice] = choose_sequence_type;
    % loads a dialog box where the user can define the filename of the
    % images to be loaded.
    [image_identifier] = load_image_dialog_box('dark');

    %Load the full time series for the dark adapted images, or only a
single averaged frame? Can do either.
```

```
    if strcmp(choice, 'single averaged image') %can pre-averaged (IDL)
dark adapted images

        for LEDs = 1:10 % indexs the stack in wavelength order (1-10)

            image_name = ([num2str(LEDs-1),image_identifier,'.tif']);
% sort the filename

            image_dir = strcat(image_location, '\', image_name); %
sort the filename

            data(LEDs,:,:) = imread(image_dir); % load the images

            data = imrotate(data,180,'bilinear'); % rotate to correct
orientation.


            clear data % reset the 'data'


        end

        disp('averaged dark adapted images loaded') % remind user
which images loaded

    end


    if strcmp(choice, 'time sequence') %can load the dark adapted
image series

        for LEDs = 1:10 % indexes the stack in wavelength order (1-10)

            image_name = ([num2str(LEDs-1),image_identifier,'.tif']);
% sort the filename

            image_dir = strcat(image_location, '\', image_name); %
sort the filename

            data(:,:,:) = double(imread(image_dir)); % load the images

            [dark] = remove_blinks_image(data); % remove blinks

            dark = imrotate(dark,180,'bilinear'); % rotate to correct
orientation.

            dark_stack(LEDs,:,:) = dark; % save the average images
into an LED indexed stack


            clear data % reset the 'data'


        end

        disp('dark time sequence loaded') % remind user which images
loaded


    end
```

```
else
    dark_stack = zeros; %empty output to keep arguments happy
    disp('dark adapted images not loaded') % remind user which images
loaded
end
end
```

Function: Remove blinks

```
function [ave_bleach] = remove_blinks_image(bleach_stack)

[nCycles, rows, columns] = size(bleach_stack);

for y = 1:125
    y;
    for x = 1:125
        %     this section of the code removes the larger blinks from
        %     the data set
        pixel_signal = bleach_stack(:,x,y); %finds the signal of the
entire frame - blinks will show up!
        %         pixel_signal = pixel_signal'; %transposes the matrix
so same dimensions as mean_matrix
        %             figure(1)
        %             plot(pixel_signal)
        %             hold on

        mean_signal = mean(pixel_signal); %finds the mean of the time
series, for a single pixel
        stdev_signal = std(pixel_signal); %%finds the STD DEV of the
time series, for a single pixel
        mean_matrix = repmat(mean_signal,nCycles,1); %creates a matrix
of mean signal
        stdev_matrix = repmat(stdev_signal,nCycles,1); %creates a
matrix of std dev signal

        %all outlying data = mean signal
        outliers = abs(pixel_signal - mean_matrix) > 1*stdev_matrix;
        pixel_signal(outliers) = mean_signal;
```

```
        average_pixel = mean(pixel_signal);


        ave_bleach(x,y) = average_pixel;
    end
end
end
```

Function: Foveal location

```
function [fovea_x, fovea_y, fovea_value] =
foveal_location(image_stack)
%find the lowest x,y location in the image. needs to be cropped out
the
%edge noise to find the lowest pixel in the retina, not image. Depends
on
%macular pigment absorption in the short wavelengths to determine the
%foveal location


[LED columns rows] = size(image_stack);


%finds the x,y locations of the min camera signal (i.e. the fovea)
if rows == 125 %the input stack is uncropped (125x125), crop it now.
    image450central(:,:) = image_stack(1,55:100,25:75); % crops full
size
    %image to central macular region for 450nm LED
else %if the image is already cropped carry on.
    image450central(:,:) = image_stack(1,:,:); % load 450nm LED
end


fovea_value = min(min(image450central(image450central>0))); % must
%ignore all values below 0 as these will be in the unimaged peripheral
noise


[fovea_y,fovea_x] = find(image450full==fovea_value); % find the
%pixel location with the 'foveal value' in the uncropped image.
end
```

Function circular crop

```
function [image_stack] = circular_crop(images, y, x)
% creates an inverse circular mask, all pixels outside the mask become
0.
% The mask is centred on the foveal pixel.

[leds, cols, rows] = size(images);

for i = 1:leds %index the stack in wavelength order
    I(:,:) = images(i,:,:); %select a single wavelength
    imageSize = size(I); %size of image (in pixels)
    ci = [y, x, 32]; % centre and radius of circle ([c_row, c_col, r])
    [xx,yy] = ndgrid((1:imageSize(1))-ci(1),(1:imageSize(2))-ci(2));
%creates a matrix for the circular mask, based on image size
    mask = ((xx.^2 + yy.^2)<ci(3)^2); % creates a matrix for the
circular mask, based on image size
    cropped_image = (zeros(size(I))); % creates matrix for the cropped
image.
    cropped_image(:,:) = I(:,:).*mask; % masked pixels become 0

    image_stack(i,:,:) = cropped_image; %index the stack
end
end
```

Function: Ocular reflection model

```
function [topography_maps, anterior_stray_light_stack, para_c,
media_density] = Chapter_8_reflection_model_May2017(images)
%Reflection model - takes the percentage retinal reflection images and
%models to obtain a stray light parameter.

[fovea_x, fovea_y, ~] = foveal_location(images(1,:,:)); %finds the
lowest %pixel in the 450nm image

[LEDs, columns, rows] = size(images); %size of image stack

%place holders for the variable 'maps'
Vr_in_map = zeros(columns, rows);
Vmelanin_map = zeros(columns, rows);
```

```
Vhaem_map = zeros(columns, rows);

Vsclera_map = zeros(columns, rows);

anterior_stray_light_stack = zeros(10, columns, rows);


%name the variables in order - this section is just a reminder, it is
not

%actually code.

% Rlens. This is a CONSTANT, defined for each participant at the fovea

% in excel (solver).

% Vmp. This is a CONSTANT, defined for each participant using the

% Kilbride(1990) equation.

% Rr_out. This is a CONSTANT, defined for each participant at the
fovea

% in excel (solver).


% x1 = Vr_in. This is a VARIABLE.

% x2 = Vhaem. This is a VARIABLE.

% x3 = Vmel. This is a VARIABLE.

% x4 = Vsclera. This is a VARIABLE.


%define the starting points and upper/lower bounds for the model
fitting

%procedure.

x0 = [0.0078,178,1.10,0.65]; %these starting values have been found to
model HM parafovea perfectly in Excel

x = [0.0078,178,1.10,0.65]; %placeholder for variables (x)

lb = [0,0,0,0]; % lower bounds, no constraint needed

ub = [10000,10000,10000,10000]; %upper bounds, no constraint needed

para_c = x; %starting variables saved so each pixel has the same
starting points.


%loads the data in table 8.5

[model_constants,titles] = xlsread('F:\PhD\Papers\Reflection
model\Model Thesis chapter 8 interpolated','Matlab Input','C6:K16');
%Loads the spectral data for the model to work.


%Define the constants age, Rlens, Dmp, Rr_out
```

```
%input the patients age. This scales the optical media absorption.
prompt={'Enter age'};
name = 'age';
defaultans = {'30'};
options.Interpreter = 'tex';
answer = inputdlg(prompt,name,[1 40],defaultans,options);
[age ~] = str2num(answer{1});

prompt={'Enter lens reflection'};
name = 'Rlens';
defaultans = {'0.01'};
options.Interpreter = 'tex';
answer = inputdlg(prompt,name,[1 40],defaultans,options);
[Rlens ~] = str2num(answer{1});

prompt={'Enter macular pigment absorption'};
name = 'Dmp_max';
defaultans = {'0.05'};
options.Interpreter = 'tex';
answer = inputdlg(prompt,name,[1 40],defaultans,options);
[Dmp_max ~] = str2num(answer{1});

prompt={'Enter outer retinal reflectance'};
name = 'Rr_out';
defaultans = {'0.09'};
options.Interpreter = 'tex';
answer = inputdlg(prompt,name,[1 40],defaultans,options);
[Rr_out ~] = str2num(answer{1});

wavelengths = model_constants(:,1); %obtains the wavelength
information
%from the loaded model constants.

%This defines media density with an age dependance. The equation has
%been taken from van de Kraats 2007 paper on the properties of the
ocular media.
media_density = ...
```

```
    ((400./(wavelengths(:,:))).^4).*...                          MRL see
VdK 2007

    (0.225+0.000031.*age.^2)+...                                 DRL see
VdK 2007

    (2.13.*exp(-((0.029.*(wavelengths(:,:)-370)).^2))).*...      MLY see
VdK 2007

    (0.998+0.000063.*age.^2)+...                                 DLY see
VdK 2007

    (11.95.*exp(-((0.021.*(wavelengths(:,:)-325)).^2))).*...     MLOUV
see VdK 2007

    (0.059+0.000186.*age.^2)+...                                 DLOUV
see VdK 2007

    (1.43.*exp(-((0.008.*(wavelengths(:,:)-325)).^2))).*...      MLO see
VdK 2007

    (0.016+0.000132.*age.^2);                                    %DLO see
VdK 2007

model_constants(:,9) = media_density; %over-writes the absorption of
the optical media based on the patients aged.


%define the macular pigment gaussian map here

FWHM = (1.93+0.03*age)/0.48; %1.93+0.03*age comes from equation in
Chen et

%al 2001 figure 6. Gives a total spread of MP of ~10degrees. 0.48 is
the

%degrees per pixel of the mark II


mp_x=1:columns; %creates a matrix the same size as a Mark II image

mp_y=1:rows; %creates a matrix the same size as a Mark II image

[MP_X,MP_Y]=meshgrid(mp_x,mp_y); %creates a matrix the same size as a
Mark II image

MacPig_matrix =((Dmp_max).*exp(-((MP_X-fovea_x).^2/(2*FWHM^2))-((MP_Y-
fovea_y).^2/(2*FWHM^2))));%+e(:,LED); %fills the matrix with macular
pigment Gaussian data


%Now, run the model itself. this model is for bleached data only

%measured reflectance is the retinal reflectance at a given pixel
location.

%create the function using the above equation

fun = @(x,wavelengths,measured_reflectance)...

    ((model_constants(:,2).*Rlens).*10.^-(model_constants(:,9)))+...
lens section of model equation
```

```
    ((model_constants(:,3).*x(1)).*10.^-
(2.*(model_constants(:,9)+(model_constants(:,4).*Dmp))))+... RNFL
section of model equation

    ((model_constants(:,5).*Rr_out).*10.^-
(2.*(model_constants(:,9)+(model_constants(:,4).*Dmp))))+... RPE
reflectance section of model equation

    ((model_constants(:,8).*x(4)).*10.^-
(2.*(model_constants(:,9)+(model_constants(:,4).*Dmp)+(model_constants
(:,6).*x(2))+(model_constants(:,7).*x(3))))) %scleral section of model
equation.


%the model fitting algorithm, (levenberg-marquardt)

options = optimoptions(@lsqcurvefit,'Algorithm','trust-region-
reflective','Display','off','MaxFunEvals', 30000, 'MaxIter',
1600);%'FunctionTolerance', 1e-7, 'OptimalityTolerance', 1e-7,
'MaxFunctionEvaluations', 30000);

x =
lsqcurvefit(fun,x0,wavelengths,measured_reflectance,lb,ub,options);
%(the equation, the variables, the Xdata, the Ydata, lower bounds,
upper bounds, options/settings)


i = 1;

% the model fitting procedure.

for columns = 1:columns %y pixel location

    for rows = 1:rows %x pixel location

        x = para_c; %reset to pre-determined constants

        measured_reflectance = double(images(:,columns,rows)); %obtain
retinal reflectance from the bleached images.

        Dmp = double(MacPig_matrix(columns,rows)); %obtain Dmp from
the macular pigment map


        if measured_reflectance(1,1) == [0]; %i.e. outside the
circular crop - don't bother modelling

            x = [0 0 0 0];

            x0 = [0 0 0 0];

        else

            %run the model

            x =
lsqcurvefit(fun,x0,wavelengths,measured_reflectance,lb,ub,options);
%(the equation, the variables, the Xdata, the Ydata, lower bounds,
upper bounds, options/settings)

        end
```

```
        modelled_stray_light =... %calculate the anterior stray light
from lens and inner retinal

            ((model_constants(:,2).*Rlens).*10.^-
(model_constants(:,9)))+... lens section of model equation

            ((model_constants(:,3).*x(1)).*10.^-
(2.*(model_constants(:,9)+(model_constants(:,4).*Dmp)))); % inner
retinal section of model equation


        % save the topography maps

        Vr_in_map(columns, rows) = x(1);

        Vhaem_map(columns, rows) = x(2);

        Vmelanin_map(columns, rows) = x(3);

        Vsclera_map(columns, rows) = x(4);

        anterior_stray_light_stack(:, columns, rows) =
modelled_stray_light;


    end

end

end
```

Function, Image fit 2 spectra to image

```
function [rod_photoreceptors_frame, cone_photoreceptors_frame] =
Image_fit_2_spectr (pigmentOD,rod,cone)

%fits the spectra from a single cycle. It then compares this to the
pre-%determined normalised rod and cone spectra from the prelim data
set and %defined in the parent routine 'topographical modelling.m'.
This routine %uses a sub routine 'Fit 2 Pigments' to compare and model
the spectra signature of the

%experimental data.


[LEDs, rows, columns] = size(pigmentOD);

% Rphotoreceptors = zeros(10,1,15,15);% this is the array populated by
RC estimates from fitpgiments

% spectra_frame = zeros(LEDs, nCycles, rows, columns);

% spectra_pixel = zeros(10,1);


%pre-index variables

rod_photoreceptors_frame = zeros(rows,columns);
```

```
cone_photoreceptors_frame = zeros(rows,columns);

spectra_pixel = zeros(LEDs,1);


%break the image down to individual pixels

for y = 1:columns

    for x = 1:rows

        for LEDs = 1:LEDs

            signal_pixel(:,:,:) = pigmentOD(LEDs,x,y); % this is a OD
at a single wavelength for a single pixel.

            spectra_pixel(LEDs,:) = signal_pixel; % this is the
spectrum for a single pixel.

        end

        spectra_pixel = spectra_pixel'; %translates the spectra into
the correct shape for fitpigments4 to work.


        [estimates] = fit2pigments(spectra_pixel,rod,cone); % this
calls up the fitpigment

        % programme to do the fitting, which eventually populates the
array

        % RCphotoreceptors defined at the beginning of this program

        r = estimates (1); %rod response for a single pixel

        c = estimates (2); %cone response for a single pixel


        rod_photoreceptors_frame(x,y) = r; %single frame of fitted rod
response

        cone_photoreceptors_frame(x,y) = c; %single frame of fitted
cone response

    end

end

end
```

Function: Fit 2 pigments

```
function [OD_estimates, ModelCurve] = fit_2_pigments(ydata,rod,cone)

% Call fminsearch with a random starting point.


%Ver2


% - this gives a good model for the data. However, the proportion

%involvement ('OD_estimates') from the rods and L cones is
insignificant and often negative.
```

```
%This needs to be constrained to a positive value whilst retaining
this

%fit.

% - ModelCurve is the 2nd function output, this corresponds to the
final

% iteration of the model and thus an accurate representation of the
model

% is now shown in pigments8


%edit by CT & TM 28.05.14


%Ver3

% - This version will only check for cones and rods, as currently our
data

% does not contain the required spectral peaks for the model to remove
3

% curves.

% - To revert to 3 pigments the arrays after start_point and in

% fminsearchbnd need to be 3, not 2). The functions c and cone need to
be

% reverted to m and mcone in both this function AND the pigments main

%program (as in fitpigments1). Finally replace

%FittedCurve = (rod*r)+(cone*C);

%with

%FittedCurve = (rod*r)+(mcone*m)+(lcone*l);

%}

%Ver4 loads the arguments absorption spectra in from the main program
(rod and cone)


start_point = [0.1 0.1]; %define starting points


OD_estimates = fminsearch(@expfun, start_point);


% expfun accepts curve parameters as inputs, and outputs sse,

% the sum of squares error for A * exp(-lambda * xdata) - ydata,

% and the FittedCurve. FMINSEARCH only needs sse, but we want to

% plot the FittedCurve at the end.
```

```
    function [sse] = expfun(params)
        r = params(1);
        c = params(2);

        ModelCurve = (rod*r)+(cone*c);
        ErrorVector = ModelCurve - ydata;
        sse = sum(ErrorVector .^ 2);
    end
end
```

Bibliography

Abelsdorff, G. 1897. Die ophthalmoskopische erkennbarkeit des sehpurpers. *Z. Psychol. Physiol. Sinnesorg* 14, pp. 77-90.

Abelsdorff, G. 1898. Physiologische beobachtungen am auge der krokodille. *Archiv für Anatomie, Physiologie und Wissenschaftliche Medicin* 19, pp. 155-167.

Alm, A. and Bill, A. 1973. Ocular and optic nerve blood flow at normal and increased intraocular pressures in monkeys (Macaca irus): a study with radioactively labelled microspheres including flow determinations in brain and some other tissues. *Experimental Eye Research* 15(1), pp. 15-29.

Alpern, M. 1971. Rhodopsin kinetics in the human eye. *The Journal of Physiology* 217(2), pp. 447-471.

Alpern, M. and Pugh, E. N. 1974. The density and photosensitivity of human rhodopsin in the living retina. *The Journal of Physiology* 237(2), pp. 341-370.

Alpern, M. and Pugh Jr., E. N. 1974. The density and photosensitivity of human rhodopsin in the living retina. *The Journal of Physiology* 237(2), pp. 341-370.

Anderson, T. W. 1963. Asymptotic theory for principal component analysis. *Annals of Mathematical Statistics* 34(1), pp. 122-148.

Bailey, A. J. 1987. Structure, Function and Aging of the Collagens of the Eye. *EYE: Transactions of the Ophthalmological Societies of the United Kingdom* 1, pp. 175-183.

Baker, H. D. et al. 1989. An improved retinal densitometer: design concepts and experimental applications.*Visual Neuroscience*. Vol. 3. England, pp. 71-80.

Baker, H. D. et al. 1991. Experimental stray light in retinal densitometry. *Visual Neuroscience* 6, pp. 615-620.

Bashkatov, A. N. et al. eds. 2009. *Optical clearing of human eye sclera*. *Conference on Ophthalmic Technologies XIX.* San Jose, CA, Jan 24-26. Bellingham: SPIE The International Soc Optical Engineering.

Behar-Cohen, F. et al. 2014. Ultraviolet damage to the eye revisited: eye-sun protection factor (E-SPF®), a new ultraviolet protection label for eyewear. *Clinical Ophthalmology* 8, pp. 87-104.

Berendschot, T. T. et al. 1996a. Origin of tapetal-like reflexes in carriers of X-linked retinitis pigmentosa. *Investigative Ophthalmology and Visual Science* 37(13), pp. 2716-2723.

Berendschot, T. T. et al. 2003. Fundus reflectance - historical and present ideas. *Progress in Retinal and Eye Research* 22(2), pp. 171-200.

Berendschot, T. T. et al. 2010. Directional model analysis of the spectral reflection from the fovea and para-fovea. *Journal of Biomedical Optics* 15(6), pp. 65005-65014.

Berendschot, T. T. et al. 1996b. Foveal cone mosaic and visual pigment density in dichromats. *The Journal of Physiology* 492(1), pp. 307-314.

Binns, A. M. and Margrain, T. H. 2005. Evaluation of retinal function using the Dynamic Focal Cone ERG. *Ophthalmic and Physiological Optics* 25(6), pp. 492-500.

Binns, A. M. and Margrain, T. H. 2007. Evaluating retinal function in age-related maculopathy with the ERG photostress test. *Investigative Ophthalmology and Visual Science* 48(6), pp. 2806-2813.

Boettner, E. A. and Wolter, J. R. 1962. Transmission of the ocular media. *Investigative Ophthalmology and Visual Science* 1(6), pp. 776-783.

Bok, D. 1993. The retinal pigment epithelium: a versatile partner in vision. *Journal of Cell Science* supplement 17, pp. 189-195.

Bone, R. A. et al. 2007. Macular pigment, photopigments, and melanin: distributions in young subjects determined by four-wavelength reflectometry. *Vision Research* 47, pp. 3259-3268.

Bone, R. A. et al. 1988. Analysis of the macular pigment by HPLC - retinal distribution and age study. *Investigative Ophthalmology and Visual Science* 29(6), pp. 843-849.

Booij, J. C. et al. 2010. The dynamic nature of Bruch's membrane. *Progress in Retinal and Eye Research* 29(1), pp. 1-18.

Brindley, G. S. and Willmer, E. N. 1952. The reflexion of light in the macular and nperipheral fundus oculi in man. *The Journal of Physiology* 116(3), pp. 350-356.

Brown, K. T. 1968. The electroretinogram: its components and their origin. *Vision Research* 8, pp. 633-677.

Bruggen, J. P. et al. 1992. Foveal photopigment kinetics - abnormality: an early sign in myotonic dystrophy? *British Journal of Ophthalmology* 76(10), pp. 594-597.

Budde, W. 1976. Calibration Reflectance Standards. *Journal of Research* 80(4), pp. 585-592.

Campbell, F. W. and Rushton, W. A. H. 1955. Measurement of the scotopic pigment in the living human eye. *The Journal of Physiology* 130(1), pp. 131-147.

Carr, R. E. and Ripps, H. 1967. Rhodopsin kinetics and rod adaptation in Oguchi's disease. *Investigative Ophthalmology* 6(6), pp. 426-436.

Charman, W. N. 1980. Reflection of plane-polarized light by the retina. *British Journal of Physiological Optics* 34, pp. 34-49.

Chylack, L. T. et al. 1993. The Lens Opacities Classification System III. *Archives of Ophthalmology* 111(6), pp. 831-836.

Cochran, R. N. and Horne, F. H. 1977. Statistically weighted principal component analysis of rapid scanning wavelength kinetics experiments. *Analytical Chemistry* 49(6), pp. 846-853.

Coile, D. C. and Baker, H. D. 1992. Foveal dark-adaptation, photopigment regeneration, and aging. *Visual Neuroscience* 8(1), pp. 27-39.

Coleman, T. F. and Li, Y. 1994. An interior trust region approach to nonlinear minimization subject to bounds. *SIAM Journal on Optimization* 6(2), pp. 418-446.

Copenhagen, D. R. and Jahr, C. E. 1989. Release of endogenous excitatory amino-acids from turtle photoreceptors. *Nature* 341(6242), pp. 536-539.

Curcio, C. A. et al. 1990. Human photoreceptor topography. *Journal of Comparative Neurology* 292(4), pp. 497-523.

Curcio, C. A. et al. 1987. Distribution of cones in human and monkey retina - individual variability ad radial asymmetry. *Science* 236(4801), pp. 579-582.

Dartnall, H. J. A. et al. 1983. Human visual pigments - microspectrophotometric results from the eyes of 7 persons. *Proceedings of the Royal Society Series B: Biological Sciences* 220(1218), pp. 115-130.

Daxer, A. et al. 1998. Collagen fibrils in the human corneal stroma: structure and aging. *Investigative Ophthalmology and Visual Science* 39(3), pp. 644-648.

de Almeida, M. S. and Carvalho, L. A. 2007. Different schematic eyes and their accuracy to the *in vivo* eye: A quantitative comparison study. *Brazilian Journal of Physics* 37(2A), pp. 378-387.

DeLint, P. J. et al. 2000. Slow optical changes in human photoreceptors induced by light. *Investigative Ophthalmology and Visual Science* 41(1), pp. 282-289.

DeLint, P. J. et al. 1996. Scanning laser densitometry in visual acuity loss of unknown origin. *British Journal of Ophthalmology* 80(12), pp. 1051-1054.

Delori, F. C. and Pflibsen, K. P. 1989. Spectral refelctance of the human ocular fundus. *Applied Optics* 28(6), pp. 1061-1077.

Demarco, P. et al. 1992. Full-spectrum cone sensitivity functions for X-chromosomes-linked anomalous trichromates. *Journal of the Optical Society of America. Series A: O ptics, Image Science and Vision* 9(9), pp. 1465-1476.

Dimitrov, P. N. et al. 2008. Measuring rod and cone dynamics in age-related maculopathy. *Investigative Ophthalmology and Visual Science* 49(1), pp. 55-65.

Elsner, A. E. et al. 1998. Foveal cone photopigment distribution: small alterations associated with macular pigment distribution. *Investigative Ophthalmology and Visual Science* 39(12), pp. 2394-2404.

Elsner, A. E. et al. 1993. Mapping cone photopigment optical density. *Journal of the Optical Society of America. Series A: Optics, Image Science and Vision* 10(1), pp. 52-58.

Elsner, A. E. et al. 1992. Reflectometry in retinal tears and detachments.

Clinical Vision Sciences 7(6), pp. 489-500.

Escudero-Sanz, I. and Navarro, R. 1999. Off-axis aberrations of a wide-angle schematic eye model. *Journal of the Optical Society of America. Series A: O ptics, Image Science and Vision* 16, pp. 1881-1891.

Faulkner, D. J. and Kemp, C. M. 1984. Human rhodopsin measurement using a T.V.-based imaging fundus reflectometer. *Vision Research* 24, pp. 221-231.

Fishman, G. A. et al. 2005. Short-Term Intervisit Variability of ERG Amplitudes in Normal Subjects and Patients with Retinitis Pigmentosa. *Retina* 25(8), pp. 1014-1021.

Fowler, R. W. et al. 1977. Reflection of light by small areas of the ocular fundus. *Investigative Ophthalmology and Visual Science* 16(10), pp. 981-986.

Fulton, A. B. and Hansen, R. M. 1987. Foveal cone pigments and sensitivity in young patients with Usher's syndrome. *American Journal of Ophthalmology* 103(2), pp. 150-160.

Fulton, A. B. and Hansen, R. M. 1988. The relation of rhodopsin and scotopic retinal sensitivity in sector retinitis pigmentosa. *American Journal of Ophthalmology* 105(2), pp. 132-140.

Gabel, V. P. et al. 1978. Visible and near infrared light absorption in pigment epithelium and choroid. In: Shimizu, K. ed. *XXIII Concilium Opthtalmologicum.* Kyoto, Excerpta Medica, Amsterdam-Oxford.

Gaffney, A. J. et al. 2011. The repeatability of the Goldmann-Weekers adaptometer for measuring cone adaptation. *Documenta Ophthalmologica* 122(2), pp. 71-75.

Gaffney, A. J. et al. 2012. Ageing and cone dark adaptation. *Optometry and Vision Science* 89(8), pp. 1219-1224.

Ginis, H. et al. 2013. Wavelength dependence of the ocular straylight. *Visual Pyschophysics and Physiological Optics* 54(5), pp. 3702-3708.

Goel, M. et al. 2010. Aqueous humor dynamics: A reivew. *The Open Ophthalmology Journal* 4, pp. 52-59.

Gorrand, J. M. et al. 1984. Diffusion of the retinal layers of the living human eye. *Vision Research* 24(9), pp. 1097-1106.

Granit, R. 1933. The components of retinal action potential in mammals and their relation to the discharge in the optic nerve. *The Journal of Physiology* 77(3), pp. 207-239.

Grover, S. et al. 2003. Variability of full-field electroretinogram responses in subjects without diffuse photoreceptor cell disease. *Ophthalmology* 110(6), pp. 1159-1163.

Halaka, F. G. et al. 1985. The use of principal component analysis to resolve the spectra and kinetics of cytochrome c oxidase reduction by 5.10-dihydro-5-methyl-phenazine. *Biophysical Journal* 48(2), pp. 209-219.

Hammer, M. and Schweitzer, D. 2002. Quantitative reflection spectroscopy at the human ocular fundus. *Physics in Medicine and Biology* 47(2), pp. 179-191.

Hayreh, S. S. 1975. Segmental nature of choroidal vasculature. *British Journal of Ophthalmology* 59(11), pp. 631-648.

Hecht, S. et al. 1937. The influence of light adaptation on subsequent dark adaptation of the eye. *Journal of General Physiology* 20(6), pp. 831-850.

Helmoltz, H. 1851. Beschreibung eines Augenspiegels zur Untersuchung der Netz haut im lebenden Auge. *Archives of Ophthalmology* (11), pp. 827-830.

Henrich, P. B. et al. 2012. Nanoscale topographic and biomechanical studies of the human internal limiting membrane. *Investigative Ophthalmology and Visual Science* 53(6), pp. 2561-2570.

Hodgkinson, I. J. et al. 1994. Point-spread function for light scattered in the human ocular fundus. *Journal of the Optical Society of America. Series A: Optics, Image Science and Vision* 11(2), pp. 479-486.

Hollins, M. and Alpern, M. 1973. Dark adaptation and visual pigment regeneration in human cones. *The Journal of General Physiology* 62(4), pp. 430-447.

Hood, C. and Rushton, W. A. 1971. The Florida retinal densitometer. *The Journal of Physiology* 217(1), pp. 213-229.

Hood, D. C. 2000. Assessing retinal function with the multifocal technique. *Progress in Retinal and Eye Research* 19(5), pp. 607-639.

Horio, N. et al. 1999. Kinetics of foveal cone photopigment in myopia without chorioretinal degeneration. *Japanese Journal of Ophthalmology* 43(1), pp. 44-47.

Jackson, G. R. et al. 2014. Diagnostic sensitivity and specificity of dark adaptometry for detection of age-related macular degeneration. *Investigative Ophthalmology and Visual Science* 55(3), pp. 1427-1431.

Jacques, S. L. 2013. Optical properties of biological tissues: A review. *Physics in Medicine and Biology* 58, pp. 37-61.

Jolliffe, I. T. and Cadima, J. 2016. Principal component analysis: a review and recent developments. *Philosophical Transactions of the Royal Society. Series A: Mathematical, Physical and Engineering Sciences* 374(2065), p. 16.

Justice, J. and Lehmann, R. P. 1976. Cilioretinal arteries - study based on review of stereo fundus photographs and fluoroscein angiographic findings. *Archives of Ophthalmology* 94(8), pp. 1355-1358.

Kemp, C. M. et al. 1988. Visual function and rhodopsin levels in humans with vitamin A deficiency. *Experimental Eye Research* 46(2), pp. 185-197.

Keunen, J. E. et al. 1989. Retinal densitometry in acute posterior multifocal placoid pigment epitheliopathy. *Investigative Ophthalmology and Visual Science* 30(7), pp. 1515-1521.

Keunen, J. E. et al. 1987. Density of foveal cone pigments at older age. *Investigative Ophthalmology and Visual Science* 28(6), pp. 985-991.

Khachik, F. et al. 1997. Identification of lutein and zeaxanthin oxidation products in human and monkey retinas. *Investigative Ophthalmology and Visual Science* 38(9), pp. 1802-1811.

Kilbride, P. E. et al. 1989. Human macular pigment assessed by imaging fundus reflectometry. *Vision Research* 29, pp. 663-674.

Kilbride, P. E. et al. 1986. Foveal cone pigment density difference and reflectance in retinitis pigmentosa. *Archives of Ophthalmology* 104(2), pp. 220-224.

Kilbride, P. E. and Keehan, K. M. 1990. Visual pigments in the human macula assessed by imaging fundus reflectometry. *Applied Optics* 29, pp. 1427-1435.

Kilbride, P. E. et al. 1983. Determination of human cone pigment density difference spectra in spatially resolved regions of the fovea. *Vision Research* 23(12), pp. 1341-1350.

King-Smith, P. E. 1971. The optical density of erythrolabe determined by retinal densitometry. *Journal of Physiology* 218(Suppl), pp. 100-101.

King-Smith, P. E. 1973a. The optical density of erythrolabe determined by a new method. *Journal of Physiology* 230(3), pp. 551-560.

King-Smith, P. E. 1973b. The optical density of erythrolabe determined by retinal densitometry using the self-screening method. *Journal of Physiology* 230(3), pp. 535-549.

Knighton, R. W. et al. 1989. The spectral reflectance of the nerve fiber layer of the macaque retina. *Investigative Ophthalmology & Visual Science* 30(11), pp. 2393-2402.

Kolb, H. 2011. *Simple Anatomy of the Retina*. Available at: http://webvision.med.utah.edu/book/part-i-foundations/simple-anatomy-of-the-retina/ [Accessed: 31/10/13].

Kolb, H. 2012. *Gross Anatomy of the Eye*. Available at: http://webvWoSon.med.utah.edu/book/part-i-foundations/gross-anatomy-of-the-eye/ [Accessed: 31/10/13].

Kolb, H. 2013. *Photoreceptors*. Available at: http://webvision.med.utah.edu/book/part-ii-anatomy-and-physiology-of-the-retina/photoreceptors/ [Accessed: 31/10/13].

Kollias, N. 1995. The spectroscopy of human melanin pigmentation. In: Zeise, L. et al. eds. *Melanin: Its Role in Human Photoprotection*. Kansas: Valdenmar Publishing Co., pp. 31-38.

Kondo, M. and Sieving, P. A. 2002. Post-photoreceptoral activity dominates primate photopic 32-Hz ERG for sine-, square-, and pulsed stimuli. *Investigative Ophthalmology and Visual Science* 43(7), pp. 2500-2507.

Kraft, T. W. et al. 1993. Visual transduction in human rod photoreceptors. *The Journal of Physiology* 464, pp. 747-765.

Kubelka, P. and Munk, F. 1931. Ein Beitrag zur Optik der Farbanstriche. *Zeitschrift für Physik* 12, pp. 593-601.

Lamb, T. D. and Pugh, E. N. 2004. Dark adaptation and the retinoid cycle of vision. *Progress in Retinal and Eye Research* 23(3), pp. 307-380.

Landrum, J. T. et al. 1997. The macular pigment: a possible role in protection from age-related macular degeneration. *Advances in pharmacology* 38, pp. 537-556.

Le Goff, M. M. and Bishop, P. N. 2008. Adult vitreous structure and postnatal changes. *Eye* 22(10), pp. 1214-1222.

Lewis, J. W. et al. 1997. Metarhodopsin III formation and decay kinetics: Comparison of bovine and human rhodopsin. *Vision Research* 37(1), pp. 1-8.

Liem, A. T. et al. 1996. Clinical applications of fundus reflection densitometry. *Survey of Ophthalmology* 41(1), pp. 37-50.

Liem, T. A. et al. 1991. Rod Densitometry in the Aging Human Eye. *Investigative Ophthalmology and Visual Science* 32(10), pp. 2676-2682.

Mahroo, O. A. R. and Lamb, T. D. 2004. Recovery of the human photopic electroretinogram after bleaching exposures: estimation of pigment regeneration kinetics. *The Journal of Physiology* 554(2), pp. 417-437.

Mahroo, O. A. R. and Lamb, T. D. 2012. Slowed recovery of human photopic ERG a-wave amplitude following intense bleaches: a slowing of cone pigment regeneration? *Documenta Ophthalmologica* 125(2), pp. 137-147.

Manjunath, V. et al. 2010. Choroidal thickness in normal eyes measured using Cirrus HD optical coherence tomography. *American Journal of Ophthalmology* 150(3), pp. 325-330.

Masella, B. D. et al. 2014. New Wrinkles in Retinal Densitometry. *Investigative Ophthalmology and Visual Science* 55(11), pp. 7525-7534.

Mata, N. L. et al. 2002. Isomerization and oxidation of vitamin a in cone-dominant retinas: A novel pathway for visual-pigment regeneration in daylight. *Neuron* 36(1), pp. 69-80.

Matsumoto, B. et al. 1984. Topographic variations in the rabbit and primate internal limiting membrane. *Investigative Ophthalmology and Visual Science* 25(1), pp. 71-82.

McBee, J. K. et al. 2001. Confronting complexity: the interlink of phototransduction and retinoid metabolism in the vertebrate retina. *Progress in Retinal and Eye Research* 20(4), pp. 469-529.

McCulloch, D. L. et al. 2015. ISCEV Standard for full-field clinical electroretinography (2015 update). *Documenta Ophthalmologica* 130(1), pp. 81-83.

Miller, R. F. and Dowling, J. E. 1970. Intracellular responses of the Müller (glial) cells of mudpuppy retina: their relation to the b-wave of the electroretinogram. *Journal of Neurophysiology* 33, pp. 323-341.

Morgan, J. I. W. and Pugh, E. N. 2013. Scanning laser ophthalmoscope measurement of local fundus reflectance and autofluorescence changes arising from rhodopsin bleaching and regeneration. *Investigative Ophthalmology and Visual Science* 54(3), pp. 2048-2059.

Neitz, M. et al. 1991. Spectral tuning of pigments underlying red-green color vision. *Science* 252, pp. 971-974.

Norren, D. V. and Vos, J. J. 1974. Spectral transmission of the human optical media. *Vision Research* 14(11), pp. 1237-1244.

Nowak, J. Z. 2006. Age-related macular degeneration (AMD): pathogenesis and therapy. *Pharmacological Reports* 58(3), pp. 353-363.

Ojima, A. et al. 2011. Photopigments in central serous chorioretinopathy. *American Journal of Ophthalmology* 151(6), pp. 940-952.

Osterberg, G. 1935. Topography of the layer of rods and cones in the human retina. *Acta Ophthalmologica Supplementum* 6, pp. 1-103.

Owsley, C. 2011. Aging and vision. *Vision Research* 51(13), pp. 1610-1622.

Oyster, C., W. 1999. *The Human Eye: Structure and Function*. Sunderland, Massachusetts: Sinauer Associates, inc.

Pauleikhoff, D. et al. 1990. Aging changes in Bruch's membrane: a histochemical and morphologic study. *Ophthalmology* 97, pp. 171-178.

Paupoo, A. A. V. et al. 2000. Human cone photoreceptor responses measured by the electoretinogram a-wave during and after exposure to intense illumination. *The Journal of Physiology* 529(2), pp. 469-482.

Pedrotti, L. S. and Pedrotti, F. L. 1998. *Optics and Vision*. Pearson.

Pepe, I. M. 2001. Recent advances in our understanding of rhodopsin and phototransduction. *Progress in Retinal and Eye Research* 20(6), pp. 733-759.

Perlman, I. 2012. *The electroretinogram: ERG*. Available at: http://webvision.med.utah.edu/book/electrophysiology/the-electroretinogram-erg/ [Accessed: 04/11/13].

Perlman, I. and Auerbach, E. 1981. The relationship between visual sensitivity and rhodopsin density in retinitis pigmentosa. *Investigative Ophthalmology and Visual Science* 20(6), pp. 758-765.

Pianta, M. J. and Kalloniatis, M. 2000. Characterisation of dark adaptation in human cone pathways: an application of the equivalent background hypothesis. *The Journal of Physiology* 528(3), pp. 591-608.

Polyak, S. L. 1941. *The retina: The anatomy and the histology of the retina in man, ape, and monkey, including the consideration of visual functions, the history of physiological optics, and the histological laboratory technique*. Chicago: University of Chicago Press.

Pugh, E. N. 1975. Rhodopsin flash photolysis in man. *The Journal of Physiology* 248(2), pp. 393-412.

Quigley, H. A. et al. 1982. Optic-nerve damage in human glacuoma. III. Quantative correlation of nerve-fibre loss and visual-field defect in glaucoma, ischeamic neuropathy, papilledema and toxic neuropathy. *Archives of Ophthalmology* 100(1), pp. 135-146.

Ramirez, J. M. et al. 1999. Choroidal vessel wall: hypercholesterolaemia-

induced dysfunction and potential role of statins. In: Sugi, H. ed. *Current basic and pathological approaches to the function of muscle cells and tissues - from molecules to humans*. InTech.

Ratanapakorn, T. et al. 2006. Single dose of 1% tropicamide and 10% phenylephrine for pupil dilation. *Journal of the Medical Association of Thailand* 89(11), pp. 1934-1939.

Reading, V. M. and Weale, R. A. 1974. Macular pigment and chromatic aberration. *Journal of the Optical Society of America* 64(2), pp. 231-234.

Ripps, H. and Weale, R. A. 1963. Cone pigments in the normal human fovea. *Vision Research* 3, pp. 532-543.

Ripps, H. and Weale, R. A. 1965. Analysis of foveal densitometry. *Nature* 205(4966), pp. 52-56.

Ripps, H. and Weale, R. A. 1969a. Flash bleaching of rhodopsin in the human retina. *The Journal of Physiology* 200(1), pp. 151-159.

Ripps, H. and Weale, R. A. 1969b. Rhodopsin Regeneration in Man. *Nature* 222, pp. 775-778.

Robson, J. G. and Frishman, L. J. 2014. The rod-driven a-wave of the dark-adapted mammalian electroretinogram. *Progress in Retinal and Eye Research* 39, pp. 1-22.

Rolfs, M. 2009. Microsaccades: Small steps on a long way. *Vision Research* 49(20), pp. 2415-2441.

Roorda, A. and Williams, D. R. 1999. The arrangement of the three cone classes in the living human eye. *Nature* 397(6719), pp. 520-522.

Rushton, W. A. H. 1956a. The difference spectrum and the photosensitivity of rhodopsin in the living human eye. *The Journal of Physiology* 134(1), pp. 11-29.

Rushton, W. A. H. 1956b. The rhodopsin density in human rods. *The Journal of Physiology* 134(1), pp. 30-46.

Rushton, W. A. H. 1961a. Dark adaptation and the regeneration of rhodopsin. *The Journal of Physiology* 156(1), pp. 166-178.

Rushton, W. A. H. 1961b. Rhodopsin measurement and dark-adaptation in a subject deficient in cone vision. *The Journal of Physiology* 156(1), pp. 193-205.

Rushton, W. A. H. 1963a. A cone pigment in protanope. *The Journal of Physiology* 168(2), pp. 345-359.

Rushton, W. A. H. 1963b. Cone pigment kinetics in protanope. *The Journal of Physiology* 168(2), pp. 374-388.

Rushton, W. A. H. 1963c. Density of chlorolabe in foveal cones of protanope. *The Journal of Physiology* 168(2), pp. 360-373.

Rushton, W. A. H. 1965. Stray light and measurement of mixed pigments in retina. *The Journal of Physiology* 176(1), pp. 46-55.

Rushton, W. A. H. and Campbell, F. W. 1954. Measurement of rhodopsin in the living human eye. *Nature* 174, pp. 1096-1097.

Rushton, W. A. H. et al. 1969. Dark adaptation and the rate of pigment regeneration. *Vision Research* 9, pp. 1473-1479.

Rushton, W. A. H. and Powell, D. S. 1972. Rhodopsin content and visual threshold of human rods. *Vision Research* 12(6), pp. 1073-1081.

Sabesan, R. et al. 2015. Characterizing the human cone photoreceptor mosaic via dynamic photopigment densitometry. *Plos One* 10(12), pp. 1-12.

Sandberg, M. A. et al. 1999. Acuity recovery and cone pigment regeneration after a bleach in patients with retinitis pigmentosa and rhodopsin mutations. *Investigative Ophthalmology and Visual Science* 40(10), pp. 2457-2461.

Schallek, J. et al. 2009a. Stimulus-evoked intrinsic optical signals in the retina: Pharmacologic dissection reveals outer retinal origins. *Investigative Ophthalmology and Visual Science* 50(10), pp. 4873-4880.

Schallek, J. et al. 2009b. Stimulus-evoked intrinsic optical signals in the retina: spatial and temporal characteristics. *Investigative Ophthalmology and Visual Science* 50(10), pp. 4865-4872.

Sekiryu, T. et al. 2009. Clinical application of autofluorescence densitometry with a scanning laser ophthalmoscope. *Investigative Ophthalmology and Visual Science* 50, pp. 2994-3002.

Sickel, W. 1972. Retinal metabolism in dark and light. In: Fuortes, M.G.F. ed. *Physiology of Photoreceptor Organs*. Cologne, pp. 667-727.

Sieving, P. A. et al. 1995. Dark-light: model for nightblindness from the human rhodopsin Gly-90-->Asp mutation. *Proceedings of the National Academy of Sciences of the United States of America* 92(3), pp. 880-884.

Smith, V. C. et al. 1981. Cone visual photo pigment measured by retinal densitometry. *Investigative Ophthalmology and Visual Science* 20(3), pp. 205-205.

Smith, V. C. et al. 1983. Densitometric measurement of human cone photopigment kinetics. *Vision Research* 23, pp. 517-524.

Snodderly, D. M. et al. 1984. The macular pigment. II. Spatial distribution in primate retinas. *Investigative Ophthalmology and Visual Science* 25, pp. 674-685.

Stockman, A. and Sharpe, L. T. 2000. Spectral sensitivities of the middle- and long-wavelength sensitive cones derived from measurements in observers of known genotype. *Vision Research* 40, pp. 1711-1737.

Strauss, O. 2005. The retinal pigment epithelium in visual function. *Physiological Reviews* 85(3), pp. 845-881.

Theelen, T. et al. 2008. Analysis of visual pigment by fundus autofluorescence. *Experimental Eye Research* 86(2), pp. 296-304.

Thomas, M. M. and Lamb, T. D. 1999. Light adaptation and dark adaptation of human rod photoreceptors measured from the a-wave of the

electroretinogram. *The Journal of Physiology* 518(2), pp. 479-496.

Tornow, R. P. et al. 1999. Scanning laser densitometry and color perimetry demonstrate reduced photopigment density and sensitivity in two patients with retinal degeneration. *Vision Research* 39(21), pp. 3630-3641.

Tsunoda, K. et al. 2009. Origins of retinal intrinsic signals: A series of experiments on retinas of macaque monkeys. *Japanese Journal of Ophthalmology* 53(4), pp. 297-314.

Tunnacliffe, A. H. 1993. *Introduction to Visual Optics*. 4th ed. London: ABDO College of Education.

van Assendelft, O. W. 1970. *Spectroscopy of haemoglobin derivatives*. Illinois: Springfield.

van Blokland, G. J. and van Norren, D. 1986. Intensity and polarization of light scattered at small angles from the human fovea. *Vision Research* 26(3), pp. 485-494.

van de Kraats, J. et al. 1996. The pathways of light measured in fundus reflectometry. *Vision Research* 36(15), pp. 2229-2247.

van de Kraats, J. and van Norren, D. 2007. Optical density of the aging human ocular media in the visible and the UV. *Journal of the Optical Society of America. Series A: Optics, Image, Science and Vision* 24(7), pp. 1842-1857.

van de Kraats, J. and van Norren, D. 2008. Directional and nondirectional spectral reflection from the human fovea. *Journal of Biomedical Optics* 13(2),

van Meel, G. J. et al. 1993. Scanning laser densitometry in multiple evanescent white dot syndrome. *Retina* 13(1), pp. 29-35.

van Norren, D. and Tiemeijer, L. F. 1986. Spectral reflectance of the human eye. *Vision Research* 26(2), pp. 313-320.

van Norren, D. and van de Kraats, J. 1981. Continuously recording retinal densitometer. *Vision Research* 21(6), pp. 897-906.

van Norren, D. and van de Kraats, J. 1989a. Imaging retinal densitometry with a confocal scanning laser ophthalmoscope. *Vision Research* 29(12), pp. 1825-1830.

van Norren, D. and van de Kraats, J. 1989b. Retinal densitometer with the size of a fundus camera. *Vision Research* 29, pp. 369-374.

Villermet, G. M. and Weale, R. A. 1966. Effect of light history on photolysability of human visual pigment *in situ*. *Proceedings of the Royal Society. Series B: Biological Sciences* 164(994), pp. 96-105.

Vos, J. J. et al. 1965. Absolute spectral reflectance of the fundus oculi. *Journal of the Optical Society of America* 55(5), pp. 573-578.

Vos, J. J. and van Norren, D. 1974. Spectral transmission of the human ocular media. *Vision Research* 14, pp. 1237-1244.

Wang, J. S. and Kefalov, V. J. 2011. The cone-specific visual cycle. *Progress in Retinal and Eye Research* 30(2), pp. 115-128.

Weale, R. A. 1988. Age and transmittance of the human crystalline lens. *The Journal of Physiology* 395(1), p. 10.

Weidner, V. R. et al. 1985. Laboratory intercomparison study of pressed polytetrafluro-ethylene powder reflectance standards. *Applied Optics* 24(14), pp. 2225-2230.

Weingeist, T. A. 1978. Structure of the ocular vessels. *Archives of Ophthalmology* 96(11), pp. 2137-2142.

Weiter, J. J. et al. 1986. Retinal-pigment epithelial lipofuscin and melanin and choroidal melanin in human eyes. *Investigative Ophthalmology and Visual Science* 27(2), pp. 145-152.

Weiter, J. J. et al. 1984. Visual acuity related to retinal distance from the fovea in macular disease. *Annals of Ophthalmology* 16(2), pp. 174-176.

Westheimer, G. 1966. The maxweillian view. *Vision Research* 6(11-12), pp. 669-683.

Wood, A. et al. 2011. The effect of bleach duration and age on the ERG photostress test. *Graefes Archive for Clinical and Experimental Ophthalmology* 249(9), pp. 1359-1365.

Wooten, B. R. and Geri, G. A. 1987. Psychophysical determination of intraocular light scatter as a function of wavelength. *Vision Research* 27(8), pp. 1291-1298.

Wooten, B. R. and Hammond, B. R. 2002. Macular pigment: influences on visual acuity and visibility. *Progress in Retinal and Eye Research* 21(2), pp. 225-240.

Wyszecki, G. and Stiles, W. S. 1982. *Colour science: concepts and methods*. 2nd ed. New York: Wiley.